Superconducting Nonlinear Kinetic Inductance Devices

Thesis by
Aditya Shreyas Kher

In Partial Fulfillment of the Requirements for the
degree of
Doctor of Philosophy

CALIFORNIA INSTITUTE OF TECHNOLOGY
Pasadena, California

2017
Defended August 30, 2016

Aditya Shreyas Kher
ORCID: 0000-0002-5994-428X

ACKNOWLEDGEMENTS

This has been a very fulfilling thesis project that has been impacted by many people around me during my time at Caltech. I must first thank Prof. Jonas Zmuidzinas for giving me the opportunity to work in his research group, and for coming up with such an interesting, novel topic for me to work on. I had struggled during my first two years at Caltech to find a research group that would suit me in the long run. During my search at the beginning of my third year, Prof. Sandra Troian, in her capacity as Option Representative of the Applied Physics department, suggested that I talk to Jonas about opportunities at JPL. I'm very grateful to Prof. Troian for her guidance, because I probably would have never approached Jonas otherwise, as I was under the impression that he was an astronomer, and that that field was distant from my interests in applied physics. Jonas ended up interviewing me for his own group, and although I'd been unprepared, he gave me the chance to think about joining. This is how I was introduced to the field of superconducting detectors, and I've found it to be one of the most interesting areas of applied physics. By joining, I became one of the few people during these years to enjoy the instruction of the very knowledgeable Prof. Zmuidzinas on topics such as superconductivity, microwave engineering, and noise. I have to also give Jonas credit for encouraging me to apply for the NASA Space Technology Research Fellowship, which I was awarded in 2012. I enjoyed four years of funding from this fellowship, including the opportunity to travel to conferences both in the US and abroad.

Many colleagues at Caltech and JPL contributed greatly to this research. Dr. Peter Day and Dr. Byeong Ho Eom's contributions to this work are invaluable and too numerous to state. Peter must be given additional credit for serving as my de-facto advisor—despite not being a professor—while Jonas was busy with his duties as Chief Technologist of JPL. Our devices would not have existed without the fabrication expertise of Dr. H. G. "Rick" Leduc. The first TES that we used was obtained from Dr. Roger O' Brient, with whom I also enjoyed many useful discussions. Dr. Andrew Beyer helped us get started using the wet dilution refrigerator. Dr. Pierre Echternach must be thanked for letting us borrow liquid helium so many times. Several postdocs, especially Dr. Chris McKenney, Dr. Loren Swenson, and Dr. Erik Shirokoff, helped in getting me up to speed on this field when I first joined the group. Dr. Ran Duan was a helpful officemate during my first year in this group, and his advisor, Prof. Sunil Golwala, graciously agreed to be my "advisor" on paper

for the purpose of the NSTRF. Finally, I have to thank Sheri Stoll, our group admin, for helping with my funding issues and for holding so many packages for me when I went overboard with online shopping.

Los Angeles has been a fantastic place to spend my twenties, and it was made better by the great friends I've been fortunate enough to make at Caltech and elsewhere. The many nights of role-playing games, board games, and everything else that I shared with Tejaswi Venumadhav, Paraj Titum, Scott Geraedts, and Utkarsh Mital helped keep me sane. I learned a lot during my many late-night, wine-fuelled conversations with Britton Sauerbrei. S. Bose was always a blast to hang out with, and was always up for trying something new. I'm also grateful for the friendships I've maintained outside Caltech, which also helped support me during my time here. I would especially like to thank Chris Blondefield and David Mandler, with whom I've somehow kept in touch as if high school never ended, and Max Dukarevich, who has encouraged me to adopt many new perspectives over the years, and has always shown an interest in my research and in learning about physics.

Finally, I would like to thank my family for their unending support. My brother, Abhishek, has become a true friend, especially during my time at Caltech. My extended family has always been supportive, and I've enjoyed indulging their curiosity about my research. And last, but certainly not least, I'd like to thank my parents, who introduced me to science at a very young age, and who have encouraged me throughout my journey. I wouldn't be where I am without them.

ABSTRACT

The transition-edge sensor (TES) is one of the most productive types of detectors currently used for observational cosmology. It is the detector technology used in modern experiments such as POLARBEAR, SPIDER, and BICEP2 for studies of the polarization of the cosmic microwave background radiation. Next-generation instruments demand larger arrays of detectors to increase the sensitivity of the measurement. However, the size of TES arrays is currently limited to $\sim 10^4$ due to the complexity of the readout system. A TES needs to be read out by a sensitive ammeter, and the most sensitive ammeters available are superconducting quantum interference devices (SQUIDs). Large detector arrays require multiplexed readouts, and SQUIDs are not inherently easy to multiplex. Thus, a large effort has taken place over the past decade to develop SQUID multiplexers for TES-based instruments. However, these multiplexers are complicated, requiring feedback electronics or other tricks in order to deal with the peculiarities of SQUIDs, such as their nonlinear, periodic transfer function. In addition, the SQUIDs themselves are complicated and expensive to fabricate, requiring up to 10 layers in the process. SQUID-based readout systems appear daunting for the arrays of 10^4–10^6 detectors that are needed for the focal planes of next-generation instruments.

In this thesis we present a class of devices called kinetic inductance parametric up-converters (KPUPs) that provide a potential solution to the TES readout problem. Broadly, a KPUP is a superconducting device operating in the microwave band that has a nonlinear kinetic inductance. Since the kinetic inductance of a superconductor is a function of the current flowing through it, a low-frequency current signal can be detected by being strongly up-converted to the microwave band by the nonlinearity of the KPUP device, and then measured using a combination of microwave and low-frequency electronics. This can be done with a microresonator, where the superconducting kinetic inductance provides a portion of the resonator's inductance. A large kinetic inductance can be achieved by using a thin film of a high-resistivity superconducting material such as TiN or NbTiN. Nanowires used as lumped-element kinetic inductors in a resonator are of particular interest: a small current in the nanowire changes its inductance and therefore shifts the resonance frequency. A device using this principle is demonstrated with a current sensitivity of $8\,\mathrm{pA}/\sqrt{\mathrm{Hz}}$, making it potentially useful for TES readout and other current-sensing applications. Since this device is a microwave resonator, it can be easily multiplexed

in the frequency domain, offering the potential of a considerably simplified readout compared to SQUID-based systems. We document efforts to integrate this device with a TES, including a successful measurement of the TES bias curve at several different temperatures of the heat bath. A two-stage TES multiplexing scheme is developed, where an array of TESs is read out by a single KPUP device, and an array of such KPUPs is read out in a microwave transmission measurement.

Another version of the device is a transmission line, where its nonlinear kinetic inductance contributes to the total inductance of the line. A DC signal current in the line changes its kinetic inductance, which in turn changes the microwave phase length of the line. The change in phase length can be detected via a microwave transmission measurement of the transmission line. This type of device is demonstrated with a current sensitivity of $5\,\mathrm{pA}/\sqrt{\mathrm{Hz}}$, meaning it is also suitable for TES readout as well as other current-sensing applications. This version of the device has the advantage of greater dynamic range and multi-gigahertz bandwidth, meaning that many more TESs can be read out by a single KPUP device. Also demonstrated is a transmission-line resonator version of the KPUP, which retains much of the dynamic range advantage of the transmission line KPUP while still being naturally easy to multiplex in the frequency domain, similar to the lumped-element device. A strong current response is demonstrated for this version of the device, and efforts to integrate it with a TES array are described. The current sensitivity of the transmission-line resonator could in principle reach levels as low as that of the other two devices.

We also demonstrate a lumped-element resonator in a loop configuration that is natively sensitive to magnetic fields, similar to a SQUID but having the advantage of being easy to multiplex in the frequency domain. A magnetic field signal perpendicular to the loop induces a loop current, changing the kinetic inductance of the nanowires that form part of the loop and in turn changing the resonance frequency of the resonator. A strong periodic response to the external magnetic field is observed for this device. Similar to SQUIDs, the ultimate flux sensitivity of this device could approach the quantum limit, but the KPUP also offers simple fabrication and ease of multiplexing. This could make it useful for many magnetometry applications such as non-destructive evaluation, materials characterization, and medical imaging. Finally, we also demonstrate parametric gain from a microwave resonator in the presence of a strong pump tone. The noise performance of this parametric amplifier is close to the quantum limit, and it exhibits gain of up to 29 dB, making it potentially useful for applications in quantum information and metrology.

PUBLISHED CONTENT AND CONTRIBUTIONS

[1] A. Kher et al. “Kinetic Inductance Parametric Up-Converter”. *Journal of Low Temperature Physics* **184**.**1**, 480–485 (2016). DOI: 10.1007/s10909-015-1364-0.
A.K. participated in the conception of the project, participated in the design and testing of the devices, analyzed the data, and wrote the manuscript.

TABLE OF CONTENTS

LIST OF ILLUSTRATIONS

Chapter 1

INTRODUCTION

1.1 Observational cosmology

The cosmic microwave background (CMB), first predicted by Ralph Alpher and Robert Herman in 1948 [1] as part of Gamow's nucleosynthesis model [2, 3], is central to the hot Big Bang paradigm of cosmology, as it provides a snapshot of the early universe [4]. Its detection in 1964 by Penzias and Wilson [5] established the Big Bang as the prevailing model for the universe. Since then, the CMB has proven to be an invaluable tool for cosmological study, as its characteristics can be predicted by theoretical models and measured to high accuracy. Significant efforts to measure the CMB in greater detail continue to this day.

The radiation signature observed by Penzias and Wilson corresponds to a black body temperature of approximately 2.725 K in all directions [5]. NASA's Cosmic Background Observer (COBE) Satellite, launched in 1989, mapped out the black body spectrum of the CMB [6], confirming hot Big Bang model predictions, and also observed angular temperature fluctuations on a scale of one part in 10^4 [7]. A number of experiments followed which had the goal of measuring this anisotropy on smaller angular scales and higher resolution than COBE. Notably, in 2000, BOOMERanG, a balloon-based experiment above the South Pole, found an angular peak in the CMB power spectrum that provided strong evidence that the universe is flat [8]. This helped establish the inflationary cold dark matter (ΛCDM) model as the standard model of cosmology, where the universe is spatially flat, is dominated by cold dark matter, and expands at an accelerated rate (given by the cosmological constant Λ) at late times [9]. In 2002, the Degree Angular Scale Interferometer (DASI), a ground-based instrument at the South Pole, reported the first detection of CMB E-mode polarization, providing further evidence for the ΛCDM model [10]. Additional evidence was provided by 2004 results from the Cosmic Background Imager (CBI), another ground-based interferometer at the Atacama desert in Chile, which measured a detailed E-mode power spectrum and showed that it is half a cycle out of phase with the total intensity spectrum [11]. In 2001, NASA launched the Wilkinson Microwave Anisotropy Probe (WMAP), its second space-based CMB instrument, with the goal of making much more detailed measurements of large-scale

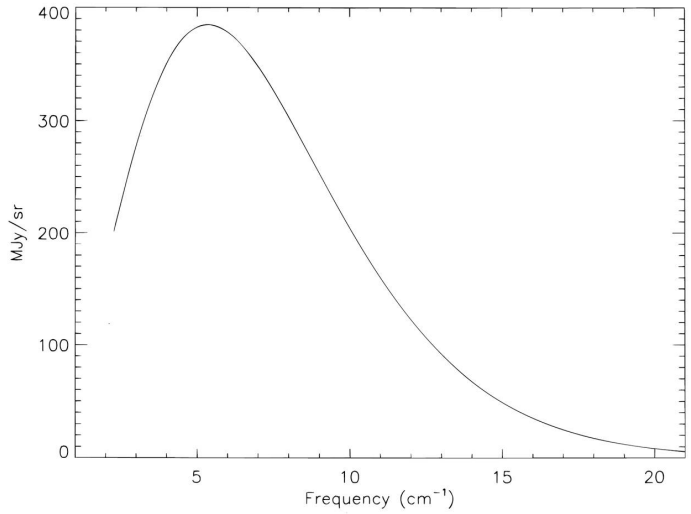

Figure 1.1: Plot of CMB spectrum as measured by the FIRAS instrument on COBE, fitted with a theoretical black body spectrum. The error bars for the data are smaller than the thickness of the line used to plot the curve. Figure reprinted from [14].

temperature fluctuations over the entire sky. Although it did not have the small-scale resolution of concurrent ground-based instruments, WMAP was able to tightly constrain a number of cosmological parameters, and its results were consistent with the standard ΛCDM model [12, 13].

Recent efforts have emphasized measuring B-mode polarization in the CMB, which had not been detected by previous polarization experiments. B-modes are particularly interesting because their existence would provide stronger evidence for cosmic inflation. Inflationary models predict that the rapid expansion of space resulted in a strong burst of gravitational waves, and that these gravitational waves would leave a unique signature on the CMB [15–21]. In particular, they would induce a B-mode pattern that could not be generated by primordial density fluctuations. The amplitude of this B-mode signal is of interest because it is a function of the energy scale of inflation. In 2014, BICEP2, a ground-based experiment at the South Pole, claimed detection of B-mode fluctuations in the CMB that were consistent with inflation [9]. However, when jointly analyzed with data from the European Space Agency's Planck satellite, the BICEP2 data was found to be explainable in terms of polarized thermal emission from interstellar dust [22]. Originally launched in 2009, the Planck mission produced the strongest constraints on cosmological parameters and the most detailed full-sky CMB maps to date, and the results were in general in excellent agreement with ΛCDM cosmology [23–25].

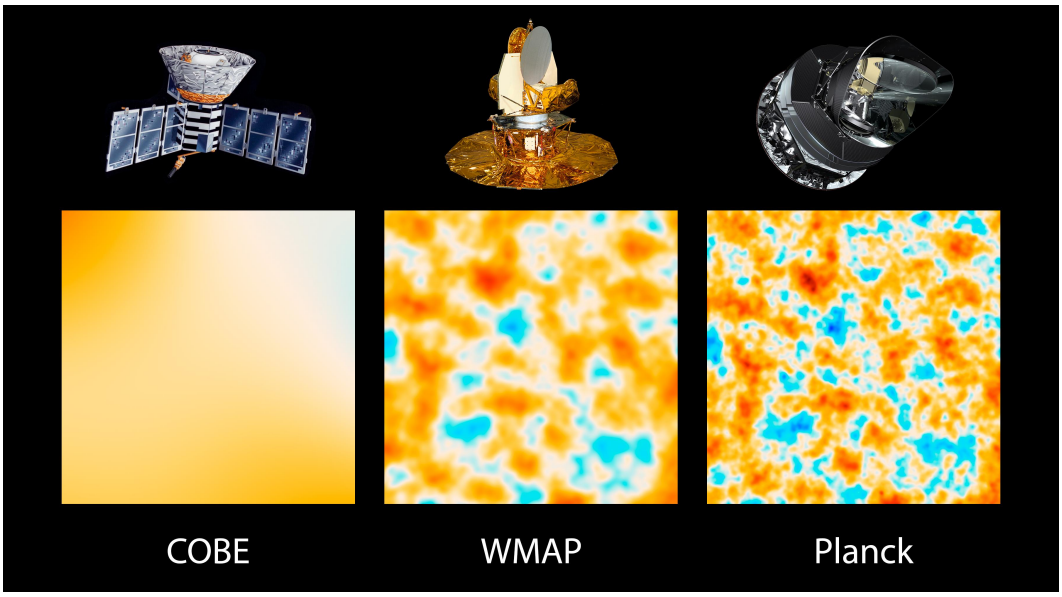

Figure 1.2: Comparison of a $10° \times 10°$ patch of sky from CMB measured by COBE (1989), WMAP (2001), and Planck (2009). Image credit: NASA/JPL-Caltech/ESA [26].

In addition to interstellar dust, B-modes can also be caused by gravitational lensing of the CMB. This was first detected by SPTpol, a polarimeter installed in 2012 at the South Pole Telescope (SPT) [27]. Additional measurements of lensing B-modes were performed by the POLARBEAR instrument in Chile [28–30]. Both of these instruments are still in operation, and are also searching for inflationary B-modes. There are a number of other new instruments with similar scientific goals, including ground-based instruments ABS [31], ACTpol [32], CLASS [33], and BICEP3 [34], as well as balloon-based instruments EBEX [35], SPIDER [36], and PIPER [37]. With many complementary results expected from these experiments and more, the cosmic microwave background will remain a useful tool for observational cosmology for years to come.

1.2 Detector technology

The photon detectors used in cosmology instruments can be grouped into coherent detectors, such as amplifiers, which preserve the phase of the detected radiation, and direct detectors, such as bolometers, which destroy the radiation's phase information [38]. Amplifiers have been responsible for many important discoveries related to the cosmic microwave background. They were used by Penzias and Wilson to first discover the CMB [5, 39] and by the DASI team to first discover CMB po-

larization [40, 41], among others. However, especially in recent years, bolometric detectors have proven to hold an important advantage in noise performance and detector count at higher frequencies [38].

Noise-equivalent power (NEP) is defined as the incident power required to achieve a signal-to-noise ratio of unity over an integration time of 0.5 s [42, 43]. A 2003 analysis by Zmuidzinas [44] shows that, for a direct detector sensitive to a single spatial mode and polarization, the statistics of photon arrival sets a limit of

$$\mathrm{NEP}^2 = 2\,(h\nu)^2 \Delta\nu\, \frac{n(\nu)\,(1 + \eta\, n(\nu))}{\eta}, \tag{1.1}$$

where h is Planck's constant, η is the absorption efficiency, $\Delta\nu$ is the bandwidth, and

$$n(\nu) = \frac{1}{e^{\,h\nu/k_B T} - 1} \tag{1.2}$$

is the Bose occupation number of the radiation [45]. For a coherent detector, the corresponding expression is

$$\mathrm{NEP}^2 = 2\,(h\nu)^2 \Delta\nu \left(\frac{1 + \eta\, n(\nu)}{\eta} \right)^2. \tag{1.3}$$

This includes quantum noise that is present even with no incident radiation, i.e., when $n \to 0$ [44]. The ratio of NEP in the coherent to direct situations is

$$\frac{\mathrm{NEP}^2_{\text{coherent}}}{\mathrm{NEP}^2_{\text{direct}}} = \frac{\eta\, n(\nu) + 1}{\eta\, n(\nu)}. \tag{1.4}$$

This is close to unity when $n \gg 1$, so there is no tradeoff for preserving phase information by using coherent detectors in that scenario. However, CMB measurements are typically made in a regime where the occupation number is comparable to unity [42]. With recent bolometer noise reaching the limit set by the CMB (see Fig. 1.3), the added quantum noise becomes significant, and thus bolometers have now become the predominant type of detector for cosmology experiments at frequencies above 100 GHz [46].

Bolometers

All thermal radiation detectors consist of an absorber of heat capacity C, a heat bath at temperature T, and a weak link with thermal conductance G [43]. The absorber converts the energy from the incident light into heat, and is connected to the bath through the weak link. If the optical power absorbed by the detector changes by

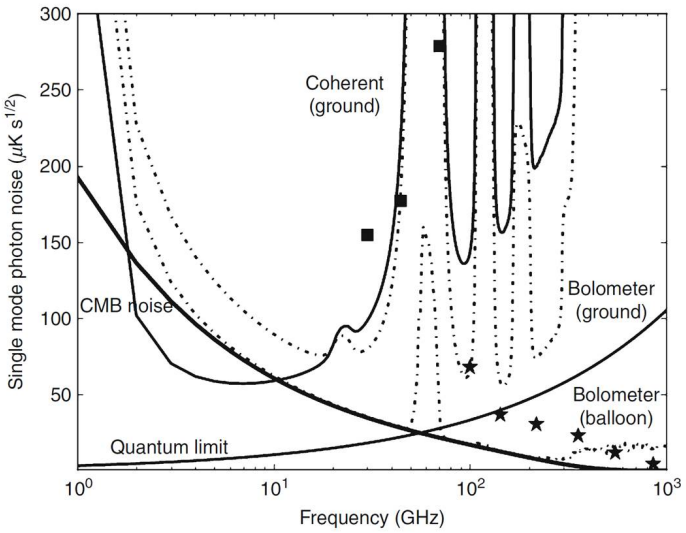

Figure 1.3: Photon noise from 1 to 1000 GHz. The thick line is the CMB intrinsic noise, which sets the limit for detector noise. On the ground, bolometers (dash-dot) perform better than coherent detectors (solid) except below 20 GHz. Balloon-based bolometers (dash-dot) are limited by the CMB noise from about 80 to 200 GHz. Planck coherent receivers (square) and bolometers (star) are also shown. The latter are close to the CMB noise limit. Figure reprinted from [46].

δP, and if all other power inputs to the device remain constant, then the device temperature changes by $\delta T = \delta P/G$ with a thermal time constant of

$$\tau = \frac{C}{G}. \tag{1.5}$$

The incident power P can be determined by measuring the change in temperature. Therefore, a sensitive thermometer is necessary. A bolometer is a type of thermal radiation detector for which the thermometer is the temperature-dependent resistance of a thermistor. We note that a complete description of bolometer operation, found for example in the 1994 review by P. L. Richards [43], would necessarily include feedback effects, as a change in resistance causes a change in the power dissipated in the resistor.

The first bolometer was developed by Langley in 1878 [47]. It consisted of two platinum strips arranged in a Wheatstone bridge which was fitted with a galvanometer and attached to a battery. The strips were covered in black pigment, and one was shielded from radiation while the other was exposed to it. The exposed strip heated up in response to incident radiation, resulting in a change in its resistance. Since then, bolometers have found wide application in astronomy, and are often operated

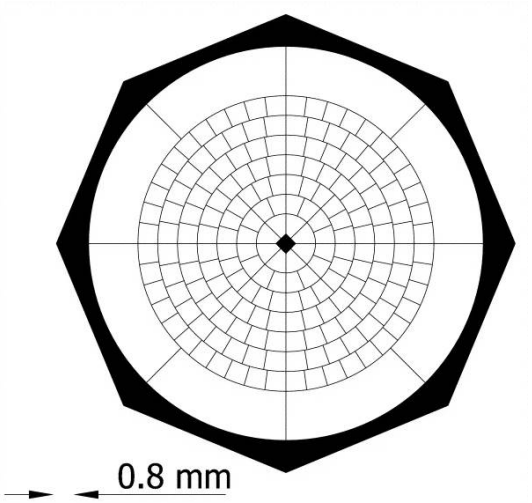

Figure 1.4: Schematic of spiderweb bolometer used in BOOMERanG. The rectangular prism in the center is the NTD germanium thermistor. The released mesh structure is fabricated from silicon nitride and is metallized in order to couple to electromagnetic radiation. Figure reprinted from [51].

at cryogenic temperatures for better sensitivity [43]. One of the best-known types of low-temperature bolometers is the germanium bolometer [48], a prominent example of which is the spiderweb bolometer [42]. Modern versions utilize a semiconducting Ge thermistor that has been modified by neutron transmutation doping (NTD), a process that results in a high, uniform doping level that is necessary for a thermistor operating at low temperature. The thermistor is suspended on a spiderweb-like mesh structure formed by etching a thin film of silicon nitride on a standard silicon wafer. The mesh is coated with a thin gold film in order to allow it to efficiently absorb microwaves, and its low-area-fill factor provides it a relatively small cross-section to cosmic rays. Spiderweb bolometers were used in experiments such as ACBAR [49], MAXIMA [50], and BOOMERanG [51]. Despite this success, germanium bolometers have the disadvantage of not being able to be fabricated in large monolithic arrays. The High Frequency Instrument on the Planck satellite had only 52 Ge bolometers [52], while the Herschel Space Observatory's SPIRE instrument had several Ge-bolometer arrays of up to 139 pixels [53]. Eventually, individual bolometers reached photon-noise limited performance [42], so in order to improve instrument sensitivity further, it became necessary to increase the total number of detectors [38, 46]. A different technology was needed, where the detectors could be monolithically integrated into large but small-area arrays.

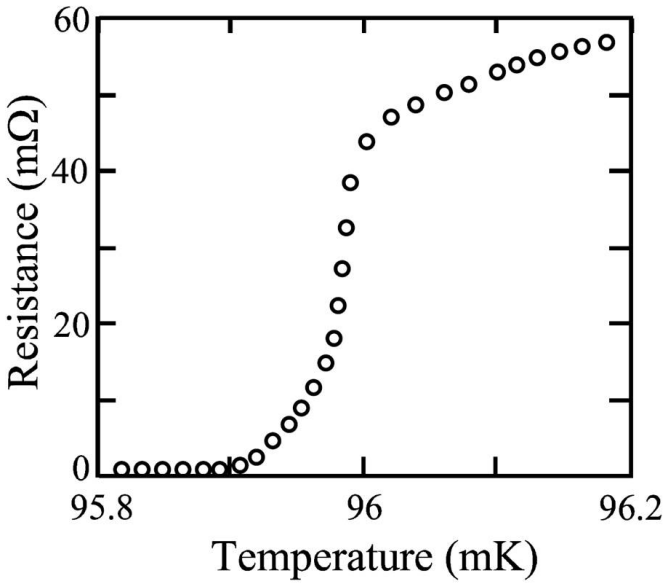

Figure 1.5: Superconducting transition of a Mo/Cu bilayer film. Figure reprinted from [54].

1.3 Transition-edge sensors

In 1911, Heike Kamerlingh Onnes discovered superconductivity by lowering the temperature of mercury to 4.2 K using liquid helium and observing that its electrical resistance abruptly dropped to zero [55]. Since then, many materials have been found to exhibit the same phenomenon at various cryogenic transition temperatures. This superconducting transition, though sharp, has been observed to have a finite width (see Fig. 1.5). It is possible to bias a superconducting sample within this finite transition region. The steep change in resistance suggests the utility of such a sample as a sensitive thermometer, particularly in application as a bolometer. If electromagnetic radiation is incident on and absorbed by the superconducting sample, its temperature will increase, and a large change in resistance could be measured. The superconductor could be biased within its transition by utilizing Joule heating from a voltage or current source. This type of bolometer is known as a transition-edge sensor (TES) [54]. D. H. Andrews demonstrated the first TES in 1941 when he applied a current to a fine tantalum wire operating in its transition region and measured the change in resistance caused by absorption of an infrared signal [56]. However, TESs were not widely used until the 1990s. One of the barriers to their adoption was the difficulty of matching their relatively low impedance ($\sim 1\,\Omega$ [42]) to the available low-noise amplifiers, e.g., JFETs, which

worked best for high impedances [54]. Another issue was temperature instability. When a TES is current-biased, as in Andrews' demonstration, the Joule heating from the source $P = I^2R(T)$ increases when the resistance of the superconductor increases (as in a detection event), and the increased Joule heating further increases the temperature of the device. This positive feedback makes it very difficult to operate the device within the narrow transition region, which typically has a width on the order of ∼1 mK or less [54].

Transition-edge sensors were first made practical by Kent Irwin in 1994 [57]. Irwin introduced a voltage-biasing scheme for TES operation, shown in Fig. 1.6. Here, the TES is biased with a constant voltage instead of a constant current. A hallmark of this scheme is strong negative electrothermal feedback (ETF). When optical power P_{opt} is incident on the device, the resistance $R(T)$ increases, and thus the Joule heating from the source

$$P_{\text{bias}} = \frac{V^2}{R(T)} \tag{1.6}$$

decreases. Conversely, a decrease in the optical loading results in a decrease in the resistance and thus an increase in the Joule heating. This strong feedback ensures a nearly-constant total loading power $P_{\text{opt}} + P_{\text{bias}}$ on the TES [42]. Thus, it is much more straightforward to keep a voltage-biased TES' temperature stable and within the narrow transition region. Stability is further improved when the bath temperature is regulated well below the TES transition temperature, as the device is then less susceptible to thermal fluctuations from the environment [54]. Another development that helped make TESs practical is the adoption of superconducting quantum interference device (SQUID) readout amplifiers. The SQUID was invented in 1964 [58] and developed extensively over the following decades [59]. They are easily impedance-matched to low-resistance TESs, and quickly became the standard readout amplifier used in TES applications [54].

Transition-edge sensors have a number of advantages over the semiconductor bolometers that were so successful in cosmology experiments of the 1990s. Their resistance is much less than that of germanium thermistors [42]. The high impedance of the latter devices was problematic because mechanical vibrations would cause fluctuations in the capacitance between bias wires. This would manifest as large voltage fluctuations, contaminating the data stream [42, 60]. The low resistance of TESs means that similar current perturbations have a smaller effect. In addition, the

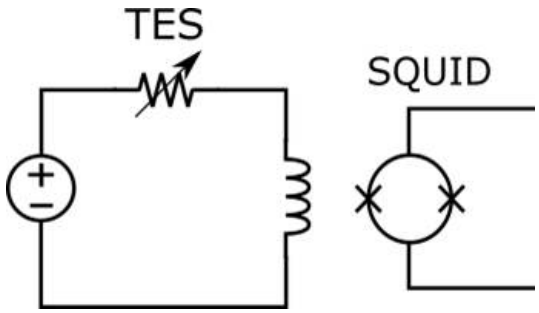

Figure 1.6: Simple readout configuration for TES. The bolometer is biased by a voltage source, so a change in the TES resistance results in a change in the current flowing through the circuit. The circuit is inductively coupled to a SQUID in order to measure this change in current.

responsivity of TESs is much higher. The dimensionless parameter

$$\alpha = \frac{\mathrm{d}\ln R}{\mathrm{d}\ln T} = \frac{T}{R}\frac{\mathrm{d}R}{\mathrm{d}T} \tag{1.7}$$

is useful for characterizing the thermometer of a bolometer [43]. Semiconductor bolometers have an α of the order unity, but TESs typically have α between 50 and 500 [42], with very-low-T_c films reaching $\alpha \approx 1000$ [57]. This is due to the extremely sharp nature of the superconducting transition. Finally, unlike germanium bolometers, it is possible to fabricate monolithic arrays of transition edge sensors using standard techniques developed by the semiconductor industry, and this has allowed continued improvement in instrument sensitivity. The superconducting material is typically deposited on a silicon nitride membrane, which is then released so that there is weak thermal contact between the absorber and the heat bath [54]. TES arrays of hundreds of pixels have been fabricated for recent experiments such as POLARBEAR [61], SPIDER [62], BICEP2 [9], and BICEP3 [34], among many others. Due to their advantages, transition-edge sensors have become the dominant technology used in modern bolometric cosmology experiments.

Applications outside cosmology

Study of the CMB has driven much of the development of TES bolometers, but there are applications for TES bolometers outside cosmology. In particular, the submillimeter-astronomy camera SCUBA-2 [63] used TES bolometers as detectors, and the results of its massive technology-development effort in fact benefitted many future TES-based cosmology experiments. Additionally, besides the bolometer, there is another mode of operation for transition-edge sensors known as the calorimeter. While a bolometer is used to measure incident power, a calorimeter is

used to measure a pulse of energy [54]. Fundamentally, the device principles are the same as in bolometers, although special considerations must be taken into account due to the different application [59]. TES calorimeters have been developed for X-ray astronomy applications [64–66], where they may help advance understanding of hot and energetic objects such as the coronae of stars, gas in galaxies and galaxy clusters, supernovae, gamma-ray bursts, and accretion disks around black holes and neutron stars [59]. Outside of astronomy, TES calorimeters have been developed for laboratory applications such as materials analysis via X-ray spectroscopy [67]. Such cryogenic microcalorimeters are also useful for mass spectrometry of large biomolecules [68, 69]. TES calorimeters are also being developed for detection of very small masses such as neutrinos and weakly-interacting massive particles (WIMPs), a major candidate for dark matter [70, 71]. In these applications, the particles of interest induce nuclear recoil in the primary detector substrate. Phonons produced by the recoil break Cooper pairs in a superconducting absorber on the surface. The absorber is connected to a TES, whose temperature rises upon diffusion of the quasiparticles.

TES calorimeters have also been developed for detection of near-infrared, optical, and ultraviolet radiation [72], which has important applications for astronomy in those frequency bands. They have even been developed as single-photon detectors, with high counting efficiency [73, 74]. These are very important for applications in quantum information, such as quantum key distribution and optical quantum computing [75, 76]. Single photon detectors are also useful for applications in biology [77], remote sensing [78], and molecular spectroscopy [79], among many others. Optical TES detectors can also be used to measure terahertz radiation [80], which is important for many security applications such as the detection of explosives, weapons, and drugs [81]. For most of the applications mentioned in this section, it is beneficial to have large arrays of detectors, similar to the cosmology instrument arrays mentioned in the previous section. Since TESs are not inherently multiplexable, a great amount of attention has been placed on developing readout systems in order to make such arrays possible.

1.4 SQUIDs

The SQUID is the most sensitive magnetometer in existence [82]. Fundamentally, it combines two phenomena of superconductivity: flux quantization and the Josephson effect. F. London was the first to predict that the magnetic flux contained within a

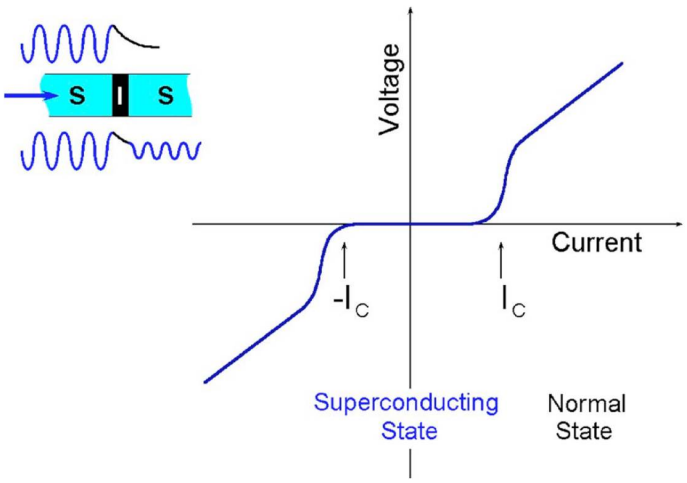

Figure 1.7: Schematic illustration of an superconductor-insulator-superconductor (SIS) Josephson junction and its I-V characteristic. In an ideal Josephson junction, the transition from superconducting to normal would be abrupt, but the smooth transition of a practical device is shown here. Figure reprinted from [82].

closed superconducting loop would be quantized in units of the flux quantum

$$\Phi_0 = \frac{h}{2e} = 2.068 \times 10^{-15}\ \text{Wb}, \tag{1.8}$$

where h is Planck's constant and e is the electronic charge [83]. This was first observed experimentally by Deaver and Fairbank [84] and Doll and Näbauer [85] in 1961. Then, in 1962, Josephson predicted that Cooper pairs—pairs of electrons that serve as the charge carriers in superconductors [86]—could tunnel through a barrier between two superconductors (now known as a Josephson junction) [87]. The two superconducting electrodes would each have a many-body wave function

$$\Psi(\mathbf{r}, t) = |\Psi(\mathbf{r}, t)|\ \exp[\mathrm{i}\,\phi(\mathbf{r}, t)] \tag{1.9}$$

that maintains phase coherence over macroscopic distances [86]. Defining $\delta = \phi_1 - \phi_2$ as the difference between the phases of the two electrodes, Josephson predicted that the tunneling current through the barrier would be given by

$$I = I_c \sin\delta, \tag{1.10}$$

where the critical current I_c is the maximum current the junction can support before it becomes resistive, as shown in Fig. 1.7 [87]. If there is a voltage V across the

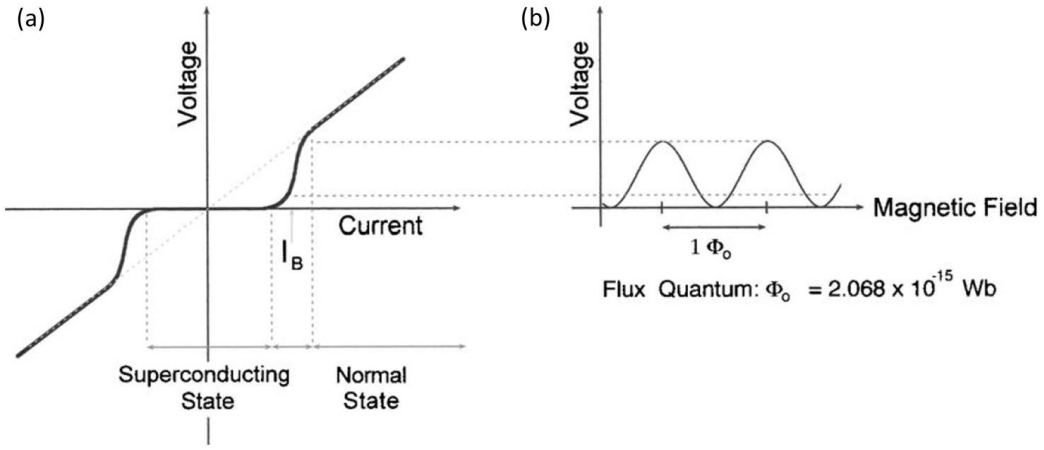

Figure 1.8: (a) In a practical SQUID, the Josephson junctions are typically biased slightly above the critical current. (b) SQUID voltage versus magnetic flux for a constant bias current. The regime where the slope is approximately linear is most sensitive. Figure reprinted from [82].

junction, the phase difference evolves with time according to

$$\frac{\mathrm{d}\delta}{\mathrm{d}t} = \frac{2eV}{\hbar} = \frac{2\pi V}{\Phi_0}. \tag{1.11}$$

Integrating both sides, we see that the Josephson current is an alternating current with frequency $\omega = 2\pi V/\Phi_0$ [86].

In 1964, Jaklevic et al. connected two identical Josephson junctions in parallel on a superconducting loop and applied a magnetic field perpendicular to the loop [58]. They found that the peak supercurrent across the loop had maxima at integer multiples of the magnetic flux, varying as

$$I_m = 2I_c \left|\cos\left(\frac{\pi\Phi}{\Phi_0}\right)\right|, \tag{1.12}$$

where I_c is the critical current of each individual junction [86]. This is analogous to the intensity pattern from two-slit diffraction in optics. This phenomenon of quantum interference gave birth to the SQUID. In practice, each of the two Josephson junctions is usually shunted by a resistor in order to eliminate hysteresis in its I-V curve [88]. For a SQUID with resistively-shunted junctions, it can be shown that the voltage is periodic in the magnetic flux (see Fig. 1.8(b)) [86]. A change in flux can be measured as a change in the voltage across the SQUID. However, due to the periodic nature of the curve, the dynamic range of a SQUID is small. In particular, it is valuable to stay within the linear regime of the curve, where the slope is greatest

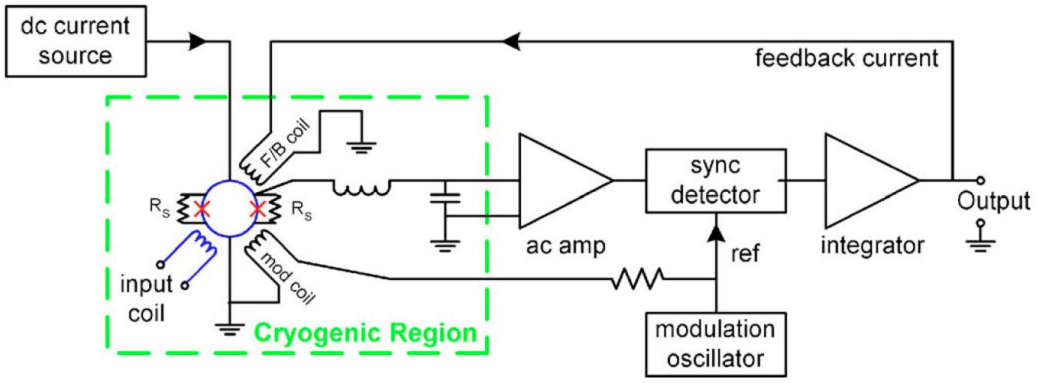

Figure 1.9: Flux-modulation SQUID readout. The bias current is applied by a DC source. An oscillator and modulation coil, inductively coupled to the SQUID loop, is used to apply an AC flux to the SQUID loop. The oscillator also provides a reference signal for a lock-in amplifier (labeled 'sync detector'). The signal is provided by an input coil. The resulting change in SQUID voltage is amplified and detected by the lock-in amplifier. The resulting DC signal is integrated and fed back to the SQUID via another coil in order to keep it at its linear operating point. Figure reprinted from [82].

and the device is most sensitive. Therefore, external feedback is typically used along with a SQUID in order to maintain a linear operating point [82]. A widely-used feedback implementation, known as a flux-locked loop, is shown in Fig. 1.9 [89].

SQUIDs are extremely sensitive, with typical flux-noise levels on the order of $10^{-6}\,\Phi_0/\sqrt{\text{Hz}}$ [59]. However, they have a number of limitations. First, Josephson junctions are difficult to fabricate. There are several different types of barriers, or weak links, used in practical Josephson junctions, including insulators, normal metals, and geometric constrictions [59]. For SQUIDs, superconductor-insulator-superconductor (SIS) and superconductor-normal-superconductor (SNS) junctions are typically used. This means that at least three layers of lithography are needed, and up to 10 are needed for some practical situations such as arrays of SQUIDs used for astronomy [90]. Moreover, the two Josephson junctions comprising a SQUID must be matched within a few percent of each other, as do the shunt resistors [82]. This means that SQUIDs easily become complicated and expensive to produce. In addition, SQUIDs are complicated to wire in a practical system. As shown in Fig. 1.9, a SQUID in a typical operating configuration requires at least four pairs of electrical leads: bias, modulation, signal, and feedback. In many cases, a heater circuit is also necessary for driving the SQUID normal in order to remove trapped flux, adding even more leads to the system [82]. This means that SQUIDs

are very difficult to multiplex, because each SQUID in an array would require its own wiring and room-temperature electronics. Because of the limited dynamic range of the SQUIDs, when dealing with signal changes greater than $\sim\Phi_0/4$, the feedback system must work rapidly to keep the voltage at the operating point [82]. If it is not fast enough, the device will "jump" to a different flux level and the measurement will be compromised. Thus, the speed of the feedback system limits the bandwidth of the signals that can be measured using SQUIDs. The type of commercial electronics used for SQUID feedback systems typically has a maximum bandwidth of 50–100 kHz [82]. In order to measure signals faster than that, the SQUID must be operated without feedback, leaving it susceptible to flux jumping. The combination of low bandwidth and low dynamic range in SQUIDs also limits their Shannon information capacity, which in turn limits their utility for reading out large arrays of detectors [91]. Finally, the vector nature of the magnetic field that SQUIDs are sensitive to also presents a limitation. The orientation of a SQUID in the Earth's magnetic field can vary the ambient field by up to ~100 μT [82]. If the SQUID is used as a rotating magnetometer, the rotation speed would also need to be within the bandwidth of the feedback electronics, imposing another limitation on this application. This even comes into play in applications where the SQUID is used to measure a current rather than a magnetic field, for example the TES readout shown in Fig. 1.6. Though it can be canceled with a bias field or blocked by a metal shield, the Earth's magnetic field must be considered in these types of applications.

TES readout

Despite their limitations, SQUIDs provide the standard way of reading out transition-edge sensors [54]. A typical single-pixel readout scheme is shown in Fig. 1.10. The TES is voltage-biased using a shunt resistor, whose resistance R_{bias} is chosen to be much less than the TES normal-state resistance R_{bolo} [54]. In series with the TES is an input coil with inductance L_{SQ}, used to couple the TES current into the SQUID. This introduces a time constant

$$\tau = \frac{L}{R(T)}, \tag{1.13}$$

where $R(T)$ is the instantaneous resistance of the TES. This electrical time constant must be several times smaller than the thermal time constant (Eq. (1.5)) in order to avoid unstable electrothermal oscillations in the TES [54]. It also sets a limit on the bandwidth of the signals that can be measured by the TES [57]. The coil inductance, commonly referred to as the SQUID input inductance, is usually on the order of ~0.1–1 μH [42, 92, 93].

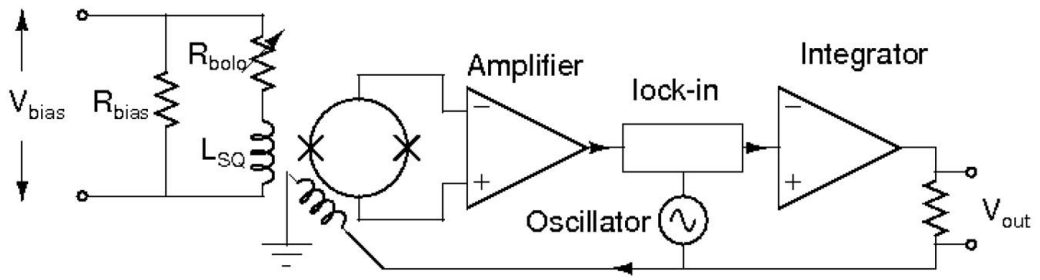

Figure 1.10: Readout configuration of a single TES using a SQUID in a flux-locked loop, from the UC Berkeley cosmology group. This implementation does not use AC flux modulation for the SQUID. The TES DC bias voltage $V_{\rm bias}$ is applied using a battery box with a potentiometer to vary the voltage. The TES is in series with an input coil that is magnetically coupled to a SQUID, which is driven by an AC flux from an oscillator. A TES signal results in a current perturbation, which in turn results in a voltage across the SQUID. This voltage is amplified and then detected by the lock-in amplifier, whose reference is provided by the same oscillator driving the SQUID. The DC signal from the lock-in is integrated and fed back to the SQUID, along with the original AC drive tone, in order to maintain the SQUID's operating point. Figure reprinted from [42].

Since large arrays of TESs are desired for cosmology experiments, much of the research effort regarding TES readout has focused on multiplexing them with SQUIDs. This is not a straightforward task. The single-pixel readout scheme of Fig. 1.10 requires multiple pairs of leads: detector bias, SQUID bias/output, and SQUID feedback. Often, a second amplifier stage consisting of an array of SQUIDs is also used, in which case wire pairs for bias/output and flux bias for this second stage are also needed [54]. All of these wires must run between room temperature and the cryostat. Simply arranging a series of these in an array of the size needed for cosmology experiments would result in thousands of leads going between room temperature and cryogenic temperatures. The complexity, cost, and power load of such a system would make it impractical. Thus, innovative solutions are necessary for reading out large arrays of TESs. A number of SQUID multiplexing schemes have been developed that reduce the number of necessary wires [54]. Broadly, they can be categorized under either time-division multiplexing (TDM) or frequency-division multiplexing (FDM).

Time-division multiplexing of SQUIDs has been developed largely at NIST [92–94]. In this approach, each TES is biased with a separate shunt resistor and inductively coupled to a separate SQUID. The TES currents are sampled sequentially by pe-

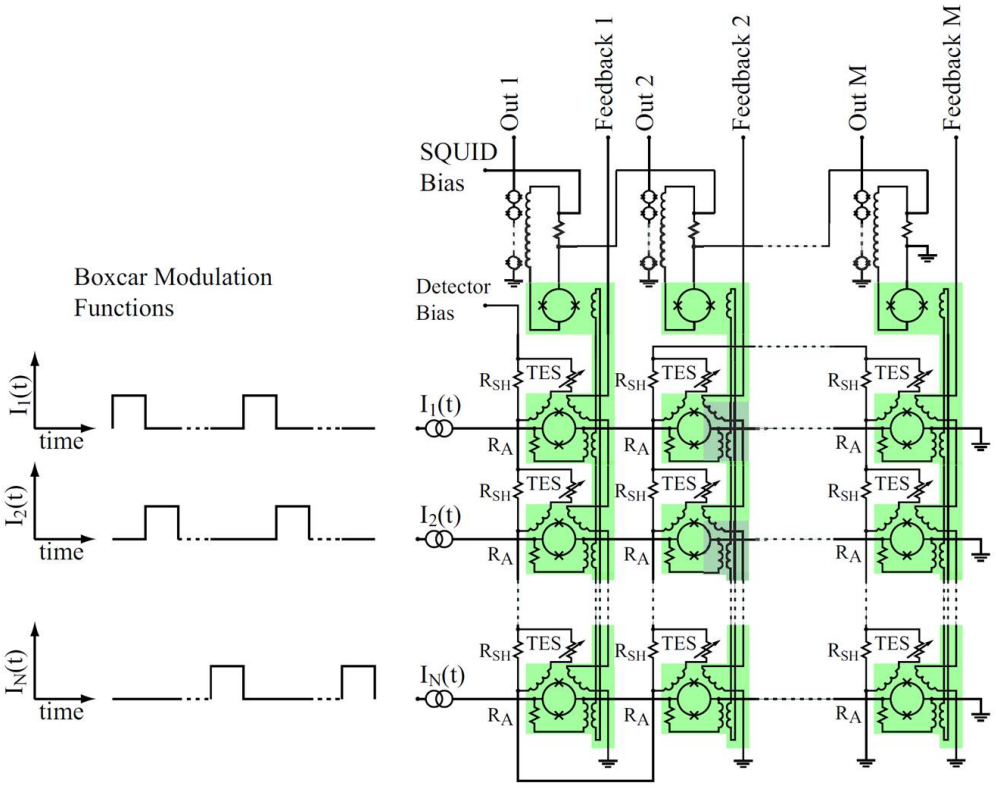

Figure 1.11: Readout of a two-dimensional TES array with a time-division SQUID multiplexer. The TESs are all on a common bias line. A series of boxcar functions is used to turn on one row of SQUIDs at a time and read their respective TES currents. Each SQUID is coupled to an output coil, and all of the output coils in a column are all connected in series so that the sum of the detected currents is read out by a single output SQUID per column. The voltage of this output SQUID is then amplified by another series-array of SQUIDs before going to the room-temperature electronics. Each column of first-stage SQUIDs is linearized by a common feedback line. Figure reprinted from [54].

riodically turning "on" their respective SQUID amplifiers while leaving the other SQUIDs "off". Typically, each SQUID is turned on for a duration of $\sim$1 µs at a time. This results in a detector sampling frequency of about 20 kHz, which is greater than the Nyquist frequency corresponding to the detector bandwidth [94]. A diagram is shown in Fig. 1.11 for two-dimensional array multiplexing. If the array has M columns and N rows, then the the total number of wires running from room temperature to the cryostat is $4M + N$ [59]. This is a substantial reduction from the brute-force situation, where the number of wires scales as $M \times N$. Time-division multiplexing is a mature TES readout technology: 32-channel multiplexers have been developed and shown to have good noise performance of less than

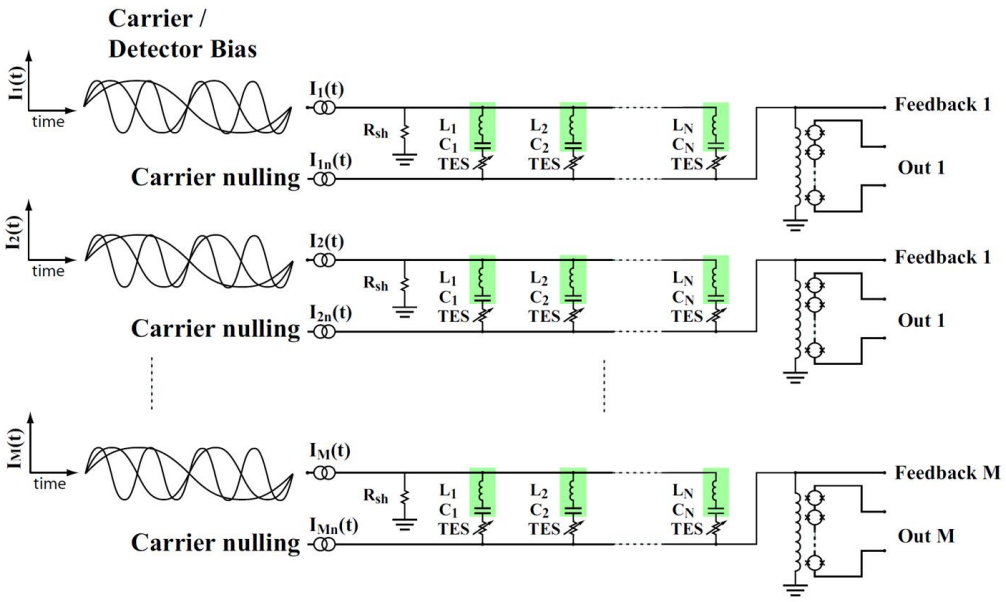

Figure 1.12: Readout of a two-dimensional TES array with a frequency-division SQUID multiplexer. Each TES is in series with an *LC* resonator/filter with a unique resonace frequency, and each row of these is in parallel with a shunt resistor. The row of resonators is excited by a frequency comb, and the output currents are summed and inductively coupled to a SQUID array. Feedback is used to keep the input coil at a virtual ground, and carrier nulling combs are applied in order to ease the SQUID dynamic range requirements. Figure reprinted from [54].

$1\,\mu\Phi_0/\sqrt{\text{Hz}}$ [93]. They have been deployed in many instruments for cosmology and astronomy such as SPIDER [36], SCUBA-2 [63], and BICEP3 [34]. However, the array size of an instrument with a TDM system is still limited. Practical constraints generally limit the multiplexing factor to 100:1 [94]. Thus, a different solution is needed for next-generation instruments requiring much larger array sizes.

An alternate approach is frequency-domain multiplexing, which has been developed by several groups [95–98]. A common implementation of FDM is shown in Fig. 1.12. Here, each TES acts as the resistor in an *LCR* tank circuit, where the inductors and capacitors are typically discrete components on a circuit board. Each tank circuit has a slightly different resonance frequency, generally on the order of ~1 MHz [99]. The frequency variation is usually achieved by varying the capacitance between the resonators and keeping the inductance constant, as that allows each resonance to have the same linewidth [59]. This linewidth sets a limit on the bandwidth of the TES, and also works to filter environmental noise. The tank circuits are continuously driven by a frequency comb, and the sum of their outputs is measured by a SQUID. When

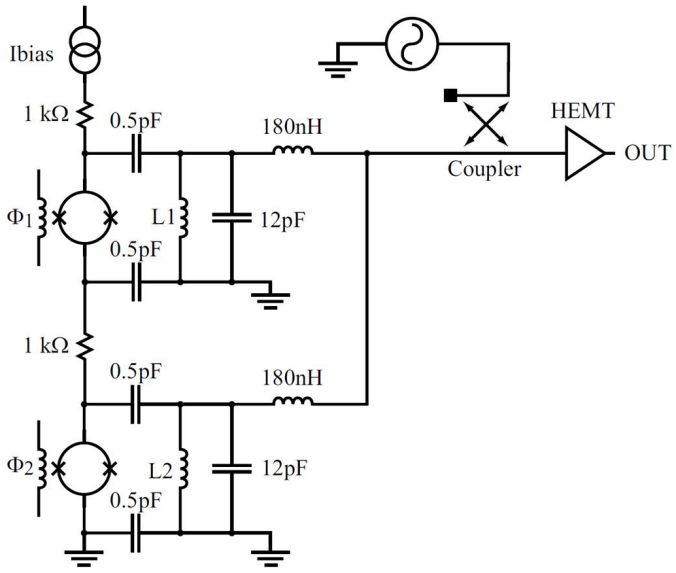

Figure 1.13: Frequency-division multiplexing of two SQUIDs using microwave resonators. Each TES current is coupled to a SQUID using an input coil (left edge of diagram). The SQUID is part of a tank circuit whose resonance frequency depends on the flux contained in its loop. The resonators are excited in parallel by a microwave source, and the reflections from the SQUIDs are coupled to a HEMT readout amplifier. Figure reprinted from [98].

the TES resistance changes, the current at its respective filter-frequency changes, and this change can be observed as a change in the SQUID voltage at that frequency. However, since many currents are summed and sent to the SQUID, its dynamic range becomes a limitation, especially because the ratio between the bias signal and the noise is typically 10^6 [59]. A solution to this is to null the carrier amplitude after the resonator and before the SQUID input. This can be done by applying a frequency comb with the same set of amplitudes as the bias, but 180° out of phase. Feedback can be utilized in order to keep the amplitudes of these two signals the same. In addition to reducing the dynamic range requirement for the SQUID, carrier nulling can also reduce crosstalk between the resonators [59]. Despite the need for nulling, the total number of wires required in an FDM scheme is substantially reduced when compared with TDM. Each row in Fig. 1.12 has four pairs of wires going to/from room temperature: carrier, nulling, feedback, and SQUID output. Thus, the number of wires simply scales with the number of SQUIDs, and in this case is $8M$.

A newer technology is frequency-division multiplexing in the microwave regime. Using microwave resonators instead of lower-frequency RF resonators has several

advantages [98]. First, the gigahertz range offers much greater available bandwidth for multiplexing. This allows for a greater number of multiplexed detectors, and it also allows for a greater bandwidth (or resonator linewidth) for each detector. In addition, the system would be more compact. Since the resonator frequencies are higher, the values of the components are reduced in comparison with the RF situation. This makes the components physically smaller, making it even easier to integrate more detectors in an array, especially if monolithic, lithographed components are used rather than discrete components connected on a circuit board. This type of scheme has other important differences from lower-frequency FDM. A simple example diagram is shown in Fig. 1.13. In this case, each TES is coupled to a SQUID, and the SQUID is part of a resonant circuit instead of the TES. The resonance frequency depends on the magnetic flux in the SQUID loop, which changes when the TES current changes [100]. The reflected signals from all of the SQUIDs are summed and sent to a high-electron-mobility transistor (HEMT), a type of low-temperature amplifier with high dynamic range [101, 102]. A 32-SQUID multiplexer of this kind has been fabricated and shown to have good noise performance below 1 $\mu\Phi_0/\sqrt{\text{Hz}}$ [103]. One issue is that, when there are so many SQUIDs, they must be operated without feedback circuits, so their dynamic range suffers [98]. This is not as much of an issue as it would be in the low-frequency case, because each SQUID is only reading out one TES. However, because of the periodic nature of the V-Φ curve, SQUIDs can easily leave the linear regime when operated without feedback, requiring a new approach to the measurement. A scheme proposed by NIST [103] involves applying a sawtooth-wave flux bias to the SQUID, where the amplitude is many flux quanta. A signal from the detector can be measured as a change in the phase of the periodic SQUID response. Crucially, the entire SQUID response curve is sampled in this technique, including portions with zero slope (where the SQUID is insensitive to changes in flux). Thus, the sensitivity is degraded by a factor of $\sqrt{2}$.

Other applications

SQUIDs have many applications beyond TES readout. To start, they can be used for readout of other types of low-temperature detectors. One such detector is the metallic magnetic calorimeter (MMC), a type of X-ray detector [104–106]. In this technology, an X-ray absorber is placed in tight thermal contact with a paramagnetic material that has a temperature-dependent magnetization. Similar to a TES, the magnetic material has a weak thermal link to a heat bath. A SQUID is used

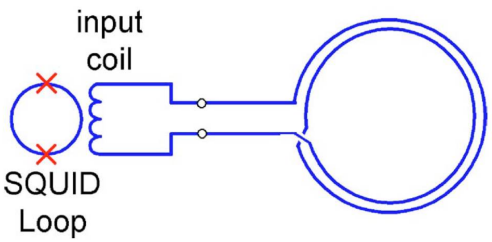

Figure 1.14: SQUID magnetometer with pickup coil. Figure reprinted from [82].

to monitor the magnetization. An MMC-SQUID system has been demonstrated that was lithographically patterned and fabricated on a single substrate, which is promising for making arrays of these detectors [107]. Another type of X-ray detector is the SIS tunnel junction [108]. This type of detector uses an SIS Josephson junction, with the one of the electrodes acting as an X-ray absorber. An incident high-energy X-ray breaks many Cooper pairs, and the resulting quasiparticles can tunnel to the other electrode. This tunneling current can be measured by a SQUID. Typically, the Josephson supercurrent is suppressed by an external magnetic field [59]. An NIS junction can be used in similar applications [109], and has additional utility as a bolometer [110]. Finally, hot-electron bolometers are being developed for terahertz radiation detection [111]. This technology utilizes a material in which the electrons absorb energy from radiation, increasing their temperature above that of the lattice. The resulting increase in resistance is detected as a change in current by a SQUID. SQUID multiplexers can be used to read out arrays of these bolometers, much like they are with TESs [111].

When operated as magnetometers, SQUIDs are typically used in conjunction with a pickup coil (see Fig. 1.14). While magnetic fields can be picked up by the SQUID loop itself, this is not ideal, as the area of the SQUID loop is small and consequently has a small inductance of ~0.1 nH [82]. An important scientific application of SQUID magnetometers is the measurement of nuclear magnetic resonance (NMR) [112]. This is a widely-used technique to investigate the structure of materials, including new pharmaceuticals [59]. The nuclear magnetic susceptibility measurement that is central to this technique was difficult with earlier methods. The sample is placed in a magnetic field, typically a combination of a static field and a perpendicular oscillating field, causing the nuclear magnetic moments in the sample to precess. This resonance can be detected by a SQUID, by arranging the sample inside the SQUID's pickup loop [113]. The advantage of using SQUIDs instead of

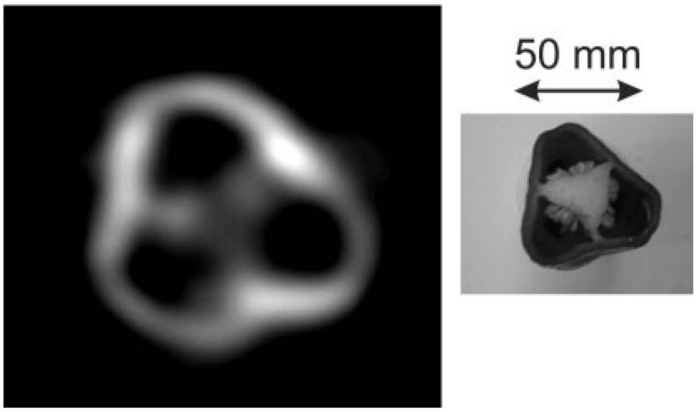

Figure 1.15: MRI of bell pepper slice taken in a 132 μT field using SQUIDs. Figure reprinted from [114].

less-sensitive magnetometers is that weaker polarizing magnetic fields can be used, reducing the overall cost of the system. SQUID-based NMR has been used for a variety of important scientific measurements [112].

Another important application of NMR is magnetic resonance imaging (MRI), a technique that is widely used in medicine to image organs and tissues. Typically, MRI systems use high magnetic fields that are expensive to obtain and maintain. If highly-sensitive magnetometers were used, smaller magnetic fields would be required, making MRI more accessible. MRI with microtesla fields and SQUID magnetometers has been demonstrated [114]. While the need for conventional high-field MRI systems will remain, low-field MRI is attractive for several situations. For example, MRIs are also needed when magnetoencephalography (MEG), another medical imaging technique using SQUIDs, is performed. A combined instrument that could use the same SQUIDs to perform both measurements would be very practical, and such a system has been demonstrated and used to image the human brain [115]. Low-field MRI is also attractive for situations where cost or convenience is a major factor, as a SQUID-based system would be inexpensive compared to one needing a large superconducting magnet [114]. A SQUID-based MRI system would benefit from using a large array of magnetometers. Much like the sensitivity of TES arrays in astronomy, it has been shown that the signal-to-noise ratio and scanning efficiency of MRI systems improve by using many detectors [116]. Thus, arrays of SQUIDs are necessary for continued improvement of low-field MRI systems.

In addition to MRI, SQUIDs are being used for several direct biomagnetic imaging techniques in medicine. Magnetoencephalography, mentioned above, is the

largest and most successful commercial application of SQUIDs to date [82]. In this technique, magnetometers are used to measure the small, picotesla-level magnetic fields that are produced by currents in the brain. MEG can localize brain activity to within a few millimeters [117], a major advantage over the widely-used technique of electroencaphalography (EEG). MEG systems, especially those covering the entire cortex, currently use hundreds of magnetometers in order to minimize noise and maximize data-collection efficiency [82]. However, since SQUIDs are difficult to multiplex, array sizes are limited and it is difficult to improve MEG systems further. In addition to MEG, SQUIDs are also attractive for newer biomagnetic imaging techniques used for the heart (magnetocardiography), muscles (magnetomyography), stomach (magnetoenterography), and lungs (magnetopneumography) [82]. All of these techniques would benefit from arrays of magnetometers like MEG does.

Another important practical application of SQUIDs is non-destructive evaluation (NDE), which seeks to detect flaws in materials and structures [118]. In magnetic NDE methods, a metallic sample is magnetized, and the presence of a defect is detected by monitoring the flux leakage outside the metal with a magnetometer. SQUIDs offer a number of advantages for this kind of technique. For example, like with MRI, the magnetizing field can be much lower with SQUIDs than with conventional methods [118]. Alternatively, the detector could be placed at a greater distance from the specimen. A SQUID is also sensitive enough to detect remnant magnetization in a sample without even applying an external magnetic field [82]. SQUID-based NDE has many commercial/public interest applications in detecting flaws in bridges, aircraft runways, and buildings. To image a large specimen efficiently and with low noise, it is beneficial to use arrays of magnetometers. SQUID arrays are thus important for NDE applications as well.

Finally, SQUIDs are being developed for a number of geophysical applications [82]. Magnetometers can be used to detect seismic, electric, magnetic, radiometric, and gravitational activity just below the Earth's surface. SQUIDs have a number of advantages over the standard methods used. First, SQUID magnetometers are typically smaller, which makes them easier to deploy and use, for example by placing them down boreholes. SQUIDs also have higher bandwidth and dynamic range than conventional systems, allowing for fewer individual detectors, as well as the ability to track diurnal variation (on the order of $\sim$100 nT) while maintaining full sensitivity [82]. This type of surveying is important for geophysical prospecting, which seeks to locate oil or mineral sources in the Earth's crust [59]. SQUIDs are

also used for laboratory geophysics in the form of scanning SQUID microscopes, which produce two-dimensional images of the magnetic fields from geological samples [119]. Multiplexed SQUID arrays would certainly improve scanning speed and precision for such applications. Given the limitations of SQUIDs, however, an alternate technology that matches their sensitivity is attractive. In this thesis we describe a novel technology that is expected to match SQUID sensitivity while offering a number of advantages over them.

Chapter 2

KINETIC INDUCTANCE PARAMETRIC UP-CONVERTER PRINCIPLES

2.1 Surface impedance of a superconducting thin film

The Drude model [120] in the theory of normal metals gives an expression for the DC electrical conductivity:

$$\sigma_{\mathrm{DC}} = \frac{ne^2\tau}{m}, \tag{2.1}$$

where n is the number of electrons per unit volume, e is the electronic charge, τ is the electron scattering time, and m is the electron mass. The conductivity appears in the local version of Ohm's law

$$\mathbf{j} = \sigma\mathbf{E}, \tag{2.2}$$

where $\mathbf{j}$ is the current density and $\mathbf{E}$ is the electric field. Further, the AC electrical conductivity is known to be complex, and is given by [121]

$$\sigma(\omega) = \frac{\sigma_{\mathrm{DC}}}{1 + \mathrm{j}\omega\tau}. \tag{2.3}$$

A normal metal has $\tau \sim 10^{-14}$ s and thus is almost completely resistive below microwave frequencies [122]. Ohm's law also applies in superconductors when the electron mean free path is short compared to the penetration depth of the electromagnetic field, a common practical scenario [123]. However, in a superconductor we have $\sigma_{\mathrm{DC}} \to \infty$ and $\omega\tau \to \infty$ (for nonzero ω), meaning that the ratio $\sigma_{\mathrm{DC}}/\omega\tau$ is finite. Thus, while the resistance is zero, there is a reactive impedance in superconductors at finite frequencies. This makes sense because the charge carriers have mass and thus inertia, so energy is required to change their kinetic energy, or, taken collectively, to cause a change in the supercurrent. This kind of impedance to a change in current is familiar from magnetostatics, where we have magnetic inductance [124]. Magnetic inductance impedes changes in current that are caused by a changing magnetic flux. Since the effect here is similar, it is useful to define a "kinetic inductance" L_k, which impedes changes in current due to the inertia of the electrons:

$$E_k = \frac{N}{2} mv^2 = \frac{1}{2} L_k I^2, \tag{2.4}$$

where E_k is the kinetic energy, N is the number of electrons, and I is the current. Kinetic inductance exists in normal metals as well, but is usually negligible because, as stated above, $\omega\tau \ll 1$ below microwave frequencies.

The modern theoretical foundation for conventional superconductivity was developed by Bardeen, Cooper, and Schrieffer (BCS) [125, 126], who showed that the zero-resistance charge carriers in a superconductor are pairs of electrons, known as Cooper pairs, that are linked by the electron-phonon interaction. A temperature-dependent energy $2\Delta(T)$ must be applied in order to break a Cooper pair and form two quasiparticles, or normal electrons. This is known as the superconducting energy gap, and for $T \ll T_c$ we have

$$\Delta(T) \approx \Delta_0 = 1.76\, k_B T_c, \tag{2.5}$$

where k_B is Boltzmann's constant and T_c is the superconducting transition temperature. The number of quasiparticles is

$$n_{qp} = 4N_0 \int_{\Delta}^{\infty} \mathrm{d}E \frac{E}{\sqrt{E^2 - \Delta^2}}\, f(E), \tag{2.6}$$

where N_0 is single-spin electron density of states at the Fermi level and

$$f(E) = \frac{1}{e^{E/k_B T} + 1} \tag{2.7}$$

is the Fermi-Dirac distribution function [45]. Thus, there is a small amount of quasiparticles at finite temperatures below T_c. Later, Mattis and Bardeen [127] applied the BCS theory to investigate the electrodynamics of superconductors, and found that the complex conductivity $\sigma(\omega) = \sigma_1(\omega) - \mathrm{j}\sigma_2(\omega)$ is given by

$$\begin{aligned}
\frac{\sigma_1(\omega)}{\sigma_n} &= \frac{2}{\hbar\omega} \int_{\Delta}^{\infty} \mathrm{d}E \frac{E^2 + \Delta^2 + \hbar\omega E}{\sqrt{E^2 - \Delta^2}\sqrt{(E + \hbar\omega)^2 - \Delta^2}} \left[f(E) - f(E + \hbar\omega)\right] \\
\frac{\sigma_2(\omega)}{\sigma_n} &= \frac{1}{\hbar\omega} \int_{\Delta}^{\Delta + \hbar\omega} \mathrm{d}E \frac{E^2 + \Delta^2 - \hbar\omega E}{\sqrt{E^2 - \Delta^2}\sqrt{\Delta^2 - (E - \hbar\omega)^2}} \left[1 - 2f(E)\right],
\end{aligned} \tag{2.8}$$

where σ_n is the DC normal-state conductivity just above T_c. As $T \to 0$, $f(E)$ decreases exponentially to zero, so σ_1 can be made arbitrarily low regardless of the frequency by operating at sufficiently low temperature. On the other hand, σ_2 remains finite. For $T \ll T_c$ and $\hbar\omega \ll \Delta_0$, we have [123]

$$\frac{\sigma_2(\omega)}{\sigma_n} \approx \frac{\pi\Delta_0}{\hbar\omega}. \tag{2.9}$$

The complex conductivity is in most cases not experimentally accessible; instead, the quantity being measured is the complex surface inductance

$$Z_s = R_s + \mathrm{j}X_s. \tag{2.10}$$

In many practical situations, the thickness t of a superconducting film is small compared to the penetration depth λ. Then we can use an effective thin-film penetration depth $\lambda_{\mathrm{thin}} = \lambda^2/t$ [86], and the surface impedance can be shown to be [122]

$$Z_s = \frac{1}{\sigma t}. \tag{2.11}$$

If one operates far below than T_c and at frequencies much lower than the gap, then the real part of the conductivity is negligible, and we can use Eq. (2.9) to write

$$Z_s = \mathrm{j}X_s = \mathrm{j}\omega \frac{\hbar \rho_n}{\pi \Delta_0 t}, \tag{2.12}$$

where $\rho_n = 1/\sigma_n$ is the normal-state resistivity. Noting the familiar form of the impedance of an inductor, we can express the surface kinetic inductance as

$$L_s = \frac{\hbar \rho_n}{\pi \Delta_0 t}. \tag{2.13}$$

Nonlinearity of the kinetic inductance

In recent years, several groups have demonstrated nonlinear behavior of the kinetic inductance in the presence of a supercurrent. It has been known since the early 1950s that superconductors exhibit nonlinear behavior in the presence of fields [128, 129]. In 1962, Parmenter gave a rigorous discussion based on the BCS theory of the nonlinearity of the complex conductivity due to a supercurrent [130]. Here we simply consider the nonlinearity in the kinetic inductance of a strip of superconducting material. A strip of length l and width w has a volume $V = lwt$ and kinetic inductance $L_k = (l/w)\, L_s$, using Eq. (2.13) for a thin film held at $T \ll T_c$. The kinetic inductance can be expanded as [123]

$$L_k(I) = L_k(0)\left(1 + \frac{I^2}{I_2^2} + \ldots\right), \tag{2.14}$$

where the constant I_2 sets the scale of the quadratic nonlinearity. The odd-ordered terms vanish due to symmetry considerations, as the strip must have the same kinetic inductance regardless of orientation. It is expected [123] that the fractional perturbation to the kinetic inductance due to the supercurrent is on the order of the

ratio of the kinetic energy to the total pairing energy:

$$\frac{\delta L_k}{L_k} = \kappa_* \frac{E_k}{E_p} = \kappa_* \frac{\frac{1}{2} L_k I^2}{2 N_0 \Delta_0^2 V} = \kappa_* \frac{J^2}{J_*^2}, \tag{2.15}$$

where N_0 here is the single-spin density of states per unit energy and unit volume. The dimensionless constant κ_* is expected to be of order unity, $J = I/wt$ is the current density, and

$$J_* = \sqrt{\frac{4\pi N_0 \, \Delta_0^3}{\hbar \rho_n}}. \tag{2.16}$$

In an analysis of tunneling density-of-states measurements based on the Usadel equations [131], Anthore et al. found that the gap varies with a supercurrent as [132]

$$\frac{\Delta}{\Delta_0} \approx 1 - 1.9 \, \frac{J^2}{J_*^2} - 3.5 \, \frac{J^4}{J_*^4}. \tag{2.17}$$

Putting $\Delta_0 \rightarrow \Delta$ in Eq. (2.13), we find

$$\frac{\delta L_k}{L_k} = -\frac{\delta \Delta}{\Delta_0} \approx 1.9 \, \frac{J^2}{J_*^2} + 3.5 \, \frac{J^4}{J_*^4}, \tag{2.18}$$

suggesting that $\kappa_* \approx 1.9$ and that a quadratic term may become important at higher currents. Additionally, they found that $J_* \approx 4.7 \, I_c/wt$, showing that the scale of the nonlinearity is on the order of the critical current.

Kinetic inductance nonlinearity in the Ginzburg-Landau theory

The Ginzburg-Landau theory of superconductivity [133] is useful for deriving a qualitative description of the kinetic inductance nonlinearity. This is a phenomenological theory that is exact only near T_c and when the number density of Cooper pairs n_s^* varies slowly in space, but it has been found to be experimentally valid (at least in a qualitative sense) in a much wider range of scenarios [86]. The basic postulate of the theory is that the free energy density of a superconductor can be written as

$$f = f_n + \alpha |\psi|^2 + \frac{\beta}{2} |\psi|^4 + \frac{1}{2m^*} \, |(\mathbf{p} - e^* \mathbf{A}) \, \psi|^2 + \frac{\mathbf{B}^2}{2\mu_0}, \tag{2.19}$$

where f_n is the free energy density in the normal state, μ_0 is the magnetic permeability, and α and β are phenomenological parameters. The complex order parameter ψ is related to the density of Cooper pairs as $|\psi|^2 = n_s^*$. The Cooper pair mass is included as $m^* = 2m$, and the Cooper pair charge is $e* = 2e$, where m and e are the electron mass and charge, respectively. The vector $\mathbf{p}$ in the kinetic energy term is

the three-dimensional momentum operator from quantum mechanics. The magnetic field $\mathbf{B}$ is related to the vector potential $\mathbf{A}$ as $\mathbf{B} = \nabla \times \mathbf{A}$. Deep in the interior of a bulk superconductor we have

$$|\psi|^2 = \psi_\infty^2 = -\frac{\alpha}{\beta}, \tag{2.20}$$

which can be found by minimizing the free energy when the particle momentum and external field are set to zero. When the field reaches the critical field B_c above which superconductivity is destroyed, the kinetic energy term is zero and the free energy must equal the free energy of the normal state. Then it can be shown, using Eq. (2.20), that

$$\alpha = -\frac{B_c^2}{\mu_0 |\psi|^2}. \tag{2.21}$$

Finally, the effective penetration depth in the Ginzburg-Landau theory is

$$\lambda_{\text{eff}} = \sqrt{\frac{m^*}{4\mu_0 |\psi|^2 e^2}}. \tag{2.22}$$

In a thin film, the energy from the magnetic field can be ignored, as it is less than the kinetic energy by a factor on the order of the ratio of the cross-sectional area of the conductor to λ_{eff}^2 [86]. In addition, the order parameter is approximately constant, so the momentum is simply $p = m^* v_s$, where v_s is the Cooper pair velocity. Then, by minimizing the free energy, we find

$$|\psi|^2 = \psi_\infty^2 \left(1 + \frac{m^* v_s^2}{2\alpha}\right). \tag{2.23}$$

Using Eq. (2.21) and the definition $J = 2|\psi|^2 e v_s$ for the current density, we get

$$|\psi|^2 = \psi_\infty^2 \left(1 - \frac{\mu_0^2 \lambda_{\text{eff}}^2 J^2}{2B_c^2}\right), \tag{2.24}$$

where we have additionally used Eq. (2.22) to simplify the expression. Thus, we find that the Ginzburg-Landau order parameter is perturbed by a supercurrent J.

We now turn our attention back to the surface kinetic inductance. It can be shown that, for temperatures much lower than T_c [122],

$$L_s = \mu_0 \frac{\lambda_{\text{eff}}^2}{t}, \tag{2.25}$$

where we use the expression λ_{eff}^2/t for the thin-film penetration depth. Then, for the strip of total kinetic inductance L_k, we have

$$\frac{\delta L_k}{L_k} = \frac{\delta L_s}{L_s} = \frac{\delta \lambda_{\text{eff}}^2}{\lambda_{\text{eff}}^2}. \tag{2.26}$$

But from Eqs (2.22) and (2.24) we have

$$\frac{\delta \lambda_{\text{eff}}^2}{\lambda_{\text{eff}}^2} = -\frac{\delta |\psi|^2}{\psi_\infty^2} = \frac{\mu_0^2 \, \lambda_{\text{eff}}^2 \, J^2}{2B_c^2}. \tag{2.27}$$

Noting that the energy density associated with the critical field, $B_c^2/2\mu_0$, is equivalent to the depairing energy per unit volume $2N_0 \, \Delta_0^2$, and using the expression $J = I/wt$ as well as applying Eq. (2.25) again, we have

$$\frac{\delta L_k}{L_k} = \frac{\mu_0^2 \, \lambda_{\text{eff}}^2 \, J^2}{2B_c^2} = \frac{\frac{1}{2} L_k I^2}{4N_0 \, \Delta_0^2 \, lwt}. \tag{2.28}$$

Finally, recalling that $2N_0 \, \Delta_0^2 \, lwt = 2N_0 \, \Delta_0^2 \, V = E_p$, we have

$$\frac{\delta L_k}{L_k} = \frac{1}{2} \frac{E_k}{E_p}. \tag{2.29}$$

That is, the fractional perturbation of the kinetic inductance due to the supercurrent is equal to half the ratio of the kinetic energy to the pairing energy, in accordance with the statement of Eq. (2.15). Though this result is not expected to be exactly valid far below T_c, it is useful for qualitatively describing the nonlinearity.

The perturbation of the kinetic inductance is a quantity that can be measured sensitively. Since it is caused by a current, this effect can be utilized to make a sensitive ammeter. In the following sections we describe the general paradigm for detecting small RF currents using kinetic inductance, and then three systems that strongly exhibit this effect and their expected advantages compared to the standard current-sensing technology based on SQUIDs.

2.2 Parametric up-conversion in superconductors

The quadratic kinetic inductance nonlinearity is analogous to the Kerr effect in nonlinear optics. In an optical fiber, nonlinear response to light originates in the anharmonic motion of bound electrons under the influence of the applied field [134]. The polarization induced by the dipoles in the dielectric is

$$\mathbf{P} = \epsilon_0 \left(\chi^{(1)} \, \mathbf{E} + \chi^{(2)} \, \mathbf{E}^2 + \chi^{(3)} \, \mathbf{E}^3 + \ldots \right), \tag{2.30}$$

where ϵ_0 is the vacuum permittivity, $\mathbf{E}$ is the electric field, and $\chi^{(i)}$ is the i^{th} order electric susceptibility. Here we have suppressed the tensor indices; for instance, the second-order term is actually $P_k^{(2)} = \chi_{klm}^{(2)} E_l E_m$. The third-order susceptibility results in the refractive index having an intensity-dependent component:

$$n(\mathbf{E}) = n(0) + n_2 |\mathbf{E}|^2. \tag{2.31}$$

This is known as the Kerr effect. Processes resulting from such nonlinearities are known as parametric processes, because they involve the modulation of a parameter (in this case the refractive index). One such process is parametric up-conversion [135], which is generally used to convert a long-wavelength signal to a short-wavelength signal while retaining its information. The signal is at frequency ω_s, and a high-frequency carrier is applied at frequency ω_c. The nonlinearity results in sidebands around the carrier, at $\omega_c - \omega_s$ and $\omega_c + \omega_s$. These are the up-converted signals. This process is useful in optics for converting infrared information to the optical spectrum [135].

In superconductors, as we have shown, the modulated parameter is the surface kinetic inductance

$$L_s = L_{s0}\left(1 + \frac{I^2}{I_*^2}\right). \tag{2.32}$$

Here, the current is analogous to the electric field in the optical Kerr effect. The third-order nonlinearity comes from the voltage drop across a strip of superconducting material with kinetic inductance L_k:

$$V = \frac{\mathrm{d}}{\mathrm{d}t}(L_k I). \tag{2.33}$$

Putting $L_k = L_{k0}\,(1 + I^2/I_*^2)$, we get

$$v = L_{k0}\,\frac{\mathrm{d}I}{\mathrm{d}t} + 3L_{k0}\,\frac{I^2}{I_*^2}\frac{\mathrm{d}I}{\mathrm{d}t}. \tag{2.34}$$

The second term is third-order. Suppose we apply three currents to the superconductor, such that the total current is

$$I = I_0 + I_c\cos(\omega_c t) + I_s\cos(\omega_s t), \tag{2.35}$$

where I_0 is a DC current, $I_c\cos(\omega_c t)$ is the carrier, and $I_s\cos(\omega_s t)$ is the signal. Then we have

$$\frac{\mathrm{d}I}{\mathrm{d}t} = -\omega_c I_c\sin(\omega_c t) - \omega_s I_s\sin(\omega_s t). \tag{2.36}$$

Suppose now that $I_0 \gg I_c$ and $I_0 \gg I_s$, so that when computing the square of the total current we ignore terms not involving the DC current. Then we have

$$I^2 \approx I_0^2 + 2I_0 \left[I_c \cos(\omega_c t) + I_s \cos(\omega_s t) \right]. \tag{2.37}$$

Suppose further that the signal frequency is much smaller than the carrier frequency, and that the system is band-limited such that it is only sensitive to frequencies near the carrier. Then, multiplying Eqs. (2.36) and (2.37), we get

$$\begin{aligned} -I^2 \frac{\mathrm{d}I}{\mathrm{d}t} = {} & \omega_c I_0^2 I_c \sin(\omega_c t) + (\omega_c - \omega_s) I_0 I_c I_s \sin\left((\omega_c - \omega_s) t\right) \\ & + (\omega_c + \omega_s) I_0 I_c I_s \sin\left((\omega_c + \omega_s) t\right), \end{aligned} \tag{2.38}$$

showing the up-converted signals at $\omega_c - \omega_s$ and $\omega_c + \omega_s$. The amplitudes of the two sidebands are very close, as $\omega_s \ll \omega_c$.

The rest of this thesis describes a class of superconducting devices, known as kinetic inductance parametric up-converters (KPUPs), for which the nonlinearity driving the parametric up-conversion is the kinetic inductance of the superconducting material. Due to advantages in fabrication and bandwidth, the KPUPs are designed to operate with a carrier in the microwave regime. Signal currents will be in the lower-frequency RF regime. A DC bias current is required in order to sensitively detect the up-converted signals. The microwave carrier and sidebands are sent through a cryogenic low-noise amplifier, and the amplifier output is demodulated at room temperature by mixing with a local oscillator at the carrier frequency, recovering the signal of interest. This paradigm offers high sensitivity to small currents and several advantages over SQUIDs.

2.3 Lumped-element resonator KPUP

Background

Superconducting microresonators have been studied extensively over the last decade [123]. Interest in superconductivity at microwave frequencies first began after the massive development of microwave technology due to the radar effort in World War II [136–138]. Superconducting cavity resonators were a focus or research throughout much of the ensuing years [139–141], because they could achieve high quality factors on the order of $Q_r \sim 10^{11}$. The development of high-quality-factor cavities was encouraged due to their utility in particle accelerators [142]. In general, a microwave resonator must be excited by a source via coupling with a waveguide or transmission line. The overall quality factor of the resonator is given by

$$\frac{1}{Q_r} = \frac{1}{Q_i} + \frac{1}{Q_c}, \tag{2.39}$$

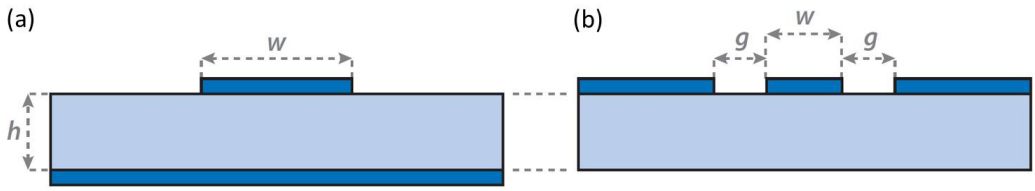

Figure 2.1: (a) Cross-section of microstrip. The dark blue areas are (super)conducting and the light blue areas are dielectric. The conducting strip of width w resides on a dielectric of thickness h that is backed by a conducting ground plane. (b) Cross-section of a co-planar waveguide. The center conductor of width w is separated from ground planes on either side by gaps of width g, and all conductors are part of a single metal layer on top of a dielectric. Figure reprinted from [123].

where Q_c characterizes the strength of the coupling and Q_i is determined by internal dissipative losses of the resonator. Despite the prediction of the Mattis-Bardeen theory, experiments with cavity resonators showed that, due to the realities of materials, fabrication techniques, and experimental conditions, the dissipation in a superconductor does not fall to zero at very low temperatures, but instead reaches a finite limit. However, the resulting internal quality factors can be very high, and cavity resonators have proven useful for applications such as low-noise oscillators [123].

For many other applications it is advantageous to use thin-film resonators, due to their lower volume and simplicity of fabrication. In the microwave regime it is straightforward to make thin-film transmission-line resonators. Typically these are quarter-wavelength or half-wavelength resonators. The first type of transmission-line resonator to be explored was the microstrip [143], shown in Fig. 2.1(a), which can be fabricated by depositing three successive film layers (superconductor, dielectric, superconductor) and patterning the top layer. The thickness of the dielectric is typically on the order of ~0.1–1 μm [123]. It was shown in 1947 [137, 138] that the phase velocity of a superconducting microstrip would be modified by the Mattis-Bardeen surface impedance $Z_s = \mathrm{j}\omega L_s = \mathrm{j}\omega\mu_0\,\lambda_{\mathrm{eff}}^2/t$. The inductance per unit length of a microstrip made of a perfect conductor is

$$\mathcal{L} = \frac{\mu_0 h}{w}, \tag{2.40}$$

where h is the thickness of the dielectric and w is the width of conducting strip. When using a superconductor, substituting $\lambda_{\mathrm{thin}} = \lambda_{\mathrm{eff}}^2/t$, the inductance per unit length is modified to

$$\mathcal{L} = \frac{\mu_0\,(h + 2\lambda_{\mathrm{thin}})}{w}, \tag{2.41}$$

as if the spacing between the two superconducting films is increased by $2\lambda_{\text{thin}}$. The fraction of the total inductance that is provided by the surface impedance (or kinetic inductance) is

$$\alpha = \frac{2\lambda_{\text{thin}}}{h + 2\lambda_{\text{thin}}}. \tag{2.42}$$

This is known as the kinetic inductance fraction. The phase velocity in a transmission line is

$$v_p = \frac{1}{\sqrt{\mathcal{L}C}}, \tag{2.43}$$

where the capacitance per unit length C is unchanged from the perfect-conductor scenario [123]. It is clear then that the phase velocity, and thus the resonance frequency in the case of a transmission-line resonator, is changed by using a superconductor instead of a perfect conductor.

The modern effort in developing superconducting microresonators began at Caltech and JPL in 2000, after J. Zmuidzinas and H. G. Leduc conceived a new type of photon detector known as the microwave kinetic inductance detector (MKID) [101]. The principle behind this detector is depicted schematically in Fig. 2.2. From the Mattis-Bardeen theory, the complex conductivity for $k_B T \ll \Delta_0$ and $\hbar\omega \ll \Delta_0$ depends on the number of quasiparticles n_{qp} as

$$\begin{aligned}
\frac{\sigma_1(n_{qp})}{\sigma_n} &= \frac{2\Delta_0}{\hbar\omega} \frac{n_{qp}}{N_0\sqrt{2\pi k_B T \Delta_0}} \sinh(\xi)\, K_0(\xi) \\
\frac{\sigma_2(n_{qp})}{\sigma_n} &= \frac{\pi\Delta_0}{\hbar\omega}\left[1 - \frac{n_{qp}}{2N_0\,\Delta_0}\left(1 + \sqrt{\frac{2\Delta_0}{\pi k_B T}}\, e^{-\xi}\, I_0(\xi)\right)\right],
\end{aligned} \tag{2.44}$$

where $\xi = \hbar\omega/k_B T$, and I_0 and K_0 are the zeroth-order modified Bessel functions of the first and second kind, respectively [90]. Thus, an increase in quasiparticles caused by absorption of light changes the complex conductivity and thus the kinetic inductance, as well as the internal dissipation. If the kinetic inductance is part of a microwave resonator, the result of the absorption is a change in the frequency and internal quality factor of the resonator, quantities that can be measured using standard microwave readout electronics. The frequency shift is related to the kinetic inductance fraction α, so materials and geometries with large α are valuable for use in MKIDs. One of the main advantages of MKIDs over other detectors such as TESs is ease of multiplexing in the frequency domain. The standard MKID multiplexing scheme is shown in Fig. 2.3. An array of MKIDs with different resonance frequencies is coupled to a single transmission line, called a feedline. Carriers at each resonance frequency are simultaneously generated and sent down the

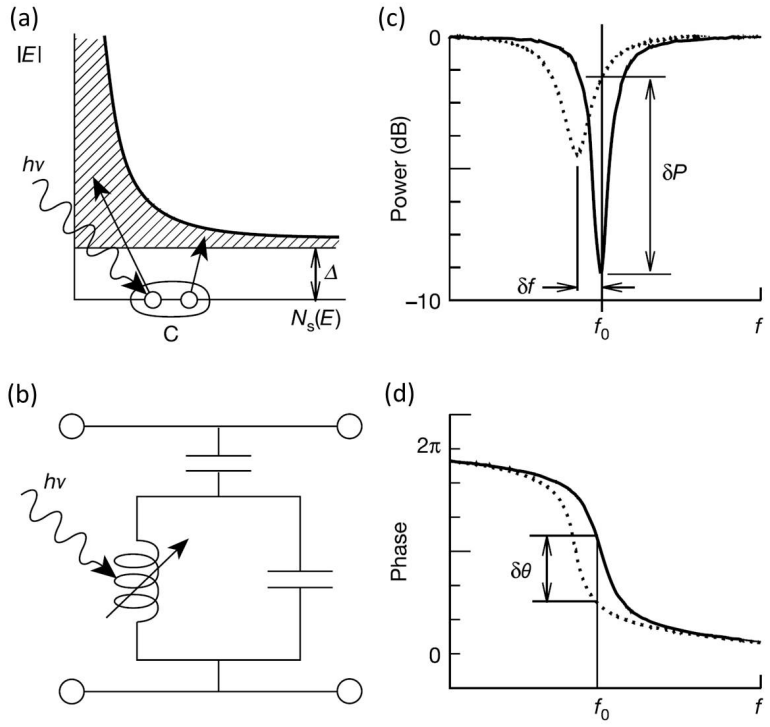

Figure 2.2: MKID detection principle. (a) A photon with energy $h\nu > 2\Delta$ is absorbed in a superconductor and breaks a Cooper pair, exciting two quasiparticles. The Cooper pairs (C) are shown at the Fermi level, and the density of states for quasiparticles $N_s(E)$ is plotted against the quasiparticle energy. The shaded area represents available quasiparticle states. (b) Upon photon absorption, the increase in quasiparticles changes the inductance in a microwave resonator, and also increases the resistance. (c) The transmission through the feedline has a dip at the resonance frequency f_0. The increased inductance and resistance due to the photon absorption reduce both the resonance frequency (δf) and the power in the resonator (δP). (d) The phase of the transmission also changes. Figure reprinted from [101].

feedline, and the transmission through the feedline exhibits dips at each resonance frequency. Since the impedance of a shunted resonator is large away from its resonance, only the carrier at its corresponding frequency couples into the resonator. The resonance shift caused by absorption of light in an MKID is read out as a change in the transmission function [122]

$$S_{21} = 1 - \frac{Q_r}{Q_c} \frac{1}{1 + \mathrm{j}2Q_r x}, \tag{2.45}$$

where $x = (\omega - \omega_r)/\omega_r$ is the fractional detuning from the resonance frequency ω_r.

The early MKID effort began with thin-film microstrip resonators [123], using superconductors such as aluminum and niobium, and using silicon dioxide as the

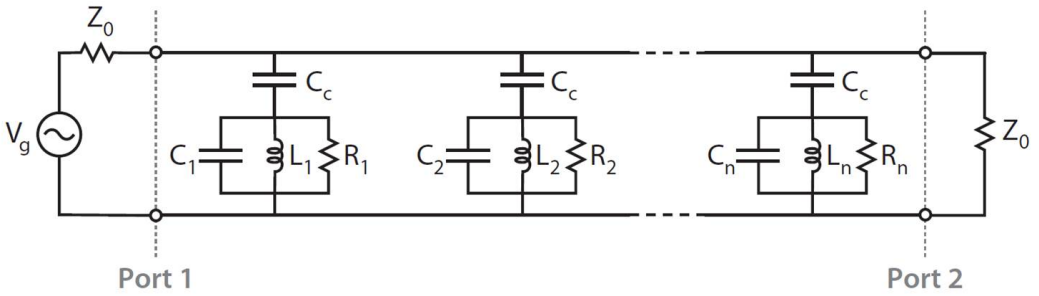

Figure 2.3: Multiplexing of MKIDs. The MKID resonators are shown schematically as RLC tank circuits, each coupled to the feedline through a small capacitance C_c. Each resonator has a unique frequency $\omega_i = 1/\sqrt{L_i C_i}$. The resonators are simultaneously driven by a frequency comb from the generator at port 1. The transmission through the array is measured at port 2 by an amplifier, represented as the input impedance Z_0. Figure reprinted from [123].

dielectric. However, the data obtained from these devices was not in good agreement with the Mattis-Bardeen theory. P. K. Day suggested that two-level systems (TLS) in the amorphous dielectric could be responsible for the discrepancies, and the TLS model was indeed a good fit to the experimental data. A 2005 paper from the Martinis group on the effect of TLS in Josephson qubits [144] convinced the Caltech/JPL team to take the idea seriously. TLS arise in amorphous materials because, due to their disordered nature, atoms can easily move between pairs of configurations [90]. The system can be described quantum-mechanically as a double potential well with the two configurations corresponding to the two local minima of the well. The two states have two different energy levels due to differences in the chemical bond configuration. Atoms can tunnel through the energy barrier between the two states. Due to the disorder in the material, the energy levels and barrier height are effectively random, leading to a uniform distribution of TLS energy splittings. The atoms have electric dipole moments that can couple to electric fields. In a microwave resonator, circulating power can be lost to this effect. The random tunneling events also result in fluctuations in the dielectric constant of the material. Since the capacitance in a resonator depends on the dielectric constant of the substrate, the TLS cause fluctuations in the resonator capacitance, resulting in frequency noise [145]. TLS noise has been measured [146] and found to exist even in resonators with a crystalline substrate [147], as a thin amorphous layer exists at the surface. A full theoretical description of TLS is not yet available, but Gao et al. provide a semi-empirical

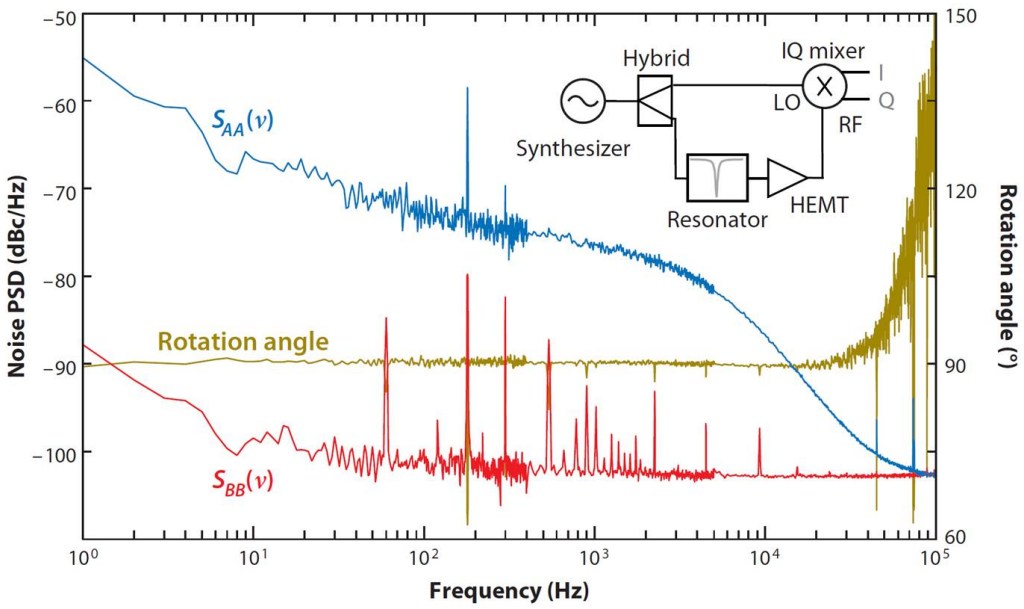

Figure 2.4: Measurement of TLS noise in a Nb/Si superconducting CPW microresonator. The inset shows the standard homodyne measurement scheme used to measure the transmission $S_{21} \propto I + jQ$. The blue curve is the noise power spectral density (PSD) in the phase direction. The roll-off at 6 kHz is due to the resonator bandwidth. The red curve is the noise PSD in the amplitude direction. The amplitude noise is limited by the readout amplifier. The gold curve is the rotation angle between the major direction of the fluctuations and the amplitude direction. Within the resonator bandwidth it is 90°, meaning that the fluctuations are entirely in the phase direction. Figure reprinted from [146].

model [148]. The fractional frequency noise due to TLS is

$$S_{\mathrm{TLS}}(\nu) = \kappa(\omega, T; \nu) \frac{\int_{V_{\mathrm{TLS}}} \mathrm{d}^3\mathbf{r}\, |\mathbf{E}(\mathbf{r})|^3}{4\left[\int_V \mathrm{d}^3\mathbf{r}\, |\epsilon(\mathbf{r})\, \mathbf{E}(\mathbf{r})|^2\right]^2}, \tag{2.46}$$

where $\mathbf{E}$ is the microwave electric field and ϵ is the dielectric constant. The integral in the numerator is over the volume where the TLS exist, while the integral in the denominator is over the total volume. The noise spectral density coefficient $\kappa(\omega, T; \nu)$ has a $\nu^{-1/2}$ spectral shape and also contains the dependence on microwave frequency and temperature. TLS have proven to be the dominant intrinsic noise source in superconducting microresonators.

Because of their difficulty with microstrip resonators, the Caltech/JPL group switched to co-planar waveguide (CPW) resonators [101], shown in Fig. 2.1(b). These were patterned from a single superconducting film deposited on a crystalline substrate.

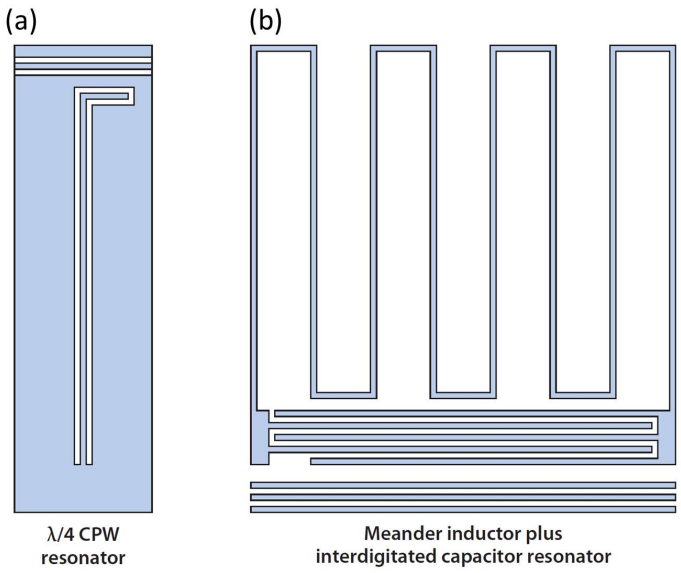

Figure 2.5: (a) An example of a quarter-wavelength CPW resonator geometry. The blue areas are superconductor, and the white areas represent regions where the superconducting film has been etched away. A CPW feedline is shown at the top. The resonator has a stub section in order for it to couple to the feedline. (b) An example of a lumped-element resonator geometry. The resonator consists of a meandered inductor and an interdigitated capacitor (IDC). A CPW feedline is shown at the bottom. The resonator is proximity-coupled to the feedline. Figure reprinted from [123].

The kinetic inductance fraction of a CPW is generally smaller than that of a microstrip, but the fabrication is greatly simplified [123]. CPW resonators have since been adopted and developed by other groups [149, 150]. In 2009, Noroozian et al. showed that hybrid resonators using an interdigitated structure to provide the capacitance have greatly reduced TLS noise [145]. Interdigitated capacitors are also used in the lumped-element kinetic inductance detector (LEKID) concept first proposed by Doyle et al. [151]. Here, not only is the capacitor a lumped element, but so is the inductor. An example is shown in Fig. 2.5(b). Both resonator components can be patterned on the same film, so the fabrication is no more difficult than that of CPW resonators. This design is advantageous for MKIDs because the meandered inductor can also serve as an absorber for the radiation. Another benefit of a lumped-element design is reduced radiative loss from the resonator to the substrate [123], resulting in a higher internal quality factor.

In 2008, Barends et al. published measurements of a CPW resonator made of NbTiN [152], a superconductor with a normal-state resistivity of $\rho_n = 170\,\mu\Omega \cdot \mathrm{cm}$,

which is several orders of magnitude higher than that of the metals usually used. The resonator had a large kinetic inductance fraction of $\alpha = 0.35$, and the measured quality factor was comparable to that of aluminum resonators [123]. The T_c of the film was about 14.8 K. Later, Leduc et al. demonstrated even higher quality factors of $Q_i = 3 \times 10^7$ with sputtered titanium nitride (TiN_x) resonators [153]. Stoichiometric TiN films had a resistivity of $\rho_n = 100\,\mu\Omega \cdot \mathrm{cm}$ and critical temperature $T_c = 4.5\,\mathrm{K}$. The lower T_c resulted in a larger surface inductance (by Eq. (2.13), recalling $\Delta_0 = 1.76\,k_B T_c$), and thus the resonator had a kinetic inductance fraction of $\alpha = 0.74$. Further, the T_c could be tuned between 0 and 5 K by altering the sputtering conditions and changing the nitrogen content of the film. TiN has since become a popular material for MKID development. An array of 100 TiN LEKIDs was demonstrated in 2012 with nearly background-limited performance [154]. Since then, arrays of ~500 pixels have been demonstrated at the Caltech Submillimeter Observatory. The numerous advantages of these devices suggest a route for other kinds of detection based on kinetic inductance variation.

Principle

The kinetic inductance parametric up-converter is a device that aims to detect small currents through their effect on its kinetic inductance. Since MKIDs, and in particular LEKIDs, have been so successful for detecting changes in kinetic inductance due to photon absorption, using a similar paradigm for detecting changes in kinetic inductance due to currents would be a promising path. A schematic of such a detector is shown in Fig. 2.6. Similar to a LEKID, it is a superconducting lumped-element resonator consisting of an inductance L and a capacitance C. The resonator is shunt-coupled to a microwave feedline via a coupling capacitance C_c. A generator sends a carrier tone at angular frequency $\omega = 1/\sqrt{LC}$ down the feedline. The transmission through the feedline, which is read out by a low-noise cryogenic amplifier, shows a dip at the resonance frequency. In addition to the microwave generator, there is another input to the circuit. The current perturbation to be detected δI, along with a DC bias current I_0, is connected directly to the resonator inductor. This is analogous to the radiation absorption in an MKID. A large inductance L_{iso} is required in order to isolate this second input from the microwave power in the resonator. The current signal δI is assumed to be slowly-varying compared to the microwave oscillations in the resonator and feedline, such that it sees the inductors and capacitors in the circuit as short circuits and open circuits, respectively. The current input to the resonator inductor causes its value to change, due to the kinetic

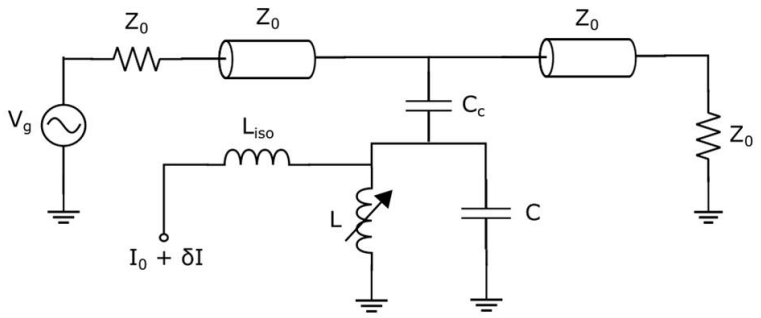

Figure 2.6: Lumped-element resonator KPUP schematic. The KPUP is an LC tank circuit. The feedline is represented as transmission line sections on either side of the resonator. A coupling capacitor is used to couple the resonator to the feedline. A carrier is generated by the microwave source and sent through the feedline, and the transmission through the feedline is measured by an amplifier represented as an input impedance Z_0. Another input line is used to send a bias and signal current through the inductor of the resonator. A large inductor L_{iso} is used to represent isolation between this port and the microwave power in the resonator. The inductance L in the resonator varies depending on the input currents due to the kinetic inductance nonlinearity.

inductance nonlinearity. This change in inductance is observed as a shift in the resonance frequency in the transmission data. In principle, a large array of KPUPs may be connected in parallel to the same feedline, each with a slightly different resonance frequency. Such an array would be useful for reading out an array of transition-edge sensors.

The current-sensing process can also be described in terms of parametric up-conversion. Suppose the microwave excitation circulating in the resonator is at frequency ω_c, and the current signal δI can be described as being at frequency ω_s, i.e., $\delta I = I_s \cos(\omega_s t)$. Due to the nonlinearity of the inductor, this signal mixes with the carrier and modulates the resonator's frequency at a frequency ω_s:

$$\omega(t) = \omega_c + \delta\omega(t) = \omega_c + \frac{\mathrm{d}\omega}{\mathrm{d}I} I_s \cos(\omega_s t). \tag{2.47}$$

The amplitude of the current in the resonator is then

$$\begin{aligned} A(t) &= A_c \exp\left[\mathrm{j}\int_0^t \omega(\tau)\,\mathrm{d}\tau\right] \\ &\approx A_c e^{\mathrm{j}\omega_c t} + \frac{A_c I_s}{2\omega_s}\frac{\mathrm{d}\omega}{\mathrm{d}I} e^{\mathrm{j}(\omega_c+\omega_s)t} - \frac{A_c I_s}{2\omega_s}\frac{\mathrm{d}\omega}{\mathrm{d}I} e^{\mathrm{j}(\omega_c-\omega_s)t}, \end{aligned} \tag{2.48}$$

where A_c is the amplitude from the carrier. Here we have used the fact that the signal is small in order to make the approximation $e^x \approx 1 + x$. We see that there are

sidebands at frequencies $\omega_c \pm \omega_s$. If $\omega_s < \omega_r/2Q$, the bandwidth of the resonator, then the sidebands can couple out of the resonator and be seen at the end of the feedline by the readout amplifier. The total output signal is then mixed with the original carrier frequency at room temperature in order to recover the signal. This mixing adds the power of both sidebands together. Since $P \propto A^2$, we find that the sideband power is

$$P_s = \frac{I_s^2}{2\omega_s^2}\left(\frac{\mathrm{d}\omega}{\mathrm{d}I}\right)^2 P_c, \tag{2.49}$$

where P_c is the carrier power. Thus, the KPUP provides gain $G \propto (\mathrm{d}\omega/\mathrm{d}I)^2\, P_c/2\omega_s^2$ to the signal. Increased gain results in stronger detection, so it is important to use a high carrier power and to maximize the device responsivity $\mathrm{d}\omega/\mathrm{d}I$.

We now derive an expression for the response of the resonator to a current perturbation. The function for the transmission through one resonator is the same as Eq. (2.45):

$$S_{21}(\omega) = 1 - \frac{Q_r}{Q_c}\frac{1}{1 + \mathrm{j}2Q_r x}, \tag{2.50}$$

recalling that $x = (\omega - \omega_r)/\omega_r$ is the fractional detuning of the generator frequency from the resonance frequency ω_r. As shown in Fig. 2.7, this function traces out a clockwise circle in the complex plane as the frequency is increased from zero to infinity. At these extreme values of the frequency, we see from Eq. (2.50) that $S_{21} \to 1$. This is because, far from the resonance, no power couples into the resonator, so the generator power travels through the feedline uninterrupted, resulting in perfect transmission. The minimum value of the transmission amplitude occurs at resonance, or $x = 0$:

$$\min|S_{21}| = 1 - \frac{Q_r}{Q_c}. \tag{2.51}$$

In the case that $Q_i \gg Q_c$, then from Eq. (2.39) we have $Q_r \approx Q_c$ and thus $\min|S_{21}| \approx 0$. In addition, as $x \to \infty$ far from the resonance, it is clear from Eq. (2.50) that $S_{21} \to 1$. The values of the quality factors may be determined from a measurement of the transmission function. The overall quality factor is determined from

$$\frac{1}{Q_r} = \frac{\Delta\omega}{\omega_r}, \tag{2.52}$$

where $\Delta\omega$ is the resonance linewidth. Eq. (2.51) may then be used to find the coupling quality factor

$$Q_c = \frac{Q_r}{1 - \min|S_{21}|}. \tag{2.53}$$

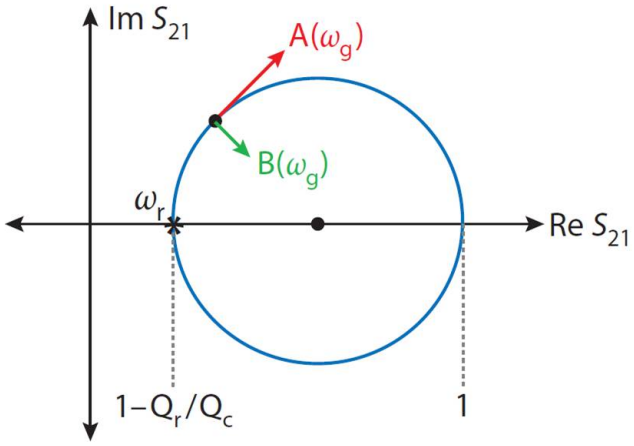

Figure 2.7: Circular trajectory of resonator transmission S_{21} as a function of generator frequency ω_g in the complex plane. The directions tangent and perpendicular to the trajectory are indicated by the complex response coefficients $A(\omega_g)$ and $B(\omega_g)$, respectively. The tangent direction corresponds to a change in frequency, and the perpendicular direction corresponds to a change in amplitude. At the resonance frequency ω_r, the magnitude of the function reaches its minimum value of $1 - Q_r/Q_c$. The function approaches its maximum value of unity far from the resonance, in both frequency directions. Figure reprinted from [123].

Finally, we can apply Eq. (2.39) to find the internal quality factor

$$Q_i = \frac{Q_r}{\min |S_{21}|}. \tag{2.54}$$

In practice, a measurement of the transmission will generally not directly yield a perfect circle such as that of Fig. 2.7: the characteristics of the readout circuit will have an effect on the data. In particular, cable delay will cause the trajectory to cross itself, and the enclosed loop will be smaller. The loop will often also be rotated due to impedance mismatch between the feedline and the source and/or load impedances. However, these effects can be corrected for during data analysis by using a resonance-fitting code, so we do not consider them in this discussion.

The change in the surface impedance due to a supercurrent is purely reactive, so x is the only quantity that changes on the right-hand side of Eq. (2.50). Then the resonator response is

$$\delta S_{21}(\omega; t) = A(\omega)\, \delta x(t) \tag{2.55}$$

for time-dependent perturbations $\delta x(t)$. The reactive response coefficient $A(\omega)$ is

$$A(\omega) = \frac{\mathrm{d}S_{21}}{\mathrm{d}x} = \mathrm{j}\frac{2Q_r^2}{Q_c}\frac{1}{(1 + \mathrm{j}2Q_r x)^2}. \tag{2.56}$$

For the response to general perturbations $\delta x(t)$, the ring-down response of the resonator must be considered [123]. This response is represented in the frequency domain as the transfer function

$$\zeta(\omega;\nu) = \frac{1 - S_{21}(\omega + 2\pi\nu)}{1 - S_{21}(\omega)}. \tag{2.57}$$

In the case of zero detuning, we have

$$\zeta(\omega_r;\nu) = \zeta(\nu) = \frac{1}{1 + \mathrm{j}2Q_r\nu/\nu_r}, \tag{2.58}$$

which has the familiar form of the transfer function for a low-pass filter. Thus, the resonator response rolls off for frequencies ν above the resonator bandwidth $\nu_r/2Q_r$. For high frequencies $\nu \gg \nu_r/2Q_r$, we get $\zeta \to 0$.

For now, we retain the general form of the ring-down response. Then the Fourier transform of the resonator response is

$$\delta S_{21}(\omega;\nu) = A(\omega)\,\zeta(\omega;\nu)\,\delta x(\nu). \tag{2.59}$$

Following the procedure of Zmuidzinas in [123], we now define three new quantities to simplify the expression of the response coefficient $A(\omega)$. First, the phase angle

$$\phi_g(\omega) = \tan^{-1}(2Q_r x). \tag{2.60}$$

Second, the coupling efficiency factor

$$\chi_c = \frac{4Q_i\,Q_c}{(Q_i + Q_c)^2}, \tag{2.61}$$

which reaches a maximum value of unity for optimum coupling $Q_c = Q_i$. Third, the detuning efficiency factor

$$\chi_g(\omega) = \frac{1}{1 + 4Q_r^2 x^2}, \tag{2.62}$$

which reaches a maximum value of unity when the carrier is on resonance ($\omega = \omega_r$). Using these expressions, the response coefficient becomes

$$A(\omega) = \mathrm{j}\,\frac{Q_i}{2}\chi_c\chi_g(\omega)\,e^{-\mathrm{j}2\phi_g(\omega)}. \tag{2.63}$$

Plugging into Eq. (2.59), we get the response

$$\delta S_{21}(\omega;\nu) = \mathrm{j}\,\frac{Q_i}{2}\chi_c\chi_g(\omega)\,e^{-\mathrm{j}2\phi_g(\omega)}\,\zeta(\omega;\nu)\,\delta x(\nu). \tag{2.64}$$

In addition to the resonance perturbation from the supercurrent, we must also consider the effects of noise on the measured transmission function. A major source of noise is the readout amplifier. The fluctuation caused by the amplifier is $\delta S_a(\nu) = \delta I_a(\nu) + \mathrm{j}\,\delta Q_a(\nu)$, which results in additive white noise in both the amplitude and phase directions. The noise level is characterized by the amplifier noise temperature T_a as

$$S_{a,A} = S_{a,\theta} = \frac{k_B T_a}{2P_g}, \tag{2.65}$$

where $S_{a,A}$ and $S_{a,\theta}$ are respectively the power spectral densities (PSDs) of the amplifier noise in the amplitude and phase directions, and P_g is the power supplied by the generator. We see that the signal-to-noise ratio improves with increasing P_g, so it is generally advantageous to use high generator powers. We also note that some of the generator power is absorbed in the resonator. This can be expressed as $P_a = \chi_a P_g$, where the absorption efficiency is defined as

$$\chi_a(\omega) = \frac{\chi_c \chi_g(\omega)}{2}. \tag{2.66}$$

This quantity reaches a maximum value of 1/2 when χ_c and χ_g are maximized, or when we have optimum coupling into and zero detuning from the resonance. For now we simply add the fluctuation from the readout amplifier to Eq. (2.64) to get

$$\delta S_{21}(\omega;\nu) = \mathrm{j}\,\frac{Q_i}{2}\chi_c\chi_g(\omega)\,e^{-\mathrm{j}2\phi_g(\omega)}\,\zeta(\omega;\nu)\,\delta x(\nu) + \delta S_a(\nu). \tag{2.67}$$

Another important noise source is the intrinsic fractional frequency noise from two-level systems in the substrate. Since it is a frequency perturbation, it enters into the resonator response expression in the same way as the kinetic inductance signal δx:

$$\begin{aligned}\delta S_{21}(\omega;\nu) = \mathrm{j}\,\frac{Q_i}{2}\chi_c\chi_g(\omega)\,e^{-\mathrm{j}2\phi_g(\omega)}\,\zeta(\omega;\nu)\\ \times\,[\delta x(\nu) + \delta x_{\mathrm{TLS}}(\nu)] + \delta S_a(\nu).\end{aligned} \tag{2.68}$$

Now we must find an expression for the frequency perturbation δx in terms of the current signal δI. Since $x = (\omega - \omega_r)/\omega_r$ and $\omega_r = 1/\sqrt{LC}$, the detuning is perturbed by a change in the inductance as

$$\delta x = -\frac{\delta\omega_r}{\omega_r} = \frac{1}{2}\frac{\delta L}{L}. \tag{2.69}$$

If the kinetic inductance fraction of the resonator is α, then we get

$$\delta x = \frac{\alpha}{2}\frac{\delta L_k}{L_k}, \tag{2.70}$$

where $L_k = \alpha L$ is the kinetic inductance. Substituting from Eq. (2.15), we have

$$\delta x = \frac{\alpha L_k I^2}{4N_0 \Delta_0^2 V}, \tag{2.71}$$

where we have taken $\kappa_* = 2$. The input current to the kinetic inductance is $I = I_0 + \delta I$. Making this substitution, we get

$$\delta x = \frac{\alpha L_k I_0^2}{4N_0 \Delta_0^2 V} + \frac{\alpha L_k I_0 \, \delta I}{2N_0 \Delta_0^2 V}, \tag{2.72}$$

where we ignore the $(\delta I)^2$ term. Now we define the fractional frequency responsivity,

$$R_x = \frac{\mathrm{d}x}{\mathrm{d}I} = \frac{\alpha L_k I_0}{2N_0 \Delta_0^2 V}. \tag{2.73}$$

We see that the resonance is most sensitive to current fluctuations when the resonator has a high kinetic inductance fraction, a high absolute kinetic inductance, a high bias current, a low pairing energy, and a low volume. We can finally write the resonator response in terms of the current perturbation:

$$\begin{aligned}\delta S_{21}(\omega; \nu) = \mathrm{j} \, \frac{\alpha Q_i L_k I_0}{4N_0 \Delta_0^2 V} \chi_c \chi_g(\omega) \, e^{-\mathrm{j}2\phi_g(\omega)} \, \zeta(\omega; \nu) \, \delta I(\nu) \\ + \mathrm{j} \, \frac{Q_i}{2} \chi_c \chi_g(\omega) \, e^{-\mathrm{j}2\phi_g(\omega)} \, \zeta(\omega; \nu) \, \delta x_{\mathrm{TLS}}(\nu) + \delta S_a(\nu).\end{aligned} \tag{2.74}$$

We now proceed to calculate the current noise of the resonator. In order to simplify the calculation, we work in the case of zero detuning from the resonance. Then $\chi_g \to 1$, $\phi_g \to 0$, and $\zeta(\omega; \nu) \to \zeta(\nu)$. Further, we assume that the perturbation is adiabatic, so we can ignore the resonator bandwidth and $\zeta(\nu) \approx 1$. Then we can write

$$\delta S_{21}(\nu) = \mathrm{j} \, \frac{\alpha \chi_c Q_i L_k I_0}{4N_0 \Delta_0^2 V} \, \delta I(\nu) + \mathrm{j} \frac{\chi_c Q_i}{2} \, \delta x_{\mathrm{TLS}}(\nu) + \delta S_a(\nu). \tag{2.75}$$

Using this equation, we can define an estimator for converting fluctuations in the phase of the transmission into estimates for changes in current:

$$\delta \hat{I}(\nu) = \frac{\partial I}{\partial \mathrm{Im} S_{21}} \, \delta \mathrm{Im} S_{21}(\nu). \tag{2.76}$$

Recalling that $\delta S_a = \delta I_a + \mathrm{j} \delta Q_a$, we have

$$\delta \hat{I}(\nu) = \delta I(\nu) + \frac{2N_0 \Delta_0^2 V}{\alpha L_k I_0} \, \delta x_{\mathrm{TLS}}(\nu) + \frac{4N_0 \Delta_0^2 V}{\alpha \chi_c Q_i L_k I_0} \, \delta Q_a(\nu). \tag{2.77}$$

Then, disregarding any noise at the current bias input, the current noise PSD for the circuit can be found by calculating the spectral density of the last two fluctuation terms:

$$S_I = \left(\frac{2N_0\,\Delta_0^2\,V}{\alpha L_k I_0}\right)^2 S_{\mathrm{TLS}} + \left(\frac{4N_0\,\Delta_0^2\,V}{\alpha\chi_c Q_i L_k I_0}\right)^2 \frac{k_B T_a}{2P_g}. \tag{2.78}$$

We can now estimate the current noise for a typical device. The above equation may be rewritten as

$$S_I = \left(\frac{2N_0\,\Delta_0^2\,V}{\alpha L_k I_0}\right)^2 \left[S_{\mathrm{TLS}} + \left(\frac{2}{\chi_c Q_i}\right)^2 \frac{k_B T_a}{2P_g}\right]. \tag{2.79}$$

Recalling that the resonator bandwidth is $\omega_r/2Q_r$, we see that if the bandwidth is to be large, the total quality factor must not be too high. In particular, if we use TiN, which has been shown to have internal quality factors over 10^7 [153], we must engineer the resonator to have $Q_r \ll Q_i$. Then, from Eq. (2.39), we must have $Q_c \ll Q_i$ and $Q_r \approx Q_c$. We may thus simplify the pre-factor on the second term of Eq. (2.79) by noting that

$$\chi_c Q_i = \frac{4\,Q_i^2\,Q_c}{(Q_i + Q_c)^2} \approx 4Q_c \approx 4Q_r. \tag{2.80}$$

The current noise expression is then

$$S_I = \left(\frac{2N_0\,\Delta_0^2\,V}{\alpha L_k I_0}\right)^2 \left(S_{\mathrm{TLS}} + \frac{k_B T_a}{8Q_r^2\,P_g}\right). \tag{2.81}$$

The generator power P_g is limited by the nonlinearity of the resonator. In addition to the bias and signal currents, the microwave current coupled in from the feedline also modulates the kinetic inductance of the resonator. This gives rise to classic Duffing oscillator dynamics [155], where the resonance shape bends downward in frequency with increasing excitation power, and may bifurcate if the power is high enough, as shown in Fig. 2.8. The behavior is characterized by the parameter

$$a = \frac{2Q_r^3}{Q_c}\frac{P_g}{\omega_r E_*} \approx \frac{2Q_r^2 P_g}{\omega_r E_*}, \tag{2.82}$$

where E_* is on the order of the pairing energy E_p [156]. The resonance enters the hysteretic regime for

$$a > a_{\mathrm{bif}} = \frac{4\sqrt{3}}{9}, \tag{2.83}$$

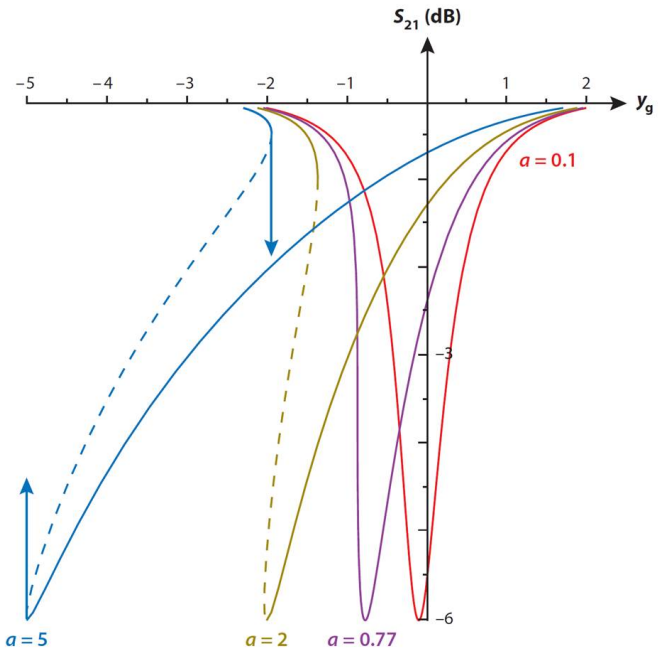

Figure 2.8: Plot of transmission amplitude versus the normalized detuning $y_g = Q_r(\omega - \omega_r)/\omega_r$ for four different values of the nonlinearity parameter a. The coupling efficiency χ_c has been chosen to be unity so that the transmission minimum is $-6\,\mathrm{dB}$. For $a > a_{\mathrm{bif}} \approx 0.77$, the resonance enters the bifurcation regime and exhibits discontinuous jumps, indicated by the arrows. The dashed portions of the curves are not experimentally accessible. Figure reprinted from [123].

and this is undesirable for our purposes. Taking this value as the limit for the generator power, we get

$$S_I = \left(\frac{2N_0\,\Delta_0^2\,V}{\alpha L_k I_0}\right)^2 \left(S_{\mathrm{TLS}} + \frac{k_B T_a}{4a_{\mathrm{bif}}\,\omega_r E_*}\right). \tag{2.84}$$

We may estimate E_* as the pairing energy $E_p = 2N_0\,\Delta_0^2\,V$. If we conservatively take the volume of the lumped-element inductor to be $0.1\,\mu\mathrm{m}^3$ (see, e.g., Fig. 3.1(b)), then for a TiN device we have $E_* \approx 60\,\mathrm{aJ}$. A reasonable upper bound on the noise temperature of a high-electron-mobility transistor (HEMT) readout amplifier is $T_a = 5\,\mathrm{K}$ [123]. Finally, we take the resonance frequency to be $\omega_r/2\pi = 5\,\mathrm{GHz}$. Then the amplifier noise is $S_{\mathrm{amp}} \approx 2 \times 10^{-17}\,\mathrm{Hz}^{-1}$. A reasonable value for the TLS noise is $S_{\mathrm{TLS}} = 2 \times 10^{-21}\,\mathrm{Hz}^{-1}$ [157]. Thus, the amplifier noise dominates, and the TLS noise may be ignored. Finally, we combine this number with the pre-factor of Eq. (2.84) to get the device current noise. We take $\alpha = 0.5$, $L_k = 5\,\mathrm{nH}$, and

$I_0 = 10\,\mu\text{A}$ as reasonable values for the parameters. Then we have

$$S_I^{1/2} \approx 10\,\frac{\text{pA}}{\sqrt{\text{Hz}}}. \tag{2.85}$$

This is to say that we may be able to detect currents as low as 10 pA in a bandwidth of 1 Hz. If demonstrated, this value would make the KPUP competitive for applications such as TES readout.

Quantum-limited noise in the bifurcation regime

The above calculation assumes that the device is not operated in the bifurcation regime, as doing so would complicate the experiments. Accordingly, the experiments in this thesis do not venture into that regime. However, it may be possible to achieve quantum-limited noise in the KPUP by operating in the bifurcation regime. Indeed, low noise approaching the quantum limit has been demonstrated in a nonlinear SQUID-based microwave resonator driven with a strong pump [158]. Let us define the noise energy density in the kinetic inductor,

$$S_\epsilon = \frac{1}{2}\,L_k S_I, \tag{2.86}$$

which has units of energy per unit frequency. Since the amplifier noise dominates for a small kinetic inductor, we may ignore the TLS contribution to Eq. (2.84). Taking $E_* \approx E_p = 2N_0\,\Delta_0^2\,V$, we have

$$S_\epsilon \approx \frac{1}{2}\,\frac{E_p^2}{\alpha^2 L_k I_0^2}\,\frac{k_B T_a}{4a_{\text{bif}}\,\omega_r E_p}. \tag{2.87}$$

Grouping the factors, we arrive at the approximate expression

$$S_\epsilon = \frac{1}{4a_{\text{bif}}}\left(\frac{1}{\alpha^2}\right)\left(\frac{E_p}{L_k I_0^2}\right)\left(\frac{k_B T_a}{\hbar\omega_r}\right) \times \frac{\hbar}{2}. \tag{2.88}$$

The first factor in parentheses is guaranteed to be greater than unity, as the kinetic inductance factor must be less than unity. The bias current I_0 must satisfy $L_k I_0^2 < E_p$ in order for the device to be superconducting, so the second factor in parentheses is also greater than unity. Finally, the quantum noise limit for an amplifier is $k_B T_a > \hbar\omega$, so the last factor in parentheses is greater than unity as well. The numerical prefactor has a value

$$\frac{1}{4a_{\text{bif}}} = \frac{9}{16\sqrt{3}} \approx \frac{1}{3}. \tag{2.89}$$

Eq. (2.88) suggests that the noise energy density of a KPUP can be of order $\hbar$. This has been shown to be true both in the case of an optimized SQUID [159] and in the case of an optimized RF-SET [160]. It can be understood heuristically by considering the time-energy uncertainty relation,

$$\Delta E \, \Delta t \geq \frac{\hbar}{2}. \tag{2.90}$$

A continuous energy measurement made in a bandwidth B has a time uncertainty $\Delta t \sim 1/B$. The uncertainty relation can then be rewritten in terms of the bandwidth:

$$\frac{\Delta E}{B} \geq \frac{\hbar}{2}. \tag{2.91}$$

The uncertainty in the energy in the above relation can be understood to be related to the noise energy density; therefore, we would expect the noise energy density for the measurement to be limited by $S_\epsilon \geq \hbar/2$.

The presence of the parenthetical factors in Eq. (2.88), all of which are individually greater than unity, would seem to guarantee that the KPUP noise energy density obeys $S_\epsilon > \hbar/2$. However, the nonlinearity parameter a_{bif} appears in the denominator. As shown in Fig. 2.8, the parameter a can be driven higher than a_{bif} by applying a stronger pump to the resonator. If we replace a_{bif} with $a > a_{\mathrm{bif}}$ in Eq. (2.88) by driving the KPUP into the bifurcation regime, it may be possible to reach the proper quantum limit. A more thorough analysis than the one presented in the previous subsection, one that includes both quantum effects and the nonlinear, possibly hysteretic behavior of the resonance, should yield quantum-limited noise for the KPUP, and presents a very interesting avenue for future research. On the experimental side, the fact that the readout amplifier noise sets the sensitivity suggests a simple strategy for reaching the quantum limit in future measurements. As shown in Fig. 2.8, the low-frequency side of a nonlinear resonance becomes very steep when approaching bifurcation. When operating on this steep portion of the curve, the KPUP readout transfer function $\partial S_{21}/\partial I$ will become very large, and thus the readout amplifier noise referred to the KPUP current input should become very small, possibly reaching the quantum limit.

2.4 Transmission line KPUP

Background

Long superconducting transmission lines have been explored for decades. Much of the utility for long superconducting transmission lines has been in delay lines [161].

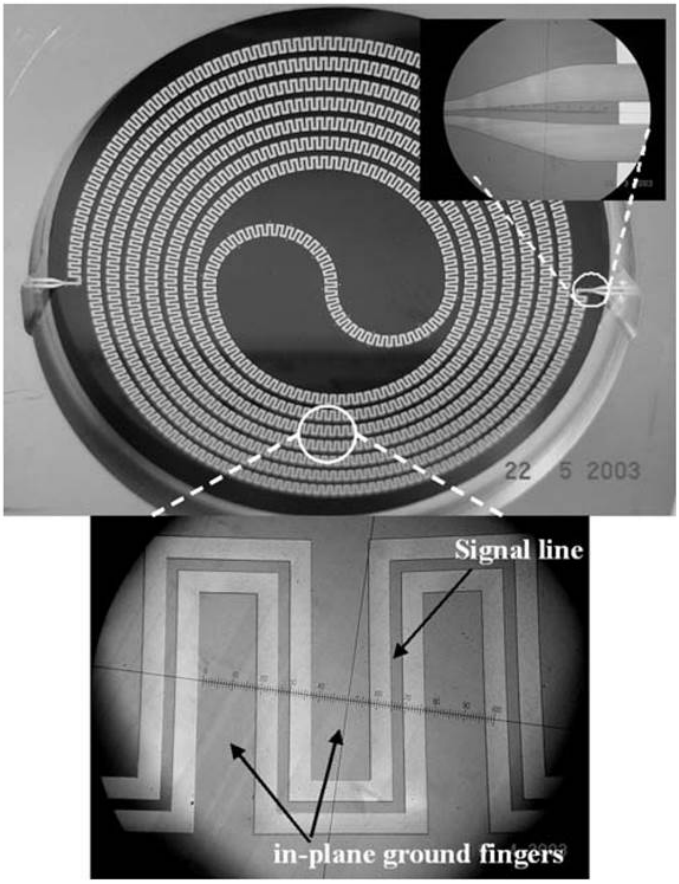

Figure 2.9: Superconducting CPW delay line made of the high-temperature superconductor YBCO on a $LaAlO_3$ substrate. It is a meander line arranged in a double-spiral trajectory. The top inset shows a taper transition to the line, and the bottom inset shows the fine-scale meander. This line provides a delay of 25 ns with very little dispersion. Figure reprinted from [161].

A delay line is simply a long transmission line meant to delay a signal for a certain duration of time. The delay time is equal to

$$\Delta t = \frac{l}{v_p}, \tag{2.92}$$

where L is the physical length of the transmission line and v_p is the phase velocity in the line. Delay lines are useful for a number of applications, particularly in radar and electronic warfare systems [162–165]. Ideally, the delay occurs without loss, so that the output signal is identical to the input signal. In practice, this is impossible with conventional materials, as dissipative losses over the length of the line attenuate the signal. However, superconductors exhibit low loss, so they are well-suited for this application. The first superconducting delay line was demonstrated in 1968 [166].

It was a meander line, and showed an insertion-loss improvement of 20 dB over a similar copper meander line. The meander has remained a popular delay line structure [167]. Another popular structure is the double spiral [168]. The advantage of the double spiral is that adjacent lines have opposite polarity, so coupling between them is reduced. Several transmission line geometries have been explored for use as delay lines, including microstrip [169], co-planar waveguide [170], and stripline [171]. Though standard in the microwave industry, microstrip has the disadvantage that two lines in close proximity can couple strongly, resulting in ripples in the transmission [161]. This can be mitigated by increasing spacing between lines, but at the cost of requiring a larger overall area for the delay line. Co-planar waveguides avoid this problem because of their in-plane grounds. The center conductors of a hypothetical pair of adjacent CPW lines are always separated by a ground in the same plane. An example of a CPW double-spiral delay line is shown in Fig. 2.9. Superconducting delay lines usually use high-temperature superconductors because of their easier operational requirements [161].

Various ideas for utilizing the kinetic inductance of a superconducting transmission line have been explored in the past several decades. As mentioned in the previous section, the reduction of the phase velocity in superconducting transmission lines has been known since 1947 [137, 138]. In 1989, Anlage et al. proposed a way of using the nonlinearity of the kinetic inductance [172]. Since the kinetic inductance increases with a supercurrent, and the phase velocity of a transmission line is a function of the kinetic inductance per unit length, it is theoretically possible to make a current-controlled microwave phase shifter. In such a device, a DC current would cause a decrease in the phase velocity and thus the wavelength, so the total phase length of the line would increase. Unfortunately, this device concept was not successfully realized in experiments.

In 2012, Eom et al. at JPL published a demonstration of a device that utilizes the kinetic inductance nonlinearity in a long superconducting transmission line to great effect [174]. The device is a traveling-wave parametric amplifier operating at microwave frequencies. The amplification is made possible by four-wave mixing, another parametric process that has been widely studied in the context of nonlinear optics, where it is employed in optical fiber parametric amplifiers [134]. Four-wave mixing can be understood intuitively in the following way [173]. Two tones are applied to the nonlinear medium (e.g., the optical fiber or superconducting transmission line) at frequencies ω_1 and ω_2. Due to the mixing provided by the

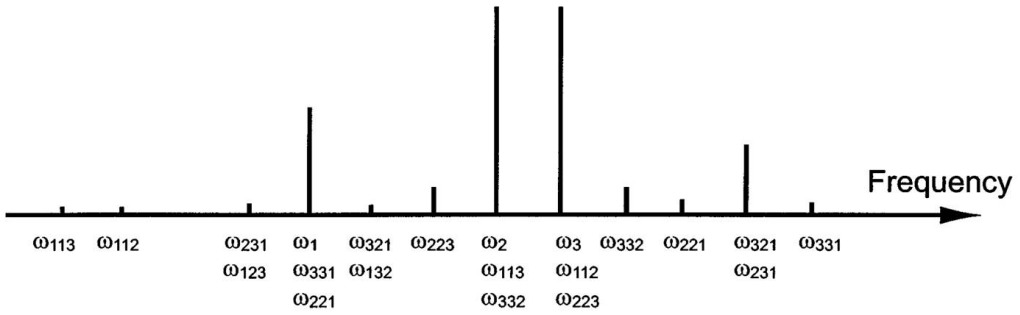

Figure 2.10: Products of four-wave mixing with three incident waves at frequencies ω_1, ω_2, and ω_3. The incident wave at ω_1 is lower in amplitude than those at ω_2 and ω_3, whose amplitudes are equal. Figure reprinted from [173].

nonlinearity, a tone at the beat frequency $\omega_2 - \omega_1$ is produced, and this modulates the refractive index (in the case of a fiber) or the surface inductance (in the case of a superconductor). If a third tone at frequency ω_3 is introduced, it becomes phase-modulated with frequency $\omega_2 - \omega_1$ due to the medium. Then this third tone develops sidebands at frequencies $\omega_3 \pm (\omega_2 - \omega_1)$, and the amplitudes of these sidebands are proportional to the amplitude of the wave at ω_3. In the same way, the relevant parameter of the medium is also modulated at the beat frequency $\omega_3 - \omega_1$, and this phase-modulates the wave at ω_2, resulting in sidebands at $\omega_2 \pm (\omega_3 - \omega_1)$. In total, with three incident frequencies, nine new frequencies are produced. Some of these products overlap with existing frequencies. For example, the previously-mentioned $\omega_2 + (\omega_3 - \omega_1)$ coincides with $\omega_3 + (\omega_2 - \omega_1)$. Fig. 2.10 shows four-wave mixing products at all nine frequencies. Here, the incident tones at ω_2 and ω_3 are stronger than the incident tone at ω_1. However, due to the overlapping mixing products, the amplitude of the signal at ω_1 is higher at the end of the fiber or transmission line. This phenomenon is called parametric gain. In a parametric amplifier, the signal to be amplifier is identified with the tone at ω_1. The tones at ω_2 and ω_3 are typically chosen to be degenerate, and are known as the pump tone. Energy from the pump tone amplifies the signal through the four-wave mixing process. Most of the other generated components are negligible, with the exception of $\omega_{321} = \omega_{231}$ (from Fig. 2.10). This component is known as the idler tone.

The superconducting parametric amplifier developed by Eom et al. is shown in Fig. 2.11(b). It is a 0.8-m-long CPW in a double-spiral trajectory. The device material was chosen to be NbTiN, as it is a high-resistivity superconductor, as mentioned in the previous section. The resistivity of the film used for this device

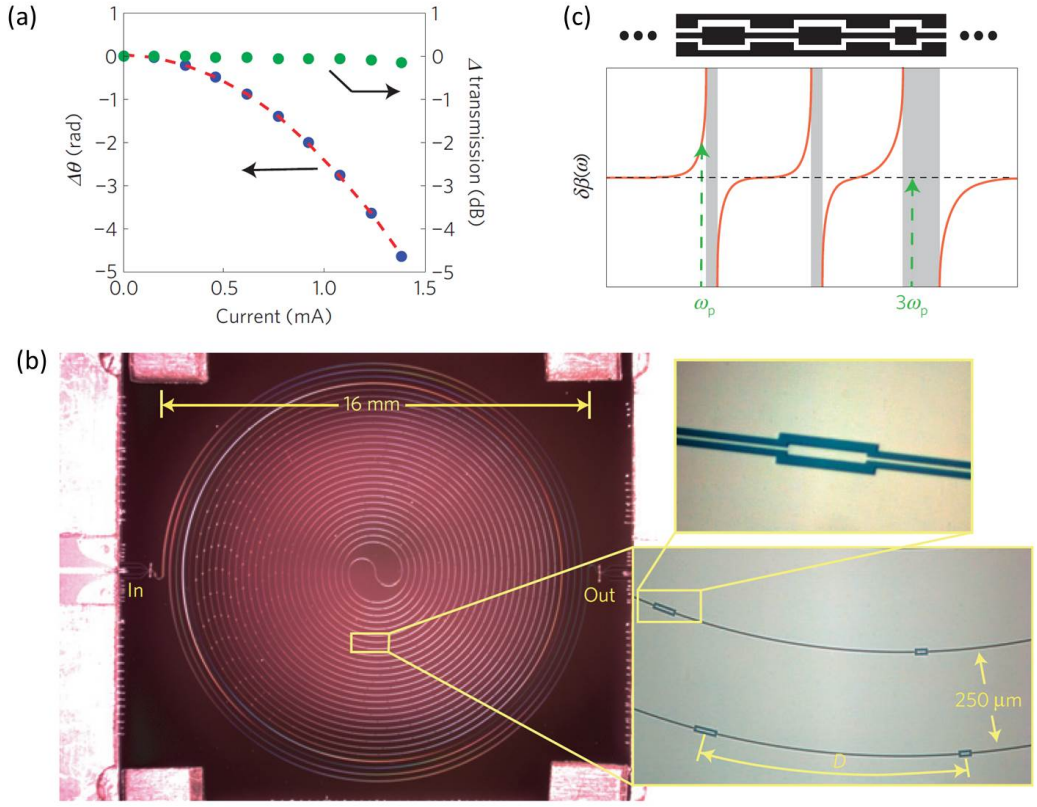

Figure 2.11: (a) Plot illustrating the nonlinearity of the traveling-wave kinetic inductance parametric amplifier in response to a DC current. The blue dots are the microwave phase shift, the green dots are the change in amplitude, and the red dashed line is a quadratic fit. The maximum phase shift observed is 5 radians out of a total phase length of 670 radians. (b) Photograph of parametric amplifier. It is a 0.8-m-long CPW made of NbTiN and fabricated in a double-spiral geometry. The line is periodically loaded by widening a short section of the center conductor, as shown in the inset. (c) The effect of the periodic loading pattern is that a large stop-band is created, suppressing the third harmonic of the pump tone. Figure reprinted from [174].

was $\rho_n \approx 100\,\mu\Omega \cdot \mathrm{cm}$. Since the coefficient of the kinetic inductance nonlinearity is proportional to the normal-state resistivity (see Eqs. (2.15) and (2.16)), this material choice ensured a strong nonlinearity in the device and thus strong parametric gain. The device achieved gain of over 7 dB from 8 to 14 GHz. This shows that the kinetic inductance nonlinearity can be useful over a large bandwidth in a transmission line. In addition to demonstrating high, wide-band parametric gain, the team also measured the phase shift of the transmission line in response to a DC bias current. The total phase length of the line was 670 radians. At a large critical current approaching 1.5 mA, the observed change in the phase length of the line was about 5 radians. The measurement also confirmed that the surface impedance nonlinearity is almost purely reactive, not dissipative. The significance of this fact in the context of a traveling-wave amplifier is that the signal is not attenuated, allowing for higher overall gain, and that the added noise of the amplifier is close to the quantum limit. After the demonstration of this device, development of a similar traveling-wave kinetic inductance parametric amplifier began at NIST for the purpose of MKID readout [175]. This type of parametric amplifier can be used as a low-noise first-stage cryogenic amplifier after an MKID feedline. Moreover, multiple parametric amplifiers can be cascaded in order to achieve a longer overall path length and thus a higher parametric gain.

Principle

In their current-response measurement, Eom et al. showed that the phase length of a long superconducting transmission line changes strongly with applied bias current. This demonstration suggests that we can utilize a long superconducting transmission line as a current sensor. A fluctuation in the input current can be observed as a shift in the phase velocity and thus the phase length of the line, as long as the system is sensitive enough to detect such a small phase shift. A schematic of such a device is shown in Fig. 2.12. A generator sends a microwave carrier tone down the transmission line. The transmission at the end is measured by a low-noise cryogenic amplifier. In addition to the microwave generator, there is another input to the circuit. The current perturbation to be detected, δI, along with a DC bias current I_0, is connected to the ends of the transmission line. Diplexers (which are commercially available) are required to isolate this second input from the microwave power traveling in the transmission line. The current signal δI is assumed to be slowly-varying compared to the oscillation of the microwave carrier, such that it sees the inductors and capacitors as short circuits and open circuits,

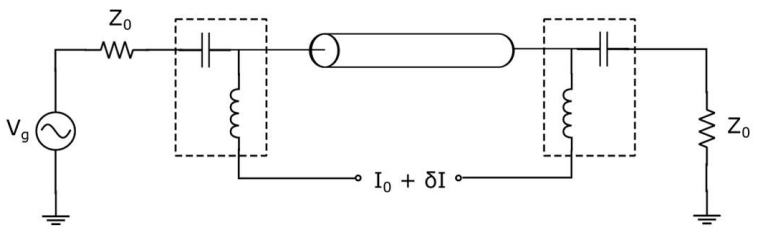

Figure 2.12: Transmission line KPUP schematic. The KPUP is a long transmission line. A microwave carrier is generated by the source and sent through the transmission line. The transmission at the end is read out by an amplifier represented by the input impedance Z_0. Another input is used to send a bias current I_0 and signal current δI through the transmission line. Diplexers (dashed lines) are used to isolate this input from the microwave power. The phase velocity in the transmission line varies depending on the input current due to the kinetic inductance nonlinearity; thus the phase of the measured signal changes.

respectively. The microwave power, in contrast, sees the capacitors as short circuits and the inductors as open circuits. The current input to the transmission line causes its phase velocity to change, due to the kinetic inductance nonlinearity. This change in phase velocity is observed as a shift in the phase of the transmission function in the data. Based on the demonstrations of the traveling wave parametric amplifier, a microwave transmission line such as the one in this device concept can be expected to have a bandwidth of several gigahertz. In addition, it can be expected to have a large critical current on the order of 1 mA. This means that its dynamic range as a current sensor would be quite large. The combination of large bandwidth and large dynamic range would make this device suitable for reading out a array of many TESs or similar detectors multiplexed in the frequency domain. It could also be used along with an array of pickup coils in order to map out a magnetic field.

The current-sensing process can also be described in terms of parametric up-conversion, just like in the case of the resonator KPUP. Suppose, as we did for that device, that the signal can be described as having a frequency ω_s, i.e., $\delta I = I_s \cos(\omega_s t)$. Then, due to the nonlinearity of the kinetic inductance in the transmission line, the phase length of the line is modulated by a term

$$\delta\theta(t) = \frac{\mathrm{d}\theta}{\mathrm{d}I} I_s \cos(\omega_s t). \tag{2.93}$$

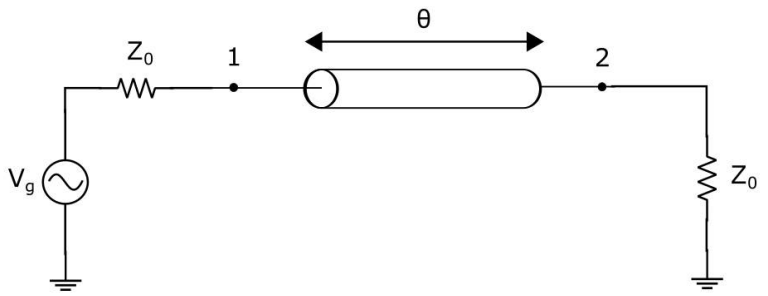

Figure 2.13: Simple schematic of a transmission line, showing two ports to define the scattering parameters.

The amplitude of the current in the line is then

$$\begin{aligned} A(t) &= A_c \exp\left[\mathrm{j}\omega_c t + \mathrm{j}\delta\theta(t)\right] \\ &\approx A_c e^{\mathrm{j}\omega_c t} + \mathrm{j}\frac{A_c I_s}{2}\frac{\mathrm{d}\theta}{\mathrm{d}I}\, e^{\mathrm{j}(\omega_c+\omega_s)t} + \mathrm{j}\frac{A_c I_s}{2}\frac{\mathrm{d}\theta}{\mathrm{d}I}\, e^{\mathrm{j}(\omega_c-\omega_s)t}. \end{aligned} \tag{2.94}$$

Thus, as we saw with the resonator device, there are sidebands created at $\omega_c \pm \omega_s$. These sidebands are seen at the end of the transmission line, along with the original carrier, by the readout amplifier. The total transmission is then mixed with the carrier frequency at room temperature in order to recover the signal. The measured sideband power is

$$P_s = \frac{I_s^2}{2}\left(\frac{\mathrm{d}\theta}{\mathrm{d}I}\right)^2 P_c. \tag{2.95}$$

Thus, this version of the KPUP also provides gain to the signal, $G \propto (\mathrm{d}\theta/\mathrm{d}I)^2 P_c/2$. Since higher gain results in stronger detection, the carrier power P_c should be high, as well as the device responsivity $\mathrm{d}\theta/\mathrm{d}I$.

We now derive an expression for the response of the transmission through the KPUP to a current perturbation. The expression for the transmission is easy to derive. For this we refer to the simplified diagram of Fig. 2.13. Although we do not expect the characteristic impedance Z_{TL} of the transmission line to be Z_0, we assume that a perfect coupler is used at the beginning of the line in order to transform the impedance from Z_0 to Z_{TL}, and another coupler is used at the end of the line to transform the impedance back to Z_0. This is equivalent to assuming the characteristic impedance is Z_0. Then, since there is a matched load, there are no reflections and thus no left-traveling waves. Then we have

$$V_1 = V_1^+ \tag{2.96}$$

$$V_2 = V_2^+, \tag{2.97}$$

where V_i is the voltage at the i^{th} port. Suppose the phase length of the line is θ. Then, assuming there is no dissipation in the line, we have

$$V_2^+ = V_1^+ e^{\mathrm{j}\theta}. \tag{2.98}$$

Then we can write the transmission [176]

$$S_{21}(\omega) = \frac{V_2^+}{V_1^+} = e^{\mathrm{j}\theta(\omega)}, \tag{2.99}$$

recalling that the phase length depends on the carrier frequency ω. The response of the transmission to a fluctuation in the phase length of the transmission line is simply

$$\delta S_{21}(\omega; t) = \mathrm{j} e^{\mathrm{j}\theta(\omega)}\, \delta\theta(t) \tag{2.100}$$

for time-dependent perturbations $\delta\theta(t)$. The bandwidth of the transmission line is so large that it can be ignored for this calculation; therefore, in the Fourier domain the response is simply

$$\delta S_{21}(\omega; \nu) = \mathrm{j} e^{\mathrm{j}\theta(\omega)}\, \delta\theta(\nu). \tag{2.101}$$

Just like we did with the resonator KPUP, we must include the additive white noise from the readout amplifier:

$$\delta S_{21}(\omega; \nu) = \mathrm{j} e^{\mathrm{j}\theta(\omega)}\, \delta\theta(\nu) + \delta S_a(\nu). \tag{2.102}$$

We must also consider TLS noise. The fractional frequency noise described in the previous section can also be interpreted as a phase noise. It is present in the transmission line as well as the resonators, because the random fluctuations of the two-level systems affect the capacitance per unit length of the transmission line. This is observed as random fluctuations in the phase velocity and, in turn, the phase length. Like before, we include the TLS fluctuations in the expression for the response in the same way as we do the signal $\delta\theta$:

$$\delta S_{21}(\omega; \nu) = \mathrm{j} e^{\mathrm{j}\theta(\omega)}\, [\delta\theta(\nu) + \delta\theta_{\mathrm{TLS}}(\nu)] + \delta S_a(\nu). \tag{2.103}$$

Now we must find an expression for the phase perturbation $\delta\theta$ in terms of the current signal δI. We begin by noting that

$$\theta = \beta l, \tag{2.104}$$

where l is the physical length of the line and $\beta = 2\pi/\lambda$ is the wavenumber. Since the phase velocity is $v_p = \omega/\beta$, we can write

$$\theta = \frac{\omega l}{v_p}. \tag{2.105}$$

From this expression we find that

$$\frac{\delta\theta}{\theta} = -\frac{\delta v_p}{v_p}. \tag{2.106}$$

Now we recall that the phase velocity of a transmission line can be expressed as

$$v_p = \frac{1}{\sqrt{\mathcal{L}C}}, \tag{2.107}$$

where $\mathcal{L}$ is the inductance per unit length of the line, and C is the capacitance per unit length. Since only the inductance per unit length changes due to the current, we can write

$$\frac{\delta\theta}{\theta} = \frac{1}{2}\frac{\delta\mathcal{L}}{\mathcal{L}}. \tag{2.108}$$

Assuming that the transmission line has a kinetic inductance fraction α, this becomes

$$\frac{\delta\theta}{\theta} = \frac{\alpha}{2}\frac{\delta\mathcal{L}_k}{\mathcal{L}_k}, \tag{2.109}$$

with $\mathcal{L}_k$ being the contribution of the surface impedance to the overall inductance per unit length.

Now, for ease of discussion, let us assume that the transmission line is a CPW, like the parametric amplifier of Eom et al. The bias and signal currents would be sent only through the center conductor of the CPW. Since we are only concerned with the part of the geometry where the kinetic inductance is changing, we can ignore the overall geometry of the transmission line and, for the purpose of this calculation, treat the entire CPW center conductor as a discrete "kinetic inductor," similar to a lumped-element inductor in a resonator. If the total kinetic inductance of the center conductor is $L_k = \mathcal{L}_k l$, then we can write

$$\frac{\delta\theta}{\theta} = \frac{\alpha}{2}\frac{\delta L_k}{L_k}. \tag{2.110}$$

We have arrived at a form identical to Eq. (2.70) from the lumped-element resonator KPUP calculation. Following the procedure used there, we get

$$\frac{\delta\theta}{\theta} = \frac{\alpha L_k I_0^2}{4N_0\Delta_0^2 V} + \frac{\alpha L_k I_0 \delta I}{2N_0\Delta_0^2 V}, \tag{2.111}$$

where the quantities in the expression now pertain to the CPW center conductor rather than a lumped-element inductor in a resonator. We can now express the phase responsivity of the device to current:

$$R_\theta = \frac{\mathrm{d}\theta}{\mathrm{d}I} = \frac{\alpha L_k I_0}{2N_0\Delta_0^2 V}\,\theta. \tag{2.112}$$

Just like with the resonator, we see that the transmission line is most sensitive to changes in current when the center conductor has a high kinetic inductance fraction, a high absolute kinetic inductance, a high bias current, a low pairing energy, and a low volume. Crucially, however, there is now the additional factor of the unperturbed overall phase length θ. This means that the length of the line should also be large in order to achieve high sensitivity. Finally, we combine this result with Eq. (2.103) to get the transmission response in terms of the current perturbation:

$$\delta S_{21}(\omega;\nu) = \mathrm{j}\theta(\omega)\, e^{\mathrm{j}\theta(\omega)} \frac{\alpha L_k I_0}{2N_0\,\Delta_0^2\,V}\,\delta I(\nu) + \mathrm{j}e^{\mathrm{j}\theta(\omega)}\,\delta\theta_{\mathrm{TLS}}(\nu) + \delta S_a(\nu). \tag{2.113}$$

We now proceed to calculate the current noise of the transmission line. In order to simplify the calculation, we choose a single carrier frequency ω_0. The phase length is then $\theta_0 = \theta(\omega_0)$. Further, we take θ_0 to be an integer multiple of 2π. Then we can write

$$\delta S_{21}(\nu) = \mathrm{j}\,\frac{\alpha L_k\,\theta_0\,I_0}{2N_0\,\Delta_0^2\,V}\,\delta I(\nu) + \mathrm{j}\,\delta\theta_{\mathrm{TLS}}(\nu) + \delta S_a(\nu). \tag{2.114}$$

As we did in the resonator calculation, we now define an estimator for converting fluctuations in the phase of the transmission into estimates for changes in current:

$$\delta\hat{I}(\nu) = \frac{\partial I}{\partial \mathrm{Im}S_{21}}\,\delta\mathrm{Im}S_{21}(\nu). \tag{2.115}$$

Recalling that $\delta S_a = \delta I_a + \mathrm{j}\,\delta Q_a$, we have

$$\delta\hat{I}(\nu) = \delta I(\nu) + \frac{2N_0\,\Delta_0^2\,V}{\alpha L_k\,\theta_0\,I_0}\left[\delta\theta_{\mathrm{TLS}}(\nu) + \delta Q_a(\nu)\right]. \tag{2.116}$$

Then, disregarding any noise at the current bias input, the current noise PSD for the circuit can be found by calculating the spectral density of the last two fluctuation terms:

$$S_I = \left(\frac{2N_0\,\Delta_0^2\,V}{\alpha L_k\,\theta_0\,I_0}\right)^2 \left(S_{\mathrm{TLS}} + \frac{k_B T_a}{2P_g}\right). \tag{2.117}$$

We can now estimate the current noise for a typical device. For this device, the generator power is limited by the saturation power of the readout amplifier (though this issue can be mitigated by nulling the carrier before the amplifier). For a HEMT, a reasonable value is $P_g = 0.1\,\mu\mathrm{W}$. Then, recalling that $T_a = 5\,\mathrm{K}$, the amplifier noise is $S_{\mathrm{amp}} = 3.5\times10^{-16}\,\mathrm{Hz}^{-1}$. Again, this dominates over the TLS noise, which is on the order of $10^{-21}\,\mathrm{Hz}^{-1}$. If we take the device material to be NbTiN and

make reasonable choices for the parameters ($V = 100\,\mu\text{m}^3$, $\alpha = 0.5$, $L_k = 100\,\text{nH}$, $\theta_0 = 100$ radians, and $I_0 = 1\,\text{mA}$), then we get

$$S_I^{1/2} \approx 5\,\frac{\text{pA}}{\sqrt{\text{Hz}}}. \tag{2.118}$$

Thus, the transmission line KPUP may be able to detect currents of the competitively-low value 5 pA in a bandwidth of 1 Hz.

Approaching quantum-limited noise

Similar to what was shown for the resonator KPUP in the previous section, it may be possible to achieve quantum-limited noise in the transmission-line KPUP in future experiments. Recalling that the amplifier noise dominates in Eq. (2.117), we may write the noise energy density $S_\epsilon = L_k S_I/2$ as

$$S_\epsilon \approx \frac{E_p^2}{2\alpha^2\,\theta_0^2\,L_k I_0^2}\,\frac{k_B T_a\,\theta_0}{\omega E_g}, \tag{2.119}$$

where $E_p = 2N_0\,\Delta_0^2\,V$, and $E_g = P_g\tau = P_g\theta_0/\omega$ is the total generator energy stored on the transmission line, having a time delay $\tau = \theta_0/\omega$. We may then group factors to get

$$S_\epsilon = \frac{1}{2}\left(\frac{1}{\alpha^2}\right)\left(\frac{E_p}{L_k I_0^2}\right)\left(\frac{E_p}{\theta_0 E_g}\right)\left(\frac{k_B T_a}{\hbar\omega}\right) \times \frac{\hbar}{2}. \tag{2.120}$$

As discussed in the previous section, the first, second, and last factors in parentheses are each greater than unity. According to a 1960 paper by Landauer [177], a shock front may be formed in a Kerr medium for $\theta_0 E_g/E_p \gtrsim 1$. Thus, it would seem that the third parenthetical factor must also be greater than unity if shock waves are to be avoided. However, shock waves can also be prevented by engineering dispersion into the line in order to block higher harmonics. This was demonstrated by Eom et al. in their kinetic inductance parametric amplifier [174], where shock waves would have prevented significant parametric gain. By implementing dispersion engineering in a future version of the KPUP, $\theta_0 E_g/E_p$ could in principle be made arbitrarily large, suggesting that the right-hand side of Eq. (2.120) could be made arbitrarily small. However, the noise energy density must approach the limit $\hbar/2$. Thus, a more thorough analysis of the noise, including quantum effects and dispersion engineering, is necessary in order to understand the quantum limit for the transmission-line KPUP. It must be emphasized that dispersion cannot be neglected in the design process for future iterations of the device in order to reach this limit.

2.5 Transmission-line resonator KPUP

Background

Most of the development of superconducting transmission line microresonators was covered in Sec. 2.3. It is important to note, however, that development of transmission line resonators did not end after the introduction of LEKIDs. For example, although the Caltech/JPL team had difficulty with microstrip resonators during the preliminary experiments for the MKID concept, much better microstrip resonators have been demonstrated since then. In 2010, Mazin et al. published a demonstration of a microstrip MKID with a thin-film dielectric [178]. An advantage of the microstrip geometry is that the transmission line can be deposited on any dielectric substrate, not just crystalline substrates. In addition, a microstrip device can be more compact than a CPW. By using a dielectric film thinner than the penetration depth of the superconductor, the magnetic inductance of the resonator was reduced, increasing the kinetic inductance fraction. The resulting MKID had competitive noise performance, comparable to concurrent CPW-based devices.

Transmission-line resonators have continued use in the detector community. For example, co-planar waveguides have remained a popular choice for MKIDs [179]. Transmission line resonators have also found utility as filters for MKID-based on-chip spectrometers. SuperSpec [180] is such a spectrometer for millimeter-wave astronomy. Millimeter-wave light is coupled through a horn into a microstrip feedline. From the feedline, the light is then coupled into a set of microstrip half-wave resonators, each corresponding to a separate spectral frequency. Each of these transmission-line resonators is in turn coupled to a LEKID, which detects the radiation through a change in its kinetic inductance. The LEKIDs are coupled to another feedline for readout. DESHIMA [181] is a similar spectrometer that uses NbTiN CPW filters instead microstrips.

Perhaps more interestingly, superconducting transmission-line resonators have been used for recent measurements of the kinetic inductance nonlinearity. In 2007, Thólen et al. demonstrated parametric amplification in a superconducting niobium CPW resonator [183]. The resonator was coupled to a feedline on either end, making this a two-point transmission measurement. They observed that the resonance bent to a lower frequency as the pump power was increased, as expected from the kinetic inductance nonlinearity. Parametric gain of 22.4 dB was achieved over a narrow bandwidth of a few kilohertz. In another experiment in 2008, Healey et al. applied a magnetic field perpendicular to a niobium CPW resonator, and found

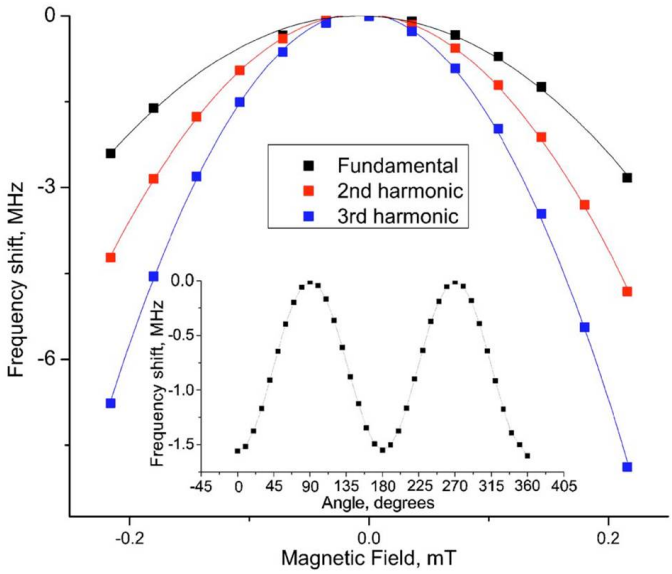

Figure 2.14: Magnetic-field dependence of the resonance frequency of a superconducting niobium CPW resonator. The response was measured for the fundamental frequency, second harmonic, and third harmonic. The inset shows the dependence of the fundamental frequency on the angle of a magnetic field with amplitude 0.2 mT. Figure reprinted from [182].

that the resonance frequency had a quadratic dependence on the magnetic field amplitude [182]. This effect was measured for several harmonics of the resonator, as shown in Fig. 2.14. This magnetic field dependence is expected due to the quadratic current dependence of the kinetic inductance. Co-planar waveguides are especially susceptible to this effect because circulating currents in the extended ground planes can focus flux lines into the narrow CPW slot regions, having a strong effect on the resonator properties [123].

Principle

The transmission-line resonator KPUP combines many features of the lumped-element resonator KPUP and the transmission line KPUP. A change in the current in a transmission-line resonator changes the phase velocity due to the kinetic inductance nonlinearity. For a resonator, the phase velocity is directly related to the resonance frequency, which can be observed as a change in the transmission through a feedline coupled to the resonator. A schematic of this device concept is shown in Fig. 2.15. The KPUP is a half-wavelength transmission-line resonator. It is shunt-coupled to a microwave feedline via a coupling capacitance C. A generator sends a carrier tone at angular frequency $\omega = \omega_r$ down the feedline. The transmission through

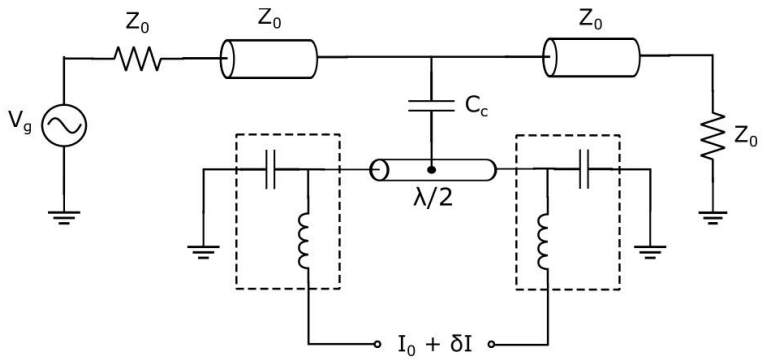

Figure 2.15: Transmission-line resonator KPUP schematic. The KPUP is a half-wavelength transmission-line resonator. The feedline is represented as the transmission line sections on either side of the resonator. A coupling capacitor is used to couple the resonator to the feedline. A carrier is generated by the microwave source and sent through the feedline, and the transmission through the feedline is measured by an amplifier represented as an input impedance Z_0. Another input line is used to send a bias current I_0 and signal current δI through the resonator. Diplexers (dashed lines) are used to isolate this input from the microwave power oscillating in the resonator. The resonance frequency of the device varies depending on the input current due to the kinetic inductance nonlinearity.

the feedline, which is read out by a low-noise cryogenic amplifier, shows a dip at the resonance frequency. In addition to the microwave generator, there is another input in the circuit. The current perturbation to be detected, δI, along with a DC bias current I_0, is connected across the transmission-line resonator. This is analogous to the radiation absorption in an MKID. Diplexers are required in order to isolate this second input from the microwave power circulating in the resonator. The current signal δI is assumed to be slowly-varying compared to the oscillations in the resonator and feedline, such that it sees the inductors and capacitors as short circuits and open circuits, respectively. The microwave power, in contrast, sees the capacitors as short circuits and the inductors as open circuits. The current input to the transmission-line resonator causes its phase velocity to change, due to the kinetic inductance nonlinearity. This change in phase velocity results in a change in resonance frequency of the resonator, which can be observed in the transmission.

This process can be described in terms of parametric up-conversion in the same way as in the lumped-element resonator, so the description will not be repeated here. The advantages of this device are similar to the advantages found in the previous two devices. Since it is a resonator, many KPUPs can be coupled to the same feedline, so

they can be multiplexed easily. However, it is also expected to have a large critical current, similar to the transmission line KPUP, meaning that this device should have a high dynamic range. If the resonance is not extremely narrow, it may be possible to read out an array of multiplexed detectors or magnetic-field pickup coils with a single transmission-line resonator KPUP. The KPUPs themselves can also be multiplexed as described above, resulting in a two-stage multiplexing scheme that may be able to read out very large arrays.

We now derive an expression for the response of the transmission through the feedline to a current perturbation. Most of the procedure and discussion from the lumped-element resonator KPUP calculation applies here. In fact, since the expression for the transmission function is the same, we may skip to the frequency-domain response including fluctuations due to noise:

$$\begin{aligned}\delta S_{21}(\omega;\nu) =& \mathrm{j}\frac{Q_i}{2}\,\chi_c\chi_g(\omega)\,e^{-\mathrm{j}2\phi_g(\omega)}\,\zeta(\omega;\nu)\\ &\times[\delta x(\nu)+\delta x_{\mathrm{TLS}}(\nu)]+\delta S_a(\nu).\end{aligned}\tag{2.121}$$

The expression for the resonance frequency is different in this case, however. Recall that $v_p = \omega_r/\beta$, where $\beta = 2\pi/\lambda$. Then the resonance frequency is $\omega_r = \beta v_p$. The wavelength is fixed by the physical length of the resonator, so β does not change. Then we have

$$\delta x = -\frac{\delta\omega_r}{\omega_r} = -\frac{\delta v_p}{v_p},\tag{2.122}$$

which is the same expression that we saw for the fractional phase shift of the transmission line KPUP. Following the procedure and discussion in that section (substituting δx for $\delta\theta/\theta$), we get

$$\delta x = \frac{\alpha L_k I_0^2}{4N_0\,\Delta_0^2\,V} + \frac{\alpha L_k I_0\,\delta I}{2N_0\,\Delta_0^2\,V},\tag{2.123}$$

with the quantities in the expression pertaining to the transmission-line resonator rather than the feedline. The fractional frequency responsivity is

$$R_x = \frac{\mathrm{d}x}{\mathrm{d}I} = \frac{\alpha L_k I_0}{2N_0\,\Delta_0^2\,V},\tag{2.124}$$

the same as for the lumped-element resonator. Just as in that case, we see that the resonance is most sensitive to current fluctuations when the transmission line has a high kinetic inductance fraction, a high absolute kinetic inductance, a high bias

current, a low pairing energy, and a low volume. We can finally write the resonator response in terms of the current perturbation:

$$\begin{aligned}\delta S_{21}(\omega;\nu) =& \mathrm{j}\,\frac{\alpha Q_i L_k I_0}{4N_0\,\Delta_0^2\,V}\,\chi_c\chi_g(\omega)\,e^{-\mathrm{j}2\phi_g(\omega)}\,\zeta(\omega;\nu)\,\delta I(\nu)\\ &+\mathrm{j}\frac{Q_i}{2}\,\chi_c\chi_g(\omega)\,e^{-\mathrm{j}2\phi_g(\omega)}\,\zeta(\omega;\nu)\,\delta x_{\mathrm{TLS}}(\nu)+\delta S_a(\nu),\end{aligned}\tag{2.125}$$

which is, again, the same expression as for the lumped-element resonator. It follows that we will also have the same expression for the current-noise power spectral density of the transmission-line resonator KPUP:

$$S_I=\left(\frac{2N_0\,\Delta_0^2\,V}{\alpha L_k I_0}\right)^2 S_{\mathrm{TLS}}+\left(\frac{4N_0\,\Delta_0^2\,V}{\alpha\chi_c\,Q_i L_k I_0}\right)^2\frac{k_B T_a}{2P_g}.\tag{2.126}$$

As with the previous two devices, we now make an estimate for the current noise of a typical transmission-line resonator KPUP. Since the same discussion from the lumped-element resonator KPUP calculation applies, we may simply restate Eq. (2.84) here:

$$S_I=\left(\frac{2N_0\,\Delta_0^2\,V}{\alpha L_k I_0}\right)^2\left[S_{\mathrm{TLS}}+\frac{k_B T_a}{4a_{\mathrm{bif}}\,\omega_r E_*}\right].\tag{2.127}$$

For a NbTiN resonator with a volume of $10\,\mu\mathrm{m}^3$, we have $E_*\approx 2N_0\,\Delta_0^2\,V\approx 130\,\mathrm{fJ}$. Taking the HEMT noise temperature as $T_a=5\,\mathrm{K}$ and the resonance frequency as $\omega_r/2\pi=5\,\mathrm{GHz}$, the amplifier noise is then $S_{\mathrm{amp}}\approx 6\times10^{-21}\,\mathrm{Hz}^{-1}$. Due to the larger volume of this device when compared with the lumped-element resonator, the TLS noise $S_{\mathrm{TLS}}=2\times10^{-21}\,\mathrm{Hz}^{-1}$ is of the same order of magnitude as the amplifier noise, and thus cannot be ignored. Finally, if we make the reasonable assumptions $\alpha=0.5$, $L_k=5\,\mathrm{nH}$, and $I_0=1\,\mathrm{mA}$, we get

$$S_I^{1/2}\approx 5\,\frac{\mathrm{pA}}{\sqrt{\mathrm{Hz}}},\tag{2.128}$$

so we may expect to be able to detect currents on the level of 5 pA in a bandwidth of 1 Hz with this device—it is competitive just like the other KPUP devices.

Approaching quantum-limited noise

It may be possible to reach quantum-limited noise in the transmission-line resonator KPUP, as was discussed for the previous two devices. For this device we have the distinction that the TLS noise was comparable to the amplifier noise, and could not be left out of the noise estimate above. However, the amplifier noise will dominate

for small enough $E_* \approx E_p$, which could be achieved by decreasing the volume of the resonator in a possible future iteration of the device. Then, as in Sec. 2.3, we can write the noise energy density as

$$S_\epsilon = \frac{1}{4a_{\text{bif}}}\left(\frac{1}{\alpha^2}\right)\left(\frac{E_p}{L_k I_0^2}\right)\left(\frac{k_B T_a}{\hbar\omega_r}\right) \times \frac{\hbar}{2}. \tag{2.129}$$

As discussed in that section, all of the factors before the quantum limit $\hbar/2$ are greater than unity, except for the numerical prefactor $1/4a_{\text{bif}} \approx 1/3$. The value of the prefactor may be decreased further by operating in the bifurcation regime so that $a_{\text{bif}} \longrightarrow a > a_{\text{bif}}$. This has not been attempted in the experiments in this thesis, but presents an interesting direction for future work. The transmission-line resonator KPUP displays the Duffing dynamics shown in Fig. 2.8, so the readout transfer function would be very large when operating on the steep left edge of the resonance right at bifurcation. It is anticipated that the device can reach quantum-limited noise in this way. It is also imperative that a more complete noise analysis is developed, including quantum effects and the full nonlinear behavior of the resonance, in order to understand how to reach the proper quantum limit for this device.

Chapter 3

LUMPED-ELEMENT RESONATOR KPUP

3.1 Preliminary experiments

Design and fabrication

Let us repeat the expression from Sec. 2.3 for the responsivity of the KPUP to small currents:

$$R_x = \frac{\alpha L_k I_0}{2N_0 \Delta_0^2 V}. \tag{3.1}$$

This quantity represents how much the fractional frequency changes in response to a signal current. It should be high in order to have a sensitive current detector. From this we can make a list of design considerations for this device:

1. The kinetic inductance fraction α should be high.
2. The kinetic inductance L_k should be high.
3. The bias current I_0 should be high.
4. The superconducting gap Δ_0 should be low.
5. The volume V of the kinetic inductor should be low.

Item 4 is the simplest of these to address. Since $\Delta_0 = 1.76\, k_B T_c$, the critical temperature of the device material should not be too high. As described in Sec. 2.3, titanium nitride has $T_c < 5\,\mathrm{K}$, and because of its many other favorable properties, it is a good choice of material for this device. The choice of TiN also helps with item 2, the total kinetic inductance, which can be expressed as

$$L_k = L_s \frac{l}{w} = \frac{\hbar \rho_n}{\pi \Delta_0 t} \frac{l}{w}, \tag{3.2}$$

where the aspect ratio l/w of the kinetic inductor is its length divided by its width. Using TiN as the device material ensures that the normal-state resistivity ρ_n is high and the superconducting gap Δ_0 is low. The thickness of the film t should also be low, and the aspect ratio of the kinetic inductor should be high. If the resulting kinetic inductance L_k is high, then the kinetic inductance fraction $\alpha = L_k/(L_m + L_k)$ of item 1 will also be high. A related consideration is that the magnetic inductance

L_m should be relatively low. Since magnetic inductance roughly scales with the length of the inductor [124], the kinetic inductor should not be very long. In order to keep the length small while preserving a large aspect ratio, it is best to use a nanowire for the kinetic inductor. A nanowire has very small volume, so item 5 is also addressed by this choice. Indeed, nanowires have already been demonstrated promisingly as nonlinear inductive elements for superconducting qubits [184]. The remaining item is item 3, the bias current. In the preliminary device we do not use a bias current, so this item will not be considered here.

The device used for preliminary testing was a lumped-element microwave resonator without any current bias input. The capacitor was chosen to be interdigitated, as is standard with LEKIDs. Igreha et al. provide an analytical model for the capacitance of an interdigitated capacitor [185]. In an IDC, there are two interdigitated electrodes, each consisting of n fingers of length L. According to the model, the capacitance for an IDC with $n > 3$ is

$$C = (n-3)\frac{C_I}{2} + 2\frac{C_I C_E}{C_I + C_E}, \tag{3.3}$$

where C_I is half the capacitance of one interior finger with respect to the ground potential, and C_E is half the capacitance of one outer finger with respect to the ground plane next to it. For an IDC on a substrate with relative permittivity ϵ_r, these quantities are given by

$$C_I = \epsilon_0(\epsilon_r + 1)\, L\, \frac{K(k_I)}{K(k_I')} \tag{3.4}$$

$$C_E = \epsilon_0(\epsilon_r + 1)\, L\, \frac{K(k_E)}{K(k_E')} \tag{3.5}$$

$$k_I = \sin\left(\frac{\pi}{2}\eta\right) \tag{3.6}$$

$$k_E = \frac{2\sqrt{\eta}}{1+\eta}, \tag{3.7}$$

where ϵ_0 is the vacuum permittivity, K is the complete elliptic integral of the first kind, and $k_\alpha' = \sqrt{1-k_\alpha^2}$ for $\alpha \in \{I, E\}$. The parameter η is known as the metallization ratio, and is given by

$$\eta = \frac{W}{W+G}, \tag{3.8}$$

where W is the width of a finger and G is width of the gap between two adjacent fingers (of opposite electrodes). We choose these two widths to be equal, so that

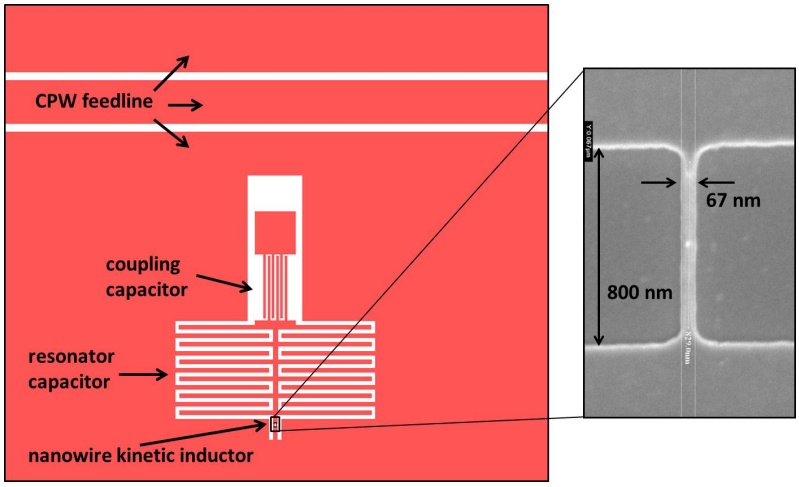

Figure 3.1: Design layout of lumped-element resonator preliminary test device. The resonator consists of a nanowire inductor and an interdigitated capacitor. It is coupled to a CPW feedline via another interdigitated capacitor. The top electrode of the coupling capacitor is connected to the center conductor of the feedline by a wire bond before testing. The capacitance of the coupling capacitor is designed to be about 0.4 pF for this device. (Inset) Scanning-electron micrograph of a fabricated nanowire for this device. This nanowire is about 800 nm long. The width is 67 nm, larger than the design value of 50 nm. The expected kinetic inductance for this nanowire is approximately 1.5 nH.

$\eta = 1/2$. Then we can evaluate the elliptic integrals to get

$$C_I = \epsilon_0(\epsilon_r + 1)\, L \tag{3.9}$$

$$C_E \approx 1.64\, \epsilon_0(\epsilon_r + 1)\, L. \tag{3.10}$$

Putting these expressions into Eq. (3.3), we get

$$C \approx \left(\frac{n-3}{2} + 1.24\right) \epsilon_0(\epsilon_r + 1)\, L \approx \frac{n}{2}\, \epsilon_0(\epsilon_r + 1)\, L, \tag{3.11}$$

where we have assumed that $n \gg 1$. Now, suppose the planar geometry of the IDC is that of a square, so that the total area is $A = L^2$. Then we can approximate the number of fingers as $n \approx L/2W$. The capacitance of the IDC can then be expressed as

$$C = \frac{A}{4W}\, \epsilon_0(\epsilon_r + 1), \tag{3.12}$$

where A is the planar area spanned by the IDC.

Our device is fabricated on a silicon substrate, so $\epsilon_r = 12.0$ [121]. The width W of both the fingers and the spacings is 20 µm, and the total area is approximately

$0.4\,\mathrm{mm}^2$. Then, according to Eq. (3.12), the design value of the capacitance is 0.6 pF. As discussed above, the geometry of the inductor was chosen to be a nanowire, and the nanowire width was chosen to be 50 nm. The nanowire width is limited by the capabilities of the fabrication system. The nanowire length is in principle not limited; however, it is not chosen to be too long, as the longer such a narrow wire is, the higher the probability of there being a fabrication defect rendering it unusable. These resonators were fabricated in a 1×8 array, and nanowire length ranged from 300 nm to 1 µm. The film thickness was chosen to be 10 nm. Taking the T_c of TiN to be 2 K, we can find from Eq. (3.2) that the design values for the kinetic inductors ranged from 0.7 nH to 2.4 nH. The array was also designed to have an array of coupling capacitances, giving a different coupling quality factor for each resonator.

A layout of one of the resonators is shown in Fig. 3.1(a). This layout was simulated using the electromagnetic simulation software Sonnet [186]. Two simulations were performed: one with the device material as TiN, and one with the device material as a perfect electric conductor. The perfect electric conductor, as mentioned earlier, has zero surface impedance. Two different resonance frequencies were obtained: ω_{sc} for the superconducting case, and ω_{pc} for the perfect conductor. We can use this to find the kinetic inductance fraction. The frequencies can be expressed as

$$\omega_{pc} = \frac{1}{\sqrt{L_m C}} \tag{3.13}$$

$$\omega_{sc} = \frac{1}{\sqrt{(L_m + L_k)\, C}}. \tag{3.14}$$

Since the kinetic inductance fraction is $\alpha = L_k/(L_m + L_k)$, the above equations yield

$$\alpha = 1 - \left(\frac{\omega_{sc}}{\omega_{pc}}\right)^2. \tag{3.15}$$

For this structure, we found $\alpha = 0.5$. Then, recalling that the resonance frequency is $f_r = 1/2\pi\sqrt{LC}$ with $L = L_k/\alpha$, we get that the design frequencies for these resonators ranged from 3.0 GHz to 5.5 GHz.

The TiN film was deposited on a silicon wafer by reactive magnetron sputtering. Most of the features of the chip were patterned via optical lithography followed by plasma etching. However, because the nanowire width of 50 nm is beyond the capabilities of optical lithography, an additional step of electron-beam lithography was required in order to pattern the nanowire. Fig. 3.1(b) shows a scanning-electron micrograph of one of the nanowires. The width of the nanowire is 67 nm, which is slightly larger than the design value of 50 nm.

Measurements

The chips used for this experiment were placed in niobium boxes and connected to SMA connectors via aluminum wire bonds, which are superconducting at low temperature. The boxes were installed in a dilution refrigerator and cooled down to a temperature of 100 mK. One of the chips from this wafer was used in a DC measurement in order to measure the critical current of a nanowire. Only one of the resonators was wired for this measurement. The coupling capacitor was short-circuited, so that the top of the nanowire was connected to the center conductor of the feedline. The bottom of the nanowire is monolithically connected to the ground plane of the CPW, as shown in the layout. Using the CPW center conductor and ground plane as large bonding pads to interface with the input and output cables, a four-wire measurement was performed. A DC current was applied through the nanowire, and the voltage across the nanowire was measured. At very low currents, the voltage was zero because the nanowire was superconducting. When the input current surpassed the critical current, the nanowire became resistive. The critical current was found to be $I_c \approx 1\,\mu\text{A}$. In its normal state, the nanowire obeys Ohm's Law. Thus, we could determine the resistance of the nanowire from the slope of the I-V curve. The normal-state resistance of the nanowire was found to be $R_n \approx 5.8\,\text{k}\Omega$. Eq. (3.2) may then be used to find the kinetic inductance:

$$L_k = \frac{\hbar R_n}{\pi \Delta_0}. \tag{3.16}$$

From another device on the same wafer, it was found that $T_c = 2.35\,\text{K}$. Using this, we get $L_k = 3.4\,\text{nH}$. This inductance is somewhat higher than the design value, but the same order of magnitude.

A separate chip was used to probe the microwave resonances. Out of the eight resonators in the array, only four were wire-bonded so that they coupled to the feedline. Every other resonator in the array was short-circuited using wire bonds. The purpose of this was to reduce the risk of crosstalk between adjacent resonators. The microwave transmission through the feedline was measured using a network analyzer. The power applied to the feedline was nominally $-120\,\text{dBm}$, or $1\,\text{fW}$. Although only four resonators were connected, six resonances were observed; two were suspected to be spurious. Fig. 3.2 shows two of the resonances. The lower-frequency resonance at 2.336 GHz is suspected to be spurious, and the higher-frequency resonance at 2.387 GHz is suspected to be a real resonator. The resonance is quite deep, meaning that the internal quality factor Q_i is high.

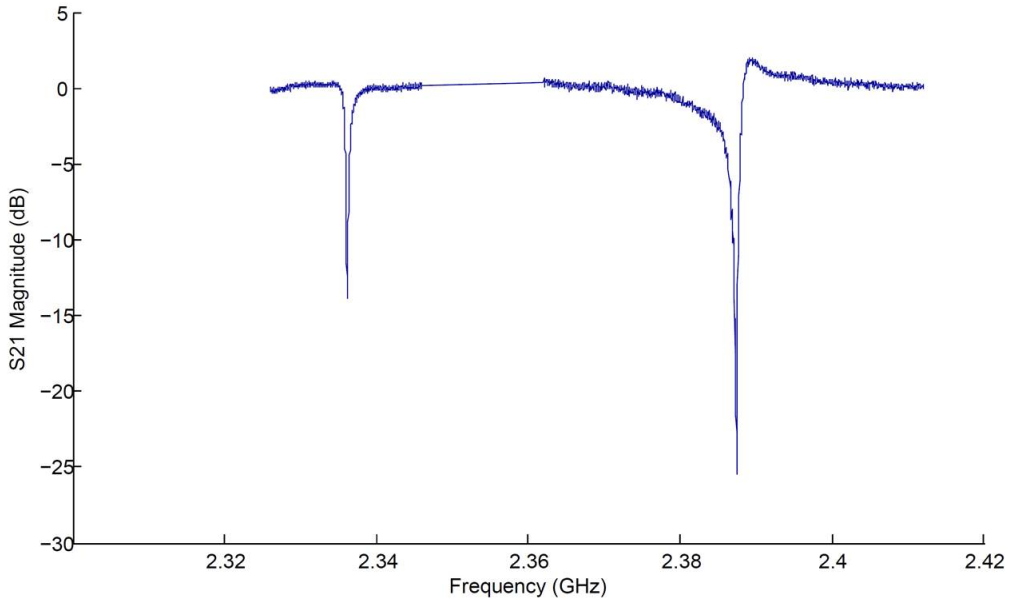

Figure 3.2: Part of the microwave transmission through the feedline of the test chip. This plot shows two resonances. The resonance at 2.387 GHz appears to be a real resonator, while the resonance at 2.336 GHz is suspected to be spurious.

After seeing resonances intact, we proceeded to investigate the nonlinear kinetic-inductance response of the resonators. If the current in a resonator is increased, we expect that the resonance will shift downward in frequency, according to

$$\frac{\delta f_r}{f_r} = -\frac{\alpha}{2}\frac{I^2}{I_*^2}. \tag{3.17}$$

This device did not have a current bias input, so in order to increase the current, we had to use the microwave apparatus. A separate pump tone was used to do this. The experiment is shown in Fig. 3.3. The transmission through the feedline of the device was monitored using a vector network analyzer. The two resonances monitored are the same ones shown in Fig. 3.2. A strong pump tone was generated by a separate microwave synthesizer, and was sent through the feedline along with the probe signal from the network analyzer. The pump tone was applied at 2.4 GHz, slightly above the frequency of the higher-frequency resonance at 2.336 GHz. Since the resonance has a bandwidth of a few megahertz, the power from the pump tone was able to couple into the resonator. This extra power increased the current in the nanowire, in turn increasing its kinetic inductance. The increased inductance caused the resonance frequency to decrease. The power of the pump tone was swept from (nominally) −100 to −60 dBm, or equivalently, approximately 0 to 1 nW. The

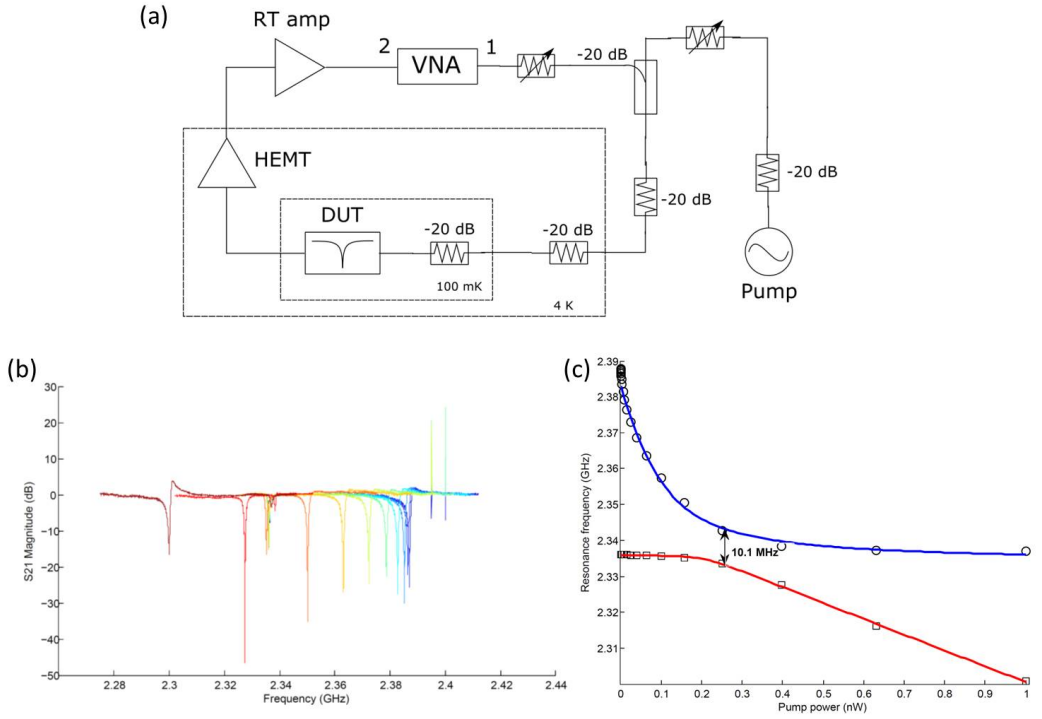

Figure 3.3: Measurement of resonance shift using pump probe technique. (a) Experimental setup for pump-probe measurement. The device is held at 100 mK in a dilution refrigerator. A vector network analyzer is used to monitor the transmission through the device's feedline. The signal from the VNA is attenuated before it enters the feedline. The transmission past the resonator is amplified in the dilution refrigerator by a HEMT amplifier, and then amplified again at room temperature before entering the VNA. A separate microwave synthesizer is used to generate a strong pump tone at 2.4 GHz. A directional coupler is used to combine the output of the synthesizer with that of the network analyzer, and the combination is sent to the device. (b) Plot of microwave transmission. There are two resonances visible in this frequency range. A pump tone is applied at 2.4 GHz, and its power is swept from -100 dBm (blue curve) to -60 dBm (red curve). Both resonances shift downward in frequency in response to increasing pump power. The lower-frequency resonance appears to respond weakly at lower pump powers and strongly at higher pump powers, while the higher-frequency resonance appears to respond strongly at lower pump powers and weakly at higher pump powers. (c) Plot of the response of both resonances to increasing pump power (in nW), along with best-fit curves. The curve trajectories display an avoided crossing, a classic feature of coupled oscillators. The coupling strength is characterized by the frequency splitting of 10.1 MHz.

higher-frequency resonance shifted downward in frequency with increasing power, as expected. However, at higher pump powers, the frequency of this resonance seemed to stabilize. The lower-frequency resonance seemed not to shift at lower pump powers, but shifted strongly at higher pump powers. When plotted against the pump power, the two resonances display anti-crossing behavior that is characteristic of coupled oscillators [187]. The resonances appear to have been coupled due to their proximity in frequency space. The stable high-power frequency of the higher-frequency resonance corresponds to the initial frequency of the lower-frequency resonance. The trajectory of the lower-frequency resonance at higher powers corresponds to the the expected continued trajectory of the higher-frequency resonance. That is to say, if the resonances were uncoupled, the plot suggests that the trajectory of the lower-frequency resonance would be a straight line of zero slope, and the trajectory of the higher-frequency resonance would cross this line, with the resonance continuing to shift downward in frequency. Since the lower-frequency resonance would not shift in response to the increasing pump power without coupling, it does not have kinetic inductance. This strongly suggests that the resonance was spurious, and did not correspond to a physical resonator on the chip. It only appeared to shift in this experiment because of the coupling to the resonator that does have kinetic inductance. The coupling strength of these two resonances is characterized by the frequency splitting $\Delta f = 10.1\,\mathrm{MHz}$. If the resonances were uncoupled, they would cross, and the frequency splitting would be zero.

3.2 Current sensor characterization

Design

The first current sensor device was fundamentally very similar to the nonlinear resonator of the previous section. The same design was used for the overall layout of the chip. The CPW feedline was the same, as well as the resonator capacitor. And, just as before, a coupling capacitor was used to couple the resonator to the feedline, and a nanowire was used as the kinetic inductor. However, for this version of the device, we intended to use a DC current bias through the nanowire. This was the most significant departure from the design of the previous chip. Naïvely, we may simply introduce the bias via another bonding pad on the chip, and connect the bonding pad to the top of the nanowire. The ground for the bias line would be identified with the ground plane of the feedline, which is monolithically connected to the bottom end of the nanowire. However, possible leakage of microwave power from the resonator is a concern. If presented with a low-impedance path to ground,

the microwave power may couple out of the resonator and go to ground through the bias port. This is undesirable because, with reduced microwave power in the nanowire, the up-converted signal in the transmission from the nonlinear kinetic inductance may be too low to detect. However, we cannot simply increase the resistance of the bias path. The low-frequency signal should travel unattenuated to the nanowire if it is to be detected, so introducing additional resistance between the bonding pad and the nanowire would be counterproductive. Thus, we must implement a low-pass filter, so that the path has a high impedance for the microwave power but a low impedance for the bias and low-frequency signal.

A standard low-pass filter implementation in microwave engineering is the stepped-impedance filter [176]. This type of filter uses alternating sections of two transmission line designs: one with high characteristic impedance, and one with low characteristic impedance. It is a popular implementation because it is easy to fabricate for the standard transmission line geometries. The disadvantage of a stepped-impedance low-pass filter is that it does not have a sharp cut-off compared to filter designs using stubs. However, this is not a concern for our purpose, which is to simply reject all frequencies much higher than those of the bias and signal inputs. A popular choice in stepped-impedance filter design is to make the length of each transmission line section equal to a quarter of the wavelength of the microwave radiation the filter intends to stop. This simplifies the design significantly, as the stepped-impedance filter can now be seen as a series of quarter-wavelength impedance transformers. The input impedance looking into a section of transmission line terminated with a load impedance Z_L is [176]

$$Z_{in} = Z_0 \frac{Z_L + \mathrm{j} Z_0 \tan(\beta l)}{Z_0 + \mathrm{j} Z_L \tan(\beta l)}, \tag{3.18}$$

where Z_0 is the characteristic impedance of the transmission line, l is the length of the line, and β is the wavenumber. If the line is a quarter of a wavelength long, then

$$\beta l = \frac{2\pi}{\lambda} \frac{\lambda}{4} = \frac{\pi}{2}, \tag{3.19}$$

where λ is the wavelength in the line. Making this substitution, we get

$$Z_{in} = \frac{Z_0^2}{Z_L}. \tag{3.20}$$

Thus, we can transform Z_L to a higher impedance by using a characteristic impedance $Z_0 > Z_L$, or we can transform Z_L to a lower impedance by using a characteristic impedance $Z_0 < Z_L$. In a stepped-impedance filter, there are alternating sections

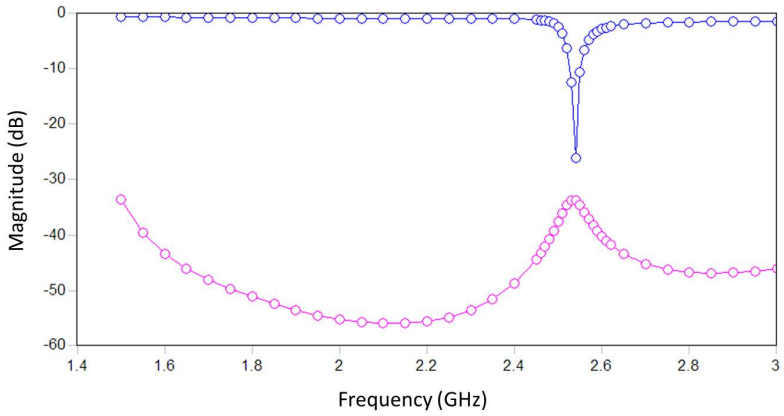

Figure 3.4: Sonnet [186] simulation of KPUP chip with resonator and stepped-impedance filter connecting the inductor to the bias port. The blue curve is the transmission from port 1 to port 2 of the feedline (the standard S_{21} that is measured). We see a resonance dip at 2.54 GHz that corresponds to the resonator. The pink curve is the transmission from port 1 of the feedline to the bias port. Thus, it measures the power coupled into the resonator and through the stepped-impedance filter to the bias port. Although this transmission is enhanced at the resonance frequency, it has a finite peak and is below -30 dB throughout the range of frequencies.

of high- and low-characteristic-impedance transmission lines. From the above observation, if we want to present a high impedance to the microwave radiation, we should place high-impedance sections at both ends of the filter, right at the input of the filter and also immediately before the load. Thus, the total number of transmission line sections n will be odd. It is straightforward to show that, for radiation at the wavelength that is four times the length of each transmission line section,

$$Z_{in} = \frac{Z_h^{n+1}}{Z_l^{n-1} Z_L}, \tag{3.21}$$

where Z_h is the high characteristic impedance and Z_l is the low characteristic impedance. This formula works for $n \geq 1$, and for $n = 1$ it reduces to Eq. (3.20). It is clear from Eq. (3.21) that, in order to achieve a very high input impedance, we can utilize a high impedance ratio Z_h/Z_l, a large number of sections, or both.

For our device, we chose $Z_h = 341\,\Omega$ and $Z_l = 102\,\Omega$. We decided to use a 50-Ω resistor as the load Z_L. The resistor would be placed between the bonding pad at the bias port and ground. We chose to have a total of nine quarter-wavelength sections to comprise the stepped-impedance filter. Then, from Eq. (3.21), the input impedance seen by the microwave power is $Z_{in} \approx 36.3\,\mathrm{M}\Omega$, which is very large. We

simulated this filter along with a resonator in Sonnet [186]. The configuration in the simulation was as it would be on the physical chip. The simulation, shown in Fig. 3.4, includes both the transmission through the feedline and the transmission from the beginning of the feedline through the bias port. The results show that the stepped-impedance filter suppresses the transmission through the bias port to a level below $-30\,\mathrm{dB}$ throughout the range of frequencies. Then, according to the simulation, this stepped-impedance filter design will work well for preventing microwave leakage from the resonator. It is also important to note that, since the stepped-impedance filter is entirely superconducting, it has no resistance and thus presents zero impedance to the DC bias signal. This also means that the load impedance Z_L is not seen by the DC signal. For low-frequency RF signals, the total kinetic inductance $L_k \approx 90\,\mathrm{nH}$ cannot be ignored, and must be seen as an input inductance for the signal. However, this is similar to the typical input inductances encountered with SQUIDs, as described in Sec. 1.4. This simulation suggests that the stepped-impedance filter design will block microwave power but pass low-frequency currents, as desired. Each resonator on the chip has a bias port and stepped-impedance filter, and there are four resonators per chip.

Another consideration for this version of the device was to improve the critical current of the nanowire. The value $I_c = 1\,\mu\mathrm{A}$ that was measured for the preliminary device would limit the KPUP's responsivity to small currents

$$R_x = \frac{\alpha L_k I_0}{2N_0 \Delta_0^2 V}. \tag{3.22}$$

Since the responsivity scales linearly with the bias current, it is necessary to apply a high bias current to achieve high current sensitivity. However, the total current in the nanowire cannot exceed its critical current. The total current is the sum of the bias current, the signal, and the microwave current, so there are other disadvantages to having a low critical current. Limiting the signal current means that the critical current limits the dynamic range of the device. Limiting the microwave current means limiting the generator power, putting a lower bound on the noise of the readout amplifier. Thus, it is imperative that the critical current not be too low.

It has been shown that, in planar superconducting geometries, the critical current is reduced by the existence of sharp corners in the geometry [189]. The current density is non-uniform and increases with proximity to a sharp corner, as shown in Fig. 3.5. Thus, the current may locally exceed the critical current close to a sharp corner. The region close to the corner may then become normal. The remaining supercurrent

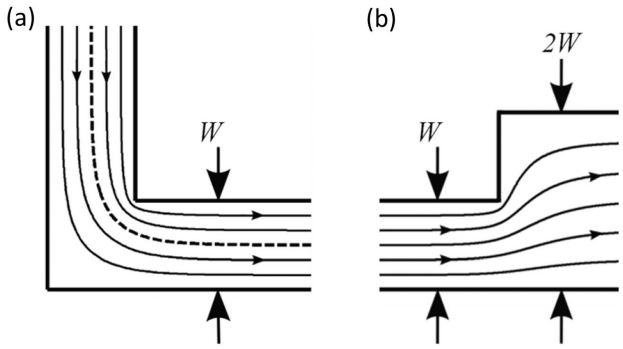

Figure 3.5: Calculated current stream lines for a planar superconducting geometry with (a) a sharp 90° bend and (b) a suddenly widening "stub" region. The density of the stream lines increases closer to the corners, showing the current crowding. The dashed line is the median path for the current: half of the integrated current density flows on one side of this line, and half flows on the other side. If the inner corner were rounded in accordance with this contour, there would be no current crowding. Figure reprinted from [188].

will avoid this normal region, as it has higher impedance than the regions that are still superconducting. The current stream lines will become more concentrated in the remaining superconducting region, and due to the increased concentration, the integrated current density will eventually exceed the critical current here as well. Thus, the whole geometry can rapidly become normal due to current crowding around a corner. Sharp corners must then be avoided. Indeed, Hortensius et al. showed in 2012 [188] that the critical current can improve by close to a factor of two by using a rounded corner as opposed to a sharp corner. In fact, the critical current of a geometry with a rounded corner is very close to the critical current of a straight wire with no corners whatsoever. We implemented this idea in our next version of the KPUP, especially because we would need to apply a large bias current for improved sensitivity. Instead of abruptly transitioning from the ends of the nanowire with 90-degree corners, we designed the nanowire ends to have round corners. The rounding was chosen to be circular with a radius of 1 μm. Then, if the critical current can be expected to be similar to the critical current if there were no corners, we can estimate it. According to the Ginzburg-Landau theory, the critical current density in a thin film is [86]

$$J_c = \frac{4}{3\sqrt{6}} \frac{B_c}{\mu_0 \lambda_{\text{eff}}}, \tag{3.23}$$

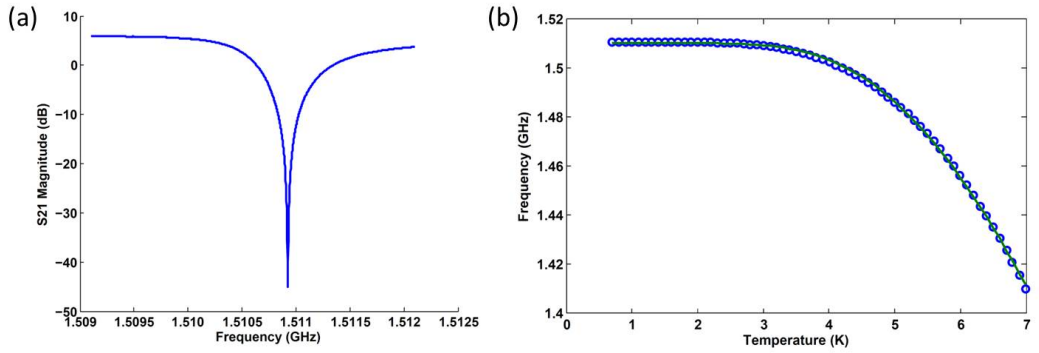

Figure 3.6: (a) NbTiN resonance taken with a vector network analyzer at a temperature of 1 K and with a nominal readout power of −52 dBm. The resonance frequency is approximately 1.511 GHz. (b) Response of resonance frequency to temperature, along with best-fit curve. The temperature of the cryostat was swept from 1–7 K.

where H_c is the critical magnetic field and λ_{eff} is the penetration depth. The critical field may be obtained from the relation

$$\frac{B_c^2}{2\mu_0} = 2N_0\,\Delta_0^2, \tag{3.24}$$

and the penetration depth is

$$\lambda_{\text{eff}}^2 = \frac{\mu_0 L_s}{t} = \frac{\hbar\rho_n}{\pi\mu_0\Delta_0}. \tag{3.25}$$

Substituting into Eq. (3.23), we find that the critical current is

$$J_c = \frac{4}{3\sqrt{6}}\sqrt{\frac{4\pi N_0\,\Delta_0^3}{\hbar\rho_n}} = \frac{4}{3\sqrt{6}}\,J_*, \tag{3.26}$$

where J_* is the nonlinearity parameter from Sec. 2.1. We take the material to be TiN with $T_c = 3\,\text{K}$. We also choose the film thickness to be $t = 10\,\text{nm}$, and the nanowire width to be $w = 150\,\text{nm}$. Then, using $I = Jwt$, we find the estimated critical current $I_c \approx 40\,\mu\text{A}$. If demonstrated, this would be an improvement over the previously-measured value of $1\,\mu\text{A}$ by over an order of magnitude, and would be a great advantage for the current-sensing performance of the device.

NbTiN resonator temperature response

Due to a miscommunication, the first batch of devices for this design was fabricated out of NbTiN instead of TiN. However, since NbTiN is also a proven nonlinear superconductor [174], we installed a chip in the dilution refrigerator and cooled it

down to perform some measurements on it. For these initial experiments, the bias port was not connected and was left as an open circuit. The coupling capacitor was connected to the feedline in order to couple the resonator to the generator power. The transmission was measured at a temperature of 1 K. The result is shown in Fig. 3.6(a). The resonance frequency is somewhat lower than expected. The temperature of the cryostat was swept in order to determine the critical temperature of the film. At low temperatures and frequencies, the density of quasiparticles in a superconducting film exhibits the relationship [123]

$$n_{qp} \propto e^{-\Delta_0/k_B T}. \tag{3.27}$$

The detection principle of MKIDs is based on the fact that the surface inductance of the film changes when the quasiparticle density changes:

$$\frac{\delta L_s}{L_s} \propto \delta n_{qp}. \tag{3.28}$$

Then, for a resonator we have

$$\frac{\delta f_r}{f_r} = -\frac{\alpha}{2}\frac{\delta L_k}{L_k} \propto -\delta n_{qp}. \tag{3.29}$$

Thus, we fit the data from the NbTiN resonator temperature sweep to the function

$$f_r(T) = f_{r0} - Ae^{-\Delta_0/k_B T}, \tag{3.30}$$

where A is a constant. From this we found that the critical temperature $T_c = \Delta_0/1.76\,k_B$ was 14.1 K, which agrees with previous measurements of NbTiN films.

Nanowire critical current

The design was finally fabricated in titanium nitride. As in the preliminary device, 10 nm of TiN was sputtered onto a silicon wafer. Photolithography was used to pattern the larger features, and electron-beam lithography was used to pattern the nanowires. Fig. 3.7 shows a photograph of the device, as well as a scanning-electron micrograph of the nanowire. The stepped-impedance filter takes up most of the area for the device. It consists of a series of co-planar waveguides whose ground planes are the same ground plane of the feedline. There are four KPUP resonators on the chip, and each resonator has its own bias connection and stepped-impedance filter. In addition to the four resonators, there is a separate area on the chip with four floating nanowires. These nanowires were intended to be used to test the nanowire critical current in a DC measurement. This way we would not have to destroy a

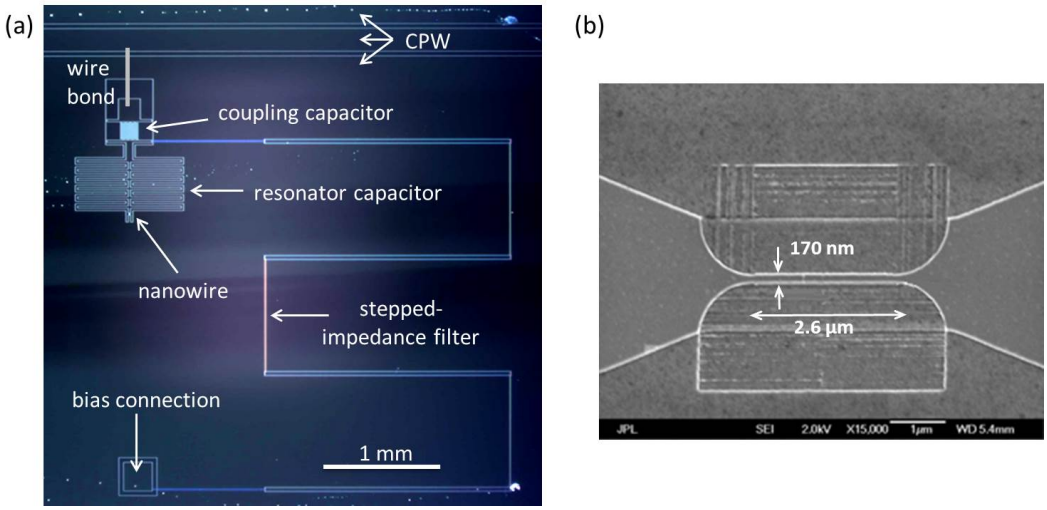

Figure 3.7: (a) Photograph of lumped-element resonator KPUP device. The feedline is seen at the top of the chip. The resonator is coupled to the feedline via a coupling capacitor whose top electrode is connected to the center conductor of the feedline with a wire bond. The bias connection is near the bottom of the chip. A stepped-impedance filter lies between the bias connection and the resonator. The transmission line sections of the stepped-impedance filter are also co-planar waveguides, and their ground planes are the same as the lower ground plane for the feedline. The full chip consists of four such devices, all coupled to the same feedline. (b) Scanning-electron micrograph of a test nanowire. This wire is approximately 170 nm wide and 2.6 µm long. It is slightly wider than the design width of 150 nm. The ends of the nanowire are curved in order to reduce current crowding. The radius of the curvature is 1 µm.

resonator to do this kind of measurement as we did with the preliminary device. The nanowires are 170 nm wide, slightly wider than the design width of 150 nm. Unlike on the previous device, the nanowires now have curved ends to reduce current crowding. Due to an issue in developing the electron-beam resist, there are striations along the nanowires, as shown in the scanning-electron micrograph. However, these striations do not affect the performance of the nanowires.

We measured the resistance of one of the test nanowires. Of the four, the second from the left was wire-bonded, and a four-wire measurement was performed in order to determine its resistance. It was necessary to dip the chip into liquid helium: the nanowire is resistive at room temperature, but it is not possible to measure its resistance because there is also conduction through the silicon substrate. The substrate is effectively a shunt resistor with an effective resistance much less than that of the nanowire, so the measured value would be approximately equal

to the effective resistance of the substrate. On the other hand, the liquid helium boiling temperature of 4.2 K is low enough that there are no charge carriers in the conduction band of the silicon substrate, so it is a perfect insulator. However, this temperature is still higher than the superconducting transition temperature of TiN, so the nanowire would still be resistive. Using this technique, a nanowire resistance of $R_n = 2.37\,\mathrm{k}\Omega$ was measured. This corresponds to a surface resistance of $R_s \approx 100\,\Omega/\square$, which is consistent with a film thickness of $t = 10\,\mathrm{nm}$ and a normal-state resistivity of $\rho_n = 100\,\mu\Omega \cdot \mathrm{cm}$, as the surface resistance is $R_s = \rho_n/t$. Additionally, from a measurement on an unrelated device from the same wafer, it was found that $T_c = 3.1\,\mathrm{K}$ for this film. Then, using the relation

$$L_s = \frac{\hbar R_s}{\pi \Delta_0}, \tag{3.31}$$

we find that the surface inductance for this film is 44.6 pH/□.

In order to measure the critical current, the nanowire must be cooled below its superconducting transition temperature. Thus, we wire-bonded another test nanowire and installed it in a dilution refrigerator. It was set up for another four-wire measurement. Because it would be a DC measurement, a series of low-pass filters was installed as part of both the input and the output circuits in order to reduce fluctuations. Such fluctuations can temporarily increase the current in the nanowire and cause it to enter its normal state at a lower nominal input current than its actual critical current. The nanowire was cooled to 20 mK in the dilution refrigerator. Using a DC voltage source, a current was applied to the nanowire through the low-pass filters, and the voltage across the nanowire was measured. The voltage was zero until the nanowire transitioned to its normal state, where it abruptly jumped to a finite value. From that point, the voltage was linear in the input current, as expected from Ohm's Law. The critical current found using this technique was $I_c = 66\,\mu\mathrm{A}$. This is over an order of magnitude greater than the previous value of 1 μA from the preliminary device. It is even higher than the theoretical prediction of 40 μA, though the same order of magnitude. Thus, we found that the rounded corners in the new nanowires yielded a major improvement in the critical current. This is important because we can apply a larger bias current to this device in order to achieve greater current sensitivity.

Resonator current response

Another KPUP chip was wire-bonded and installed in the dilution refrigerator for a microwave transmission measurement. All four resonators were coupled to the feedline by wire-bonding their coupling capacitors to the center conductor. However,

due to limited space in the sample box and a limited number of connections to room temperature on the dilution refrigerator, we could only wire-bond two of the resonator bias inputs. The first and third resonators were chosen for current-bias experiments. A 51-Ω resistor was installed between the bias pad of each resonator and ground in order to terminate the stepped-impedance filter. The DC bias lines within the dilution refrigerator were simply coaxial cables that were terminated in this 51-Ω resistor. The DC bias current was applied using a DC voltage source, and the output was sent through a low-pass filter before going into the dilution refrigerator in order to avoid unwanted current fluctuations in the nanowire. This was an *RC* filter with a T topology: two 100-kΩ resistors were used, and a 1-μF capacitor was placed between them to provide a path to ground for high-frequency noise. It was important that a T topology be used, because the second resistor presents a high impedance from the other side. Without this, the capacitor would provide a low-impedance path to ground for microwave frequencies coming from the device. The 51-Ω resistor in the sample box would then be shorted out, and microwave power would leak from the resonator because the stepped-impedance filter would not work as intended. These large room-temperature resistors also serve to turn the DC voltage source into a DC current source, as well as to attenuate potential voltage fluctuations from the source.

The chip was cooled to 20 mK, and the transmission was measured using a vector network analyzer. Although there were only four resonators, seven resonances were observed. As an initial test, the resonances were probed for nonlinearity by applying a high readout power and seeing if they would start bending downward in frequency, as described in Sec. 2.3. The highest- and lowest-frequency resonances did not show any such response, making it clear that they were spurious. That left five resonances that showed a power response, even though there were only four resonators. One of these was necessarily spurious as well, and likely showed a power response due to coupling similar to what was described in the previous section. It is unknown why these spurious resonances appeared in the system.

The DC current response of the first resonator, whose resonance frequency was 4.69 GHz, was measured. A nominal readout power of −70 dBm was applied using the vector network analyzer, and the output of the DC voltage source was swept. A range of bias currents from zero to 60 μA was applied to the nanowire, and the transmission through the feedline was observed using the network analyzer. The results of this experiment are shown in Fig. 3.8. The resonance frequency of the

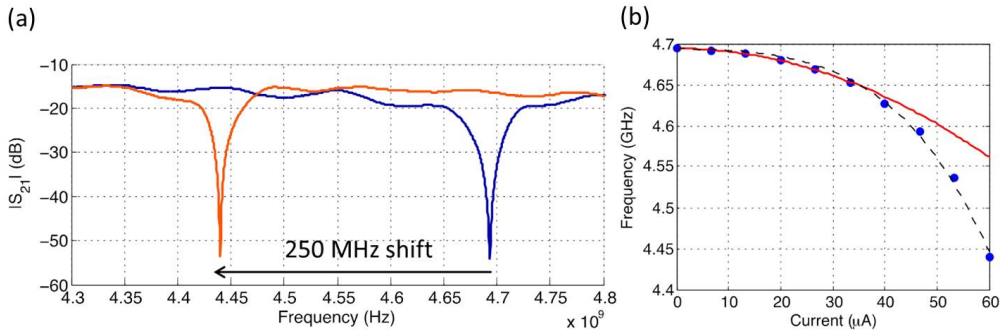

Figure 3.8: (a) Amplitude of transmission through feedline of KPUP chip, measured at a temperature of 20 mK and nominal readout power of −70 dBm. There is one resonance in this frequency range, corresponding to the left-most resonator on the chip. The blue curve shows the transmission without any bias current applied. The unperturbed resonance frequency is about 4.69 GHz. The red curve shows the transmission with a 60-μA DC bias current applied to the nanowire. The resonance frequency under this condition is about 4.44 GHz. The total frequency shift is about 250 MHz, or 5% of the resonance frequency. (b) Full current-response data for the KPUP resonator. The bias current was swept from zero to 60 μA. Above 60 μA, the nanowire surpasses its critical current and the resonance disappears. The red curve is a quadratic-function fit to the data. The quadratic function agrees well with the data at low currents, but diverges at higher currents. The dashed line is a quartic-function fit to the data. The quartic function agrees well with the data throughout the range of bias currents.

resonator shifted downward with increasing bias current, as expected. It continued to shift until the critical current of the nanowire was surpassed, at which point the nanowire transitioned to its normal state. In the normal state there is no Mattis-Bardeen surface impedance, so all of the inductance in the resonator is magnetic. The magnetic inductance is low, so the resonance frequency is very high and the resonance is not observed. The critical current in this measurement was found to be slightly higher than 60 μA. This is not necessarily in disagreement with the 66-μA result obtained from the DC four-wire measurement on the test nanowire, because there is additional microwave current in the nanowire for this experiment. The maximum resonance frequency shift, occurring at a bias current just below the critical current, was 250 MHz. This corresponds to a fractional frequency shift of 5%, which is much higher than any fractional frequency shift observed by increasing the microwave current via the readout power. Overall, the resonance shift appears to follow a quadratic trajectory at low values of the bias current, but at higher bias currents it is clear that the trajectory is actually quartic. This is similar to what was

suggested by Anthore et al. for the suppression of the superconducting gap [132]. However, the data does not seem to agree with their result. According to their result, the fractional frequency shift would be

$$\frac{\delta f_r}{f_r} = -\frac{\alpha}{2}\frac{\delta L_k}{L_k} = -0.95\,\alpha\frac{I^2}{I_*^2} - 1.75\,\alpha\frac{I^4}{I_*^4}, \tag{3.32}$$

where we have used Eq. (2.18) to obtain the right-hand side. If this function is used to fit the data from our measurement, we get $\alpha \approx 0.01$ and $I_* \approx 47\,\mu\text{A}$. The value for I_* is reasonable, since it is expected to be of order the critical current $I_c \gtrsim 60\,\mu\text{A}$. However, it is unlikely that the kinetic inductance fraction is so low. If it were, the resonance would not disappear when the nanowire enters the normal state, because the total inductance would not change significantly. Further, from the above equation it is clear that if $\alpha = 0.01$, for a fractional frequency shift of 5% the kinetic inductance would have to increase by a factor of ten, which is highly unlikely. Thus, the quartic behavior of the kinetic inductance does not seem to be explained by the suppression of the superconducting gap according to Anthore et al. Instead, we may characterize the nonlinearity by fitting our data to the form

$$\frac{\delta L_k}{L_k} = \kappa_2\,\frac{J^2}{J_*^2} + \kappa_4\,\frac{J_4}{J_*^4}. \tag{3.33}$$

Using Eq. (2.16), for TiN we have $J_* = 52.6\,\text{mA}/\mu\text{m}^2$. Then, if we assume $\alpha = 0.5$ according to our simulation, we get $\kappa_2 = 0.11$ and $\kappa_4 = 0.43$. The ratio of the two coefficients is $\kappa_4/\kappa_2 = 4.1$.

Current noise

Since the KPUP showed a strong response to current, we proceeded to measure its current noise. The experimental setup for this measurement is shown in Fig. 3.9(a). The device was maintained at a temperature of 20 mK. Instead of a vector network analyzer, a microwave synthesizer was used to excite the resonance. A bias current was applied to the nanowire in the same way as in the previous measurement. However, this time an AC current was also applied to the nanowire. An RF source was used to generate a signal at 11 MHz. After some attenuation, this signal was sent through a 65.1-kΩ resistor, resulting in an rms current of 0.3 µA. This current was combined with the DC bias current, and both were sent to the bias connection for the nanowire. Due to the kinetic inductance nonlinearity in the nanowire, the RF signal was up-converted to the microwave regime. The up-converted signal coupled out of the resonator and traveled down the feedline. The transmission through the

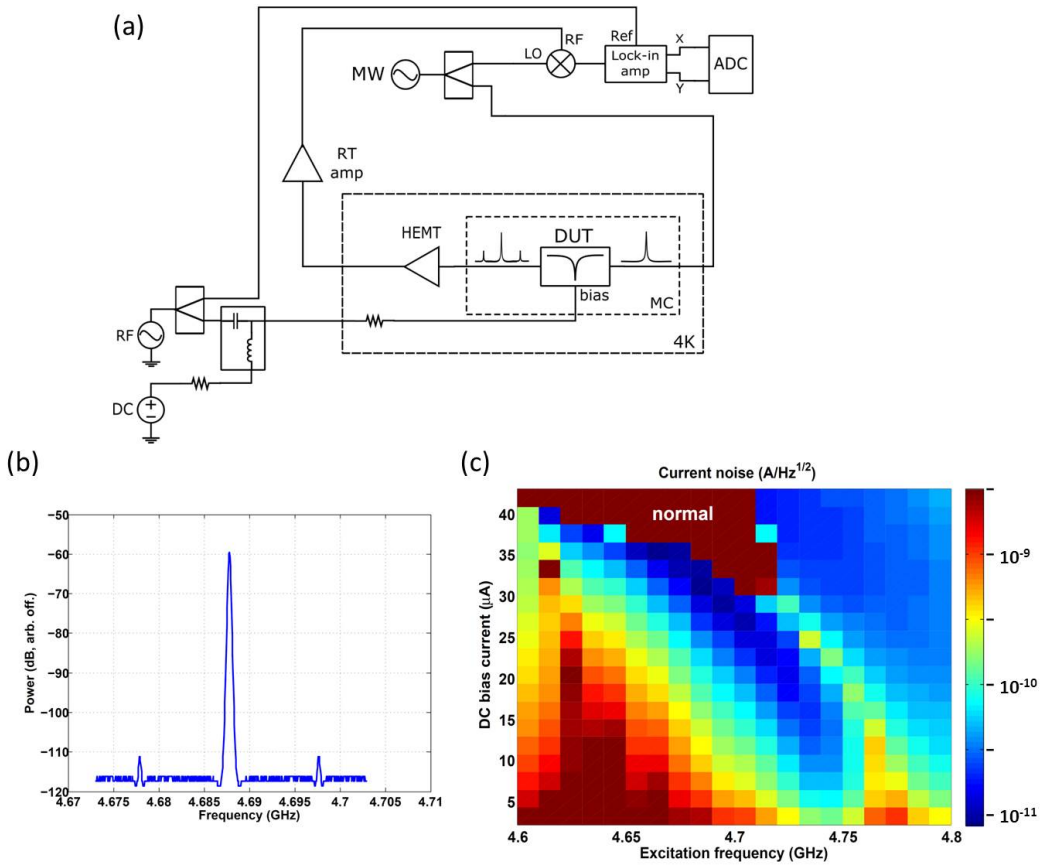

Figure 3.9: (a) Setup for KPUP noise measurement (attenuators and filters omitted for clarity). A microwave source pumps the resonator through the feedline. A DC source applies a bias current through a room-temperature low-pass filter. An RF source applies an AC current, which is combined with the DC current and sent to the nanowire through the bias connection. Due to the nonlinearity, the RF current is up-converted. It then couples out of the resonator, travels down the feedline, and is amplified before being mixed with the original carrier, resulting in a signal at the RF generator frequency that is then sent to a lock-in amplifier. The lock-in outputs are sent through *RC* filters to an ADC, where they are sampled at 200 kHz. (b) Spectrum of feedline transmission, showing the carrier along with sidebands at a distance corresponding to the RF frequency, 10 MHz. The noise measurement can be interpreted as sampling the amplitude and phase of the sidebands. (c) Map of current noise with nominal pump power −50 dBm. The highest noise (dark red) is in the region marked "normal", where the nanowire surpasses its critical current. Because it no longer has kinetic inductance, it is no longer sensitive to currents. The lowest noise (dark blue) is close to the normal region, where the bias current is highest. As the bias current increases, the resonance frequency decreases. The lowest noise for each bias current occurs when the pump frequency matches the shifted resonance frequency. The noise is high when the pump frequency is far from the resonance frequency, as the resonance is not excited and thus there is no up-conversion. The lowest noise observed in this measurement is $8\,\mathrm{pA}/\sqrt{\mathrm{Hz}}$.

feedline was amplified by a HEMT amplifier at 4 K within the dilution refrigerator, and then amplified again at room temperature. The output was mixed with the original microwave carrier, resulting in a signal at the RF frequency. This signal was sent to a lock-in amplifier which was locked to the RF generator frequency. The outputs of the lock-in amplifier were sent through *RC* low-pass filters with a cutoff frequency of 1 kHz, and sampled by an analog-to-digital converter at a rate of 200 kHz. The resulting noise spectrum showed $1/f$ behavior below 20 Hz, but was flat above that point in frequency.

Three external parameters must be tuned in order to optimize the KPUP sensitivity: microwave power, microwave frequency, and DC current. All three parameters were swept in order to find the optimum condition for the device. The lowest noise was $8\,\mathrm{pA}/\sqrt{\mathrm{Hz}}$, observed at a nominal microwave power of -50 dBm, microwave frequency of 4.68 GHz, and bias current of 30 μA. The map of current noise across bias currents and drive frequencies for this power is shown in Fig. 3.9(c). The lowest noise occurs at a bias just below the critical current, which was expected because the device responsivity increases with bias current. The device is not sensitive to currents when the nanowire is normal, because it does not have kinetic inductance. Thus, the noise in the normal region is very high. In general, the noise is low when the drive frequency matches the resonance frequency. This is expected because the up-conversion efficiency is low when the power in the resonator is low, and the power in the resonator is low when it is not being pumped at its resonance frequency. The resonance frequency changes with the bias current, so the region of lowest noise is different for every value of the bias current. The drive power is also important because it has an effect on the HEMT amplifier noise. Thus, the lowest noise occurred at a relatively high drive power. The high drive power increased the total current in the resonator, decreasing the maximum bias current. The current noise value of $8\,\mathrm{pA}/\sqrt{\mathrm{Hz}}$ is close to the value estimated in Sec. 2.3. This value is low enough to make the KPUP a promising candidate for TES readout applications.

3.3 TES readout with DC bias

Shared bias line

We obtained a transition-edge sensor chip from colleagues in the UC Berkeley cosmology group. A photograph of the chip is shown in Fig. 3.10(a). The TESs on this chip are coupled to an antenna in order to absorb incident radiation. Each TES is comprised of an aluminum layer with $T_c = 1.2$ K and a titanium layer with $T_c = 0.4$ K. The rest of the electrical leads on the chip are niobium. Below the metal

is silicon dioxide, and below the silicon dioxide is silicon nitride. The substrate is a silicon wafer. The patterned silicon nitride is released so that the devices are suspended, providing a weak thermal link to the heat bath. The antenna-coupled radiation flows through an electrical heater that sits on an island along with the TES. When the temperature of the island rises, the TES resistance changes. The quoted thermal conductance between the TES and the heat bath was 70 pW/K.

We decided to use the titanium transition for our experiments, because it occurs at a lower temperature and thus is easier to access with our system. The normal-state resistance of the titanium was quoted as approximately 1 Ω. For our experiment we had to estimate the current required to bias the TES within its transition. To this end, we note that, in order to maintain the transition temperature in the TES, the Joule heating must be equal to the power flow to the heat bath. This power flow can be estimated as [54]

$$P_{\text{bath}} = G(T_c - T), \tag{3.34}$$

where G is the thermal conductivity of the link. Given that, in the middle of the transition, the TES resistance is approximately half its normal resistance R_n, the required current is then

$$I = \sqrt{\frac{2P_{\text{bath}}}{R_n}} = \sqrt{\frac{2G(T_c - T)}{R_n}}. \tag{3.35}$$

Thus, if we use a bath temperature of $T = 200$ mK, the required current is $I \approx 8$ μA. However, it is also important to note that the TES will have hysteretic behavior. Therefore the most reliable way to bias it would be to start with a very large current around ~50–100 μA and then reduce it to about 8 μA.

We planned to voltage-bias the TES by placing it in parallel with a small shunt resistor, in accordance with standard practice [54]. We used 10 mΩ for the shunt resistance. This resistance is typically chosen to be much less than the normal resistance of the TES. A constant bias current is applied to the parallel combination. When the TES is in its superconducting state, its resistance is zero, so all of the current goes through the TES. However, when the TES is in its transition, its resistance is about half of its normal resistance, which is much greater than the resistance of the shunt resistor. Thus, in the transition and in the normal state, most of the current flows through the shunt resistor. This is important because, without the shunt resistor, it would be very difficult to bias the TES within its transition. A large current is required to drive the TES normal, and if there were no other path

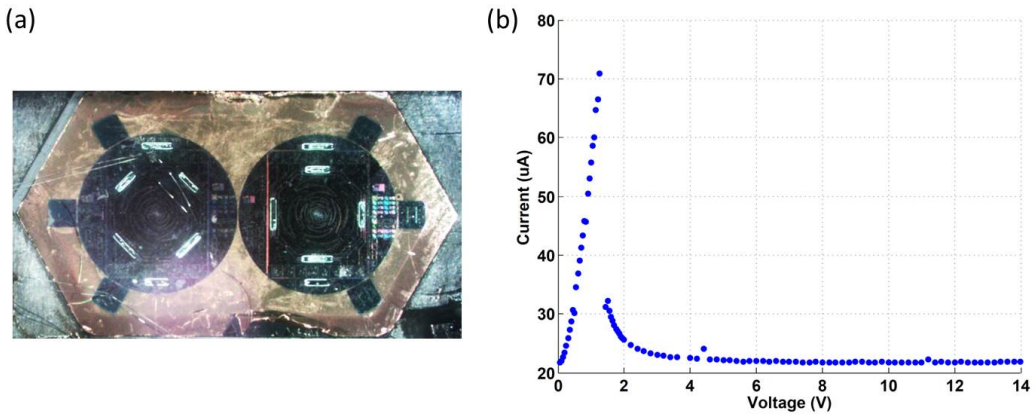

Figure 3.10: (a) Photograph of TES chip obtained from UC Berkeley cosmology group. The large structure in the center is a planar antenna used to couple radiation into the TES. (b) Measurement of TES current versus source output voltage. Because of the hysteretic behavior of the TES, the initial voltage was high and the voltage was swept down to zero. The current was determined through the frequency shift of the KPUP, as the TES current was the same as the KPUP bias current. At low voltages, the TES is superconducting and its current is determined by the resistance in the bias line. Beyond 1.25 V, the TES enters its transition and its current drops sharply. Within the transition region, the resistance increases gradually, and thus the current decreases gradually. When it is fully in its normal state, the TES should obey Ohm's law and there should be a constant, finite slope to the curve continuing to higher voltages. This is not observed in our measurement.

for the current to go, this large current would continue flowing through the TES in its normal state.

Because the voltage across the TES is approximately constant in the transition region, the TES resistance is found by measuring the current flowing through it. The idea of our experiment was to use the KPUP to measure this current. The TES bias current would also flow through the KPUP nanowire, changing its kinetic inductance and thus the resonance frequency of the resonator. For simplicity, we decided to use the same bias current for the TES and the KPUP. Thus, there were two inputs to the circuit: the microwave excitation and readout signal for the KPUP resonance, and the DC bias current for both the TES and KPUP. Both the TES chip and the KPUP chip were installed in the same sample box. We had to use a different KPUP chip than previous measurements, because the bonding pads on the old chip had been overused. Wire bonds were used to connect the TES to the KPUP bias input.

The devices were cooled to 200 mK in the dilution refrigerator. A lower temperature was not used as in previous experiments because that would require a larger current

in order to bias the TES. A vector network analyzer was used to monitor the KPUP resonance frequency, and a DC voltage source was used to generate the bias current. The output voltage of the source was swept down from 14 V to zero, and the KPUP resonance was measured for each value of the DC voltage. Previously, a DC current sweep measurement had been done with this KPUP but without the TES, and this earlier measurement was used as a calibration in order to convert the measured resonance frequencies into currents. The result of this experiment is shown in Fig. 3.10(b). At low values of the DC voltage, the TES is superconducting, so the slope of the *I*-*V* curve is determined by the resistance in the bias line. At 1.25 V, the TES current decreases sharply, and then with increasing voltage it gradually decreases further. This is the transition region of the TES. Since it has entered its transition, its resistance suddenly becomes much larger than that of the shunt resistor, so most of the current goes through the shunt resistor instead of through the TES, where it was previously all going. As the voltage increases further, the TES resistance increases, so the current flowing through it decreases. When the TES is fully in its normal state, it is simply a resistor that obeys Ohm's law. The current flowing through the TES should increase linearly with the voltage across it. While the voltage across the TES does continue increasing in our experiment, the expected ohmic behavior of the TES is not observed. Instead, the TES current appears to stay at zero. This is because, in its normal state, the TES current is very low, as almost all of the current is flowing through the shunt resistor. Because the KPUP nanowire bias current is the same as the TES current, the KPUP is effectively biased with a very small current in this regime. The sensitivity of the KPUP suffers, and it is not able to detect the TES current. Thus, for further experiments with TESs, it is important to have a separate bias line for the KPUP in order to ensure that its sensitivity remain high independent of the TES current.

TES bias curve with temperature

We proceeded to install separate bias lines for the TES and KPUP in order to get a good measurement of the TES bias curve. Two separate DC voltage sources were used to provide the bias currents. The output of each voltage source was sent to the dilution refrigerator, where it was sent down a stainless steel coaxial cable. It was then attenuated by 20 dB at the 4-K stage of the refrigerator. This was followed by another stainless steel coaxial cable leading to the mixing chamber, and then two commercial low-pass filters, at cutoff frequencies of 200 MHz and then 1.9 MHz. Finally, the bias signals were sent into the sample box. The TES bias

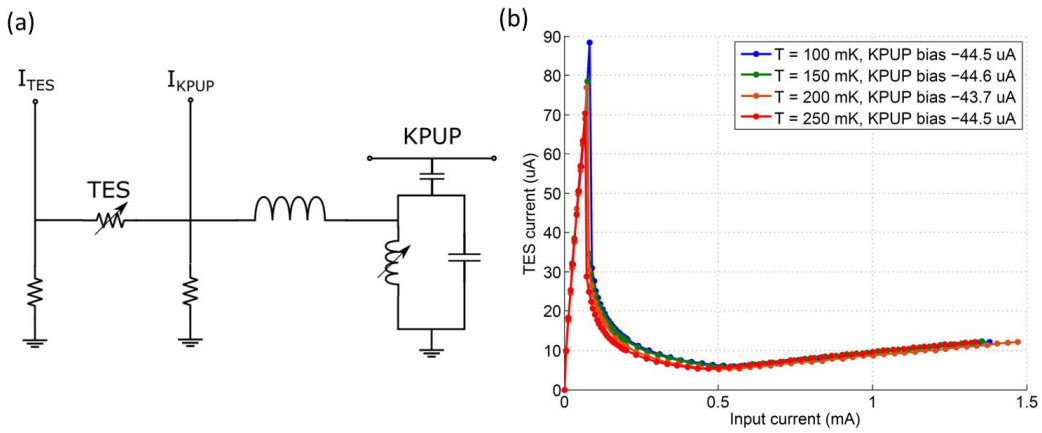

Figure 3.11: (a) Diagram of test circuit with independent biasing for TES and KPUP. The stepped-impedance filter and KPUP nanowire provide a path that is always superconducting and thus zero impedance for the DC bias inputs. The KPUP bias current flows only through this branch, because even when the TES is superconducting, the shunt resistor impedes the path to ground. Similarly, the TES current after the TES only flows through this path as well, as there is no zero-impedance path to ground in the KPUP bias line. (b) TES bias curve measured at four different temperatures. The TES current is plotted against the input current to the TES/shunt-resistor combination. The general features of the bias curve agree with expectations. When the TES is superconducting at low input currents, the slope of the bias curve is unity, as the TES current is equal to the input current. When the input current is high enough, the TES enters its transition and the TES current drops sharply. This point decreases with increasing temperature, as expected.Within the transition region, the TES resistance increases gradually until it reaches its normal-state value, and the current decreases accordingly. After it is in its normal state, the TES obeys Ohm's Law and there is a constant, finite slope to the bias curve.

was connected across the shunt resistor. The KPUP was connected across the 50-Ω resistor before the stepped-impedance filter. A schematic of this biasing circuit is shown in Fig. 3.11(a). The stepped-impedance filter and KPUP nanowire are always superconducting, and thus they provide a path to ground that always has zero impedance. On the other hand, even when the TES is superconducting, there is no path in the TES bias line that is zero impedance, due to the presence of various resistors (including the shunt resistor). Thus, the KPUP bias flows only through the KPUP and not through the TES. There is also no zero-resistance path in the KPUP bias line except for the path through the stepped-impedance filter and nanowire, so the TES current does not flow through any other part of the KPUP bias line. Thus, the TES and KPUP are truly independently biased.

The KPUP resonance was excited and read out using a vector network analyzer. A constant KPUP bias current was chosen such that the KPUP would have enough dynamic range to read out the entire TES bias curve. The TES bias current was then applied, starting at a very high current close to 1.5 mA, and sweeping down to zero. The resonance frequency of the KPUP was monitored using the network analyzer, and a resonance curve was taken at each value of the TES bias current. This measurement was performed at four different temperatures. The KPUP resonance frequency was converted into a current using the KPUP device calibration data along with the value of the constant KPUP bias current. The resulting current was the TES current, which was then plotted against the TES bias input current. The result is shown in Fig. 3.11(b). Unlike the previous measurement with a shared bias line, all of the expected features of a TES bias curve are observed here. At low input currents, the TES is superconducting and the current is determined by the resistance of its bias line. At a certain point, the TES current drops sharply as it enters its transition. This point decreases with increasing temperature, which is expected. If we equate the TES Joule heating with the power flowing to the bath [54],

$$I_{\mathrm{TES}}^2 \, R(T_{\mathrm{TES}}) = \xi (T_{\mathrm{TES}}^4 - T^4), \tag{3.36}$$

then we see that when the bath temperature T increases closer to the transition temperature of the TES, the TES current decreases. After entering its transition, the TES resistance increases gradually, and in turn the TES current decreases gradually. At an input current slightly above 0.5 mA, the TES is fully in its normal state, and the bias curve has a finite constant slope as expected from Ohm's Law. This is in contrast to the previous measurement, where the apparent TES current went to zero and remained there. The independent KPUP bias allowed us to measure the Ohmic portion of the bias curve. Because of the quadratic nonlinearity, the KPUP frequency shift is proportional to $I_{\mathrm{TES}} \, I_{\mathrm{KPUP}}$, whereas in the previous measurement it was proportional to I_{TES}^2. The constant KPUP bias current was large, so the KPUP was sensitive to the smaller TES current signal in this measurement.

By measuring the TES bias curve at several different temperatures, we were able to estimate several properties of the TES. It is straightforward to show that the TES normal-state resistance is

$$R_n = \left(\frac{G_{sc}}{G_n} - 1 \right) R_s, \tag{3.37}$$

where G_{sc} is the effective electrical conductance of the TES bias line in the superconducting state, G_n is the effective electrical conductance of the TES bias line in

the normal state, and R_s is the value of the shunt resistor. These parameters can be calculated from the bias curve. Using the data from the measurement at 200 mK, we get $R_n = 1.3\,\Omega$, which is close to the quoted value of approximately $1\,\Omega$. We can also estimate the thermal conductance G of the link between the TES and the bath by using Eq. (3.36). The Joule heating may be obtained by plotting $P = I_{\mathrm{TES}}\, V_{\mathrm{TES}}$ against V_{TES}, where $V_{\mathrm{TES}} \approx I_{in}\, R_s$ above the superconducting state. At each value of the bath temperature, the value of the Joule heating is taken at the point on this plot with zero slope, which occurs in the middle of the transition when $T_{\mathrm{TES}} = T_c$. We may then fit this array of powers to the function

$$P = \xi(T_c^4 - T^4), \tag{3.38}$$

where ξ is a constant. We find from the fit that $\xi \approx 1.6\,\mathrm{nW/K^4}$ and $T_c \approx 350\,\mathrm{mK}$. The latter value agrees with our experience of trying to measure the TES at even higher temperatures. We may then estimate the thermal conductance

$$G = \frac{\partial P}{\partial T_c} = 4\,\xi\, T_c^3. \tag{3.39}$$

Using the values from the fit, we get $G \approx 280\,\mathrm{pW/K}$, which is a factor of four higher than the quoted value. We may also estimate the TES current noise. The TES noise is typically limited by the phonon noise in the thermal link. The noise-equivalent power (NEP) for a TES can be calculated as [190]

$$\mathrm{NEP}^2 = 4\gamma k_B G\, T_c^2 \tag{3.40}$$

$$\gamma = \frac{5}{9}\frac{1-(T/T_c)^9}{1-(T/T_c)^5}. \tag{3.41}$$

Using $T = 200\,\mathrm{mK}$, we get $\mathrm{NEP} = 3.39 \times 10^{-17}\,\mathrm{W}/\sqrt{\mathrm{Hz}}$. This is the radiation power that can be detected by the TES in a bandwidth of 1 Hz. Now we must convert this into a current noise. This is simply

$$S_I = \left(\frac{\mathrm{d}I}{\mathrm{d}P}\right)^2 \mathrm{NEP}^2 = \frac{1}{2R_nP}\,\mathrm{NEP}^2, \tag{3.42}$$

where we use the Joule heating formula $P = I^2R$ and choose $R = R_n/2$ at the middle of the transition. The value for the power is obtained from the P vs. V_{TES} plot as above. Then we get that the TES current noise from thermal carriers at 200 mK is $S_I^{1/2} = 4.48\,\mathrm{pA}/\sqrt{\mathrm{Hz}}$, when referenced to the KPUP input. This may in fact be too low to detect using our KPUP, which has an optimal current noise of $8\,\mathrm{pA}/\sqrt{\mathrm{Hz}}$. However, it may be possible if the KPUP is operated on the steep, sensitive edge

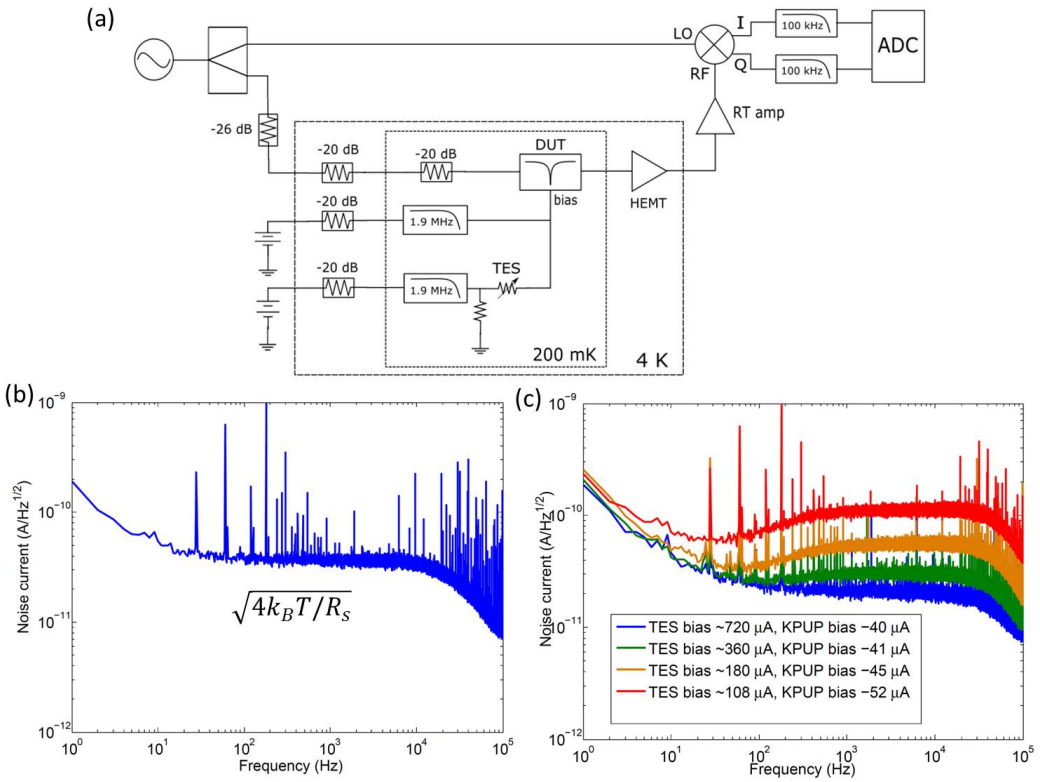

Figure 3.12: (a) Experimental setup for measuring TES noise. Separate battery boxes are used to apply bias currents, through cold attenuators, for the TES and KPUP. The bias currents travel through low-pass filters at the mixing chamber before entering their respective devices. The TES bias is combined with the KPUP bias after the TES, and both are sent to the bias input of the KPUP. A microwave synthesizer is used to excite the KPUP resonance through seperate attenuation at room temperature, 4 K, and at the mixing chamber. The transmission through the KPUP feedline is amplified at 4 K and at room temperature, and is sent to an IQ mixer where it is mixed with the microwave carrier. The outputs of the IQ mixer are filtered and then sent to an analog-to-digital converter. (b) Current noise spectrum measured by the KPUP with TES bias off and KPUP bias $-37\,\mu$A. There is $1/f$ noise below 20 Hz, and the roll-off at 20 kHz corresponds to the sampling frequency. The noise level of $\sim 37\,\mathrm{pA}/\sqrt{\mathrm{Hz}}$ is in agreement with the expected Johnson noise of the TES shunt resistor. (c) Current noise spectra taken for different levels of the TES bias current. The TES out-of-band noise rises with decreasing current. The phonon noise feature is not observed.

of its nonlinear resonance. Additionally, the TES current noise would be greater if its resistance were smaller, as seen in Eq. (3.42). Thus, the current KPUP device would be more likely to detect the phonon noise of a less resistive TES.

Current noise measurement with TES

Although it was unlikely that we would be able to see the TES phonon noise with the KPUP, we proceeded to measure the noise regardless. The setup and results are shown in Fig. 3.12. The noise measurement was done using a microwave IQ mixer. The KPUP and TES were biased as described in the previous section, except that we used battery boxes instead of DC voltage sources because they have comparatively lower output noise. A microwave source was used to excite the KPUP resonance through the feedline. The transmission through the feedline was amplified by a HEMT at 4 K as well as a room temperature amplifier, and the output was sent to the IQ mixer, whose reference frequency was set by the microwave source. The in-phase and quadrature components of the signal, proportional to the real and imaginary components of the transmission function, were extracted by the IQ mixer, filtered, and finally sampled by an analog-to-digital converter at a rate of 20 kHz.

The measurement was made at 200 mK, and noise spectra were taken at several different values of the TES bias current. First, a noise spectrum was taken with the TES bias input off. We expected the result to be characteristic of the Johnson noise of the TES shunt resistor. Since the TES is superconducting under this condition, the thermal noise current of the resistor has a zero-impedance path to the KPUP nanowire. The expected noise current is [191]

$$I_n = \sqrt{\frac{4k_B T}{R_s}}, \tag{3.43}$$

where R_s is the value of the shunt resistance. For $T = 200\,\mathrm{mK}$ we have $I_n = 33.2\,\mathrm{pA}/\sqrt{\mathrm{Hz}}$. The measured noise level is approximately $37\,\mathrm{pA}/\sqrt{\mathrm{Hz}}$, which is in agreement with the Johnson noise estimate. It should also be noted that the resistance of the shunt resistor is expected to be slightly less than its room-temperature value. Given this, the predicted Johnson noise current may be closer to the measured value.

The TES battery input was then turned on, and noise spectra were taken at four different TES input currents. All four spectra show similar $1/f$ behavior below 20 Hz, with a roll-off at 20 kHz due to the finite sampling frequency. The flat TES out-of-bandwidth noise is observed above about 400 Hz. The level of this noise decreases with increasing TES current, showing that the TES noise does indeed change according to the bias conditions, and the KPUP is able to detect this effect. The TES phonon noise feature is expected to occur in the spectrum between 10 and 100 Hz. However, the feature is not observed in our measurement. This is not very

surprising because the expected phonon noise level for this TES is lower than the optimal noise for the KPUP.

3.4 TES readout with AC bias

Multiplexing filters

We decided to AC-bias the TES for the next experiment. One reason for this was that we expected a possible improvement in the $1/f$ noise, so it might allow the KPUP to see the TES phonon noise. Another reason is that it would allow us to multiplex TESs in the frequency domain, similar to what was described in Sec. 1.4. The bandwidth of the KPUP (half the linewidth) is on the order of 100 MHz. This is much higher than that of a SQUID. We decided to make use of this bandwidth by AC-biasing multiple TESs, with each at a different frequency within this bandwidth. In order to do this, we needed biasing filters, similar to the biasing filters used in low-frequency SQUID-based TES FDM.

Since our TES bias frequencies would be on the order of tens of megahertz, it was reasonable to use microfabricated, lithographed filter components instead of discrete components on a circuit board. Superconducting bias filters were designed and fabricated, and a photograph is shown in Fig. 3.13(a). The filters are series-LC resonators made of a single layer of NbTiN on a silicon substrate. The device material was chosen to be NbTiN because of its high kinetic inductance, and the filter frequency was chosen to be on the order of 10 MHz due to the KPUP bandwidth. In order to make a resonator at lower frequencies, larger component values are required. The photograph shows that the physical size of these resonators is much greater than the physical size of the KPUP resonator. The best way to achieve a large inductance in a compact physical area is to use a meander structure. The relative advantage of using a material with a high kinetic inductance increases when using a meander. Indeed, in our filters, the inductance was mostly kinetic. There are 16 filters on a chip, and they all have the same inductance of approximately 4 μH. In order for the different filters to have different resonance frequencies, their capacitances were designed to be different. The capacitors were interdigitated, just like for the KPUP, and were spaced around an approximate center value of 20 pF. The resonators were placed on the chip in an alternating pattern with respect to their resonance frequencies in order to reduce potential crosstalk [192]. The resulting resonance frequencies ranged from 16–20 MHz, as seen in the transmission plot in Fig. 3.13(b). The transmission was measured using a vector network analyzer, and dips in the transmission were observed at the resonance frequencies of the filters.

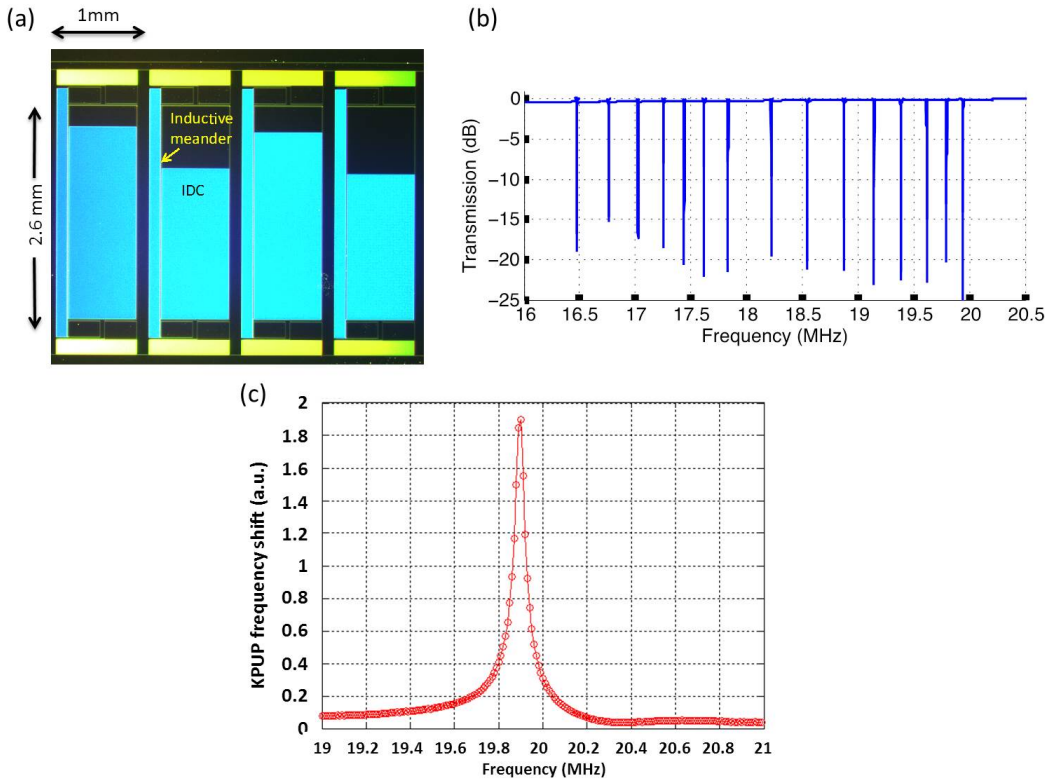

Figure 3.13: (a) Photograph of filter chip intended for TES AC bias. Each filter is a superconducting series-*LC* resonator made of a single layer of NbTiN on a silicon substrate. The inductor is a meander, and the inductance is mostly kinetic inductance. The capacitor is an interdigitated capacitor. There are 16 resonators on the chip. The inductors are identical among the resonators, but the capacitors differ in order to give each a unique frequency. Resonators that are close in frequency space are not placed next to each other on the chip, in order to avoid crosstalk. (b) Transmission through the filter chip, taken with a vector network analyzer. Fifteen of the expected sixteen resonances are observed. (c) KPUP frequency modulation through a 19.9-MHz filter. As the filter drive frequency sweeps through the resonance, the current flowing through the filter peaks. This current goes through the KPUP nanowire, and causes the KPUP frequency to shift.

Out of the total 16, 15 resonances are observed.

Fig. 3.13(c) shows a measurement of a filter resonance using the KPUP. For this measurement, an RF source was used to send a current through the filter. The output of the filter was connected to the KPUP bias connection along with a KPUP bias current. The KPUP was excited via a microwave tone at a constant power and frequency. The microwave and RF currents mixed in the nanowire, creating sidebands that coupled out of the KPUP and down the feedline. The sidebands were down-converted at room temperature using a mixer and the original microwave frequency. The resulting RF current was measured using a lock-in amplifier whose reference frequency was set by the original RF source. The RF frequency was swept, and the current flowing through the filter increased and decreased according to the shape of the filter resonance. This current also flowed into the KPUP nanowire and modulated the KPUP resonance frequency through the kinetic inductance nonlinearity. The KPUP frequency modulation was observed as a change in the amplitude of the carrier sidebands as the RF generator frequency was swept.

AC TES measurements

We proceeded to integrate a TES with a bias filter for AC readout with the KPUP. A new TES had to be chosen due to overuse of the bonding pads of the old TES. However, the same chip was used, and a different TES on the chip was selected. The TES was wire-bonded to be in series between the filter and the KPUP bias connection. The eventual goal would be to have an array of TESs, with each TES wired between the KPUP bias connection and a separate biasing filter. This concept is shown schematically in Fig. 3.14(a). For this experiment, we used only one TES and one bias filter. Additionally, we installed a thermal radiation emitter in the box. Essentially, it was a "reverse bolometer" that emitted light when a voltage was applied across it. This was required in order to drive the TES normal, because we found from other measurements of the bias filters that the electrical power required to drive the TES normal was greater than the bifurcation power of the resonators. The reverse bolometer was placed above the TES, so that the emitted light would be absorbed by the TES and increase its temperature above the transition.

We measured the TES bias curve at a refrigerator temperature of 200 mK. An RF current was applied through the filter at a value that was high but still below the filter's bifurcation power. Then the reverse bolometer was turned on in order to drive the TES into its normal state. The reverse bolometer was then immediately

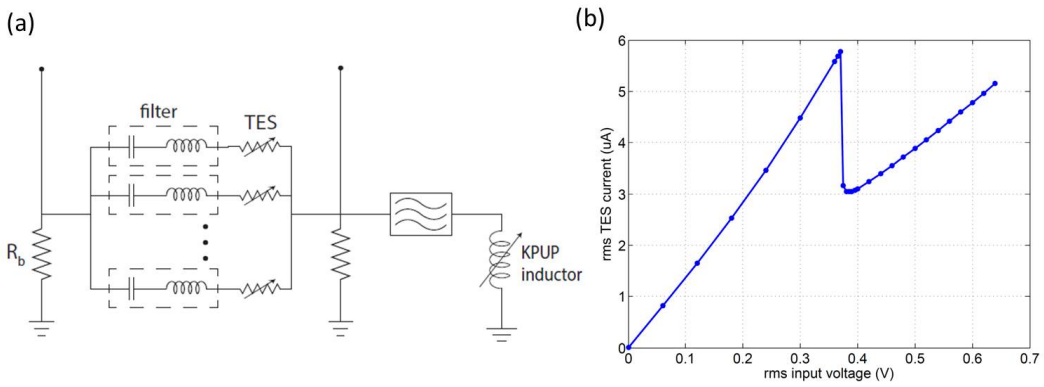

Figure 3.14: (a) TES frequency-division multiplexing scheme with KPUP. It is a modification on the TES readout scheme of Fig. 3.11(a). The TES is replaced by an parallel array of series-*RLC* filters. The resistive component of each filter consists of a unique TES. The resonance frequency of each filter, determined by its inductance and capacitance, is unique. Instead of a DC bias current, a comb of RF bias currents is sent through the common TES bias input, across the shunt resistor. The sum of the currents flowing through the TESs goes through the stepped-impedance filter and into the KPUP nanowire. The KPUP resonance frequency is modulated at each TES frequency. (b) TES bias curve measured by AC-biasing the TES through an *LC* filter. Compared to the bias curve from the DC measurement, the slope of the superconducting region is very low, and the transition region is very small.

turned off, as the RF current was high enough to keep the TES normal. Then the RF current amplitude was swept down in order to map out the TES bias curve, similar to the DC measurement. For the KPUP, a constant DC bias current was applied. The KPUP resonance was excited via a microwave source, and the RF TES bias current was up-converted due to the kinetic inductance nonlinearity. The carrier sidebands were down-converted at room-temperature by mixing with the frequency of the microwave source, and the output of the mixer was sent to an RF lock-in amplifier to be measured. KPUP calibration data was used to convert the measured sideband level to a current value.

The measured TES bias curve is shown in Fig. 3.14(b). There are important differences between this measurement and the DC bias curve measurement. The horizontal axis does not go as high, as a large input power could not be applied due to the bifurcation of the filter resonance. The transition region is very small. It is unclear why this is the case. Also, the slope of the TES superconducting region is very low compared to the DC measurement. When the TES current is plotted against the input current rather than the input voltage, the slope is 0.03, where it

should be unity. This suggests that there may be a finite resistance in series with the TES. Unfotunately, we were unable to locate any series resistance. Regardless, the AC biasing circuit can clearly be improved, since the bias curve could not be measured properly.

We also attempted to measure the TES noise while it was AC-biased. This was a challenge because the TES noise must be measured while the TES is in its transition, and the transition region was so narrow with the current AC-biasing setup. In order to measure the noise, we had to apply an additional RF signal to the KPUP in order to cancel the steady-state RF current from the TES bias. This was necessary because, in order to get a good noise measurement, the KPUP sensitivity had to be optimized by applying a large DC bias current. However, due to the finite nanowire critical current, the maximum-allowable KPUP bias current is suppressed by the presence of the TES RF signal. This type of carrier nulling is standard in SQUID-based FDM readout schemes, as discussed in Sec. 1.4. However, even after nulling the RF in the KPUP, we were unable to get a meaningful noise measurement. This is actually not surprising, because at the TES bias frequency, the impedance of the stepped-impedance filter for the KPUP is comparable to the TES resistance. This means that the RF nulling tone, which is sent down the KPUP bias line, also travels through the TES and to ground through the TES shunt resistor. Because of this, it is very difficult to know the actual TES current, since it is a sum of the bias current and the nulling current, which have opposite polarities. One approach to solving this problem for the future is to redesign the KPUP chip to have two separate bias pads, each with a separate stepped-impedance filter. One connection would be used for the KPUP bias and RF nulling, and the other connection would be used for reading the TES current. In this configuration, the nulling tone would not flow through the TES bias line, as it would be impeded by a stepped-impedance filter, and the impedance of the KPUP nanowire is very small in comparison.

Chapter 4

TRANSMISSION LINE KPUP

4.1 Preliminary experiments

Millimeter-wave parametric amplifier features

The transmission line KPUP project was inspired by the measurement of Eom et al.'s parametric amplifier shown in Fig. 2.11(a). They sent a DC current through the parametric amplifier and monitored the phase of the transmission. They observed a quadratic phase shift with increasing DC current. Using the principles we have been developing throughout this thesis, it follows that monitoring the phase of the transmission through the parametric amplifier device while applying a DC bias current would be a promising way to detect small currents. Thus, we took one of their parametric amplifier devices in order to measure it in this mode. Unlike the microwave parametric amplifier described in Sec. 2.4, this device was designed for millimeter-wave frequencies. However, since it is a broadband, traveling-wave device, it can be measured at microwave frequencies as well. A photograph of the device is shown in Fig. 4.1. This device is similar to the microwave parametric amplifier in that it is a CPW made of NbTiN with a length on the order of 1 m that follows a double-spiral trajectory. The center conductor has a width of 1 μm.

We measured the total normal-state resistance of the device. In order to do this, we had to reduce the conductivity of the silicon substrate to zero. When we measured the TiN nanowire resistance (Sec. 3.2), we dipped the nanowire in liquid helium and performed a four-wire measurement. This was possible because the TiN critical temperature was below the temperature of the liquid helium, so the nanowire was

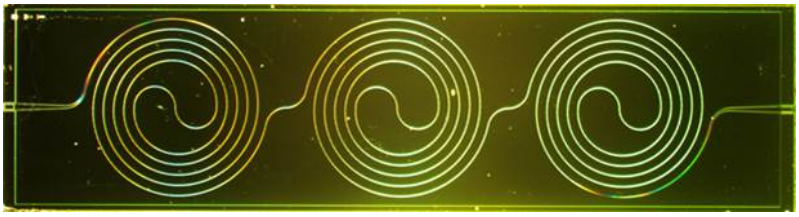

Figure 4.1: Photograph of millimeter-wave parametric amplifier. The device is a co-planar waveguide made of NbTiN on a silicon substrate. The width of the center conductor is 1 μm, and it has a length on the order of 1 m following a trajectory consisting of three double spirals.

still in its normal state, even though the silicon conductivity was effectively zero. However, for the millimeter-wave parametric amplifier, it was not so straightforward, as the device was made of NbTiN, which has a higher transition temperature of around 12 K. The device would become superconducting if dipped in liquid helium. The resistance measurement had to be performed as the device was partially dipped inside a dewar of liquid helium, but not fully immersed in the liquid. This way, the cooling power of the liquid helium was low enough that the silicon conductivity was reduced to zero, but left the NbTiN still resistive. Since we had to hold the dip-stick above the bottom of the dewar, it was not possible to perform a careful four-wire measurement. Instead, we simply probed the connections at the top of the dip apparatus (which the device terminals were wire-bonded to) using a digital multimeter. The resistance of the center conductor was found to be 6.8 MΩ. Then we could calculate the total kinetic inductance of the center conductor by using the relation

$$L_k = \frac{\hbar R_n}{\pi \Delta_0}. \tag{4.1}$$

Using $T_c = 14$ K, we found that the kinetic inductance was approximately 0.7 μH.

Device performance

The device was mounted in a sample box with both microwave and DC connectors, because we had to send both signals through the same terminals on the chip. Commercially-available diplexers were used to isolate the DC connections from the microwave connections and vice versa. The box was installed in a dilution refrigerator and cooled to a temperature of 30 mK. The transmission through the device was measured using a vector network analyzer. The DC bias current was applied using a battery box across a 97.6-Ω resistor at room temperature. The output of the battery box was measured using a digital multimeter. A nominal microwave power of −76 dBm was applied to the transmission line. The voltage from the battery box was swept from zero to 33.45 mV. The resulting phase shift is shown in Fig. 4.2(a). The phase shift shows the same quadratic dependence on the bias current as that of the microwave parametric amplifier. The maximum phase shift observed was almost 3 radians, which occurred at a bias current of 270 μA. This is significantly higher than the critical current of the nanowire device described in the previous chapter. Strictly speaking, 270 μA does not appear to be the critical current of the device, because it does not fully transition to its normal state at that point; instead, it starts becoming somewhat resistive, and the result is a small but abrupt drop in the phase shift. It is possible that this is due to the periodic widening of the center conductor,

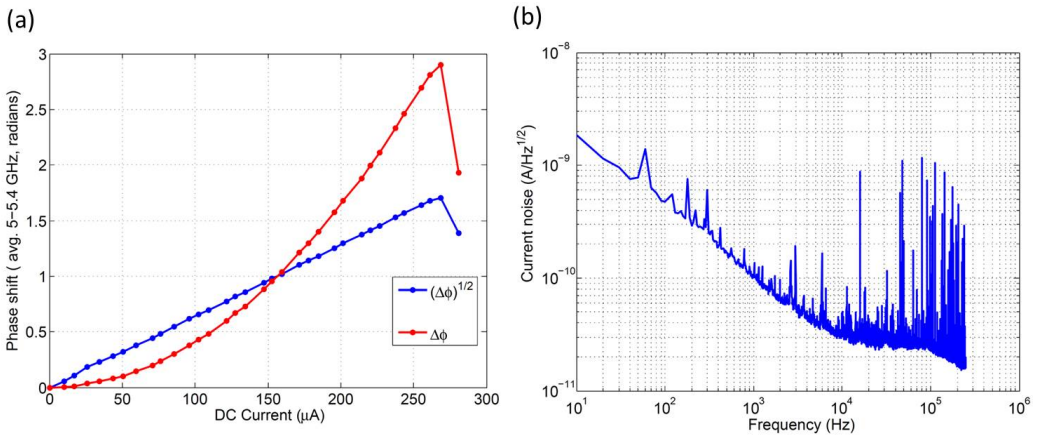

Figure 4.2: (a) Phase shift measurement of millimeter-wave parametric amplifier. The phase of the transmission through the device was measured on a vector network analyzer. A DC current was applied through the center conductor, and the phase for each value of the current was averaged from 5 to 5.4 GHz. The square-root of the phase shift is linear, showing that the phase shift is quadratic in the current. The phase shift suddenly decreases above a certain value of the bias current. (b) Noise measurement of millimeter-wave parametric amplifier with a bias current of about 260 μA. There is $1/f$ behavior below 10 kHz, and the spectrum rolls off at 100 kHz. Between those points it has a value of 27 pA/$\sqrt{\text{Hz}}$.

similar to what was described for the microwave parametric amplifier in Fig. 2.11. Because of the sharp corners it introduces into the geometry, it may be responsible for current crowding. At 270 μA, sections of the geometry close to the corners may be becoming normal. Because the center conductor is wide compared to the nanowires of the previous chapter, this does not cause it to immediately become fully normal due to positive feedback. Instead, since a portion of the line is no longer superconducting, the kinetic inductance is reduced, so the response to the current decreases.

We also measured the noise of the millimeter-wave parametric amplifier. A lock-in amplifier was used, similar to previously-described measurements. A constant microwave tone at 5.18 GHz and −50 dBm was sent through the device. A constant bias current of about 260 μA was also used. An RF tone at 16 MHz was combined with the bias current at room temperature using a bias tee, and also sent through the device. The kinetic inductance nonlinearity created sidebands around the microwave carrier at 16 MHz. The transmission was mixed with the original carrier at room temperature in order to recover the sidebands. The resulting RF signal was sent to the lock-in amplifier, and the outputs of the lock-in amplifier were filtered and

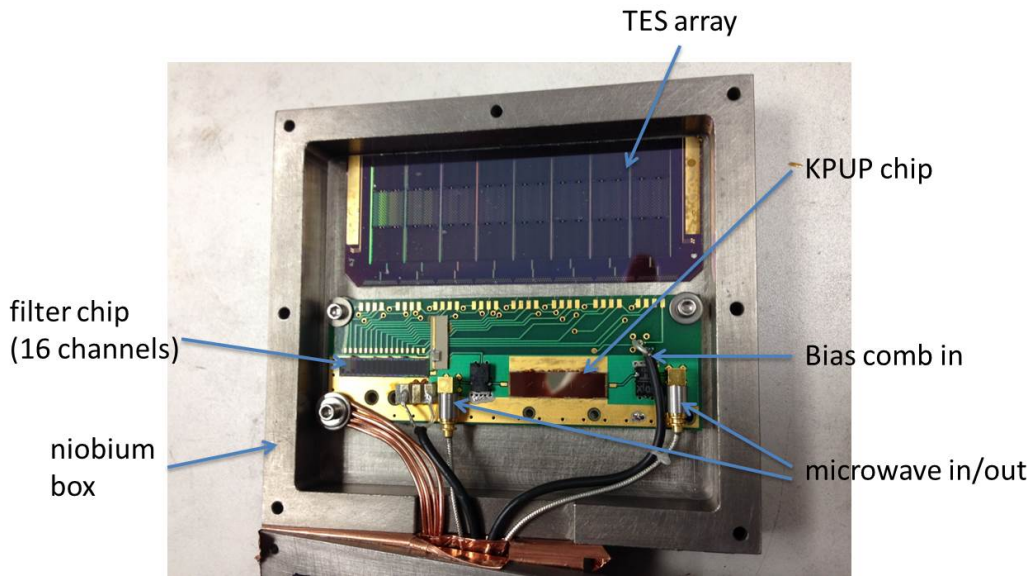

Figure 4.3: Photograph of TES multiplexing setup with KPUP. The TES array chip is a test chip for a cosmology experiment. The KPUP chip is the millimeter-wave parametric amplifier. The filter chip is the bank of NbTiN bias filters described in Sec. 3.4. A printed circuit board is used to interface the three chips, as well as to provide input and output connections. The KPUP and filter chips are mounted directly on the PCB. Wire bonds are used to connect the PCB with the TES array. The entire setup is contained within a niobium box.

sampled by an analog-to-digital converter at a rate of 200 kHz. The resulting noise spectrum is shown in Fig. 4.2(b). Although there is large $1/f$ noise, the spectrum is flat above the $1/f$ knee until the roll-off, which is due to the finite sampling rate. The noise level is $27\,\mathrm{pA}/\sqrt{\mathrm{Hz}}$. This is an impressively low current noise for a device that was not designed to be a current sensor. If, for example, the critical current was improved, this type of device could reach lower noise levels.

TES readout

Since the current-sensing performance of the millimeter-wave parametric amplifier was reasonably good, we proceeded to try to read out transition-edge sensors with the device. One of the main advantages of the traveling-wave device over the resonator is its very large bandwidth. Thus, we went straight to a AC-biasing scheme for the TES, with the intention of multiplexing an array of TESs in the frequency domain. The schematic for this biasing scheme is the same as in Fig. 3.14(a), except that the combination of the stepped-impedance filter and the KPUP inductor is replaced by the length of the transmission line. An array of TESs is multiplexed using RF

biasing filters, which are excited by a frequency comb. The output of the filters is sent to the KPUP, which in this case is the millimeter-wave parametric amplifier device. This scheme was implemented with this device, as shown in Fig. 4.3. A TES array chip was obtained from colleagues at JPL. It is a test array similar to those used for a particular cosmology mission. The biasing filters are the same ones described in Sec. 3.4. The KPUP, filter, and TES chips are interfaced by a printed circuit board (PCB) that was designed by Peter Day. The KPUP and filter chips were mounted directly on the PCB, as well as the diplexers. The TES chip was mounted within the same box, but beside the PCB. Wire bonds were used to connect the PCB to the TES array. The PCB also provides connectors for the microwave and RF+DC signals. Finally, all of the above is contained within a niobium sample box that provides electromagnetic shielding.

Unfortunately, we were not able to get any good measurement using this setup. As mentioned above, the inductance of the KPUP is 0.7 μH. At a TES bias frequency of 20 MHz, this presents a large input impedance of almost 100 Ω. Furthermore, this input inductance is large enough to affect the resonance frequencies of the filters, each of whose inductance is 4 μH. We tried to mitigate these unwanted effects by placing a series capacitor between the TESs and the KPUP in order to transform the impedance. The intention was to use the capacitor to cancel the impedance of the KPUP at the TES bias frequency. Unfortunately, when we tried this, the resonance of the capacitor-KPUP combination did not match our prediction, and the input impedance presented to the TES currents was high. We were unable to figure out the reason for this discrepancy. However, it would be useful in the future to design a transmission line KPUP with a lower inductance, so that it would not affect the TES filters so much.

4.2 Transmission line current sensor

Design and fabrication

The performance of the millimeter-wave parametric amplifier device proved that a long transmission line could make a good current sensor. However, the design of that device was not optimal for current sensing. Because it was very long, it had a large inductance, and this presents a large input inductance for the current signal. This results in a large time constant

$$\tau = \frac{L}{R}, \tag{4.2}$$

Figure 4.4: Photograph of transmission line KPUP device. It is a NbTiN CPW on a silicon substrate. The total length of the line is 6 mm. The width of the center conductor is 120 µm at the ends and 0.5 µm in the straight, central part of the device. A meandering tapered section smoothly varies the width of the center conductor between these two values.

where R is a characteristic resistance of the signal input line. In the case of TES readout, R is the TES resistance. In addition to the large inductance, the millimeter-wave parametric amplifier had complications in its geometry, particularly the periodic widening of the center conductor, that may have caused current crowding and reduced the critical current. A transmission line optimized for current sensing purposes would be somewhat shorter in length, in order to have a smaller inductance, and would not have any sharp corners, in order to have a larger critical current.

A design of such a device is shown in Fig. 4.4. This version of the transmission line KPUP is also made of NbTiN. Although TiN has a lower T_c and thus a greater kinetic inductance than NbTiN, our group has found that NbTiN is a more reliable material for long transmission lines. The NbTiN film for this device was sputtered directly on a silicon wafer. The thickness of the film is 30 nm. The film was patterned using photolithography. Like the parametric amplifier, the device is simply a co-planar waveguide. The length of the line is 6 mm, and the width of the center conductor as well as the width of the gap between the center conductor and either ground plane is 0.5 µm. A relatively small width was chosen in order to keep the kinetic inductance high. The characteristic impedance of the line is approximately 230 Ω. At either end of the transmission line is an impedance transformer that smoothly transforms the characteristic impedance from 230 to 50 Ω in order to efficiently couple power to and from the 50-Ω cables at the input and output. The impedance transformation was achieved by smoothly tapering the width of the center conductor from 120 µm at the ends to 0.5 µm in the central part of the transmission line.

The resistance of the transmission line KPUP was measured. Since the device was made out of NbTiN, the same technique used for the millimeter-wave parametric amplifier was used again. The device was partially dipped in a dewar of liquid helium, and the resistance was measured using a digital multimeter. The value

obtained using this technique was $R_n = 1.187\,\mathrm{M\Omega}$. Using Eq. (4.1) with $T_c = 14\,\mathrm{K}$, this corresponds to a kinetic inductance $L_k \approx 130\,\mathrm{nH}$. This is considerably lower than the kinetic inductance of the millimeter-wave parametric amplifier.

Current response

We measured the current response of the transmission line KPUP at 4 K. The device was mounted on a dip probe and fully immersed in a dewar of liquid helium. A vector network analyzer was used to measure the microwave transmission. A microwave tone with nominal power of −50 dB was swept from 4 GHz to 4.5 GHz and sent through the device. A DC voltage source was used to provide the bias current. There was a total resistance of 200 Ω at room temperature after the voltage source output in order to convert it into a current. In order to find the critical current of the transmission line, we increased the bias current until the transmission dropped abruptly. This was expected to occur when the device surpassed its critical current. Since the normal-state resistance of the transmission line was measured to be 1.187 MΩ, it would present a very large impedance to the VNA signal if it were to be driven normal. For power flowing through a 50-Ω cable towards the device, the reflection coefficient

$$\Gamma = \frac{R_n - Z_0}{R_n + Z_0} \tag{4.3}$$

would be approximately unity. Thus, the transmission would be very low. Using this technique, the critical current was measured to be $I_c = 3.61\,\mathrm{mA}$. This critical current is an order of magnitude larger than that of the millimeter-wave parametric amplifier, even though the width of the line is half the width of that device. It is possible that the improvement is due to the simpler geometry with no sharp corners.

The bias current was swept from zero to close to the critical current, and the transmission was measured at each point. The phase of the transmission was averaged over the frequency range and plotted against the bias current. The result is shown in Fig. 4.5. The maximum observed phase shift was 2.2 radians. The phase shift was converted to a change in the total inductance using the relation

$$\frac{\delta\theta}{\theta} = \frac{1}{2}\frac{\delta L}{L}. \tag{4.4}$$

We found from simulations in Sonnet [186] that the total phase length is 24 radians. Using this value in Eq. (4.4), we find that the maximum observed inductance change is over 30%. If we are able to change the inductance by such a large amount, we can use a large bias current to make a very sensitive current detector.

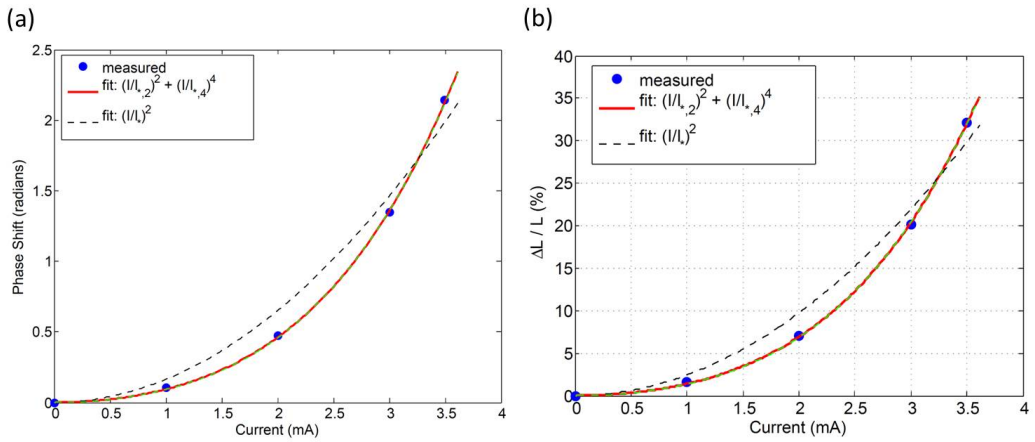

Figure 4.5: (a) Phase shift of transmission line KPUP in response to DC bias current, measured with a vector network analyzer at 4 K. The maximum observed phase shift is 2.2 radians. The data follow a quartic trajectory. (b) Phase-shift data converted into fractional change of total inductance of the transmission line. An inductance change of over 30% is observed.

The phase shift data follow a quartic trajectory, much like the frequency shift data of the lumped-element resonator KPUP. We fit the data to the function

$$\delta\theta = \frac{I^2}{I_2^2} + \frac{I^4}{I_4^4}, \tag{4.5}$$

where I_2 and I_4 are constants. From the fit, we get $I_2 = 12\,\mathrm{mA}$ and $I_4 = 6.2\,\mathrm{mA}$. Like we did with the resonator KPUP result, we can compare this to the quartic model presented by Anthore et al. [132]. According to their paper, the phase shift would obey

$$\delta\theta = 0.95\,\alpha\theta\,\frac{I^2}{I_*^2} + 1.75\,\alpha\theta\,\frac{I^4}{I_*^4}. \tag{4.6}$$

Comparing our fit parameters to this function, we get $I_* = 4.35\,\mathrm{mA}$ and $\alpha\theta = 0.14$. The former value is reasonable, as it is on the order of the critical current, which is what we expect. However, the value for the combination $\alpha\theta$ is unlikely. From our simulation, θ is expected to be about 24, and α is expected to be close to unity. These results are very similar to the results for the lumped-element resonator, further suggesting that the quartic behavior is not due to the suppression of the superconducting gap. We can also compare the results of our two experiments. As before, we compare our fit to a function of the form

$$\frac{\delta L_k}{L_k} = \kappa_2\,\frac{J^2}{J_*^2} + \kappa_4\,\frac{J^4}{J_*^4}. \tag{4.7}$$

Using Eq. (2.16), for NbTiN we have $J_* = 505\,\mathrm{mA}/\mu\mathrm{m}^2$. Then, using our values for θ and α obtained from simulations, we get $\kappa_2 = 0.03$, $\kappa_4 = 0.19$, and $\kappa_4/\kappa_2 = 5.6$. These results are of similar order of magnitude to the results from the lumped-element resonator measurement.

Noise measurement

Since the current response of the transmission line KPUP was very strong, we expected that the current noise would be low. From the fit of the phase vs. bias current data, we find that the slope at a 3-mA bias current is $\mathrm{d}\theta/\mathrm{d}I = 1.3\,\mathrm{rad/mA}$. Recalling from Sec. 2.4 that we can ignore the TLS noise relative to the amplifier noise for this device, the expected current noise is

$$S_I = \left(\frac{\mathrm{d}\theta}{\mathrm{d}I}\right)^{-2} \frac{k_B T_a}{2P}, \tag{4.8}$$

where P is the readout power. The saturation power for our HEMT amplifier is approximately 1 μW. Using this value as the readout power, with a noise temperature of 5 K, we get $S_I^{1/2} = 4.5\,\mathrm{pA}/\sqrt{\mathrm{Hz}}$ as our estimate for the current noise.

We proceeded to set up the noise measurement. The setup is shown in Fig. 4.6(a). The device was installed in a dilution refrigerator and cooled to a temperature of 60 mK. A microwave synthesizer was used to generate a carrier tone at 6.32 GHz. The carrier was attenuated at room temperature, at the 4-K stage, and at the mixing chamber before the device. It was sent through the high-frequency port of a diplexer before entering the KPUP transmission line. The nominal microwave power at the KPUP was −16.6 dBm, or about 20 μW. A 5-MHz RF tone was also generated at room temperature at by an RF source. It was attenuated and then sent to the RF port of a bias tee. The DC bias for the KPUP was provided by a DC voltage source, whose output was combined with the RF signal at the bias tee. The combined bias current was sent through the KPUP via the low-frequency port of a diplexer. The RF signal was up-converted in the KPUP due to the kinetic inductance nonlinearity. The carrier and sidebands exited the KPUP through the high-frequency port of another diplexer. Before being amplified by the HEMT, they were combined with a nulling tone from room temperature. The nulling tone was provided by the same microwave source, so it was the same frequency. A variable attenuator was used at room temperature in order to make the amplitude of the nulling tone equal to the amplitude of the carrier at the output of the KPUP, and a phase shifter was used to make the nulling tone 180° out of phase with the carrier at the output of the KPUP. These two microwave signals were combined using a directional coupler, amplified

by the HEMT, and then amplified again at room temperature. Then the microwave signal was mixed with the original carrier in order to recover the sideband, which was sent to a lock-in amplifier. The outputs of the lock-in amplifier were filtered by *RC* low-pass filters with cut-off frequencies of 30 kHz, and then they were sampled by an analog-to-digital converter at a rate of 500 kHz.

The carrier nulling tone was necessary because, as mentioned above, the saturation power of the HEMT was about 1 μW, and the power in the KPUP was close to 20 μW. A high carrier power was used in the KPUP because it increases the power in the up-converted RF signal. Eq. (2.38) shows that the amplitude of the sidebands is proportional to the amplitude of the carrier. By increasing the level of the sidebands, we increase the signal-to-noise ratio in the measurement. We were able to effectively null the carrier after the KPUP but before the HEMT. Fig. 4.6(b) shows a spectrum of the transmission with the carrier and the sidebands at 5 kHz. The carrier was suppressed using the nulling tone to a level below the level of the sidebands. In addition, the nonlinearity efficiently generated sidebands 60 dB above the noise level. By sampling the sideband level using the lock-in amplifier, we were able to measure the noise of the system. The noise spectrum has no $1/f$ component, and is flat until a roll-off at about 3 kHz. This roll-off is due to the internal filtering of the lock-in amplifier. The noise level is $5\,\mathrm{pA}/\sqrt{\mathrm{Hz}}$. This corresponds to the amplifier phase noise referred to the KPUP current input, which we estimated above. The Johnson noise of the room-temperature DC bias resistor is $3.8\,\mathrm{pA}/\sqrt{\mathrm{Hz}}$, which is similar, but since it is less than the noise of the amplifier, we expect that the amplifier is responsible for the measured noise level. It is very close to our estimate, and is also equal to the original estimate we made in Sec. 2.4. This shows that the current noise is limited by the amplifier noise. Any noise intrinsic to the KPUP is below the amplifier noise level and cannot be measured without a quieter readout amplifier. This noise level is promising for current sensing applications such as TES readout.

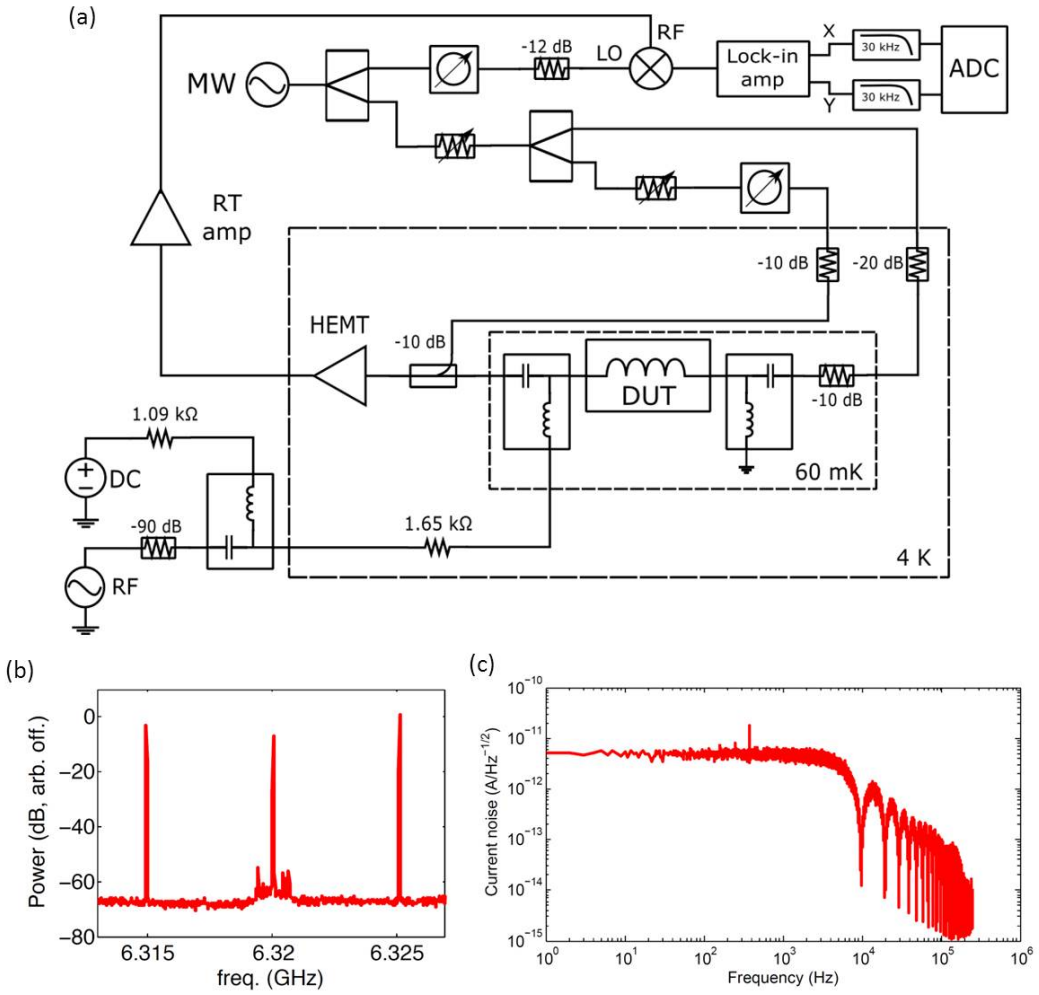

Figure 4.6: (a) Experimental setup for transmission line KPUP noise measurement. A carrier tone is generated by a microwave synthesizer, attenuated at room temperature, at 4 K, and at the mixing chamber, and sent through the KPUP via the high-frequency port of a diplexer. A low-frequency RF tone is generated and attenuated at room temperature, and then combined with a DC current via a bias tee before going through the low-frequency port of a diplexer to bias the KPUP. Sidebands are created around the carrier at the RF frequency and sent to a HEMT amplifier through a directional coupler. Part of the original microwave power is attenuated and phase-shifted and also sent through the coupler in order to cancel the carrier before the HEMT. After the HEMT, the sidebands are amplified at room temperature and then mixed with the original carrier. The resulting signal is sent to a lock-in amplifier, and the outputs are filtered and sampled by an ADC. (b) Spectrum analyzer measurement of transmission, showing sidebands and suppressed carrier. (c) Measured current noise spectrum. The level before the roll-off is $5\,\mathrm{pA}/\sqrt{\mathrm{Hz}}$.

Chapter 5

TRANSMISSION-LINE RESONATOR KPUP

5.1 Design

The transmission-line resonator KPUP aims to combine the advantages of the transmission line KPUP and the lumped-element resonator KPUP. The transmission line KPUP had a high critical current, allowing us to bias the device to a very sensitive regime, where we saw that the noise was limited by the readout amplifier. The lumped-element resonator KPUP had the advantage that it could be easily multiplexed in the frequency domain by coupling many devices to a single feedline. Based on this, a transmission-line resonator could both have a high critical current and be easy to multiplex. In order to satisfy the first goal, the transmission-line resonator could be designed with similar dimensions to the center conductor of the transmission line KPUP. The second goal is automatically satisfied by the fact that it is a microwave resonator. The device may also retain a large bandwidth by designing the coupling quality factor to be low, recalling that

$$\Delta f = \frac{f_r}{2Q_r}, \tag{5.1}$$

and that $Q_r \approx Q_c$ for TiN and NbTiN.

Quarter-wavelength resonators have historically been popular in the MKID community [123]. For our purposes, however, a half-wavelength resonator would be advantageous. This is because of the symmetry that can exist in a half-wavelength device. If we refer back to Fig. 2.15, the idea is to couple the resonator at its midpoint. This way, the potential in the resonator is symmetric about the point where it is coupled to the feedline. The point of highest rms potential is the point where the resonator is coupled. The ends, then, should be nodes of the resonator. Referring to the MKID literature [123], the ends of the resonator are forced to be at zero potential by connecting them (usually monolithically) to the ground plane. However, we cannot do that in our device. We need to utilize the ends of the resonator as connections for the bias and signal currents, just like we did with the transmission line KPUP. This is the reason for using a half-wave resonator. In a quarter wave resonator, one end is grounded and the other is the point where the resonator is coupled to the feedline. The coupling end cannot be used for a hypothetical low-frequency connection, because that would put the low-frequency connection in close proximity to

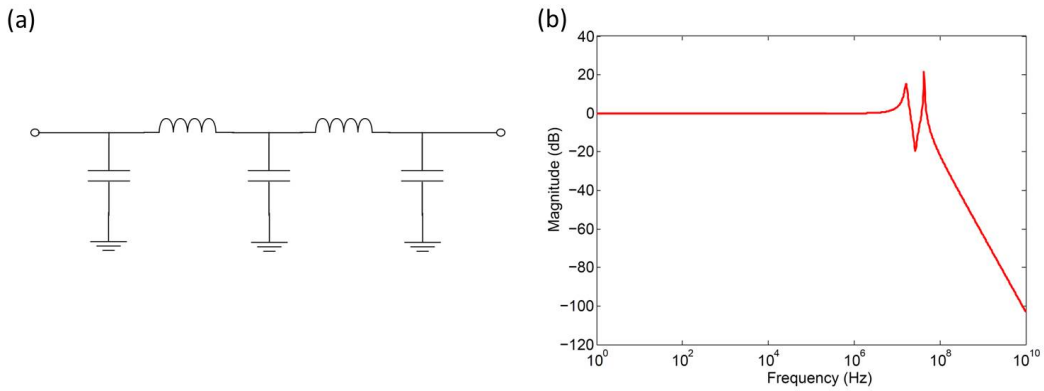

Figure 5.1: (a) Schematic of 3-pole filter used to isolate high frequencies from low frequencies on the transmission-line resonator KPUP chip. (b) Calculated frequency response of 3-pole filter. The cut-off frequency is approximately 50 MHz.

the feedline, and microwave power might be lost to the low frequency line through proximity coupling. It is thus better to have the ends of the resonator far from the feedline, and a half-wavelength resonator allows for this feature.

This leaves the problem that the ends of the resonator cannot be grounded if we are to use them as terminals for the bias current, but they should look like grounds to the microwave power in the resonator. Thus, we place a capacitor between each resonator end and the ground plane. The capacitor presents a very low impedance to the microwave power, but isolates the low-frequency current from ground. The low-frequency connection must also be isolated from the microwave power. The lumped-element resonator KPUP utilized a stepped-impedance filter to provide this isolation, and the transmission line KPUP used a diplexer. Although a diplexer is shown in the schematic of Fig. 2.15 for this device, we decided to use an on-chip, lithographed multipole filter instead. A schematic of the filter is shown in Fig. 5.1(a). The filter consists of a ladder of inductors and capacitors. The capacitance is 26 pF, and the inductance is 1.4 μH. The frequency response of the filter is shown in Fig. 5.1(b). The cutoff frequency is approximately 50 MHz, and the magnitude of the response drops by $\sim$ 40 dB/decade above that. Thus, the microwave power should be effectively blocked by this filter, and since the frequency response is unity at DC, the low-frequency signals will pass unimpeded. In order to maintain the symmetry of the device, one of these filters is placed at each of its ends.

The transmission line of the resonator was chosen to be a microstrip. Although that entails multiple fabrication layers, the overall design of the chip is simpler when

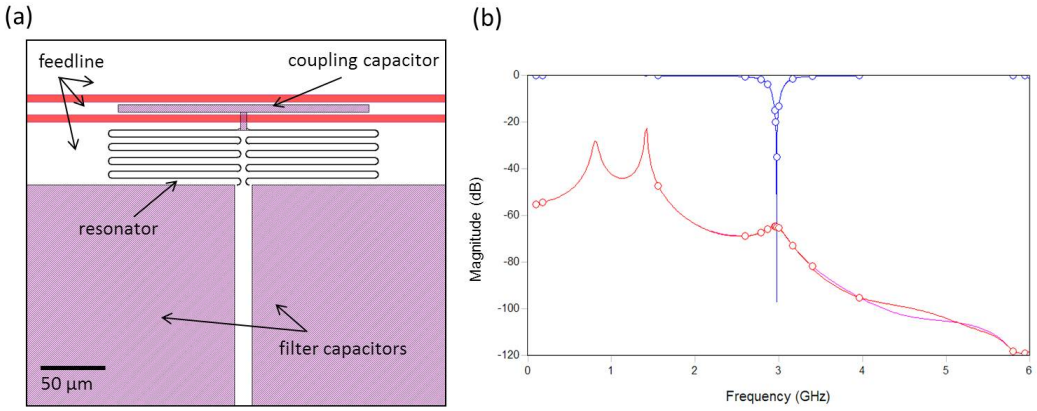

Figure 5.2: (a) Zoomed-in layout of transmission-line resonator KPUP design. The CPW feedline is in white, and is separated from the device layer by a dielectric layer. The bottom electrode of the coupling capacitor is the center conductor of the CPW, and the top electrode is a stub that is monolithically connected to the midpoint of the resonator. The resonator is a meander with a length of 400 µm and a width of 0.5 µm. The ends of the resonator are each monolithically connected to the first capacitor of a filter, whose bottom electrode is the ground plane of the feedline. (b) Electromagnetic simulation of chip design in Sonnet. The blue curve is the transmission through the feedline, showing the resonance at 3 GHz. The pink and red curves are the transmission from the left port of the feedline to either end of the isolation filter. Since there is a filter at each end of the resonator, there are two potential paths for the microwave power to leak. The transmission through the filters is suppressed at the resonance frequency.

using a microstrip. It allows us to use parallel-plate capacitors for the filters. The ground for each filter is simply the ground plane of the microstrip. In addition, this is also the ground plane of the feedline. We patterned a CPW on the bottom layer, and the ground plane of the CPW was also the ground plane for the microstrip resonator. Additionally, we used a parallel-place capacitor between the resonator and the center conductor of the CPW as the coupling capacitor. The top electrode was monolithically connected to the resonator, eliminating the need for wire bonds that we had with the lumped-element device. Part of the layout is shown Fig. 5.2(a). The resonator is a meander with length 1.75 mm and width 0.5 µm. The thickness of the device layer is 30 nm, and the material is NbTiN. Because of the high critical current we achieved in the transmission line KPUP, we chose the transmission-line resonator KPUP to have the same material and cross-sectional dimensions. Each end of the resonator is connected directly to the first capacitor of a three-pole filter. The top electrode of the capacitor is a rectangle of NbTiN that is 300 µm × 400 µm in area. The bottom electrode is simply the ground plane. All three capacitors of

the filter have the same geometry. The inductors of the filter are sections of NbTiN that are 2 µm wide and 400 µm long. Their inductance is mostly kinetic inductance, so they are essentially discrete kinetic inductors. The feedline is made of niobium, and is a few hundred nanometers thick. The dielectric layer between the feedline and the device and filters is silicon nitride, and its thickness is 300 nm. There are three devices on the chip.

The entire structure was simulated in Sonnet [186], and the result is showed in Fig. 5.2(b). The resonance frequency is 3 GHz. Since the length of the resonator is $\lambda/2 = 1.75$ mm, the phase velocity $v_p = f\lambda$ in the microstrip is 1.05×10^7 m/s. The simulation also shows the power leakage through the far end of the filter, for both filters. The magnitude of that transmission is below −20 dB throughout the frequency range, and as expected from Fig. 5.1(b), it decreases with frequency. The simulation was also done with the device material being a perfect electric conductor, in order to determine the expected kinetic inductance fraction. Since there was no surface impedance in that case, the resonance frequency was 14.7 GHz. Then, as in Sec. 3.1, we can determine the kinetic inductance fraction as

$$\alpha = 1 - \frac{f_{sc}^2}{f_{pc}^2}, \tag{5.2}$$

where f_{sc} is the resonance frequency of the superconducting resonator, and f_{pc} is the resonance frequency of the perfectly-conducting resonator. For the transmission-line resonator KPUP, the kinetic inductance fraction is 0.96, which is quite high. With such a high kinetic inductance fraction, the resonance frequency shift

$$\frac{\delta f_r}{f_r} = -\frac{\alpha}{2}\frac{I^2}{I_*^2} \tag{5.3}$$

for this device will be quite large, especially if the critical current is also high. A high kinetic inductance fraction also confirms that the filter inductors can be treated as discrete kinetic inductors.

5.2 Measurements

Device characterization

Out of the three resonators on the chip, the center device was wire-bonded to the DC bias line. The chip was cooled to 50 mK in a dilution refrigerator. A vector network analyzer was used to measure the transmission through the feedline. A nominal power of −70 dB was applied to the feedline by the network analyzer. The unperturbed resonance frequency of the KPUP was 3.924 GHz. This is close to the

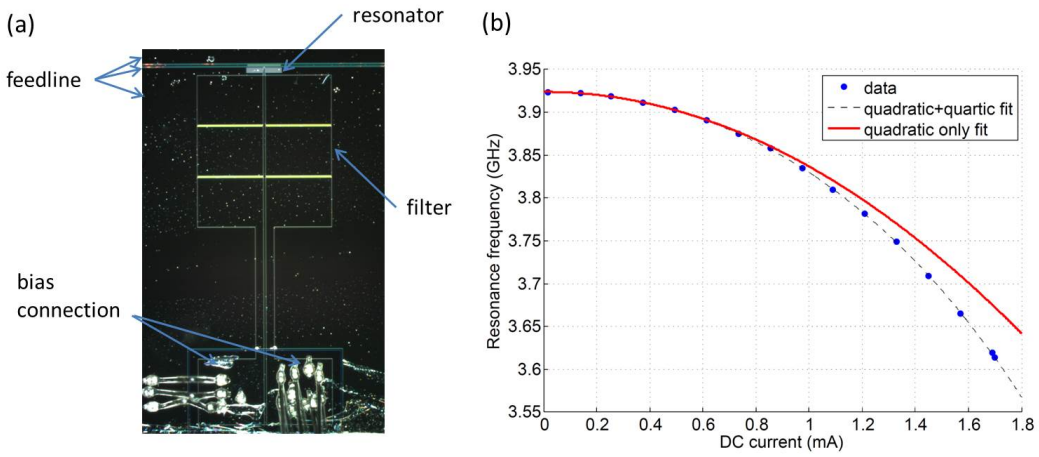

Figure 5.3: (a) Photograph of transmission-line resonator KPUP chip, showing feedline, resonator, filter, and bias connection. Each adjacent pair of capacitors in the filter is connected by a narrow strip that serves as an inductor. Wire bonds are used to connect one of the bias electrodes to the DC biasing line, and to connect the other electrode to ground. (b) DC-current response of transmission-line resonator KPUP. The data fits very well to a quartic function. The device transitions to its normal state above 1.7 mA.

design frequency. The center resonator is not the same resonator that was simulated; it is 400 µm shorter in length than the simulated resonator. If $\lambda/2 = 1.35$ mm and $f = v_p/\lambda$, then using the value for the phase velocity that we obtained from the simulation, we get 3.89 GHz for the estimated frequency. After the unperturbed resonance was measured, a battery box was used to apply the DC bias current. Two low-pass filters were placed after the battery box in order to suppress high-frequency fluctuations. They were commercial filters with cut-off frequencies of 2.7 GHz and then 98 MHz. A T-shaped *RC* filter was used at the 4-K stage of the refrigerator in order to convert the voltage of the battery box to a current. This filter consisted of two 825-Ω resistors in series with a 10.2-pF capacitor to ground between them. The cut-off frequency of this last filter was 19 MHz. Finally, the bias line was wire-bonded to the bias inputs on the chip.

The voltage from the battery box was swept in order to measure the current response of the transmission-line resonator KPUP. The result of the measurement is shown in Fig. 5.3(b). The maximum current shift before the device surpasses its critical current is 300 MHz, or an 8% change in the resonance frequency. The critical current is 1.7 mA, which is about half the critical current of the transmission line KPUP. Notably, it is much larger than the lumped-element resonator KPUP's critical

current of 66 µA. The current response for the transmission-line resonator KPUP, like that of the other devices, follows a quartic trajectory. The best-fit function is

$$\frac{\delta f_r}{f_r} = -\frac{I^2}{I_2^2} - \frac{I^4}{I_4^4}, \tag{5.4}$$

with $I_2 = 6.72\,\mathrm{mA}$ and $I_4 = 4.85\,\mathrm{mA}$. Like we did with the previous devices, we can characterize the nonlinearity by comparing it with the form

$$\frac{\delta f_r}{f_r} = -\frac{\alpha}{2}\frac{\delta L_k}{L_k} = -\frac{\alpha}{2}\left(\kappa_2 \frac{J^2}{J_*^2} + \kappa_4 \frac{J^4}{J_*^4}\right), \tag{5.5}$$

recalling that $J_* = 505\,\mathrm{mA}$ for NbTiN. Using the value for α obtained from simulations, we get $\kappa_2 = 2.65$ and $\kappa_4 = 12.4$. These are much larger than the respective coefficients for the previous two devices. However, the ratio $\kappa_4/\kappa_2 = 4.7$ is similar to the coefficient ratio for both other devices.

We can also estimate the current noise for the transmission-line resonator KPUP. Recall from Secs. 2.5 and 2.3 that the current noise is

$$S_I = \left(\frac{\mathrm{d}x}{\mathrm{d}I}\right)^{-2}\left(S_{\mathrm{TLS}} + \frac{k_B T_a}{8Q_r^2 P_g}\right), \tag{5.6}$$

where $x = \delta f_r/f_r$. From the fit to our current response measurement, if we bias at a current of 1.5 mA, we have $\mathrm{d}x/\mathrm{d}I = 91\,\mathrm{A}^{-1}$. The generator power P_g is limited by the bifurcation of the resonance. From the discussion in Sec. 2.3, the limiting value of the power is

$$P_{\mathrm{bif}} = \frac{4\sqrt{3}}{9}\frac{\omega_r E_*}{2Q_r^2}. \tag{5.7}$$

The characteristic bifurcation energy E_* is [156]

$$E_* = \frac{L_k I_*^2}{\alpha^2}, \tag{5.8}$$

where $I_*^2 = \alpha I_2^2/2$. Using $\alpha = 0.96$ from the simulations, we get $I_* = 4.7\,\mathrm{mA}$. For this resonator, the total kinetic inductance is $L_k = 19\,\mathrm{nH}$. Then $E_* = 455\,\mathrm{fJ}$. The quality factor for the resonance is approximately 30, which was the design value. Then, going back to Eq. (5.7), we have $P_g = 4.8\,\mu\mathrm{W}$. This is actually higher than the HEMT amplifier saturation power, which is $\sim 1\,\mu\mathrm{W}$. Then we cannot use the bifurcation power in Eq. (5.6), and must use the HEMT saturation power instead. Taking $T_a = 5\,\mathrm{K}$ for the amplifier noise temperature, we get $S_I^{1/2} = 1.1\,\mathrm{pA}/\sqrt{\mathrm{Hz}}$ for the noise estimate. This is lower than the expected and measured noise for both the lumped-element resonator and the transmission line KPUPs.

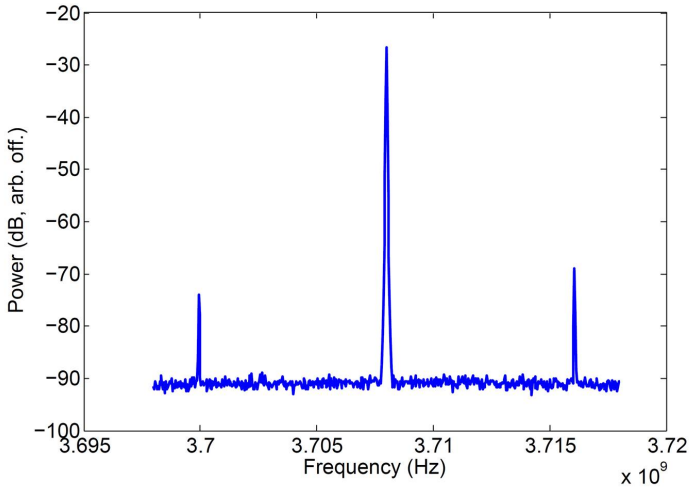

Figure 5.4: Spectrum of transmission, showing carrier and sidebands 8 MHz away from the carrier on either side. The carrier power is nominally −24 dBm, the bias current is 1.45 mA, and the RF current is nominally 225 µA.

We proceeded to try to measure the noise, using the same technique as for the lumped-element resonator KPUP at first. The device was excited with a microwave source, and a DC bias was applied along with an RF signal at 8 MHz. Sidebands were generated around the carrier at the RF frequency in the device due to the kinetic inductance nonlinearity. This is shown in Fig. 5.4. The sideband level is 40 dB below the carrier level, compared with 50 dB for the lumped-element resonator KPUP. Thus, the transmission-line resonator seems to be more efficient at parametric up-conversion. However, we were unable to get a good noise measurement for this device, even though we used the same technique of down-mixing the sidebands at room temperature, feeding to a lock-in amplifier, and sampling the outputs of the lock-in amplifier. Then we tried the technique that we used for the transmission line KPUP, which was to cancel the carrier power at the input of the HEMT amplifier in order to apply a larger power to the device. As discussed in the previous paragraph, the feedline power for the device is greater than the saturation power of the HEMT. Since a greater carrier power increases the sideband level, it is advantageous to apply a larger power on the feedline and then cancel it at the HEMT input so that mainly the sidebands are amplified. However, even with this technique we were not able to get a good noise measurement. The lowest noise we saw was about 40 $\mathrm{pA}/\sqrt{\mathrm{Hz}}$, which is much greater than our estimate of 1.1 $\mathrm{pA}/\sqrt{\mathrm{Hz}}$. It is unclear why the measured noise is so high. It is possible that it could be improved by operating the device on the steep edge of its nonlinear resonance.

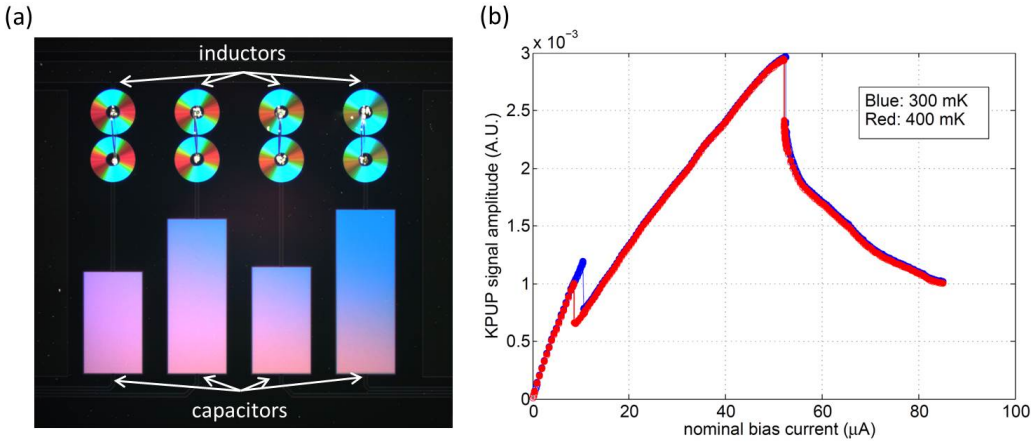

Figure 5.5: (a) Photograph of RF biasing filters used between transmission-line resonator KPUP and TES array. The filters are made of niobium. The inductor is a two-part spiral (magnetic) inductor, where the two parts are joined by a wire bond. The capacitor is interdigitated. Of the 16 total filters on the chip, all have the same inductance. The capacitances vary in order to have an array of resonance frequencies. (b) TES bias curve taken with transmission-line resonator KPUP. The bias curve was measured at both 300 mK and 400 mK. The TES is AC-biased, and the constant KPUP bias current is 1.39 mA. Two superconducting transitions are visible, due to the two layers that comprise the TES. The lower-temperature transition is for the titanium layer, and the higher-temperature transition is for the aluminum layer. The titanium transition is narrow.

TES readout

Even though the measured noise for the transmission-line resonator KPUP was unsatisfactory, we proceeded to integrate it with a TES array. The setup is the same shown in Fig. 4.3, including the same TES array chip. The KPUP and filter chips are different, however. The transmission line KPUP chip has been replaced by the transmission-line resonator KPUP chip, and the filter chip has been replaced by a new filter design. The new filters are made of niobium, and shown in Fig. 5.5(a). Similar to the old filter design, there are 16 filters per chip, each with a different resonance frequency. They are *LC* resonators again, with the inductance constant between resonators and the capacitance varying. The capacitors are interdigitated, just like in the old filters. Since the material is niobium, which has a low kinetic inductance fraction, the inductor design had to change. The new design is a spiral inductor, which has mostly magnetic inductance. The inner radius of the spiral is 100 μm, and there are 110 turns of a wire with a width of 1 μm. Each inductor consists of two such spirals in series, yielding a total inductance of 8 μH. The center

capacitance is about 20 pF. The resonance frequencies range from 10 to 15 MHz.

The transition-edge sensors used in this experiment are bi-layer devices consisting of aluminum and titanium. The superconducting transition of titanium occurs at 0.4 K, while that of aluminum occurs at 1.2 K [121]. Thus, we expect to see the titanium transition at a lower value of the TES bias current. In order to measure the TES bias curve, the niobium box was installed in a dilution refrigerator and cooled to 300 mK. The KPUP was excited using a microwave source with a frequency of 3.735 GHz and nominal power of −38 dBm. A DC bias current of 1.39 mA was applied across the KPUP. The TES was AC-biased using an RF source at 14.14 MHz, which corresponds to a filter resonance frequency. The TES current went through the KPUP, and was up-converted to the microwave regime, where it was coupled out of the resonator and down the feedline. The up-converted signal was recovered at room temperature by using a microwave mixer and then measuring with a lock-in amplifier. The level of the sideband was proportional to the TES current. The power output of the RF source was swept down in order to map out the TES bias curve. The measurement is shown in Fig. 5.5(b). The two superconducting transitions are observed for the two different layers of the TES. The aluminum transition, occurring at higher bias current, appears to be very wide. The titanium transition, occurring at a lower bias current, appears to be rather narrow, similar to the AC bias curve measurement with the lumped-element resonator KPUP (Fig. 3.14(b)). The bias curve was measured at two bath temperatures: 300 mK and 400 mK. We see that, for both transitions, the transition occurs at a higher bias current at 300 mK than at 400 mK. This is the same effect that was observed in Sec. 3.3, and is to be expected given Eq. (3.36).

We proceeded to try to measure the noise with the TES setup, even though the lowest KPUP noise we measured was $40\,\mathrm{pA}/\sqrt{\mathrm{Hz}}$. The experimental setup was the same as for the bias curve measurement. This time, the lock-in amplifier outputs were sampled at a rate of 500 kHz. We first tried to measure the noise with the TES superconducting, just like with the lumped-element resonator KPUP. Fig. 5.6(a) shows this measurement. The noise taken with no TES bias applied corresponds to the Johnson noise of the TES shunt resistor, as expected. When the AC bias is turned on, there appears to be additional noise, even though the TES is still superconducting. This could be related to the finite impedance of the KPUP. The KPUP has an input inductance of 5.6 µH including the 3-pole filter, and this corresponds to an impedance of 0.5 mΩ at the TES bias frequency of 14.14 MHz.

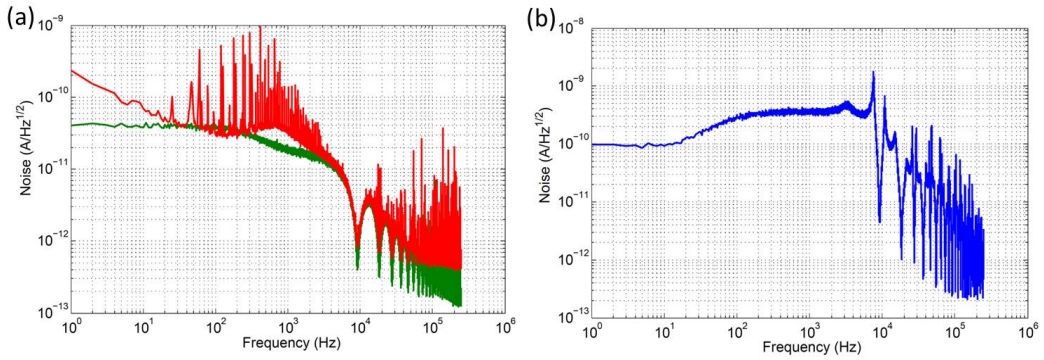

Figure 5.6: (a) Measurement of noise using transmission-line resonator KPUP with TES superconducting. The green curve is the noise with no TES bias applied. The red curve is the noise with an AC TES bias applied. Measurement was taken at 300 mK. (b) Measurement of noise with TES biased in the middle of its transition. This measurement was taken at a bath temperature of 300 mK.

We also note that the noise spectrum taken with the bias on has a $1/f$ component, while the one with bias off does not.

In order to measure the TES noise, we wanted to bias it in the middle of the titanium transition. The aluminum transition was not used because the current going through the KPUP is higher than in the titanium transition. A lower TES current is advantageous, as it allows us to use a higher KPUP bias current and put the KPUP in a more sensitive regime. Unfortunately, the titanium transition was narrow, so just like with the AC measurement using the lumped-element resonator KPUP, it was a challenge to bias the TES in the middle of its transition. We still attempted to measure the noise when the TES was biased as close to the middle of the transition as possible. The result is shown in Fig. 5.6(b). The shape of the noise spectrum is similar to the result of the DC-biased TES measurement with the lumped-element resonator KPUP (Fig. 3.12(c)). The main difference is that there is no $1/f$ noise in the new measurement. However, the out-of-band noise is seen at about 100 Hz, just like in the DC measurement. The roll-off at about 10 kHz is due to an *RC* filter that was placed before the ADC. The TES phonon noise feature, which is expected to occur at about 10–100 Hz, is not visible, just like in the earlier measurement. An improvement in the measurement of the KPUP intrinsic noise might lead to a measurement of the TES phonon noise with this device.

Chapter 6

OTHER DEVICES

6.1 Magnetic field sensor

Introduction

As discussed in Sec. 1.4, SQUIDs are the most sensitive magnetometer available. In many applications such as TES readout, SQUIDs are operated as current sensors by using an input coil to transduce a change in electric current to a change in magnetic flux, which is then measured by the SQUID. The KPUP devices discussed so far in this thesis address similar current sensing applications. However, the SQUID is natively a magnetic field sensor, as it is geometrically a loop, and is best characterized by its flux sensitivity, which is typically $\sim 1\,\mu\Phi_0/\sqrt{\text{Hz}}$. It is possible to make a similarly flux-sensitive KPUP device by simply using a loop geometry. A similar device was independently developed and demonstrated by another group in 2014 [193]. A schematic of such a device is shown in Fig. 6.1. The device is very similar to the lumped-element resonator KPUP current sensor. It is also a lumped-element microwave resonator, with the main difference being that two kinetic inductors are used in parallel, in order to form a current loop. Because nanowires were effective as kinetic inductors in the current sensor, we employ nanowires as the kinetic inductors in this device as well. The resonance frequency of the device is $\omega_r = \sqrt{2/LC}$, where C is the device capacitance and L is the total inductance of each branch. The magnetic inductance is expected to be significant due to the loop geometry. The device is coupled to a feedline via a coupling capacitance C_c. A generator sends a carrier tone down the feedline. The transmission through the feedline, which is read out by a low-noise cryogenic amplifier, shows a dip at the resonance frequency. Due to the loop geometry, the device is sensitive to magnetic fields. A DC bias field is provided by an external coil. The magnetic flux within the loop induces a current, causing the resonator inductance to change due to the kinetic inductance nonlinearity. The change in inductance is observed as a shift in the resonance frequency in the transmission data.

A magnetic field perturbation δB corresponds to a flux signal $\delta\Phi = A\,\delta B$ in the device, where A is the area of the loop. A current signal $\delta I = \delta\Phi/L$ is induced in the loop, and mixes with the current from the microwave excitation tone in the resonator

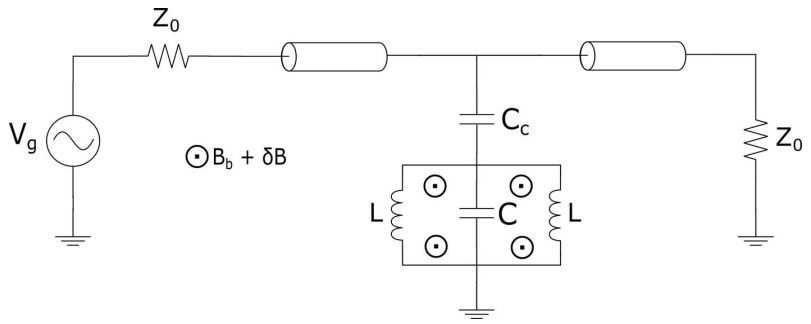

Figure 6.1: Circuit diagram for magnetic-field sensor KPUP. The device is an LC resonator coupled to a feedline, which is represented as the two transmission line sections. The coupling is achieved via a coupling capacitor. A carrier is generated by a microwave source and sent through the feedline, and the transmission is read out by an amplifier represented as the input impedance Z_0. The device has a loop geometry with two inductors in parallel. An external coil is used to provide bias and signal magnetic fields, which change the resonance frequency of the resonator by inducing a circulating current which changes its kinetic inductance.

due to the nonlinearity in the kinetic inductors. If the microwave frequency is ω_c and the signal frequency is ω_s, then sidebands are created in the device at frequencies $\omega_c \pm \omega_s$, in the same way as in the previously-discussed resonator devices. If $\omega_s < \omega_r/2Q_r$, the bandwidth of the resonator, then the sidebands can couple out of the resonator and be seen at the end of the feedline by the readout amplifier. The total transmission is then mixed with the microwave excitation frequency at room temperature in order to recover the signal. Since it is a microwave resonator, this device has many of the same advantages of the resonator current-sensor KPUPs we have discussed. A large number KPUPs can be coupled to the same feedline if they have different resonance frequencies, yielding an array of magnetic field sensors. A unique advantage of this device is that, if the bias field is roughly constant over the area of the array, a single coil can be used to bias all of the detectors in the array. Such an array would be useful for mapping out small variations in magnetic field over a finite area, for applications such as non-destructive evaluation or characterization of magnetic materials.

Response and sensitivity

The magnetic-field sensor KPUP is essentially the same device as the lumped-element version of the current sensor KPUP, except with two kinetic inductors

instead of one. The expression for the transmission through the feedline is the same:

$$S_{21}(\omega) = 1 - \frac{Q_r}{Q_c}\frac{1}{1 + \mathrm{j}2Q_r x}, \tag{6.1}$$

with Q_c and Q_r respectively the coupling and total resonance quality factors and $x = (\omega - \omega_r)/\omega_r$ the detuning. We refer to the discussion of Sec. 2.3 to obtain the response to a perturbation in the detuning:

$$\begin{aligned}\delta S_{21}(\omega;\nu) =& \mathrm{j}\,\frac{Q_i}{2}\chi_c\chi_g(\omega)\,e^{-\mathrm{j}2\phi_g(\omega)}\,\zeta(\omega;\nu) \\ &\times[\delta x(\nu) + \delta x_{\mathrm{TLS}}(\nu)] + \delta S_a(\nu),\end{aligned} \tag{6.2}$$

where δx_{TLS} and δS_a are fluctuations due to TLS noise and amplifier noise, respectively. The coupling efficiency χ_c, detuning efficiency χ_g, phase angle ϕ_g, and ringdown response ζ are defined as

$$\chi_c = \frac{4Q_iQ_c}{(Q_i + Q_c)^2} \tag{6.3}$$

$$\chi_g(\omega) = \frac{1}{1 + 4Q_r^2x^2} \tag{6.4}$$

$$\phi_g(\omega) = \tan^{-1}(2Q_rx) \tag{6.5}$$

$$\zeta(\omega;\nu) = \frac{1 - S_{21}(\omega + 2\pi\nu)}{1 - S_{21}(\omega)}. \tag{6.6}$$

We must now find an expression for the frequency perturbation δx in terms of the magnetic flux signal $\delta\Phi$. As with the current sensor, we can express the frequency perturbation as

$$\delta x = -\frac{\delta\omega_r}{\omega_r} = \frac{1}{2}\frac{\delta L}{L}, \tag{6.7}$$

where we are careful to note that $\omega_r = \sqrt{2/LC}$ in this case, as the two inductance branches are in parallel. If the kinetic inductance fraction for each branch is α, then we have

$$\delta x = \frac{\alpha}{2}\frac{\delta L_k}{L_k}. \tag{6.8}$$

Then, as in Eq. (2.71), we have

$$\delta x = \frac{\alpha L_k I^2}{4N_0\,\Delta_0^2\,V}, \tag{6.9}$$

where, again, all of the quantities pertain to a single inductive branch of the two in the resonator.

The current can be found from the relation [86]

$$\Phi + \mu_0 \lambda^2 \oint \mathbf{J} \cdot \mathrm{d}\mathbf{s} = n\Phi_0, \tag{6.10}$$

where the integral is over a path encircling the loop of the device. Here, λ is the penetration depth and not the Pearl length. The quantity on the right-hand side, first discussed by London [83], is known as the fluxoid, and is quantized in units of the magnetic flux quantum Φ_0. It is easy to see that the left-hand side of Eq. (6.10) is zero when the integration path encloses no hole. Thus, the integration path may be deformed such that it is further than λ away from the perimeter of the hole. If this can be done throughout the entire integration path, then the integral is zero because the current density is zero away from the hole. In that case, the flux is equal to the fluxoid, which gives rise to the popular notion of "flux" quantization. However, in our case we assume that the nanowires are narrower than the penetration depth. Since the path must go through the nanowires, they give a finite contribution to the integral:

$$\oint \mathbf{J} \cdot \mathrm{d}\mathbf{s} = 2l \, \frac{I}{wt}, \tag{6.11}$$

where l and w are the length and width of the nanowire, t is the thickness of the film, and the factor of two is due to the fact that there are two nanowires. We have assumed as usual that the current density is uniform within the nanowire. Combining the above two equations, we find the relationship between the external flux and the current:

$$\Phi + 2L_k I = n\Phi_0. \tag{6.12}$$

Now we let $\Phi = \Phi_b + \delta\Phi$, with Φ_b being the bias and $\delta\Phi$ being the signal. Then we can write the frequency perturbation in terms of the external flux,

$$\delta x = \frac{\alpha(n\Phi_0 - \Phi_b)^2}{16 N_0 \, \Delta_0^2 \, V L_k} - \frac{\alpha(n\Phi_0 - \Phi_b)\, \delta\Phi}{8 N_0 \, \Delta_0^2 \, V L_k}. \tag{6.13}$$

The fractional frequency responsivity to the magnetic flux signal is

$$R_x = \frac{\mathrm{d}x}{\mathrm{d}\Phi} = \frac{\alpha(\Phi_b - n\Phi_0)}{8 N_0 \, \Delta_0^2 \, V L_k}. \tag{6.14}$$

We see that the resonance is most sensitive to fluctuations in the external magnetic flux when the kinetic inductance fraction of each branch is high, the pairing energy is low, and the volume of the kinetic inductors is low. Although the kinetic inductance L_k appears in the denominator, since α appears in the numerator it is still important

to have a high kinetic inductance for each branch. Thus, following the same logic as for the lumped-element current sensor KPUP, it makes sense to use titanium nitride nanowires as the kinetic inductors. We also note that it is important for the external bias flux Φ_b to be far from the fluxoid $n\Phi_0$. We can now finally write the resonator response in terms of the external flux perturbation:

$$\delta S_{21}(\omega;\nu) = \mathrm{j}\frac{\alpha(\Phi_b - n\Phi_0)}{8N_0\,\Delta_0^2\,VL_k}\,\chi_c\chi_g(\omega)\,e^{-\mathrm{j}2\phi_g(\omega)}\,\zeta(\omega;\nu)\,\delta\Phi(\nu) \tag{6.15}$$

$$+\,\mathrm{j}\frac{Q_i}{2}\chi_c\chi_g(\omega)\,e^{-\mathrm{j}2\phi_g(\omega)}\,\zeta(\omega;\nu)\,\delta x_{\mathrm{TLS}}(\nu) + \delta S_a(\nu). \tag{6.16}$$

We now proceed to estimate the flux noise for this device. As we did with the current sensor, we make a number of assumptions to simplify the calculation. With adiabatic perturbations and zero detuning from the resonance, we have $\chi_g \to 1$, $\phi_g \to 0$, and $\zeta \to 1$. We also choose $n = 0$ so that $\Phi_b = -2L_kI_b$, where I_b is the effective bias current induced by the flux. Then we can write

$$\delta S_{21}(\nu) = -\mathrm{j}\frac{\alpha\chi_cQ_iI_b}{8N_0\,\Delta_0^2\,V}\,\delta\Phi(\nu) + \mathrm{j}\frac{\chi_cQ_i}{2}\,\delta x_{\mathrm{TLS}}(\nu) + \delta S_a(\nu). \tag{6.17}$$

Using this equation, we can define an estimator for converting fluctuations in the phase of the transmission into estimates for changes in external magnetic flux:

$$\delta\hat{\Phi}(\nu) = \frac{\partial\Phi}{\partial\mathrm{Im}S_{21}}\,\delta\mathrm{Im}S_{21}(\nu). \tag{6.18}$$

Recalling that $\delta S_a = \delta I_a + \mathrm{j}\,\delta Q_a$, we have

$$\delta\hat{\Phi}(\nu) = \delta\Phi(\nu) + \frac{4N_0\,\Delta_0^2\,V}{\alpha I_b}\,\delta x_{\mathrm{TLS}}(\nu) + \frac{8N_0\,\Delta_0^2\,V}{\alpha\chi_cQ_iI_b}\,\delta Q_a(\nu). \tag{6.19}$$

Then the flux noise level for the system can be calculated by taking the spectral density of the last two fluctuation terms:

$$S_\Phi = \left(\frac{4N_0\,\Delta_0^2\,V}{\alpha I_b}\right)^2 S_{\mathrm{TLS}} + \left(\frac{8N_0\,\Delta_0^2\,V}{\alpha\chi_cQ_iI_b}\right)^2 \frac{k_BT_a}{2P_g}. \tag{6.20}$$

We can now estimate the noise for a typical device. Following the procedure of Sec. 2.3, the above expression becomes

$$S_\Phi = \left(\frac{4N_0\,\Delta_0^2\,V}{\alpha I_b}\right)^2 \left(S_{\mathrm{TLS}} + \frac{k_BT_a}{4a_{\mathrm{bif}}\,\omega_rE_*}\right). \tag{6.21}$$

We may estimate E_* as the pairing energy $E_p = 2N_0\,\Delta_0^2\,V$. The total volume of a pair of TiN nanowire kinetic inductors can be taken as $V = 0.001\,\mu\text{m}^3$; then we get $E_* \approx 0.6\,\text{aJ}$. Then, with $\omega_r/2\pi = 5\,\text{GHz}$ and $T_a = 5\,\text{K}$ as the resonator frequency and amplifier noise temperature respectively, the added noise of the amplifier is approximately $10^{-15}\,\text{Hz}^{-1}$, dominating over the TLS noise $S_{\text{TLS}} \leq 2\times10^{-21}\,\text{Hz}^{-1}$. We take $\alpha = 0.75$ as a reasonable value for the kinetic inductance fraction of each branch, and set the bias as $I_b = 10\,\mu\text{A}$. Then we have

$$S_\Phi^{1/2} \approx 1\,\frac{\mu\Phi_0}{\sqrt{\text{Hz}}}. \tag{6.22}$$

That is to say, we may be able to detect magnetic flux signals as low as 10^{-6} of the flux quantum in a bandwidth of 1 Hz. If demonstrated, this would make this version of the KPUP competitive with SQUIDs as a magnetometer.

Quantum-limited noise in the bifurcation regime

As was discussed for the previous two resonator devices above, it is anticipated that the magnetometer KPUP should be able to achieve quantum-limited noise by operating in the strongly nonlinear regime. We begin to show this by defining the noise energy density as is done in the SQUID literature [159],

$$S_\epsilon = \frac{S_\Phi}{2L}, \tag{6.23}$$

where L is the total inductance of the resonator. Taking $E_* \approx E_p = 2N_0\,\Delta_0^2\,V$ and ignoring the TLS noise as we did above, we then get

$$S_\epsilon \approx \frac{1}{a_{\text{bif}}}\left(\frac{1}{\alpha}\right)\left(\frac{E_p}{L_k I_b^2}\right)\left(\frac{k_B T_a}{\hbar\omega_r}\right)\times\frac{\hbar}{2}. \tag{6.24}$$

As discussed for the previous devices, the factors in parentheses are all greater than unity. In this case, the prefactor $1/a_{\text{bif}} = 9/4\sqrt{3} \approx 1.3$ is also greater than unity, so it appears that it will be slightly more difficult to reach the quantum limit for this device. However, it may still be possible in future experiments by operating in the bifurcation regime with $a > a_{\text{bif}}$. Experimentally, operating on the steep left side of the nonlinear resonance gives a very large transfer function which would lead to a very small noise. It would seem from Eq. (6.24) that the noise energy could then be arbitrarily small, which is not physically possible. Thus, a theory of the noise including quantum effects and the nonlinear behavior of the resonance is needed in order to show how to reach the proper quantum limit, and presents an interesting direction for future research.

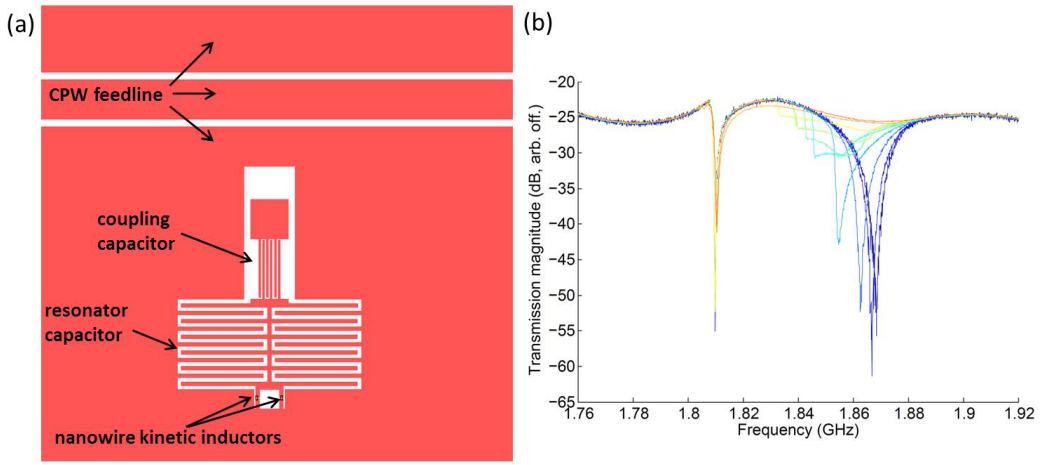

Figure 6.2: (a) Preliminary magnetic field sensor device. It has the same design as preliminary lumped-element KPUP of Fig. 3.1, except that there are two nanowires in parallel. They form a square loop that serves as the detection loop for external magnetic flux. (b) Sweep of readout power in a transmission measurement on the preliminary device. The readout power was swept from a nominal −97 dBm (dark blue) to −76 dBm (red). The lower-frequency resonance does not appear to shift.

Preliminary measurements

The preliminary magnetic field sensor device was the same as the preliminary current sensor device discussed in Sec. 3.1, except that there were two nanowire inductors in parallel. The parallel geometry formed a square loop of which each side had a length of 100 µm. This loop was intended to serve as a detection loop for external magnetic flux. Part of the layout for this device is shown in Fig. 6.2(a). The device was cooled to 20 mK in a dilution refrigerator, and the feedline was probed with a vector network analyzer. A power sweep measurement was done on the resonance at 1.87 GHz, shown in Fig. 6.2(b). The nominal readout power was swept using the network analyzer from −97 dBm to −76 dBm. There are two resonances in the measured frequency range. The lower-frequency resonance does not appear to shift, suggesting that it is spurious. The higher-frequency resonance displays behavior characteristic of a Duffing oscillator, which is expected due to the kinetic inductance nonlinearity. However, the resonance appears to be distorted at higher values of the readout power. In addition, the depth of the resonance seems to decrease drastically with increasing readout power. This is unexpected, because the change in the surface impedance should be purely reactive, and there should be no additional dissipation relative to the low-power resonance. It is likely that, if the resonance depth did not change, the two resonances would couple at higher readout

powers, similar to the two resonances examined in Sec. 3.1. As it is, the power in the resonator is too low when it is close to the other resonance in frequency space in order for them to couple.

We attempted to measure the magnetic field response of this resonator as well. A Helmholtz coil was arranged such that the chip was roughly in its center. The current through the coil was increased, and the resonance was monitored on the vector network analyzer. However, the device did not respond as expected. While the resonance did appear to shift in response to the magnetic field from the Helmholtz coil, the shifts were fractions of a linewidth, when several linewidths were expected. The resonance shift also exhibited a transient effect. Immediately after the coil current was increased, a large shift was observed, but the resonance relaxed to a frequency very close to its original frequency on a time scale on the order of $\sim$1 s. It is likely that this issue was caused by an additional current loop in the geometry. It is clear from Fig. 6.2(a) that, in addition to the loop between the two inductors, there is another loop going around the hole in the ground plane where the resonator is situated. A screening current was probably induced in this larger loop in response to the magnetic field. In the inductors, this current has opposite polarity to the current from the intended detection loop, and thus cancels it out. The result is a very small frequency shift. It is also likely that this outer current loop was responsible for the apparent dissipation from the power sweep measurement. The RF magnetic field induced from the microwave power in the resonator could have coupled to the outer loop and induced an RF current along the hole in the ground plane. Thus, power was lost from the resonance, and the apparent quality factor was reduced. Thus, it was necessary to redesign the chip and remove potential current loops.

Design

The first step for the new design of the magnetic-field sensor KPUP chip was to redesign the feedline. The feedline in the preliminary device had not had a characteristic impedance of 50 Ω, and the resulting reflections had caused ripples in the transmission data. For the new chip we wanted to design a feedline that would be 50 Ω. In addition, a primary concern for the new chip was to eliminate extra loops that could pick up external magnetic fields. The reason why there was an extra loop in the previous chip was that the resonator was situated in a hole in the ground plane. One way to couple a resonator to the feedline without making a hole in the ground plane is to put the resonator between the center conductor and one of the ground planes. This type of design has several advantages over the usual

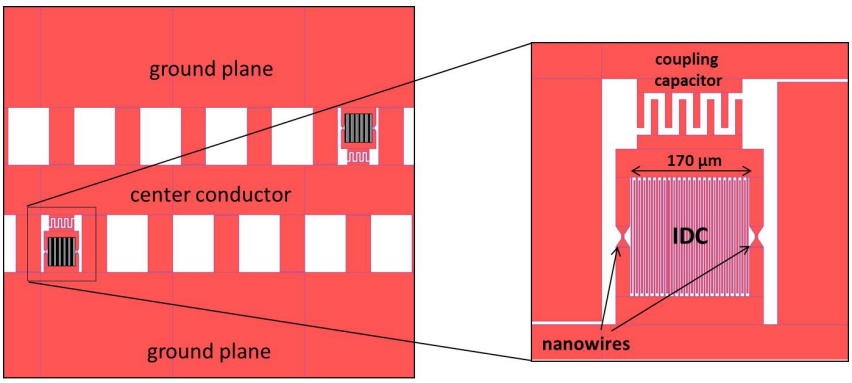

Figure 6.3: Part of layout of magnetic-field sensor KPUP chip. The feedline is still a CPW, but now has a zipper structure. The resonators are placed between the center conductor and the ground planes in an alternating pattern. There are eight resonators per chip. (Inset) Layout of one of the resonators. The resonator is a square loop with interdigitated capacitor in the interior of the loop. Each side of the square is 170 µm long. The bottom of the resonator is monolithically connected to the ground plane, and the top is connected to the center conductor through a coupling capacitor. The other two sides of the loop contain nanowire kinetic inductors.

approach. Usually, the resonator is coupled to the center conductor of the feedline via a coupling capacitor. In most cases, including in the preliminary device, the top electrode of the capacitor has to be wire bonded to the center conductor. However, if the resonator is placed between the center conductor and the ground plane, the top electrode of the coupling capacitor can be monolithically connected to the center conductor. In addition, the bottom of the resonator, which must be grounded, can be monolithically connected to the ground plane. Thus, we eliminate the need for wire bonds while maintaining a single-layer, planar geometry.

Since the resonator had to fit between the center conductor and the ground plane, the gap had to be quite large. In order to achieve a characteristic impedance of 50 Ω for the feedline, a zipper structure was used, as it would increase the capacitance per unit length of the feedline. There are zipper-like "teeth" alternating between the center conductor and each ground plane. The teeth from the center conductor come to a distance of 5 µm from the ground plane, and vice versa. The width of the center conductor is 800 µm. The width of each tooth is 150 µm, and the length is 345 µm. This design is shown in Fig. 6.3.

The resonator was designed to have a square loop, as before. However, for this version of the device, the capacitor of the resonator was interdigitated within the loop itself. This design is more compact, and exactly resembles the schematic of

Fig. 6.1. The fingers of the capacitors do not screen the magnetic field, as the field penetration depth is expected to be much greater than the thickness of the film. We chose the film thickness to be 10 nm, and the material to be titanium nitride. Using the corresponding $T_c = 3$ K and the equation

$$L_s = \frac{\hbar \rho_n}{\pi \Delta_0 t}, \tag{6.25}$$

we get $L_s = 46\,\mathrm{pH}/\square$. Then the penetration depth

$$\lambda = \sqrt{\frac{L_s t}{\mu_0}} \tag{6.26}$$

is approximately 600 nm, which is indeed much greater than the film thickness.

There is a nanowire kinetic inductor on either side of the interdigitated capacitor. The length of each side of the loop was chosen to be 170 µm. The capacitor finger width and spacing were chosen to both be 1.8 µm. Then, using the formula

$$C = \frac{A}{4W} \epsilon_0 (\epsilon_r + 1) \tag{6.27}$$

from Sec. 2.3, the capacitance of the resonator is approximately 0.46 pF. This capacitor design was simulated using Sonnet [186], and the value for the capacitance was found to be 0.45 pF, so the simulation agrees with the approximate analytical formula.

There are eight resonators on the chip. The resonators are arranged in an alternating pattern, with resonators adjacent in frequency space in contact with opposite ground planes. This was done in order to reduce the potential for crosstalk between the resonators [192]. Each resonator had the same capacitance, but a different resonance frequency was desired for each, so the nanowire kinetic inductors were designed to be different. The nanowires were all designed to be 150 nm wide, and their lengths increased linearly from 1 to 8 µm. The corresponding inductances of the individual nanowires increased linearly from 0.3 nH to 2.4 nH. Assuming a kinetic inductance fraction of 0.75, the design values for the resonance frequencies

$$f_r = \frac{1}{2\pi} \sqrt{\frac{2\alpha}{L_k C}} \tag{6.28}$$

ranged from 5.4 GHz to 10.6 GHz, where we have also included the contribution of the sections that taper to either end of the nanowire to the total kinetic inductance.

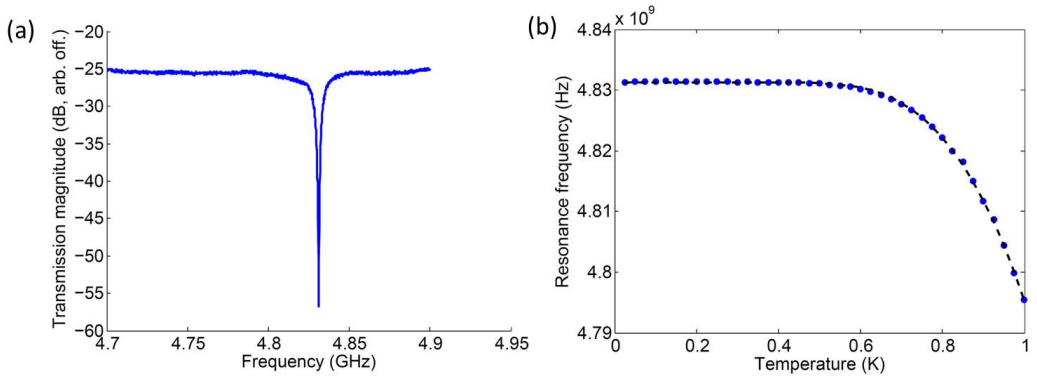

Figure 6.4: (a) Transmission through feedline of magnetic-field sensor KPUP chip, showing lowest-frequency resonance at 4.381 GHz. The uncorrected data shows a symmetric resonance with no significant ripple in the transmission. (b) Temperature sweep measurement for magnetic-field sensor KPUP. The resonance frequency of the lowest-frequency resonance was monitored with a vector network analyzer as the temperature was swept down from 1 K to 20 mK. Data (blue dots) and best-fit curve (dashed line) are shown.

Temperature response

The chips were fabricated to specifications, and then one was installed in a dilution refrigerator. It was cooled to a temperature of 20 mK, and the transmission through the feedline was measured using a vector network analyzer. All eight resonances were observed, though there were several extra resonances as well. The resonance frequencies of the resonators were somewhat lower than the design values, and ranged from 4.8 GHz to 9.1 GHz. It is likely that we overestimated the kinetic inductance fraction for this design. Since it is a loop, the magnetic inductance may be significant. Assuming this is the reason for the discrepancy, the true kinetic inductance fraction should be $\alpha \approx 0.6$.

The lowest frequency resonance occurred at 4.831 GHz. The transmission data, shown in Fig. 6.4(a), shows that the resonance is quite symmetric and that the transmission has no significant ripple even without correction. The zipper-like CPW feedline design appears to have reduced reflections.

In order to find the critical temperature of this film, the temperature of the dilution refrigerator was swept, and the resonance frequency of the lowest-frequency resonator was monitored using the vector network analyzer. A nominal readout power of −96 dBm was used throughout the measurement. The temperature was swept down from 1 K to 20 mK, in steps of 25 mK. The data from the measurement is shown in Fig. 6.4(b). The quasiparticles generated by thermal fluctuations at higher

temperatures caused the resonance frequency to shift according to

$$\frac{\delta f_r}{f_r} \propto -e^{-\Delta_0/k_B T}, \tag{6.29}$$

as discussed in Sec. 3.2. The fit to the data, shown in the plot, shows that the critical temperature $T_c = \Delta_0/1.76\,k_B$ was 3.11 K.

Magnetic field response

In order to measure the magnetic field response of the KPUP, we constructed a Helmholtz coil by winding superconducting wire around an aluminum frame. The coil was installed in the dilution refrigerator around the device, such that the device was approximately in the center of the coil, and such that the field produced by the coil would be normal to the plane of the device. The magnetic field provided by the coil was approximately $2.4\,\mu\mathrm{T/mA}$. A separate pair of wires ran out of the refrigerator in order to send a current through the coil. The setup was cooled to a temperature of 20 mK, and the transmission was measured using a vector network analyzer. A nominal power of −86 dBm was applied to the feedline. A DC voltage source along with a 6.5-kΩ resistor was used to supply the current to the Helmholtz coil. The voltage was swept, and all of the resonances were measured. All eight of the resonators showed a strong response to the magnetic field. The data from the resonator with the strongest response is shown in Fig. 6.5. The unperturbed resonance frequency of this resonator was 6.386 GHz. The resonance shifts downward in frequency with increasing magnetic field, as expected. However, when the field reaches a certain value, the resonance frequency jumps back to 6.386 GHz and begins shifting downward from that point again as the magnetic field continues increasing. This happens again with a regular periodicity of about 1.12 μT. Within each period, the data appears to follow a quartic trajectory, similar to the other devices we have discussed. The data from the first period for this resonator was fit to the function

$$\frac{\delta f_r}{f_r} = -\frac{B^2}{B_2^2} - \frac{B^4}{B_4^4}. \tag{6.30}$$

The quartic function agreed very well with the data, with fit parameters $B_2 = 3.44\,\mu\mathrm{T}$ and $B_4 = 2.16\,\mu\mathrm{T}$.

The probable explanation for the periodicity is that, at a certain point, the current flowing through the loop surpasses the critical current of one (or both, if they are truly identical) of the nanowires. At that point the nanowire stops superconducting,

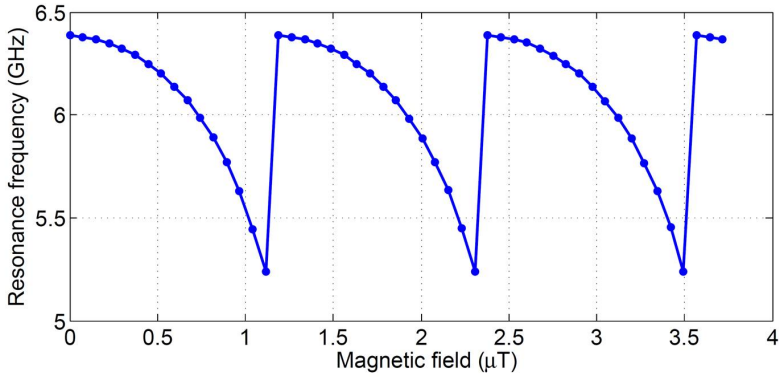

Figure 6.5: Measurement of magnetic-field response of KPUP device. Data from the resonator with the strongest response is shown. The response is quadratic with increasing magnetic field, until the current goes back to zero. The period for this sudden change is approximately 1.12 μT.

so the supercurrent can no longer flow along the loop of the resonator. The induced current then abruptly returns to zero, and thus the resonance frequency returns to its unperturbed value, as seen in Fig. 6.5. Although the current is zero, there is still a finite applied flux, and the fluxoid quantization condition (Eq. (6.10)) must still be satisfied. Thus, at this point the fluxoid increases by a finite integer number of flux quanta. For this device, the number is $n = 16$. Then, as the applied flux is increased further, the fluxoid remains constant and the induced current increases from zero up until it equals the critical current again, at which point the fluxoid increases by $n = 16$ once more. Thus, the response of the device is periodic in the applied flux, with a period of $16\Phi_0$. The critical current corresponding to the period of 16 flux quanta is $I_c = 9.74\,\mu\text{A}$. It is unclear why the critical current is less than that of the nanowire in the lumped-element current sensor, but it is of similar order of magnitude. Out of the eight resonators, this one had the greatest critical current, which is expected because it had the strongest magnetic field response. However, the critical currents of all eight resonators were in the range ~8–10 μA. It was expected that they be similar, because all of the nanowires nominally have the same cross-sectional dimensions.

The resonance frequency of the 6.386-GHz resonance shifted by over one gigahertz in a single period. The maximum frequency shift corresponds to a fractional frequency shift of 18%. Such a strong magnetic field response suggests that this resonator could be useful as a magnetic field sensor. From the fit to the field response, the device responsivity is $\mathrm{d}f/\mathrm{d}B = 2.25\,\text{GHz}/\mu\text{T}$ and the resonance frequency is

$f = 5.553\,\mathrm{GHz}$ at a bias of $B = 1\,\mu\mathrm{T}$. We may use this to estimate the noise in magnetic field units:

$$S_B = \left(\frac{1}{f}\frac{\mathrm{d}f}{\mathrm{d}B}\right)^{-2} \frac{k_B T_a}{8Q^2 P}. \tag{6.31}$$

This device has $Q \approx 375$, and a carrier power of $P \approx 2.5\,\mathrm{pW}$ was used. Assuming an amplifier noise temperature $T = 5\,\mathrm{K}$, we get $S_B^{1/2} = 12\,\mathrm{fT}/\sqrt{\mathrm{Hz}}$. In units of magnetic flux, this is equivalent to $S_\Phi^{1/2} = 0.17\,\mu\Phi_0/\sqrt{\mathrm{Hz}}$. If this sensitivity is demonstrated, the KPUP would similarly sensitive to state-of-the-art SQUIDs, while having the advantage of being easy to multiplex. We attempted to measure the noise, but a good noise level was not achieved. The lowest noise observed was $\sim 10\,\mu\Phi_0/\sqrt{\mathrm{Hz}}$. This measurement was taken with the device inside a normal metal shield. The noise measurement could likely be improved if a superconducting shield is used.

6.2 Resonant parametric amplifier

Background

Efforts to use nonlinearities in physical systems for amplification date back to the 19th century [194]. Interest in electronic amplifiers surged in the 1950s, when the development of varactors allowed for parametric amplifiers to be constructed in the microwave and millimeter-wave bands [195]. The capacitance of a varactor can vary based on an applied voltage. If a "pump" tone is applied to the capacitance, and a weaker signal tone is also applied to the circuit, four-wave mixing may occur and power may be transferred from the pump to the signal, achieving amplification. The process of four-wave mixing was described in Sec. 2.4 and will not be repeated here. Although it was described in the context of traveling-wave devices, four-wave mixing can occur just as easily in standing-wave devices, as well as in diodes such as in the varactor circuits. Because the process relies on a nonlinear reactance, in principle a parametric amplifier need not produce excess thermal or shot noise. In fact, the noise performance of a parametric amplifier can be limited solely by quantum fluctuations [196]. However, varactor-based amplifiers did have excess noise in practice, and were eventually out-performed by cryogenic transistor amplifiers such as HEMT and bipolar silicon-germanium (SiGe) transistor amplifiers [197]. These amplifiers are now standard for many microwave applications, and have noise temperatures dropping below 1 K/GHz. However, this noise performance is much higher than the quantum limit of $h/k_B \approx 48\,\mathrm{mK/GHz}$, and is inadequate for some applications. There is currently increasing interest for low-noise microwave amplifiers for applications such as quantum information [198].

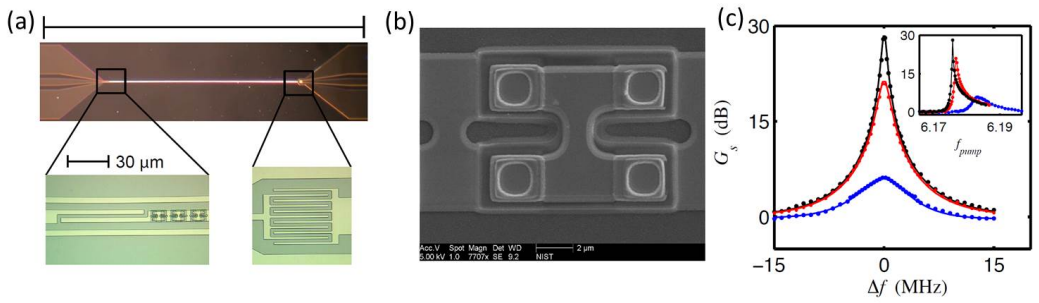

Figure 6.6: Standing-wave Josephson parametric amplifier developed at NIST [199]. (a) The device consists of a 5-mm-long transmission line interrupted periodically by Josephson junctions. The zoomed-in images below show the input and output coupling capacitors, which serve as end nodes of the standing wave on the line. (b) Scanning-electron micrograph of the Josephson junctions. They are placed in a SQUID (i.e., a loop) geometry so that their inductance may be tuned by application of an external magnetic field. (c) Measured gain of the device. The gain-bandwidth product is about 40 MHz. Figure reprinted from [200].

The first superconducting parametric amplifier was proposed in 1963 [201] after early measurements of the nonlinear kinetic inductance of superconducting indium [202]. These early proposed parametric amplifiers were standing-wave transmission-line devices [203]. The first such device was demonstrated in 1964 by Clorfeine [204], who achieved 11 dB of gain at 6 GHz with a gain-bandwidth product of 1 MHz, using a thin film of superconducting tin. It was conjectured [205] that the result was actually due to the nonlinearity from naturally-occurring Josephson junctions in the film. Since then, intentionally-fabricated Josephson junctions have been found to reliably exhibit parametric gain with nearly quantum-limited noise performance and better gain-bandwidth products than Clorfeine's result [206–208]. Standing-wave transmission line Josephson parametric amplifiers have also been developed [199]. In a recent device developed at NIST (Fig. 6.6), a series-array of Josephson junctions is distributed along a transmission line in order to create a nonlinear medium where four-wave mixing can occur. The noise performance of this device approaches the quantum limit as well. In addition, when operated in the degenerate mode with pump and signal frequencies coinciding, the device only amplifies the quadrature component that is in phase with the pump, thus having noise even lower than the standard quantum limit for this quadrature.

In recent years, attention has returned to superconducting parametric amplifiers utilizing the nonlinearity of the kinetic inductance. In 2007, Thólen et al. [183] demonstrated niobium CPW microresonators that exhibited parametric gain of 22.4 dB at

3 GHz and 6 GHz. These were very narrow-band devices, with resonator linewidths of several kilohertz. Then, in 2012, Eom et al. demonstrated a traveling-wave kinetic inductance parametric amplifier with nearly quantum-limited noise and with a bandwidth of 8–14 GHz [174]. This device was described in Sec. 2.4, and the details will not be repeated here. This amplifier has a modest gain of ∼10 dB. For applications at a defined, narrow band requiring higher gain and low-noise performance, it may be advantageous to use a resonant parametric amplifier based on the kinetic inductance nonlinearity. The effective path length for such a device can be much larger than what can be practically achieved in an on-chip traveling-wave device, resulting in higher parametric gain.

Preliminary measurements

Our first TiN nanowire resonators, described in Sec. 3.1, were also used for preliminary measurements of parametric gain. The experiment was very similar to the experiment shown in Fig. 3.3; the experimental setup is the same. The device was cooled in a dilution refrigerator, and the transmission through the feedline was monitored with a vector network analyzer. The resonance that was probed in this case was at 1.9 GHz. A pump tone was applied close to the resonance frequency. In the pump-probe experiment, the pump tone was applied higher than the frequency of the resonance. Power coupled into the resonance, and it shifted further from the frequency of the pump tone. Here, we apply the pump tone below the frequency of the resonance. As power couples into the resonator, it shifts downward in frequency, and its resonance frequency approaches the frequency of the pump tone. This allows the pump tone to couple additional power into the resonator, driving the process of four-wave mixing in the nonlinear kinetic inductor. The pump power amplifies the readout frequencies from the network analyzer. The resulting power couples out of the resonator and is seen as a peak in the transmission through the feedline. As the readout frequency is swept, the gain profile is mapped out in frequency.

The frequency and power of the pump tone were swept in order to characterize the parametric gain of this resonator. The highest gain observed is shown in Fig. 6.7(a). The pump tone was applied at 1.879 GHz, with a nominal power of −86.3 dBm. The device provided parametric gain of about 35 dB over a −3-dB bandwidth of about 150 kHz. Fig. 6.7(b) shows a gain peak with one of the largest bandwidths observed for this resonator. The pump tone was applied at 1.8732 GHz, with a nominal power of −88.7 dBm. The observed gain peak had a height of about 18 dB, with a −3-dB bandwidth of about 2 MHz.

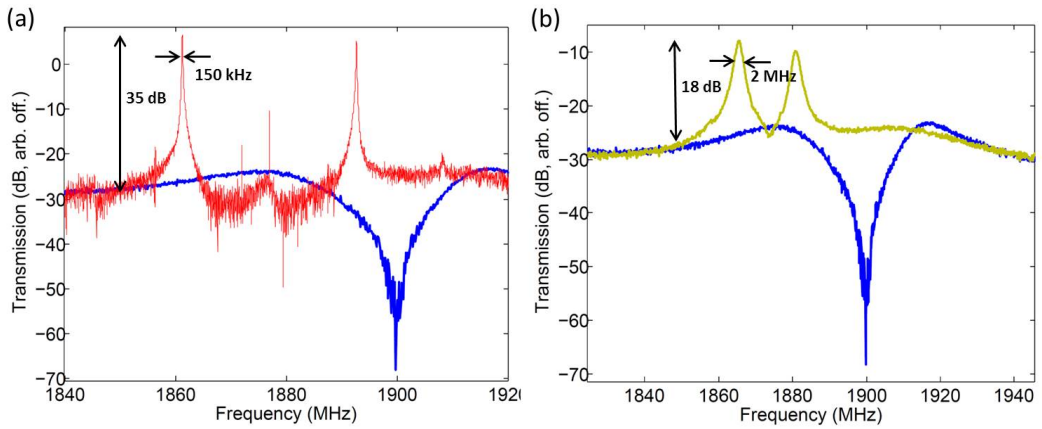

Figure 6.7: (a) Transmission measurement of nanowire resonator chip. The blue curve is with pump off, and the red curve is with pump on. A pump tone at a frequency of 1.879 GHz and nominal power of −86.3 dBm is applied to the feedline. Parametric gain of about 35 dB over a −3-dB bandwidth of approximately 150 kHz is observed. (b) Transmission with pump tone at 1.8732 GHz and with a nominal power of −88.7 dBm. The blue curve shows the transmission with pump off. Parametric gain of about 18 dB over a −3-dB bandwidth of approximately 2 MHz is observed.

Design

A new device was designed to perform specifically as a resonant parametric amplifier. However, since good values of gain were achieved with the preliminary device, minimal changes were made. The primary change was the use of shorter nanowires, because this would reduce the inductance of the resonator and thus increase the resonance frequency. Another group at Caltech was interested in possibly using a resonant parametric amplifier operating at about 6 GHz, so we designed the new devices for that frequency range. A 10-nm-thick film of titanium nitride was to be used as the device layer. The chip consisted of an array of eight lumped-element resonators. Each resonator was coupled to a CPW feedline through a coupling capacitor. The capacitance of each resonator was the same, and was designed to be about 0.6 pF. The inductors were nanowires with a common width of 50 nm and lengths ranging from 390 to 620 nm. Just like with the lumped-element current sensor device, the nanowires were designed with curved ends in order to reduce current crowding. The resulting estimates for the inductances ranged from 0.35 to 0.56 nH. The resonance frequencies were designed to be between 6.15 and 7.75 GHz. The resonators were arranged in an alternating pattern in frequency space in order to reduce crosstalk.

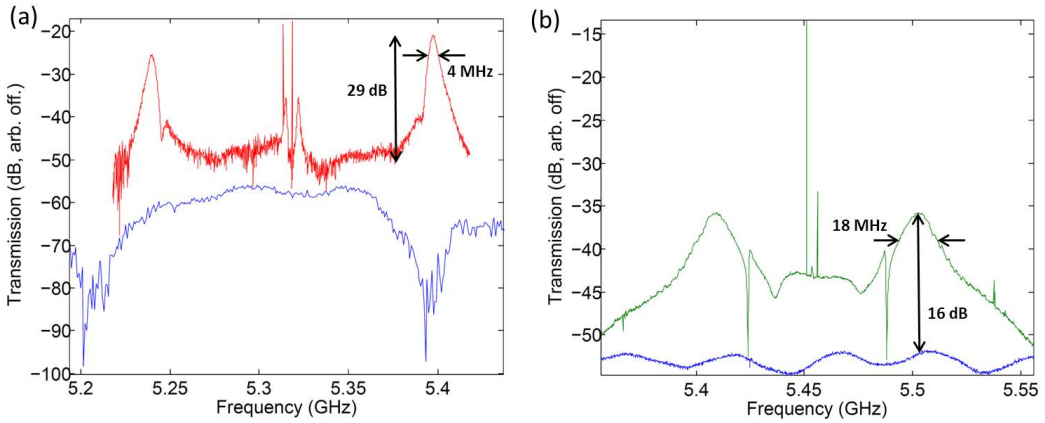

Figure 6.8: (a) Transmission through feedline of parametric amplifier chip. The blue curve shows transmission with pump off, and the red curve is with pump on. The resonance probed is at 5.393 GHz. The pump is applied at 5.318 GHz. Parametric gain of about 29 dB is observed over a −3-dB bandwidth of about 4 MHz. (b) A different resonance. The blue curve is with pump off, and the green curve is with pump on. The pump is applied at 5.546 GHz. The observed parametric gain is 16 dB over a −3-dB bandwidth of 18 MHz.

Measurements

The devices were fabricated and a chip was installed in a dilution refrigerator. The refrigerator was cooled down, and the transmission through the feedline was measured using a vector network analyzer. The resonance frequencies were somewhat smaller than the design values. This is probably because the kinetic inductance of the tapered sections on either end of the nanowires was not considered in the design. It is also possible that the kinetic inductance fraction is lower than expected, and the resonators have higher magnetic inductance.

Parametric gain was measured for each resonance by applying a pump tone at a frequency slightly below the resonance frequency, and sweeping its power and frequency. The highest gain observed with this chip is shown in Fig. 6.8(a). Gain of about 29 dB was observed over a −3-dB bandwidth of 4 MHz. This gain is less than the highest gain of the preliminary device, but the bandwidth is even greater than the highest bandwidth found on the preliminary device. The gain-bandwidth product for this mode is approximately 3 GHz, whereas the gain-bandwidth product for the highest-gain mode in the preliminary device was approximately 0.5 GHz. In Fig. 6.8(b), the mode with the highest bandwidth is shown. Gain of about 16 dB was observed over a −3-dB bandwidth of about 18 MHz. The gain-bandwidth product of this mode is approximately 0.7 GHz.

The added noise of the second mode was measured. Along with the pump tone, another microwave source was used to send a weaker signal tone at 5.502 GHz, corresponding to the peak of the gain profile. The power output from the feedline was measured using a spectrum analyzer at room temperature. The noise level was measured in a narrow band around the signal frequency, with the pump on and off. These noise levels were compared to each other in order to determine the added noise of the parametric amplifier. The added noise was measured to be approximately 0.8 microwave photons. In order to perform this measurement, two 50-Ω resistor terminations were used: one at the mixing chamber of the dilution refrigerator, and one at the 4-K stage. A cold switch was used at the HEMT input in order to switch between the mixing-chamber resistor, 4-K resistor, and the device. When the HEMT input was connected to the resistor at the mixing chamber, the noise power spectrum was measured:

$$[(T_{\mathrm{MC}} + T_H)\, G_H + n_R]\, G_R + n_A = P_{\mathrm{MC}}. \tag{6.32}$$

Here, T_{MC} is the noise temperature corresponding to the Johnson noise of the resistor, T_H is the HEMT noise temperature, G_H is the HEMT gain, n_R is additional noise before the room-temperature amplifier, G_R is the gain of the room-temperature amplifier, and n_A is additional noise after the room-temperature amplifier. The noise power is averaged over the flat part of its spectrum. The room-temperature gain can be absorbed into the HEMT gain as $G'_H = G_H G_R$, and the additional noise can be combined as $n'_A = n_R G_R + n_A$, so that we have the simplified expression

$$(T_{\mathrm{MC}} + T_H) G'_H + n'_A = P_{\mathrm{MC}}. \tag{6.33}$$

The noise is also measured with the 4-K resistor connected, and then it is measured with the device connected, first with the pump off and then with the pump on:

$$(T_{\mathrm{4K}} + T_H)\, G'_H + n'_A = P_{\mathrm{4K}} \tag{6.34}$$

$$(T_{\mathrm{off}} + T_H)\, G'_H + n'_A = P_{\mathrm{off}} \tag{6.35}$$

$$(T_{\mathrm{on}} G_p + T_H)\, G'_H + n'_A = P_{\mathrm{on}}, \tag{6.36}$$

where G_p is the gain of the parametric amplifier, a measured quantity. Then Eq. (6.33) is subtracted from Eq. (6.34), and Eq. (6.35) is subtracted from Eq. (6.36):

$$(T_{\mathrm{4K}} - T_{\mathrm{MC}})\, G'_H = P_{\mathrm{4K}} - P_{\mathrm{MC}} \tag{6.37}$$

$$(T_{\mathrm{on}} G_p - T_{\mathrm{off}})\, G'_H = P_{\mathrm{on}} - P_{\mathrm{off}}. \tag{6.38}$$

Finally, Eq. (6.37) is divided by Eq. (6.38) to obtain the noise temperature of the device:

$$T_{\text{on}} = \frac{1}{G_p}\left[T_{\text{off}} + \frac{P_{\text{on}} - P_{\text{off}}}{P_{\text{4K}} - P_{\text{MC}}}(T_{\text{4K}} - T_{\text{MC}})\right]. \tag{6.39}$$

Since T_{off} is not a known quantity, it is assumed that it is equal to T_{MC}, because the device is not expected to add any noise when the pump tone is off.

A truly quantum-limited amplifier has an added noise of half a photon [209], as the vacuum energy is $\hbar\omega/2$. Thus, this parametric amplifier is close to being quantum-limited, but there is still excess noise. It is likely that the additional noise is due to imperfections in the apparatus rather than the device, given that the nonlinearity is nondissipative. The noise of 0.8 photons corresponds to an amplifier noise temperature of approximately 200 mK.

Chapter 7

CONCLUSIONS AND OUTLOOK

We have demonstrated a set of devices utilizing the nonlinearity in the kinetic inductance of a superconducting thin film. All of the devices operate in the microwave regime, where there is ample bandwidth and they can be easily integrated to work with systems used in astronomy and quantum information. Because the nonlinearity is purely reactive, all of the devices are non-dissipative, even when the nonlinearity is driven strongly.

Of the five devices we have presented, all but one can be classified as parametric upconverters. In these devices, a lower-frequency signal is converted to the microwave domain, where it can be sensitively detected using microwave electronics. The other device is a parametric amplifier, where photons from a strong pump tone mix with those from a weak signal, resulting in amplification of the signal.

All but one of the five devices are resonators, and we have shown that the resonance frequencies of such superconducting microwave resonators are quite sensitive to increased electric current in their inductive elements. In particular, the resonance frequency strongly shifts downward in response to additional current from a direct electrical connection, a perpendicular magnetic field, or increased microwave power from the feedline. The other device is a transmission line, which responds to increased electrical current by increasing its total phase length.

All but one of the devices presented consist of a single layer of superconducting thin film on a crystalline silicon substrate. This simple design paradigm results in efficient, low-cost fabrication with fewer variables. Yield has generally been high for our devices. The other device, a microstrip resonator, could in principle be re-designed as a co-planar waveguide and fabricated on a single layer as well.

While most other efforts with superconducting microwave devices have avoided working in the nonlinear regime, our devices perform best when they are highly nonlinear. For continued development of such devices, we identify a set of general design and operation considerations, based on the work in this thesis, in order to make sure the device performance is optimized:

- The device material should be chosen to have a high intrinsic kinetic in-

ductance fraction. The high normal-state resistivity of titanium nitride and niobium titanium nitride ensures this, and they additionally have been shown to have very low intrinsic loss.

- The superconducting condensation energy should be low. Using materials with low critical temperature ensures this. Titanium nitride is attractive because the T_c can be tuned between 0 and 5 K by controlling the film deposition parameters.

- The total kinetic inductance of the kinetic inductance element should be high. Thus, it should have a large aspect ratio. It should be much longer than it is wide with respect to the direction of current flow.

- The volume of the kinetic inductance element should be low, while allowing the aspect ratio to remain high; thus the cross-section must be small. To ensure this, the film thickness can be chosen to be as low as 10 nm.

- The magnetic inductance should be low, in order to ensure a high total kinetic inductance fraction. The device geometry should be designed such that it does not have a large magnetic inductance.

- In order to increase dynamic range and sensitivity, it is important for the device to have a large critical current. Larger cross-sectional dimensions can increase the critical current, and it is especially important to avoid sharp corners in the geometry in order to reduce crowding of the current density.

- In order to make use of the available bandwidth in the microwave regime, it is important to design devices to have a large bandwidth. Traveling-wave devices are already wide-band devices; for a resonant device, the coupling quality factor can be designed to be low.

- It is important to use a large microwave readout power in order to reduce the added noise of the readout amplifier. If a lower-noise amplifier is available, it should be used. A large microwave power also drives the parametric processes, resulting in stronger device performance.

Further, a quantum, nonlinear theory of device operation should be developed. This will provide a foundation to optimize the devices further and potentially achieve quantum-limited operation. This is discussed in the final section of this chapter. First, we present conclusions for each individual device we have discussed.

7.1 Lumped-element resonator KPUP

We demonstrated a lumped-element superconducting microresonator that showed a strong response to a DC bias current. The bias current was applied directly into the kinetic inductor through a microwave stepped-impedance filter that blocked power from leaking from the resonator. The inductor was designed to be a nanowire with curved ends, resulting in a large critical current. The resonance frequency of the device shifted downward in response to the current, and a total shift of 5% was observed. The response followed a quartic trajectory, and the reason for the quartic term is not understood. The current noise of the device was measured to be $8\,\mathrm{pA}/\sqrt{\mathrm{Hz}}$ under optimal bias conditions, which is low enough for TES readout. The device was then connected to a TES, and the bias curve of the TES was measured by using the KPUP to measure the TES current. By measuring the bias curve at several different bath temperatures, we were able to estimate the thermal conductance of the link between the TES and the bath, as well as the expected phonon noise level. The phonon noise level was too low to be seen with the KPUP, but the out-of-bandwidth noise of the TES was observed. A scheme for multiplexing an array of TESs in the frequency domain for readout with a single KPUP was developed. The TES was AC-biased, but the resulting transition in the bias curve appeared to be very narrow, and a good noise measurement was not achieved.

In principle, it should be possible to measure the TES phonon noise with this type of KPUP. In possible future measurements, the signal provided by a less-resistive TES could be large enough to be detected by the KPUP. In order to improve the AC measurement, it is necessary to improve the isolation between the TES and the KPUP bias line that is used to null the steady-state AC current in the KPUP. This can be achieved by implementing a separate input on the chip for the nulling comb, along with its own stepped-impedance filter. Another possible approach is to use a loop geometry in the KPUP and to magnetically couple both currents into the device through coupling coils.

If the phonon noise is detected with an AC-biased TES, the KPUP will be ready for use in a TES array-based instrument. Since the KPUP has a bandwidth on the order of 100 MHz, a single device could be used to multiplex a small array of TESs, following the scheme we have developed in this thesis. Then, since the KPUPs can be easily multiplexed in the microwave domain, the entire system can consist of an array of KPUPs that each read out an array of TESs. Using this two-stage multiplexing scheme, it will be possible to have very large arrays of TESs. It may

also be possible to fabricate the TESs and the KPUPs on the same substrate, making the overall system simpler.

The same paradigm can be applied to other potential KPUP applications. Detectors other than TESs can be multiplexed in the same way. The KPUP can also be operated as a magnetic field sensor by reading out the current from pickup coils rather than from detectors. If such pickup coils are multiplexed in the frequency domain, the KPUP would be useful for mapping out a large area of magnetic field data, especially when using the two-stage multiplexing paradigm described in the previous paragraph.

Due to its intrinsic ability to be multiplexed in the microwave domain, the KPUP will be a compelling alternative to the standard technology of SQUIDs. Since SQUIDs have low bandwidth and dynamic range, they are not natively suited to work with large arrays of detectors. The necessity of making Josephson junctions is also a drawback of SQUIDs, as they complicate the fabrication process and make it more expensive. The single-layer design of the KPUP thus gives it another major advantage over the SQUID. Even the additional step of electron-beam lithography to create the nanowires could be avoided in future iterations, as modern photolithography systems are capable of writing features as small as 150 nm. The lumped-element resonator KPUP has a promising future if its noise performance when reading out a TES is improved.

7.2 Transmission line KPUP

We demonstrated a long superconducting transmission line whose phase length responded strongly to a current flowing through it. Along with a microwave carrier, a bias current was applied across the ends of the CPW center conductor. The phase length changed in a quartic fashion with the magnitude of the bias current. The total inductance of the line changed by a maximum of 30%. The device had a large critical current due to its very simple geometry and moderate cross-sectional dimensions. The current noise of the device was measured to be $5\,\mathrm{pA}/\sqrt{\mathrm{Hz}}$, which suggests that the noise performance of the device is limited by the noise of the readout amplifier following it.

The noise of this device is low enough for TES readout, and if good performance with a TES is demonstrated, the device could be as promising for applications as the lumped-element resonator KPUP. The transmission line KPUP has the advantage of a larger dynamic range and bandwidth, so a single device could be used to read

out a larger number of TESs or other detectors. Although it is not as intrinsically easy to multiplex as the resonator KPUP, the transmission line KPUP can also be multiplexed in the microwave domain by putting a microwave band-pass filter at either end of the device. An array of transmission lines could be fabricated with each line having a different corresponding band-pass filter frequency. A comb of microwave carriers could be sent to the entire array, and the phase delay at each carrier frequency would be related to the current in its respective transmission line. Thus, a two-stage multiplexing scheme could be implemented with the transmission line KPUP as well.

7.3 Transmission-line resonator KPUP

A half-wavelength microstrip resonator was demonstrated that showed a strong response to a DC bias current. The bias was applied across the ends of the resonator, through a 3-pole filter designed to isolate the bias line from the microwave power in the resonator. The resonance frequency of the device shifted downward in response to the bias current, following a quartic trajectory. The maximum shift observed was 8% of the original resonance frequency. The critical current was much larger than that of the lumped-element device, and only 50% smaller than that of the transmission line. Good noise performance of this device was not achieved, even though the predicted noise performance was as good as that of the previous devices. The device was used to read out an AC-biased TES. A bias curve measurement was made, but the measurement had similar issues to the AC TES measurement with the lumped-element device. The TES phonon noise could not be seen with this device, but the out-of-bandwidth noise was observed.

Improving the AC TES measurement is a priority for all of the KPUP devices. It is not clear why the apparent resistance of the superconducting branch is higher than it should be, or why the transition appears to be so narrow. It could be related to the finite input impedance of the isolation filter for this KPUP, similar to the issue with the lumped-element device. A more careful design of the KPUP chip, possibly reducing the input impedance, could improve these measurements.

If satisfactory performance is demonstrated for this device, it could be very promising for applications involving readout of an array of detectors or magnetic field pickup coils. Because of its large critical current, this device has a larger dynamic range than the lumped-element KPUP, so it may be able to read out a larger array of detectors. Then, due to its intrinsic ability to be multiplexed as a microwave

resonator, a two-stage multiplexing scheme could be easily implemented.

7.4 Magnetic field sensor

We demonstrated a superconducting microresonator that showed a strong response to externally-applied magnetic flux. The device is a planar resonator in the shape of a loop, with two nanowires as kinetic inductors. A magnetic field bias was applied normal to the loop by using a Helmholtz coil. The resonance frequency shifted downward in response to the magnetic field. The frequency shift was periodic, and the periodicity is due to the finite nanowire critical current, along with the phenomenon of fluxoid quantization. Within each period, the frequency shift was quartic in the applied magnetic field. The maximum frequency shift observed was 18%. Although the predicted noise based on this shift was very low, a good noise measurement was not achieved. The noise measurement could be improved by using a superconducting shield.

The periodicity of the response of this device is a drawback, because it limits the dynamic range. Using a feedback network such as those used with SQUIDs is a possibility, although it complicates the overall system. For magnetic field detection, it is straightforward to use one of the current sensor devices with a pickup coil, so that type of setup could be pursued in order to develop a future KPUP magnetometer. Using a current sensor as the detector also has the advantage that, since it does not contain a loop, it is less sensitive to environmental fluctuations or the Earth's field. However, given the very strong response of the loop-based magnetic field sensor, it may still be worthwhile to continue to develop it. If the noise could be shown to be lower than that of a SQUID as predicted, the device could become very useful, and could even be used for the current-sensing applications we have discussed by utilizing an input coil.

7.5 Resonant parametric amplifier

A superconducting microwave resonator was demonstrated to exhibit parametric gain when pumped slightly below its resonance frequency. A maximum gain of 29 dB with a gain-bandwidth product of 3 GHz was observed. A gain mode with a bandwidth of 18 MHz was also observed, and the added noise for this mode was measured to be 0.8 microwave photons.

If developed further carefully, this type of device could be engineered to have higher gain or higher bandwidth. The linewidth of the resonance is related to the width of the gain profile, so a resonator with a low coupling quality factor could have

larger bandwidth as an amplifier. In addition, if the excess noise is reduced, this device would be a quantum-limited amplifier, making it potentially very attractive for applications such as readout of qubits in quantum information experiments.

The idea of the resonator parametric amplifier could be further developed as well. It may be possible to combine the processes of parametric up-conversion and parametric gain in a single device. A low-frequency signal could be sent into the resonator using a bias input or a magnetic field, and it would be up-converted to the microwave regime through the kinetic inductance nonlinearity. Then, if the resonator is pumped slightly below its resonance frequency, it could amplify the up-converted signal through four-wave mixing. The amplified signal could be recovered at room temperature in the usual way, using a mixer and lock-in amplifier. The parametric amplifier could also be designed such that its resonance frequency could be tuned. This would be possible by sending a bias current through the kinetic inductor, like we have done in the current sensor and magnetic field sensor devices. A parametric amplifier with a loop geometry may be the most promising design, as the loop-shaped resonator's frequency could be shifted by over a gigahertz via an external magnetic field. This feature would be similar to the Josephson parametric amplifier developed by NIST. Ideally, it would allow the gain profile to be shifted in frequency space without distortion, making the device much more versatile than a simple, stationary narrow-band amplifier.

7.6 Quantum-limited noise in KPUP devices

In the above sections we have discussed strategies for reducing the noise of the various KPUP devices. These discussions were based on the design and experimental paradigms that were employed in the work presented in this thesis. Ultimately, as discussed in various sections of Chapt. 2, measurements made with these devices may reach the quantum limit of $\Delta E\, \Delta t = \hbar/2$. To begin, a quantum theory of the KPUP noise performance must be developed. The preliminary expressions for the noise energy density found in Chapt. 2 can be made arbitrarily small, which is unphysical due to the Heisenberg uncertainty principle. The new theory should lead to a lower bound of $\hbar/2$ for the noise energy density. For the resonator devices, the theory must include the full nonlinear dynamics of the resonance, because driving the resonance into the bifurcation regime will be important for approaching the quantum limit. Similarly, for the transmission line KPUP, the theory should include the effects of dispersion engineering, which will be important to reach the quantum limit for that device. Following the theory, design and experimental considerations for the

KPUP devices will be modified slightly in order to optimize the performance, though the bullet points earlier in this chapter will largely still apply. If quantum-limited KPUPs are successfully demonstrated, they should become even more attractive in comparison to SQUIDs. This presents perhaps the most interesting direction for future work on kinetic inductance parametric up-converters.

BIBLIOGRAPHY

[1] R. A. Alpher and R. Herman. "Evolution of the Universe". *Nature* **162**.**4124**, 774–775 (1948).

[2] G. Gamow. "The Origin of Elements and the Separation of Galaxies". *Physical Review* **74**.**4**, 505–506 (1948).

[3] G. Gamow. "The Evolution of the Universe". *Nature* **162**.**4122**, 680–682 (1948).

[4] G. F. Smoot. "CMB anisotropy experiments". *Physics Reports* **333**, 269–308 (2000).

[5] A. A. Penzias and R. W. Wilson. "A Measurement of Excess Antenna Temperature at 4080 Mc/s." *The Astrophysical Journal* **142**, 419–421 (1965).

[6] D. J. Fixsen et al. "Cosmic microwave background dipole spectrum measured by the COBE FIRAS instrument". *The Astrophysical Journal* **420**.**2**, 445–449 (1994).

[7] F. Melchiorri et al. "Fluctuations in the microwave background at intermediate angular scales". *The Astrophysical Journal* **250**, L1–L4 (1981).

[8] P. de Bernardis et al. "A flat Universe from high-resolution maps of the cosmic microwave background radiation". *Nature* **404**.**6781**, 955–959 (2000).

[9] P. A. R. Ade et al. "Detection of *B*-Mode Polarization at Degree Angular Scales by BICEP2". *Physical Review Letters* **112**.**24**, 241101 (2014).

[10] J. M. Kovac et al. "Detection of polarization in the cosmic microwave background using DASI". *Nature* **420**.**6917**, 772–787 (2002).

[11] A. C. S. Readhead et al. "Polarization Observations with the Cosmic Background Imager". *Science* **306**.**5697**, 836–844 (2004).

[12] G. Hinshaw et al. "Nine-year Wilkinson Microwave Anisotropy Probe (WMAP) observations: cosmological parameter results". *The Astrophysical Journal Supplement Series* **208**.**2**, 19 (2013).

[13] C. L. Bennett et al. "Nine-year Wilkinson Microwave Anisotropy Probe (WMAP) observations: final maps and results". *The Astrophysical Journal Supplement Series* **208**.**2**, 20 (2013).

[14] D. J. Fixsen et al. "The Cosmic Microwave Background Spectrum from the Full COBE* FIRAS Data Set". *The Astrophysical Journal* **473**.**2**, 576–587 (1996).

[15] V. A. Rubakov, M. V. Sazhin, and A. V. Veryaskin. "Graviton creation in the inflationary universe and the grand unification scale". *Physics Letters B* **115**.**3**, 189–192 (1982).

[16] R. Fabbri and M. D. Pollock. "The effect of primordially produced gravitons upon the anisotropy of the cosmological microwave background radiation". *Physics Letters B* **125**.**6**, 445–448 (1983).

[17] L. F. Abbott and M. B. Wise. "Constraints on generalized inflationary cosmologies". *Nuclear Physics B* **244**.**2**, 541–548 (1984).

[18] L. M. Krauss and F. Wilczek. "Using cosmology to establish the quantization of gravity". *Physical Review D* **89**.**4**, 047501 (2014).

[19] U. Seljak. "Measuring Polarization in the Cosmic Microwave Background". *The Astrophysical Journal* **482**.**1**, 6–16 (1997).

[20] M. Kamionkowski, A. Kosowsky, and A. Stebbins. "A Probe of Primordial Gravity Waves and Vorticity". *Physical Review Letters* **78**.**11**, 2058–2061 (1997).

[21] U. Seljak and M. Zaldarriaga. "Signature of Gravity Waves in the Polarization of the Microwave Background". *Physical Review Letters* **78**.**11**, 2054–2057 (1997).

[22] P. A. R. Ade et al. "Joint Analysis of BICEP2/*Keck Array* and *Planck* Data". *Physical Review Letters* **114**.**10**, 101301 (2015).

[23] R. Adam et al. "Planck 2015 results – I. Overview of products and scientific results". *Astronomy & Astrophysics* **594**, A1 (2016).

[24] R. Adam et al. "Planck 2015 results – X. Diffuse component separation: Foreground maps". *Astronomy & Astrophysics* **594**, A10 (2016).

[25] P. A. R. Ade et al. "Planck 2015 results – XIII. Cosmological parameters". *Astronomy & Astrophysics* **594**, A13 (2016).

[26] NASA/JPL-Caltech/ESA. *PIA16874: The Universe Comes into Sharper Focus*. 2013. URL: `http://photojournal.jpl.nasa.gov/catalog/PIA16874` (visited on 07/29/2016).

[27] D. Hanson et al. "Detection of *B*-Mode Polarization in the Cosmic Microwave Background with Data from the South Pole Telescope". *Physical Review Letters* **111**.**14**, 141301 (2013).

[28] P. A. R. Ade et al. "Evidence for Gravitational Lensing of the Cosmic Microwave Background Polarization from Cross-Correlation with the Cosmic Infrared Background". *Physical Review Letters* **112**.**13**, 131302 (2014).

[29] P. A. R. Ade et al. "Measurement of the Cosmic Microwave Background Polarization Lensing Power Spectrum with the POLARBEAR Experiment". *Physical Review Letters* **113**.**2**, 021301 (2014).

[30] P. A. R. Ade et al. "A Measurement of the Cosmic Microwave Background *B*-Mode Polarization Power Spectrum at Sub-Degree Scales with POLARBEAR". *The Astrophysical Journal* **794**.**2**, 171 (2014).

[31] T. Essinger-Hileman et al. “The Atacama B-Mode Search: CMB Polarimetry with Transition-Edge-Sensor Bolometers”. *AIP Conference Proceedings* **1185**.**1**, 494–497 (2009).

[32] M. D. Niemack et al. “ACTPol: a polarization-sensitive receiver for the Atacama Cosmology Telescope”. *Proceedings of SPIE* **7741**, 77411S (2010).

[33] J. R. Eimer et al. “The cosmology large angular scale surveyor (CLASS): 40 GHz optical design”. *Proceedings of SPIE* **8542**, 845220 (2012).

[34] Z. Ahmed et al. “BICEP3: a 95GHz refracting telescope for degree-scale CMB polarization”. *Proceedings of SPIE* **9153**, 91531N (2014).

[35] B. Reichborn-Kjennerud et al. “EBEX: a balloon-borne CMB polarization experiment”. *Proceedings of SPIE* **7741**, 77411C (2010).

[36] A. A. Fraisse et al. “SPIDER: probing the early Universe with a suborbital polarimeter”. *Journal of Cosmology and Astroparticle Physics* **2013**.**04**, 047 (2013).

[37] D. T. Chuss et al. “The Primordial Inflation Polarization Explorer (PIPER)”. *Proceedings of SPIE* **77411**, 77411P (2010).

[38] C. R. Lawrence. “Ongoing and future ground-based and balloon-borne CMB temperature and polarization experiments”. *Proceedings of Science* **CMB2006**, 012 (2006).

[39] A. B. Crawford, D. C. Hogg, and L. E. Hunt. “A Horn-Reflector Antenna for Space Communication”. *Bell System Technical Journal* **40**.**4**, 1095–1116 (1961).

[40] E. M. Leitch et al. “Measurement of polarization with the degree angular scale interferometer”. *Nature* **420**.**6917**, 763–771 (2002).

[41] E. M. Leitch et al. “Experiment Design and First Season Observations with the Degree Angular Scale Interferometer”. *The Astrophysical Journal* **568**.**1**, 28–37 (2002).

[42] R. O’Brient. “A Log-Periodic Focal-Plane Architecture for Cosmic Microwave Background Polarimetry”. PhD thesis. University of California, Berkeley, 2010.

[43] P. L. Richards. “Bolometers for infrared and millimeter waves”. *Journal of Applied Physics* **76**.**1**, 1–24 (1994).

[44] J. Zmuidzinas. “Thermal noise and correlations in photon detection”. *Applied Optics* **42**.**25**, 4989–5008 (2003).

[45] M. Kardar. *Statistical Physics of Particles*. Cambridge University Press, 2007.

[46] S. Hanany, M. D. Niemack, and L. Page. “CMB Telescopes and Optical Systems”. In: *Planets, Stars and Stellar Systems*, 431–480. Springer, 2013.

[47] S. P. Langley. “The Bolometer and Radiant Energy”. *Proceedings of the American Academy of Arts and Sciences* **16**, 342–358 (1880).

[48] F. J. Low. “Low-Temperature Germanium Bolometer”. *Journal of the Optical Society of America* **51**.**11**, 1300–1304 (1961).

[49] M. C. Runyan et al. “ACBAR: The Arcminute Cosmology Bolometer Array Receiver”. *The Astrophysical Journal Supplement Series* **149**.**2**, 265–287 (2003).

[50] S. Hanany et al. “MAXIMA-1: A Measurement of the Cosmic Microwave Background Anisotropy on Angular Scales of 10′–5°”. *The Astrophysical Journal Letters* **545**.**1**, L5–L9 (2000).

[51] F. Piacentini et al. “The BOOMERANG North America Instrument: A Balloon-borne Bolometric Radiometer Optimized for Measurements of Cosmic Background Radiation Anisotropies from 0°.3 to 4°”. *The Astrophysical Journal Supplement Series* **138**.**2**, 315–336 (2002).

[52] W. A. Holmes et al. “Initial test results on bolometers for the Planck high frequency instrument”. *Applied Optics* **47**.**32**, 5996–6008 (2008).

[53] M. J. Griffin et al. “The Herschel-SPIRE instrument and its in-flight performance”. *Astronomy & Astrophysics* **518**, L3 (2010).

[54] K. D. Irwin and G. C. Hilton. “Transition-Edge Sensors”. In: *Cryogenic Particle Detection*, 63–150. Springer, 2005.

[55] H. K. Onnes. “Further experiments with liquid helium. C. On the change of electric resistance of pure metals at very low temperatures etc. IV. The resistance of pure mercury at helium temperatures”. *Koninklijke Nederlandsche Akademie van Wetenschappen Proceedings* **13**.**2**, 1274–1276 (1911).

[56] D. H. Andrews et al. “Attenuated Superconductors I. For Measuring Infra-Red Radiation”. *Review of Scientific Instruments* **13**.**7**, 281–292 (1942).

[57] K. D. Irwin. “An application of electrothermal feedback for high resolution cryogenic particle detection”. *Applied Physics Letters* **66**.**15**, 1998–2000 (1995).

[58] R. C. Jaklevic et al. “Quantum Interference Effects in Josephson Tunneling”. *Physical Review Letters* **12**.**7**, 159–160 (1964).

[59] J. Clarke and A. I. Braginski. *The SQUID Handbook*. WILEY-VCH Verlag GmbH & Co. KGaA, Weinheim, 2004.

[60] B. R. Johnson et al. “MAXIPOL: a balloon-borne experiment for measuring the polarization anisotropy of the cosmic microwave background radiation”. *New Astronomy Reviews* **47**.**11**, 1067–1075 (2003).

[61] Z. D. Kermish et al. “The POLARBEAR experiment”. *Proceedings of SPIE* **8452**, 84521C (2012).

[62] B. P. Crill et al. “SPIDER: a balloon-borne large-scale CMB polarimeter”. *Proceedings of SPIE* **7010**, 70102P (2008).

[63] W. Holland et al. “SCUBA-2: a 10,000-pixel submillimeter camera for the James Clerk Maxwell Telescope”. *Proceedings of SPIE* **6275**, 62751E (2006).

[64] K. D. Irwin et al. “X-ray detection using a superconducting transition-edge sensor microcalorimeter with electrothermal feedback”. *Applied Physics Letters* **69**.**13**, 1945–1947 (1996).

[65] J. A. Chervenak et al. “Fabrication of transition edge sensor X-ray microcalorimeters for Constellation-X”. *Nuclear Instruments and Methods in Physics Research Section A: Accelerators, Spectrometers, Detectors and Associated Equipment* **520**.**1**, 460–462 (2004).

[66] N. A. Miller et al. “High resolution x-ray transition-edge sensor cooled by tunnel junction refrigerators”. *Applied Physics Letters* **92**.**16**, 163501 (2008).

[67] D. A. Wollman et al. “Superconducting transition-edge-microcalorimeter X-ray spectrometer with 2eV energy resolution at 1.5 keV”. *Nuclear Instruments and Methods in Physics Research Section A: Accelerators, Spectrometers, Detectors and Associated Equipment* **444**.**1**, 145–150 (2000).

[68] G. C. Hilton et al. “Impact energy measurement in time-of-flight mass spectrometry with cryogenic microcalorimeters”. *Nature* **391**.**6668**, 672–675 (1998).

[69] D. Twerenbold et al. “Detection of single macromolecules using a cryogenic particle detector coupled to a biopolymer mass spectrometer”. *Applied Physics Letters* **68**.**24**, 3503–3505 (1996).

[70] K. D. Irwin et al. “A quasiparticle-trap-assisted transition-edge sensor for phonon-mediated particle detection”. *Review of Scientific Instruments* **66**.**11**, 5322–5326 (1995).

[71] B. Cabrera et al. “Cryogenic detectors based on superconducting transition-edge sensors for time-energy-resolved single-photon counters and for dark matter searches”. *Physica B: Condensed Matter* **280**.**1**, 509–514 (2000).

[72] B. Cabrera et al. “Detection of single infrared, optical, and ultraviolet photons using superconducting transition edge sensors”. *Applied Physics Letters* **73**.**6**, 735–737 (1998).

[73] D. Rosenberg et al. “Noise-free high-efficiency photon-number-resolving detectors”. *Physical Review A* **71**.**6**, 061803 (2005).

[74] A. E. Lita, A. J. Miller, and S. W. Nam. “Counting near-infrared single-photons with 95% efficiency”. *Optics Express* **16**.**5**, 3032–3040 (2008).

[75] R. H. Hadfield. “Single-photon detectors for optical quantum information applications”. *Nature Photonics* **3**.**12**, 696–705 (2009).

[76] M. D. Eisaman et al. “Invited Review Article: Single-photon sources and detectors”. *Review of Scientific Instruments* **82**.**7**, 071101 (2011).

[77] T. Isoshima et al. “Ultrahigh sensitivity single-photon detector using a Si avalanche photodiode for the measurement of ultraweak biochemiluminescence”. *Review of Scientific Instruments* **66**.**4**, 2922–2926 (1995).

[78] M. Viterbini, A. Adriani, and G. Di Donfrancesco. “Single photon detection and timing system for a Lidar experiment”. *Review of Scientific Instruments* **58**.**10**, 1833–1839 (1987).

[79] S. A. Soper, Q. L. Mattingly, and P. Vegunta. “Photon Burst Detection of Single Near-Infrared Fluorescent Molecules”. *Analytical Chemistry* **65**.**6**, 740–747 (1993).

[80] F. Sizov. “THz radiation sensors”. *Opto-Electronics Review* **18**.**1**, 10–36 (2010).

[81] J. F. Federici et al. “THz imaging and sensing for security applications—explosives, weapons and drugs”. *Semiconductor Science and Technology* **20**.**7**, S266–S280 (2005).

[82] R. L. Fagaly. “Superconducting quantum interference device instruments and applications”. *Review of Scientific Instruments* **77**.**10**, 101101 (2006).

[83] F. London. *Superfluids*. John Wiley & Sons, Inc., 1950.

[84] B. S. Deaver Jr and W. M. Fairbank. “Experimental Evidence for Quantized Flux in Superconducting Cylinders”. *Physical Review Letters* **7**.**2**, 43–46 (1961).

[85] R. Doll and M. Näbauer. “Experimental Proof of Magnetic Flux Quantization in a Superconducting Ring”. *Physical Review Letters* **7**.**2**, 51–52 (1961).

[86] M. Tinkham. *Introduction to Superconductivity, Second Edition*. Dover Publications, Inc., 2004.

[87] B. D. Josephson. “Possible new effects in superconductive tunnelling”. *Physics Letters* **1**.**7**, 251–253 (1962).

[88] C. D. Tesche and J. Clarke. “dc SQUID: noise and optimization”. *Journal of Low Temperature Physics* **29**.**3**, 301–331 (1977).

[89] R. L. Forgacs and A. Warnick. “Digital-Analog Magnetometer Utilizing Superconducting Sensor”. *Review of Scientific Instruments* **38**.**2**, 214–220 (1967).

[90] O. Noroozian. “Superconducting Microwave Resonator Arrays for Submillimeter/Far-Infrared Imaging”. PhD thesis. California Institute of Technology, 2012.

[91] K. D. Irwin et al. “Shannon Limits for Low-Temperature Detector Readout”. *AIP Conference Proceedings* **1185**.**1**, 229–236 (2009).

[92] J. A. Chervenak et al. “Superconducting multiplexer for arrays of transition edge sensors”. *Applied Physics Letters* **74**.**26**, 4043–4045 (1999).

[93] P. A. J. de Korte et al. “Time-division superconducting quantum interference device multiplexer for transition-edge sensors”. *Review of Scientific Instruments* **74**.**8**, 3807–3815 (2003).

[94] K. D. Irwin et al. “Time-Division SQUID Multiplexers”. *AIP Conference Proceedings* **605**.**1**, 301–304 (2002).

[95] J. Yoon et al. “Single superconducting quantum interference device multiplexer for arrays of low-temperature sensors”. *Applied Physics Letters* **78**.**3**, 371–373 (2001).

[96] M. Kiviranta et al. “SQUID-based Readout Schemes for Microcalorimeter Arrays”. *AIP Conference Proceedings* **605**.**1**, 295–300 (2002).

[97] T. Miyazaki et al. “AC Calorimeter Bridge; a new multi-pixel readout method for TES calorimeter arrays”. *AIP Conference Proceedings* **605**.**1**, 313–316 (2002).

[98] K. D. Irwin and K. W. Lehnert. “Microwave SQUID multiplexer”. *Applied Physics Letters* **85**.**11**, 2107–2109 (2004).

[99] T. M. Lanting et al. “Frequency-domain multiplexing for large-scale bolometer arrays”. *Proceedings of SPIE* **4855**, 172–181 (2003).

[100] K. D. Osborn et al. “Frequency-Tunable Josephson Junction Resonator for Quantum Computing”. *IEEE Transactions on Applied Superconductivity* **17**.**2**, 166–168 (2007).

[101] P. K. Day et al. “A broadband superconducting detector suitable for use in large arrays”. *Nature* **425**.**6960**, 817–821 (2003).

[102] T. R. Stevenson et al. “Multiplexing of radio-frequency single-electron transistors”. *Applied Physics Letters* **80**.**16**, 3012–3014 (2002).

[103] J. A. B. Mates et al. “Demonstration of a multiplexer of dissipationless superconducting quantum interference devices”. *Applied Physics Letters* **92**.**2**, 023514 (2008).

[104] C. Enss et al. “Metallic Magnetic Calorimeters for Particle Detection”. *Journal of Low Temperature Physics* **121**.**3**, 137–176 (2000).

[105] A. Fleischmann et al. “Metallic magnetic calorimeters (MMC): detectors for high-resolution X-ray spectroscopy”. *Nuclear Instruments and Methods in Physics Research Section A: Accelerators, Spectrometers, Detectors and Associated Equipment* **520**.**1**, 27–31 (2004).

[106] A. Fleischmann, C. Enss, and G. M. Seidel. “Metallic Magnetic Calorimeters”. In: *Cryogenic Particle Detection*, 151–216. Springer, 2005.

[107] B. L. Zink et al. “Lithographically patterned magnetic calorimeter X-ray detectors with integrated SQUID readout”. *Nuclear Instruments and Methods in Physics Research Section A: Accelerators, Spectrometers, Detectors and Associated Equipment* **520**.**1**, 52–55 (2004).

[108] C. A. Mears et al. “High-Resolution Superconducting X-Ray Spectrometers With an Active Area of 282 µm × 282 µm”. *IEEE Transactions on Applied Superconductivity* **7**.**2**, 3415–3418 (1997).

[109] J. N. Ullom. “Physics and Applications of NIS Junctions”. *AIP Conference Proceedings* **605**.**1**, 135–140 (2002).

[110] M. Nahum and J. M. Martinis. “Ultrasensitive-hot-electron microbolometer”. *Applied Physics Letters* **63**.**22**, 3075–3077 (1993).

[111] J. Wei et al. “Ultrasensitive hot-electron nanobolometers for terahertz astrophysics”. *Nature Nanotechnology* **3**.**8**, 496–500 (2008).

[112] Y. S. Greenberg. “Application of superconducting quantum interference devices to nuclear magnetic resonance”. *Reviews of Modern Physics* **70**.**1**, 175–222 (1998).

[113] R. A. Webb. “New technique for improved low-temperature SQUID NMR measurements”. *Review of Scientific Instruments* **48**.**12**, 1585–1594 (1977).

[114] R. McDermott et al. “Microtesla MRI with a superconducting quantum interference device”. *Proceedings of the National Academy of Sciences of the United States of America* **101**.**21**, 7857–7861 (2004).

[115] V. S. Zotev et al. “Microtesla MRI of the human brain combined with MEG”. *Journal of Magnetic Resonance* **194**.**1**, 115–120 (2008).

[116] K. P. Pruessmann et al. “SENSE: Sensitivity Encoding for Fast MRI”. *Magnetic Resonance in Medicine* **42**.**5**, 952–962 (1999).

[117] M. Hämäläinen et al. “Magnetoencephalography—theory, instrumentation, and applications to noninvasive studies of the working human brain”. *Reviews of Modern Physics* **65**.**2**, 413–497 (1993).

[118] W. G. Jenks, S. S. H. Sadeghi, and J. P. Wikswo Jr. “SQUIDs for nondestructive evaluation”. *Journal of Physics D: Applied Physics* **30**.**3**, 293–323 (1997).

[119] B. P. Weiss et al. “A Low Temperature Transfer of ALH84001 from Mars to Earth”. *Science* **290**.**5492**, 791–795 (2000).

[120] P. Drude. “Zur Elektronentheorie der Metalle”. *Annalen der Physik* **306**.**3**, 566–613 (1900).

[121] N. W. Ashcroft and N. D. Mermin. *Solid State Physics*. Brooks/Cole, Cengage Learning, 1976.

[122] J. Gao. "The Physics of Superconducting Microwave Resonators". PhD thesis. California Institute of Technology, 2008.

[123] J. Zmuidzinas. "Superconducting Microresonators: Physics and Applications". *Annual Review of Condensed Matter Physics* **3.1**, 169–214 (2012).

[124] J. D. Jackson. *Classical Electrodynamics, Third Edition*. John Wiley & Sons, Inc., 1999.

[125] J. Bardeen, L. N. Cooper, and J. R. Schrieffer. "Microscopic Theory of Superconductivity". *Physical Review* **106.1**, 162–164 (1957).

[126] J. Bardeen, L. N. Cooper, and J. R. Schrieffer. "Theory of Superconductivity". *Physical Review* **108.5**, 1175–1204 (1957).

[127] D. C. Mattis and J. Bardeen. "Theory of the Anomalous Skin Effect in Normal and Superconducting Metals". *Physical Review* **111.2**, 412 (1958).

[128] A. B. Pippard. "Field Variation of the Superconducting Penetration Depth". *Proceedings of the Royal Society of London A: Mathematical, Physical and Engineering Sciences* **203.1073**, 210–223 (1950).

[129] A. B. Pippard. "An Experimental and Theoretical Study of the Relation between Magnetic Field and Current in a Superconductor". *Proceedings of the Royal Society of London A: Mathematical, Physical and Engineering Sciences* **216.1127**, 547–568 (1953).

[130] R. H. Parmenter. "Nonlinear Electrodynamics of Superconductors with a Very Small Coherence Distance". *RCA Review* **23.3**, 323–352 (1962).

[131] K. D. Usadel. "Generalized Diffusion Equation for Superconducting Alloys". *Physical Review Letters* **25.8**, 507–509 (1970).

[132] A. Anthore, H. Pothier, and D. Esteve. "Density of States in a Superconductor Carrying a Supercurrent". *Physical Review Letters* **90.12**, 127001 (2003).

[133] L. D. Landau and V. L. Ginzburg. "On the theory of superconductivity". *Zhurnal Éksperimental'noĭ i Teoreticheskoĭ Fiziki* **20**, 1064 (1950).

[134] G. P. Agrawal. *Nonlinear Fiber Optics, Fourth Edition*. Elsevier Inc., 2007.

[135] É. S. Voronin and V. Strizhevskiĭ. "Parametric up-conversion of infrared radiation and its applications". *Soviet Physics Uspekhi* **22.1**, 26–45 (1979).

[136] F. Bitter et al. "Superconductivity of Lead at 3-Cm Wave-Length". *Physical Review* **70.1–2**, 97–98 (1946).

[137] A. B. Pippard. "The surface impedance of superconductors and normal metals at high frequencies – I. Resistance of superconducting tin and mercury at 1200 Mcyc./sec." *Proceedings of the Royal Society of London A: Mathematical, Physical and Engineering Sciences* **191.1026**, 370–384 (1947).

[138] A. B. Pippard. “The surface impedance of superconductors and normal metals at high frequencies – II. The anomalous skin effect in normal metals”. *Proceedings of the Royal Society of London A: Mathematical, Physical and Engineering Sciences* **191**.**1026**, 385–399 (1947).

[139] J. P. Turneaure and I. Weissman. “Microwave Surface Resistance of Superconducting Niobium”. *Journal of Applied Physics* **39**.**9**, 4417–4427 (1968).

[140] A. Septier and N. T. Viet. “Microwave applications of superconducting materials”. *Journal of Physics E: Scientific Instruments* **10**.**12**, 1193 (1977).

[141] J. Halbritter. “On the oxidation and on the superconductivity of niobium”. *Applied Physics A* **43**.**1**, 1–28 (1987).

[142] G. Ciovati. “Effect of low-temperature baking on the radio-frequency properties of niobium superconducting cavities for particle accelerators”. *Journal of Applied Physics* **96**.**3**, 1591–1600 (2004).

[143] P. V. Mason and R. W. Gould. “Slow-Wave Structures Utilizing Superconducting Thin-Film Transmission Lines”. *Journal of Applied Physics* **40**.**5**, 2039–2051 (1969).

[144] J. M. Martinis et al. “Decoherence in Josephson Qubits from Dielectric Loss”. *Physical Review Letters* **95**.**21**, 210503 (2005).

[145] O. Noroozian et al. “Two-level system noise reduction for Microwave Kinetic Inductance Detectors”. *AIP Conference Proceedings* **1185**.**1**, 148–151 (2009).

[146] J. Gao et al. “Noise properties of superconducting coplanar waveguide microwave resonators”. *Applied Physics Letters* **90**.**10**, 102507 (2007).

[147] J. Gao et al. “Experimental evidence for a surface distribution of two-level systems in superconducting lithographed microwave resonators”. *Applied Physics Letters* **92**.**15**, 152505 (2008).

[148] J. Gao et al. “A semiempirical model for two-level system noise in superconducting microresonators”. *Applied Physics Letters* **92**.**21**, 212504 (2008).

[149] D. S. Wisbey et al. “Effect of metal/substrate interfaces on radio-frequency loss in superconducting coplanar waveguides”. *Journal of Applied Physics* **108**.**9**, 093918 (2010).

[150] J. M. Sage et al. “Study of loss in superconducting coplanar waveguide resonators”. *Journal of Applied Physics* **109**.**6**, 063915 (2011).

[151] S. Doyle et al. “Lumped Element Kinetic Inductance Detectors”. *Journal of Low Temperature Physics* **151**.**1**, 530–536 (2008).

[152] R. Barends et al. “Contribution of dielectrics to frequency and noise of NbTiN superconducting resonators”. *Applied Physics Letters* **92**.**22**, 223502 (2008).

[153] H. G. Leduc et al. “Titanium nitride films for ultrasensitive microresonator detectors”. *Applied Physics Letters* **97**.**10**, 102509 (2010).

[154] C. M. McKenney et al. “Design considerations for a background limited 350 micron pixel array using lumped element superconducting microresonators”. *Proceedings of SPIE* **8452**, 84520S (2012).

[155] G. Duffing. *Erzwungene Schwingungen bei veränderlicher Eigenfrequenz und ihre technische Bedeutung*. R, Vieweg & Sohn, 1918.

[156] L. J. Swenson et al. “Operation of a titanium nitride superconducting microresonator detector in the nonlinear regime”. *Journal of Applied Physics* **113**.**10**, 104501 (2013).

[157] R. Barends et al. “Reduced frequency noise in superconducting resonators”. *Applied Physics Letters* **97**.**3**, 033507 (2010).

[158] M. Hatridge et al. “Dispersive magnetometry with a quantum limited SQUID parametric amplifier”. *Physical Review B* **83**.**13**, 134501 (2011).

[159] R. H. Koch, D. J. Van Harlingen, and J. Clarke. “Quantum noise theory for the dc SQUID”. *Applied Physics Letters* **38.5**, 380–382 (1981).

[160] R. J. Schoelkopf et al. “The Radio-Frequency Single-Electron Transistor (RF-SET): A Fast and Ultrasensitive Electrometer”. *Science* **280**.**5367**, 1238–1242 (1998).

[161] H. T. Su et al. “Superconducting delay lines”. *Journal of Superconductivity and Novel Magnetism* **21**.**1**, 7–16 (2008).

[162] T. C. L. G. Sollner et al. “Superconducting Cueing Receiver for Space Experiment”. *IEEE Transactions on Applied Superconductivity* **5**.**2**, 2071–2074 (1995).

[163] G.-C. Liang et al. “Space-Qualified Superconductive Digital Instantaneous Frequency-Measurement Subsystem”. *IEEE Transactions on Microwave Theory and Techniques* **44**.**7**, 1289–1299 (1996).

[164] R. F. Jeffries et al. “Further Development of a Future ESM Channeliser with High Temperature Superconducting Filters”. *IEEE Transactions on Applied Superconductivity* **11**.**1**, 410–413 (2001).

[165] D. J. Kapolnek et al. “Integral FMCW Radar Incorporating an HTSC Delay Line with User-Transparent Cryogenic Cooling and Packaging”. *IEEE Transactions on Applied Superconductivity* **3**.**1**, 2820–2823 (1993).

[166] D. A. Gandolfo, A. Boornard, and L. C. Morris. “Superconductive Microwave Meander Lines”. *Journal of Applied Physics* **39**.**6**, 2657–2660 (1968).

[167] G. K. G. Hohenwarter et al. “Forty five nanoseconds superconducting delay lines”. *IEEE Transactions on Applied Superconductivity* **3**.**1**, 2804–2807 (1993).

[168] S. H. Talisa et al. “High-Temperature Superconducting Wide Band Delay Lines”. *IEEE Transactions on Applied Superconductivity* **5.2**, 2291–2294 (1995).

[169] E. K. Track, R. E. Drake, and G. K. G. Hohenwarter. “Optically modulated superconducting delay lines”. *IEEE Transactions on Applied Superconductivity* **3.1**, 2899–2902 (1993).

[170] N. Fenzi et al. “Development of high-temperature superconducting 100-ns delay line”. *Proceedings of SPIE* **2156**, 143–151 (1994).

[171] G. C. Liang et al. “High-Temperature Superconducting Delay Lines and Filters on Sapphire and Thinned $LaAlO_3$ Substrates”. *IEEE Transactions on Applied Superconductivity* **3.3**, 3037–3042 (1993).

[172] S. M. Anlage, H. J. Snortland, and M. R. Beasley. “A current controlled variable delay superconducting transmission line”. *IEEE Transactions on Magnetics* **25.2**, 1388–1391 (1989).

[173] J. Hansryd et al. “Fiber-Based Optical Parametric Amplifiers and Their Applications”. *IEEE Journal of Selected Topics in Quantum Electronics* **8.3**, 506–520 (2002).

[174] B. H. Eom et al. “A wideband, low-noise superconducting amplifier with high dynamic range”. *Nature Physics* **8.8**, 623–627 (2012).

[175] C. Bockstiegel et al. “Development of a Broadband NbTiN Traveling Wave Parametric Amplifier for MKID Readout”. *Journal of Low Temperature Physics* **176.3-4**, 476–482 (2014).

[176] D. M. Pozar. *Microwave Engineering*. Addison-Wesley Publishing Company, Inc., 1990.

[177] R. Landauer. “Shock Waves in Nonlinear Transmission Lines and Their Effect on Parametric Amplification”. *IBM Journal of Research and Development* **4.4**, 391–401 (1960).

[178] B. A. Mazin et al. “Thin film dielectric microstrip kinetic inductance detectors”. *Applied Physics Letters* **96.10**, 102504 (2010).

[179] J. Li et al. “Development of an 8×8 CPW Microwave Kinetic Inductance Detector (MKID) Array at 0.35 THz”. *Journal of Low Temperature Physics* **184.1**, 103–107 (2016).

[180] E. Shirokoff et al. “MKID development for SuperSpec: an on-chip, mm-wave, filter-bank spectrometer”. *Proceedings of SPIE* **8452**, 84520R (2012).

[181] A. Endo et al. “Design of an Integrated Filterbank for DESHIMA: On-Chip Submillimeter Imaging Spectrograph Based on Superconducting Resonators”. *Journal of Low Temperature Physics* **167.3**, 341–346 (2012).

[182] J. Healey et al. “Magnetic field tuning of coplanar waveguide resonators”. *Applied Physics Letters* **93.4**, 043513 (2008).

[183] E. A. Tholén et al. "Nonlinearities and parametric amplification in superconducting coplanar waveguide resonators". *Applied Physics Letters* **90**.**25**, 253509 (2007).

[184] J. Ku, V. Manucharyan, and A. Bezryadin. "Superconducting nanowires as nonlinear inductive elements for qubits". *Physical Review B* **82**.**13**, 134518 (2010).

[185] R. Igreja and C. J. Dias. "Analytical evaluation of the interdigital electrodes capacitance for a multi-layered structure". *Sensors and Actuators A: Physical* **112**.**2**, 291–301 (2004).

[186] Sonnet Software, Inc. *Sonnet*. Version 13.56. URL: `http://www.sonnetsoftware.com/`.

[187] L. Novotny. "Strong coupling, energy splitting, and level crossings: A classical perspective". *American Journal of Physics* **78**.**11**, 1199–1202 (2010).

[188] H. L. Hortensius et al. "Critical-current reduction in thin superconducting wires due to current crowding". *Applied Physics Letters* **100**.**18**, 182602 (2012).

[189] J. R. Clem and K. K. Berggren. "Geometry-dependent critical currents in superconducting nanocircuits". *Physical Review B* **84**.**17**, 174510 (2011).

[190] J. C. Mather. "Bolometer noise: nonequilibrium theory". *Applied Optics* **21**.**6**, 1125–1129 (1982).

[191] L. R. Fortney. *Principles of Electronics: Analog and Digital*. Harcourt Brace Jovanovich, 1987.

[192] O. Noroozian et al. "Crosstalk Reduction for Superconducting Microwave Resonator Arrays". *IEEE Transactions on Microwave Theory and Techniques* **60**.**5**, 1235–1243 (2012).

[193] J. Luomahaara et al. "Kinetic inductance magnetometer". *Nature Communications* **5**, 4872 (2014).

[194] W. Mumford. "Some Notes on the History of Parametric Transducers". *Proceedings of the IRE* **48**.**5**, 848–853 (1960).

[195] L. Nergaard. "Nonlinear-capacitance amplifiers". *RCA Review* **20**.**1**, 3–17 (1959).

[196] W. H. Louisell, A. Yariv, and A. E. Siegman. "Quantum Fluctuations and Noise in Parametric Processes. I." *Physical Review* **124**.**6**, 1646–1654 (1961).

[197] J. J. Whelehan. "Low-Noise Amplifiers—Then and Now". *IEEE Transactions on Microwave Theory and Techniques* **50**.**3**, 806–813 (2002).

[198] A. A. Clerk et al. "Introduction to quantum noise, measurement, and amplification". *Reviews of Modern Physics* **82**.**2**, 1155 (2010).

[199] M. Castellanos-Beltran et al. “Amplification and squeezing of quantum noise with a tunable Josephson metamaterial”. *Nature Physics* **4**.**12**, 929–931 (2008).

[200] J. Zmuidzinas and P. K. Day. *Dispersion-engineered traveling wave kinetic inductance parametric amplifier*. U.S. Patent 8,878,626. Nov. 2014.

[201] R. A. Connell. “Parametric Amplification in Thin Film Superconducting Transmission Lines”. *Proceedings of the IEEE* **51**.**4**, 616–617 (1963).

[202] R. A. Connell. “Characteristics of the Penetration Depth of Superconducting Indium Alloys”. *Physical Review* **129**.**5**, 1952–1958 (1963).

[203] R. Landauer. “Parametric standing wave amplifiers”. *Proceedings of the Institute of Radio Engineers* **48**.**7**, 1328–1329 (1960).

[204] A. S. Clorfeine. “Nonlinear reactance and frequency conversion in superconducting films at millimeter wavelengths”. *Applied Physics Letters* **4**.**7**, 131–132 (1964).

[205] H. Zimmer. “Parametric amplification of microwaves in superconducting Josephson tunnel junctions”. *Applied Physics Letters* **10**.**7**, 193–195 (1967).

[206] A. Smith et al. “Low noise microwave parametric amplifier”. *IEEE Transactions on Magnetics* **21**.**2**, 1022–1028 (1985).

[207] B. Yurke et al. “Observation of 4.2-K Equilibrium-Noise Squeezing via a Josephson-Parametric Amplifier”. *Physical Review Letters* **60**.**9**, 764–767 (1988).

[208] R. Movshovich et al. “Observation of Zero-Point Noise Squeezing via a Josephson-Parametric Amplifier”. *Physical Review Letters* **65**.**12**, 1419–1422 (1990).

[209] C. M. Caves. “Quantum limits on noise in linear amplifiers”. *Physical Review D* **26**.**8**, 1817–1839 (1982).